Aircraft air data system based on the measurement of Raman and elastic backscatter via active optical remote-sensing

Dissertation zur Erlangung des Doktorgrades
der Naturwissenschaften (Dr. rer. nat.)

Fakultät Naturwissenschaften
Universität Hohenheim

Institut für Physik und Meteorologie

vorgelegt von
Michael Darius Fraczek

aus Krakau, Polen
2012

This thesis was accepted as a doctoral dissertation in fulfillment of the requirements for the degree "Doktor der Naturwissenschaften" by the Faculty of Natural Sciences at the University of Hohenheim, Stuttgart, Germany on 13 June 2013.

Date of submission:	10 December 2012
Date of oral examination:	19 September 2013

Examination committee:

Supervisor and reviewer:	Prof. Dr. Volker Wulfmeyer Institute of Physics and Meteorology, University of Hohenheim, Stuttgart, Germany
Co-reviewer:	Prof. Dr. Paolo Di Girolamo Scuola di Ingegneria, University of Basilicata, Potenza, Italy
Additional examiner:	Prof. Dr.-Ing. Jörg Hinrichs Institute of Food Science and Biotechnology, University of Hohenheim, Stuttgart, Germany
Dean:	Prof. Dr. Heinz Breer Faculty of Natural Sciences, University of Hohenheim, Stuttgart, Germany

To my grandparents.

Dla moich dziadków.

Abstract

Flight safety in all weather conditions demands exact and reliable determination of flight-critical air parameters. Conventional aircraft air data systems can be impacted by probe failure caused by mechanical damage or impairment due to different environmental influences. In this thesis, a novel measurement concept for optically measuring the air temperature, density, pressure, moisture and particle backscatter for aircrafts is presented. The detection of volcanic ash is possible as well. This concept is independent from assumptions about the atmospheric state and eliminates the drawbacks of conventional aircraft probes. The measurement principle is based on a laser emitting pulses into the atmosphere from inside the aircraft and a receiver detecting the light signals backscattered from a defined region just outside the disturbed area of the fuselage air flow. With four receiver channels, different spectral portions of the Raman backscatter of dry air and water vapor, as well as the elastic backscatter are extracted. Measurements at daytime and in any atmospheric condition, including very dense clouds, are possible.

In the framework of this thesis, a first laboratory prototype of such a measurement system using 532 nm laser radiation was developed, comprising all relevant theoretical and experimental studies. These were notably the comparative feasibility assessment of the measurement methodology, the computational modeling of the measurement concept, the laboratory setup and the experimental validation.

Detailed and realistic performance and optimization calculations were made based on the parameters of the first prototype. The impact and the correction of systematic errors due to solar background and elastic signal cross-talk appearing in optically dense clouds were analyzed in computational simulations. The simulations supplement the experimental results for measurement scenarios that are not generable in the laboratory.

The laboratory experiments validate the predictions from the simulations with regard to systematic errors and statistical measurement uncertainties. Where possible, the experimental setup and the signal and data analysis were optimized. Residual differences between the experimental and the model results were analyzed in detail. Concrete further hardware optimizations were suggested.

The resulting experimental systematic measurement errors at air temperatures varying from 238 K to 308 K under constant air pressure are < 0.05 K, < 0.07 % and < 0.06 % for temperature, density and pressure, respectively. The systematic errors for measurements at air pressures varying from 200 hPa to 950 hPa under constant air temperature are < 0.22 K, < 0.36 % and < 0.31 %, respectively.

The experimentally achieved 1-σ statistical measurement uncertainties for the analysis of each single detected signal pulse range from 0.75 K to 2.63 K for temperature, from 0.43 % to 1.21 % for density, and from 0.51 % to 1.50 % for pressure, respectively, for measurement altitudes from 0 m to 13400 m.

In order to meet measurement error requirements specified in aviation standards, minimum laser pulse energies were experimentally determined to be used with the designed measurement system. With regard to 100-pulse-averaged temperature measurements, the pulse energy at 532 nm has to be larger than 11 mJ (35 mJ), when regarding 1-σ (3-σ) uncertainties at all measurement altitudes. For 100-pulse-averaged pressure measurements, the laser pulse energy has to be respectively larger than 95 mJ (355 mJ). Based on these experimental results, the laser pulse energy requirements were extrapolated to the ultraviolet wavelength region as well, resulting in much lower laser pulse energy demand.

The successful results of this thesis do not only prove the viability of the concept implementation, but also demonstrate its high potential for aircraft air data system application.

Zusammenfassung

Flugsicherheit bedingt die genaue und zuverlässige Bestimmung von flugkritischen Luftparametern in allen Wetterlagen. Messsonden konventioneller Flugzeugluftdatensysteme können durch mechanische Beschädigung oder Beeinträchtigung in extremen Witterungsbedingungen ausfallen. In dieser Arbeit wird ein neues Messkonzept zur optischen Messung von Lufttemperatur, -dichte, -druck, -feuchte und Partikelrückstreuung für Flugzeuge vorgestellt. Die Detektion von Vulkanasche ist ebenso möglich. Das Konzept ist unabhängig von Annahmen über den atmosphärischen Zustand und umgeht die Nachteile herkömmlicher Luftdatensysteme. Das Messprinzip beruht auf der Emission von Laserpulsen in die Atmosphäre aus dem Flugzeuginneren und der Detektion der Lichtsignale, welche in definiertem Abstand zum Flugzeug von der ungestörten Luftströmung rückgestreut werden. Mit vier Empfangskanälen werden unterschiedliche spektrale Bereiche der Raman-Rückstreuung von trockener Luft und Wasserdampf, sowie das elastische Rückstreusignal extrahiert. Messungen bei Tag und in sämtlichen Witterungsverhältnissen inklusive sehr dichten Wolken sind möglich.

Im Rahmen dieser Arbeit wurde der erste Laborprototyp eines solchen Messsystems basierend auf 532 nm Laserstrahlung entwickelt. Die Realisierung dieses Messsystems beinhaltete alle relevanten theoretischen und experimentellen Studien. Diese waren insbesondere eine vergleichende Bewertung der Durchführbarkeit der Messmethodik, die computergestützte Modellierung des Messkonzeptes, der Laboraufbau und die experimentelle Validierung.

Anhand der Parameter des Prototyps wurden detaillierte und realistische Berechnungen zur Leistungsfähigkeit und zur Systemoptimierung durchgeführt. Die Auswirkungen und die Korrekturmöglichkeiten von systematischen Fehlern wurden mittels Computersimulationen analysiert. Das Hauptaugenmerk wurde hierbei auf solare Hintergrundstrahlung und elastisches Signalübersprechen in dichten Wolken gerichtet. Diese Simulationen ergänzen die experimentellen Ergebnisse für Messszenarien, welche nicht im Labor generierbar sind.

Die Laborversuche bestätigen die Vorhersagen der Simulationen in Hinsicht auf systematische Fehler und statistische Messunsicherheiten. Die Auswertung der experimentellen Ergebnisse wurde begleitet von Optimierungen des Versuchsaufbaus sowie der Signal-und Datenanalyse. Unterschiede zwischen den experimentellen und simulierten Ergebnissen wurden im Detail analysiert und erklärt. Konkrete Verbesserungsvorschläge bezüglich des Messequipments wurden aufgezählt.

Die experimentell erzielten systematischen Messfehler bei Lufttemperaturen von 238 K bis 308 K und konstantem Luftdruck sind < 0,05 K, < 0,07 % und < 0,06 % für Temperatur-, Dichte- bzw. Druckmessungen. Die systematischen Fehler für Messungen bei unterschiedlichen Luftdrücken von 200 hPa bis 950 hPa jedoch konstanter Lufttemperatur betragen analog < 0,22 K, < 0,36 % und < 0,31 %.

Die experimentell erzielten 1-σ statistischen Messunsicherheiten für die Analyse von einzelnen Signalpulsen reichen von 0,75 K bis 2,63 K für Temperaturmessungen, von 0,43 % bis 1,21 % für Dichtemessungen sowie von 0,51 % bis 1,50 % für Druckmessungen - jeweils für Messhöhen von 0 m bis 13400 m.

Mindestenergiewerte für die Laserpulse des entworfenen Messsystems wurden experimentell ermittelt, mit welchen die in Luftverkehrsnormen spezifizierten Messfehleranforderungen erfüllt werden können. Für Temperaturmessungen, bei denen 100 Signalpulse gemittelt werden, müssen die Pulsenergien größer als 11 mJ (35 mJ) sein, damit die 1-σ (3-σ) Messunsicherheit die erwähnten Spezifikationen in allen Flughöhen unterschreitet. Analog muss die Laserpulsenergie für über 100 Pulse gemittelte Druckmessungen mindestens 95 mJ (355 mJ) betragen. Die Resultate hinsichtlich der

minimalen Pulsenergien wurden für den Fall eines im ultravioletten Spektralbereich emittierenden Lasers extrapoliert, was zu einem wesentlich geringeren Bedarf an Laserpulsenergie führte.

Die erfolgreichen Ergebnisse dieser Dissertation belegen nicht nur die Durchführbarkeit des Messkonzeptes. Sie zeigen auch das hohe Potenzial für den Einsatz eines darauf basierenden Messsystems für die flugzeuggestützte Luftdatenerfassung in unterschiedlichen atmosphärischen Verhältnissen.

Table of contents

Table of contents i

1 Introduction 1

2 Standards for aircraft air temperature and pressure sensors 4

3 Active optical remote-sensing methods 6

4 Relevant atmospheric light scattering processes 14

4.1 Overview of laser light scattering processes in the atmosphere 14
4.2 Energetic description of Raman scattering 16
4.3 RR backscattering cross sections and spectral shifts 17
4.4 Rayleigh and Cabannes scattering 20
4.5 Raman spectra of water vapor 21
4.5.1 Pure RR spectrum 22
4.5.2 Rotational-vibrational Raman spectrum 23
4.6 Elastic particle scattering - extinction coefficient and backscatter ratio 24
4.7 Solar spectral radiance 26

5 Measurement methodology 30

5.1 Air temperature and molecular number density measurement 30
5.2 Calibration of temperature and density measurement 32
5.3 Measurement of moist air density, atmospheric pressure, backscatter ratio, particle backscatter coefficient, and volcanic ash 34

6 Instrumental description 37

6.1 Laser and receiver system 37
6.2 Measurement volume 42
6.3 Atmospheric simulator 46
6.4 Interference filters 48
6.4.1 Modeled spectral transmission functions 48
6.4.2 Effect of beam divergence inside the receiver channels 50
6.4.3 Modeled and real RR filter transmission functions 52

7 Computational performance, error and optimization calculations for an aircraft-integrated sensor 53

7.1 Stability of calibration 53
7.2 Doppler-shift of backscattered radiation 55
7.3 Lidar equation for short-range detection and power of detected signal pulses 56
7.4 Choice of optimum detectors for the receiver channels 57
7.5 Optimum spectral RR filter positioning and statistical measurement uncertainties 58

7.6 Measurements during daytime 62
7.7 Measurements in optically very dense clouds 63
7.7.1 Elastic-signal leakage 63
7.7.2 Atmospheric extinction 65
7.8 Influences of water vapor on measurement error 69
7.8.1 Influence of the pure rotational Raman spectrum of water vapor 69
7.8.2 Influence of the vibrational-rotational Raman spectrum of water vapor 70
7.9 Laser power requirements obtained from simulations 72
7.10 UV versus VIS laser wavelengths - theoretical considerations 73

8 Experimental results in flight altitude atmospheric conditions 75

8.1 Optical measurements 76
8.1.1 Signal analysis and processing 76
8.1.2 RR signal recordings as function of air temperature 79
8.1.3 RR signal recordings as function of air pressure 82
8.2 Analysis of systematic measurement errors 83
8.2.1 Calibration and error at different air temperatures 83
8.2.2 Linearity of detector response and error at different air pressures 85
8.2.3 Discussion on systematic errors 89
8.3 Analysis of statistical measurement uncertainties 93
8.3.1 Optimum spectral RR-filter positions and detector gains 93
8.3.2 Comparison of uncertainties from computational model and experiment 96
8.3.3 Discussion on statistical uncertainties and refined computational model 98
8.3.4 Influence of water vapor measurement on statistical uncertainties 100
8.4 Statistical measurement uncertainties as a function of flight altitude 103
8.4.1 Measured data 103
8.4.2 General uncertainty functions 105
8.4.3 Required laser pulse energies at 532 nm 108
8.4.4 Required laser pulse energies at UV wavelengths 110

9 Summary, conclusions and outlook 115

Appendix A 119

Appendix B 120

Appendix C 124

Appendix D 126

References 127

Acknowledgments 136

1 Introduction

Continuous and precise in-flight measurements of properties of local, undisturbed, atmospheric air like the relative air flow velocity vector, air temperature and pressure are crucial for aircraft control and thus aircraft safety. Flight critical parameters as the flight speed, the angle of attack, or the flight level are derived from these data. Nowadays, the acquisition of such data is mainly based on measuring the dynamic pressure, static pressure and total temperature using Pitot tubes, static pressure ports, and electro-mechanical temperature probes [1]. These sensors are all integrated into the aircraft's skin and are measuring the properties of the airflow close to the fuselage. This has two disadvantages: Firstly, the measurements are disturbed by the fuselage flow with regard to direction, speed and compression and have to be corrected to account for undisturbed air by complicated probe calibrations. Secondly, since most probes are protruding and/or possess small apertures, they are susceptible to mechanical failure sources like icing, dust and volcanic ash plugging the probe apertures, hail damage, bird strike, corrosion and other kind of mechanical damage. On this account, normally three sets of such probes are mounted on an aircraft for redundancy reasons. But there is a residual risk that all three systems suffer from the same failure mechanism. A solution to further increase the overall reliability of aircraft sensor operation in a redundant way, is to use at least one flush-mounted air data system based on a different physical measurement principle and technology providing an independent measurement of all necessary air parameters.

For this reason, air data systems based on optical active remote-sensing technology have been studied for years [2-4], mainly focused on the measurement of air speed replacing the Pitot tube standard instrument. Funded research activities by the European Commission including flight experiments were carried out or are currently ongoing [5-8]. These activities deal with the measurement of the air velocity vector and air turbulences using direct as well as coherent optical detection. However, concepts for the measurement of the other air related parameters are rare.

In this thesis, as a further contribution to that general effort, a newly developed concept of an optical measurement system is presented. This system provides air temperature and density as direct measurement parameters at a fixed distance from the aircraft, close to the aircraft's surface, but outside the disturbed air flows and not sensitive to the aforementioned sources of failure. In addition to these parameters, the designed system will also provide atmospheric pressure needed for aircraft flight level determination, relative humidity, particle backscatter coefficient of clouds and aerosol particles, e.g. volcanic ash, and will account for atmospheric extinction. Together with the mentioned optical air speed sensors it is designed to form a fully optical air data system. It is shown, that this system has the potential to match the accuracy requirements set by standards in aviation.

A first prototype of the airborne apparatus resulting from detailed computational simulations (*Matlab*) made preliminary in this dissertation was set up in the laboratory. The measurement methodology is based on the rotational Raman temperature measurement technique suggested for lidar by Cooney in the early 1970s [9]. This measurement technique is independent of any external input parameters and knowledge about the atmospheric state. In principle, it is based on two measurement channels each extracting temperature dependent signals from the pure rotational Raman (RR) scattering of air molecules. The RR temperature measurement technique is extended to four interference-filter-based measurement channels in order to also reliably provide correct air density and pressure in all flight operation states and at all flight altitudes, during night- and daytime, as well as in clear air, clouds or aerosol layers. Within the framework of this study, the use of the RR lidar

technique is transferred into and adapted to the airborne, fixed-distance and short-range application using the latest technology. The short-range RR technique is introduced and the relevant aspects for the accurate functioning of an aircraft system are outlined.

To the knowledge of the author, the measurement principle for density and pressure is novel and described for the first time. The same applies to the application of the measurement techniques in the airborne short-range measurement configuration. The intention of this thesis is thus to show the applicability and feasibility of that concept for the purpose described. The main focus is to theoretically and experimentally assess and compare in detail the performance of the prototype in terms of accuracy and precision under separate analysis of the most important systematic and statistical error sources. The comparison of the computational simulations and the experimental results is done where possible. Some simulations, however, cannot be validated in the laboratory and are thus complementary to the experimental results.

Whereas the former systems mentioned above used integration times from several seconds to several hours, the system described here is designed to provide the atmospheric parameters with high accuracy and precision at temporal measurement resolutions of ≤ 1 s. The weakness of the detected RR signal as well as parasitic daylight and strong elastic backscatter in dense clouds give rise to concerns about the optical properties of the two RR interference filters with regard to systematic and statistical error reduction. Consequently, requirements to be satisfied by these filters were specified within detailed simulations. Optimization calculations for range-resolved temperature measurements by rotational Raman lidar had already been carried out concerning the spectral bandwidths and central wavelengths of the two RR filters [10, 11]. The results impose, firstly, highly transmissive and sufficiently broad band shapes to minimize losses of the already weak RR signals. Secondly, they impose a high optical density at the laser wavelength to suppress the leakage of elastic particle and Cabannes backscatter. Here, similar calculations were made for the short-range system and for the specific temperature range from 210 K to 330 K. On the basis of the simulation results for the temperature measurements, the exact RR interference filter properties were specified. The optimum trade-off between filter performance and technical feasibility of the filter coating was elaborated and the filters were manufactured. Then the optimization calculations were repeated for the real filters and extended to the case of density and pressure measurements in order to optimize the filter alignments in each RR channel for the altitudes operated in ranging from 0 m to 13000 m. These results are presented as well.

Performance simulations implying properties of the prototype laser source, the scattering atmosphere, the ray propagation geometry and all relevant optical and electrical properties of the receiver, allow for estimations on the signal intensities to be detected. On the basis of these signal intensities, the expected statistical air temperature and density measurement uncertainties achievable with the optimized system settings are calculated. In addition to photon shot-noise coming from the light signal itself, also electronic noise generated by the photo-detector electronics is included into the uncertainty analysis. Furthermore, the magnitudes of the mentioned systematic error sources like parasitic solar background radiation at daytime, elastic signal leakage through the RR filters in optically very dense clouds, as well as water vapor and atmospheric extinction are assessed. Correction methods are described to eliminate these systematic errors by using two additional measurement channels detecting elastic and water vapor Raman backscatter, respectively. These corrections mostly lead to a large reduction or even elimination of the systematic measurement errors,

but in turn cause a smaller increase of the statistical measurement uncertainties. The increase of these statistical measurement uncertainties is calculated as well.

The theoretical simulations are then adapted to the limited measurement scenarios generable in the laboratory and compared with the correspondent experimental results. The experiments carried out evaluate the real performance of the designed apparatus giving information about the real systematic measurement errors and statistical measurement uncertainties. The deviations of these experimental errors and uncertainties from the theoretical values obtained from the simulations are then analyzed in detail. The different atmospheric states and measurement situations are replicated with an atmospheric-simulation chamber system for the experiments. This chamber system was designed and custom-made for this purpose within this thesis as well. It allows an adjustment of the air temperatures and pressures appearing at varying flight altitudes and the calibration of the measurement system as well as the determination of the measurement uncertainties as a function of these virtual flight altitudes.

This thesis consists of 9 chapters. The requirements for air data systems to be used in civil aviation are described in chapter 2. In chapter 3, different lidar techniques are analyzed for potential suitability for the application in the air data system. The decision on the RR technique is justified. In chapter 4, all atmospheric light scattering processes being relevant for the computational analysis in the subsequent chapters are depicted. The methodology of the measurement approach is given in chapter 5, followed by a description of the whole laboratory instrumental setup in chapter 6. The results of the model performance analysis and the optimization calculations are presented in chapter 7. These include the expected measurement errors and uncertainties of the designed laboratory measurement apparatus for operation during day- and nighttime and in clouds. Calculations concerning the leakage error magnitude in the RR channels as well as the atmospheric extinction error magnitude are made. Here, methods of error reduction are given. The special role of water vapor is detailed together with its influence on the measurement errors for temperature, density and pressure. Chapter 8 provides the experimental results and compares them to the computed ones. From the basis of the obtained experimental results, the necessary laser pulse energies are derived, which are needed in order to fulfill the accuracy requirements for aviation. Furthermore, an extrapolation of the measurement performance to UV wavelengths is made. The thesis ends with a summarizing conclusion and an outlook in chapter 9.

2 Standards for aircraft air temperature and pressure sensors

The accuracies to be achieved by each air data computer used for flight control in civil aircrafts are defined for temperature and pressure measurements in the aerospace standard *AS8002* [12] from *SAE International - The Engineering Society For Advancing Mobility Land Sea Air and Space* (SAE). The maximum allowable temperature and pressure measurement errors ΔT_{max} and Δp_{max} are illustrated in Figure 2-1 for different flight / measurement altitudes. The error values for temperature measurements are directly extracted from *AS8002* and are ΔT_{max} = 1.5 K for all measurement altitudes. Those for pressure measurements are obtained by converting the accuracy requirements for altitude measurements specified in *AS8002* with the help of the *International Standard Atmosphere* (ISA) model [13] and are Δp_{max} = 0.1 % for 0 m and 0.5 % for 13000 m. The altitude dependency of pressure and temperature according to the ISA model are illustrated in Figure 2-2. For density measurements, a similar error specification is not defined in the aerospace standards. Indeed, the maximum allowable errors for density measurements could be derived from ΔT_{max} and Δp_{max} with the help of the ideal gas equation. However, here, attention has to be paid to the correlation between ΔT_{max} and Δp_{max} and to the error type (systematic or statistic) of ΔT_{max} and Δp_{max}.

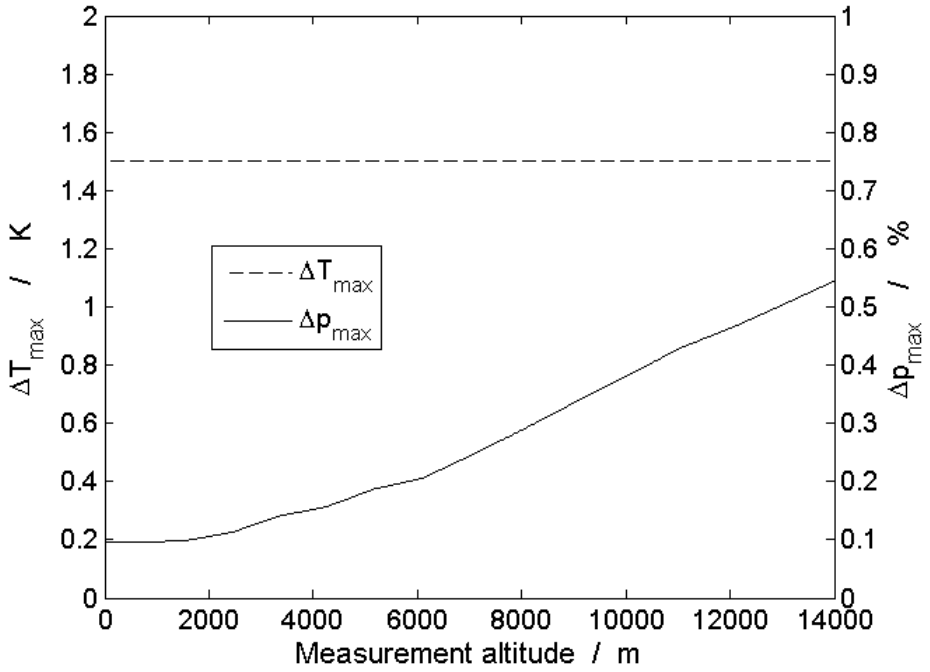

Figure 2-1. Maximally allowable measurement errors to be reached when measuring air temperature and pressure for aircraft control. These data were extracted from the aerospace standard *AS8002* [12].

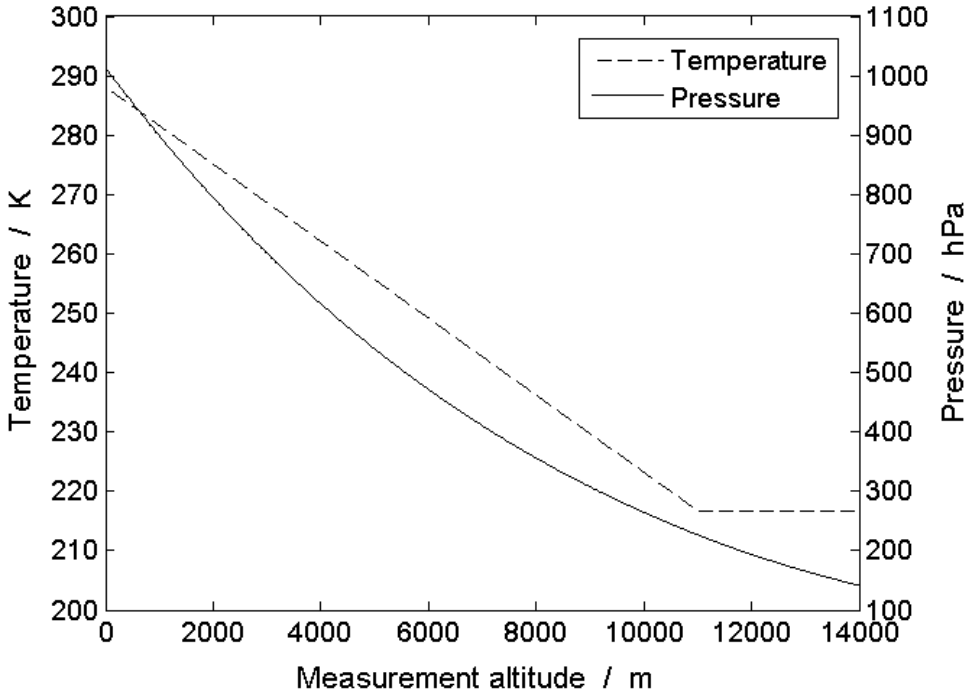

Figure 2-2. Temperatures and pressures present in different altitudes according to the *International Standard Atmosphere* (ISA) model [13].

3 Active optical remote-sensing methods

With the invention of the laser in the sixties of the past century possibilities arose for an optical measurement of air data as temperature, density and pressure. Lidar systems (LIght Detection And Ranging) based on lasers, nowadays, are increasingly and successfully used for remote sensing of the atmosphere, however, mostly for climatological monitoring and research. The lidar principle is based on the emission of a laser beam into the atmosphere and the detection and analysis of the backscattered radiation scattered from targets as molecules, atoms, ions and atmospheric particles like aerosols, water droplets or ice crystals. In general, the spectrum, the extinction, the time-of-flight, the polarization and other properties of the backscattered radiation can be analyzed. Depending on what physical principle underlies the exploited backscattering or radiation changing key mechanism, various types of lidar systems are distinguished. For most lidar systems the wavelength and the power of the emitted and detected radiation are of fundamental interest. The wavelength of the emitted light is chosen in that manner that it is significantly spectrally changed by the atmospheric parameter of interest or that it increases the efficiency of the radiation changing processes of interest.

The range-resolving lidar techniques for climatological research are mostly applied in ground-based systems, but can in principle be transferred into the short-range, fixed-distance and airborne application to optically measure local air data for aircrafts. If such measurement techniques are used for aircraft control, they have to fulfill several demands which are of vital concern for aviation, but which have been of minor importance for climatological research. Such demands are, first, autarky concerning the measurement operation, i.e. air data have to be derived without any external information input about the atmospheric state. Second, the desired air parameters have to be provided over the whole range of flight altitudes. These issues, which seem trivial for state-of-the-art air data systems commonly used in aviation, lead to a strong confinement of possible lidar principles being applicable for the purpose described. Atmospheric parameters of flight critical interest are air temperature, density and pressure, whereby already two describe the thermodynamic state of the atmosphere. The third can be calculated by the ideal gas equation when assuming the atmosphere being in thermodynamic equilibrium. Common measurement techniques for gas temperature, density and pressure acquisition can be classified into techniques based on differential-absorption lidar (DIAL), fluorescence lidar, high-spectral-resolution lidar (HRSL) and Raman lidar. In the following, these techniques are compared with respect to their suitability and feasibility for an air data system. See sect. 4.1 for an overview and the nomenclature of the spectral backscattering components of laser light from air constituents.

The measurement principle of DIAL firstly proposed in 1975 by Mason [14] is based on the exploitation of single absorption lines or broad absorption bands of a certain atomic or molecular species. The absorption behavior is attributed to electronic, vibrational as well as rotational transitions within the atoms or molecules. Two laser beams are emitted having differing wavelengths. The “on-line” wavelength is tuned to an absorption line or band and thus highly absorbed, whereas the “off-line” wavelength is tuned to a nearby spectral location where the absorption of the gas of interest is significantly lower. Knowing exactly the spectral shape of the absorption line or band of the gas and assuming all other beam propagation properties of the two wavelengths to be equal, the ratio of the two backscattered signals can be used for temperature or concentration measurements. However, the

spectral shape has complex dependencies on the atmospheric state itself. The atmospheric temperature, for instance, determines the spectral Doppler broadening of the single absorption lines [15]. Pressure gives rise to (inelastic and elastic) pressure broadening. The gas density indicates the number of scatterers and thus the overall absorption strength. Due to these complex dependencies, a measurement of one parameter without the knowledge of the others is hardly possible. For example, the measurement of a gas density requires the exact knowledge of the line strength and the spectral shape of the absorptions cross section, which are at least temperature dependent themselves. Conversely, if the temperature is to be measured, the density of the absorbing species has to be known. This fact is opposed to the mentioned requirements for an air data system. Nevertheless, some application examples are given in the following.

Concerning temperature measurements using the DIAL technique, so far, only one attempt has been reported by Theopold and Bösenberg [16], who used temperature dependent oxygen absorption lines in the A-band near 760 nm for their measurements. Systematic errors of up to 10 K were yield at heights of 1 km above ground, which is to a great extent too large to be practicable. Apart from the multiple dependencies of the DIAL signals on the above mentioned atmospheric parameters, a further issue of the DIAL technique, notably the availability and the finding of suitable absorption lines is impacting the measurement accuracy. The usage of narrow absorption lines with a width comparable to the width of the thermally broadened Cabannes backscatter leads to large systematic measurement errors. In [16, 17] this was shown to be a significant error source at those temperature retrievals. On the other hand, the employment of relatively broad spectral bands, like e.g. for ozone retrievals, necessitates a larger on-off-wavelength separation. In this case, the lack of information about the wavelength dependent changes for the absorption process and especially for the backscattering process induced by atmospheric particles generates systematic errors [18]. In 1998, Bösenberg described a high-spectral-resolution DIAL technique which promised to lower the temperature measurement accuracies to < 1 K throughout the whole troposphere by taking into account the Doppler-broadening of the Cabannes backscatter [19]. However, the latter has to be exactly known beforehand as well as the vertical density profile of the absorbing oxygen or the relation of the backscattering coefficients for the two wavelengths. In the same year Wulfmeyer [20] presented a high-performance laser transmitter which also was expected to lower the tropospheric DIAL temperature measurement error attributed to the laser properties to < 1 K. Since then, no further attempts concerning temperature measurements were published.

The DIAL technique is capable of retrieving molecular number densities as well. Amongst others, measurements of ozone densities in the ultraviolet and water vapor retrievals in the near-infrared were carried out. Because the ultraviolet ozone absorption spectrum is continuous and relatively broad (> 100 nm), the “on-line” and “off-line” wavelength have to be separated by several nanometers to raise the differential absorption. This leads again to sensitivity to aerosol and necessitates the application of, e.g. the Klett-inversion or the Dual-DIAL method. Also cross-interference to spurious gases, for example SO_2 and NO_2 in the case of ozone measurements [21], deteriorates the accuracy of this measurement technique. The generation of high power UV radiation possessing exactly the optimum wavelengths needed for this measurement technique is still a challenge, which is mostly met by the usage of technically demanding optical-parametric-oscillators. With regard to DIAL water vapor density measurements, the absorption lines of water vapor are much narrower. This necessitates the employment of laser radiation having a bandwidth on the order of only a couple of MHz. An active stabilization of the laser is required to guarantee narrow-bandwidth

operation as well as compensation of appearing frequency drifts. Measurements of atmospheric pressure and temperature were performed using a tunable alexandrite laser and two isolated absorption lines of oxygen [22]. The determination of these two parameters was not carried out on the same absorption line, but on two different lines, which respectively have a strong dependence on the searched parameter. This approach, however, was not further pursued.

In 1969 sodium densities were measured with a fluorescence or resonance-scattering lidar for the first time [23]. As the nomenclature is indicating, this type of lidar system excites an electronic transition within the gas of interest using laser light of matched wavelength and subsequently records the reemitted fluorescence light. Since the introduction of the technique, many fluorescence lidar activities have been concentrated on the observation of atomic layers of metallic species such as sodium [24-26], potassium [27], lithium [28], calcium [29] or iron [30]. Because, generally, the fluorescence cross sections of these mono-atomic species are relatively large and each generated spectral line has a small width making highly selective spectral filtering possible, already early measurements reached up to altitudes of over 100 km. For molecules at tropospheric temperatures, however, fluorescence measurements turn difficult. In this region, the molecules have broad fluorescence bands instead of single distinct lines due to the excitation of rotational and vibrational states. Furthermore, in lower altitudes radiationless decay of the excited states due to collisions (quenching), pre-dissociation and photoionization is lowering the fluorescence activity. These processes depend in a complex way on temperature, pressure and gas composition themselves. Derivations of gas densities from fluorescence measurements are thus not feasible without further considerable knowledge about the atmosphere.

Apart from the determination of concentrations, temperature measurements were carried out as well with the fluorescence technique. Similar to the DIAL technique, the Doppler-broadening of fluorescence lines can theoretically be used to determine the gas temperature. Temperatures from the analysis of the Doppler-broadening of the sodium D_2 doublet were retrieved by Gibson et al. [31] in a special way. The spectral distribution of the doublet was measured at different spectral locations with a tunable laser and the obtained fluorescence data were fitted to the theoretical model. As sodium is neither abundant nor homogeneously distributed in the lower atmosphere, this technique is not applicable for the purpose described herein. Instead of analyzing the Doppler-broadening of a fluorescence line, other interesting principles were proposed for temperature measurements circumventing the issue of radiationless collision-induced decay, e.g. for mesospheric temperature measurements exploiting iron atoms [32] or for measurements in flames exploiting OH molecules [33]. Here, the temperature dependent populations of two energetic states were interrogated measuring the fluorescence from two transitions similar to the rotational Raman temperature measurement technique (see below). The ratio of the two fluorescence signals is then a function of temperature. Calculations and experiments for measurements of fluctuations of temperature and density in turbulence using fluorescence of oxygen had been also described [34].

In summary, techniques using DIAL or fluorescence lidar for temperature and density retrievals have been reported. However, such measurements are restricted to high altitudes or gases which are neither abundant nor well mixed in the atmosphere at common flight altitudes. Furthermore, the fundamental physical principles underlying and affecting DIAL and fluorescence measurements are not only dependent on (only one) of the searched parameters notably temperature, density or

pressure, but also on additional information about the atmospheric state, like e.g. the exact molecular gas and particle compositions and concentrations. Thus, these techniques are not solely suitable in single systems for the application described herein. Beyond that, as further technical challenge, the application of DIAL or fluorescence lidar prerequisites the usage of discrete and specific laser wavelengths and limits thus the choice of laser sources. DIAL systems additionally need either a laser, which can be switched between the "on" and "off" wavelength, or two lasers, making such a system technically intricate.

In the context of atmospheric probing, high-spectral-resolution lidar (HSRL) techniques have been applied to extract properties of a gas by analyzing the Cabannes backscatter. The integrated spectral power density of the Cabannes backscatter is proportional to the air molecular number density. The width of the spectrum is determined by thermally induced broadening effects and thus linked to the atmospheric temperature. The typical width of the spectrum is a few gigahertz or a few picometers using visible wavelengths and thus relatively small. Depending on the laser wavelength used, the atmospheric pressure and temperature and the scattering angle, the Cabannes line can assume different spectral shapes (see sect. 4.1), which call for different approaches for the extraction of the air data. A kinetic model was set up by Tenti [35, 36] and is often used to describe the actual shape of the Cabannes line in dependence of the mentioned atmospheric parameters. If long laser wavelengths, e.g. in the infrared, are used together with large scattering angles (close to forward scattering), scattering from air density fluctuations begins to contribute. These density fluctuations are generated by acoustic waves propagating with the speed of sound. In this so called hydrodynamic regime, the spectral power density within the appearing Brillouin side-bands is strongly enhanced. Since the spectral distance of these Brillouin peaks is a function of the speed of sound, which in turn is dependent on gas temperature, it was proposed by Rye [37] to use this fact for atmospheric temperature measurements with an infrared heterodyne lidar. Here, the scattered and detected Cabannes radiation is interfered with the one of the local oscillator in order to form a beat signal. The frequency of the beat signal indicates directly the spectral separation of the Brillouin peaks and thus the air temperature. Thus, the temperature measurement can be transferred into a frequency measurement. However, up to now, no experimental implementation of such a measurement system could be satisfactorily established.

Under some boundary conditions, in the so called Knudsen regime, the tropospheric Cabannes spectrum can be approximated by a Gaussian, for example when detecting the atmospheric backscatter of UV laser radiation at low air densities. The Gaussian shape is a consequence of the Doppler broadening of the backscattered radiation resulting from the uncorrelated thermal movement of the scattering molecules. Direct-detection interferometric techniques (*interferometric Rayleigh scattering*) using e.g. Fabry-Perot interferometers (FPIs) were employed to resolve such a spectrum and to extract the temperature from its Doppler-broadened spectral width [38]. In the approach described by Hua [39], two FPIs are positioned at two differing wavelengths on one edge of the Cabannes spectrum (*edge technique*). From the ratio of the filtered signals the temperature is inferred. The signals are passing these FPIs twice in order to augment the rejection of appearing elastic particle backscatter. Additionally, one further FPI is used to measure this particle signal in order to correct errors due to remaining leakage of elastically scattered photons passing through the other two FPIs. FPIs were also used in the *scanning mode* in order to sweep the spectrum sequentially or locked to a certain wavelength. Knowing the FPI instrument function and the spectral distribution of the laser, the Cabannes line can be reconstructed from the measured signal amplitudes. Another method consists in

resolving the backscattered frequency components geometrically (*fringe imaging technique*). Here, an FPI is illuminated with the slightly divergent signal beam and the generated interference fringe-pattern is imaged onto an array detector. The width of the generated fringes is a function of temperature, their intensity a function of scattering gas density. In experiments performed by NASA [40-42] this imaging technique was used in high-speed gas flows for the extraction of amongst others gas temperature and density. Due to the spectral narrowness of the Cabannes spectrum, the determination of these parameters is very sensitive to changes of properties of the measurement equipment. Thus, a pressure and temperature stabilization of the measurement setup is essential for stable operation. Another issue much more difficult to handle are mechanical vibrations and acoustic noise. In [42] the equipment for the spectral analysis thus had to be positioned in a separate noise-isolating room, although an active stabilization routine for the FPI was implemented. In an aircraft such an issue could become the dominant experimental challenge. Another issue is the relatively spectrally narrow elastic particle backscatter superimposing the Cabannes spectrum. This particle backscatter can exceed the Cabannes intensity by up to 4 orders of magnitude in polluted or cloudy air (see sect. 4.6). Thus, the spectral resolution power and thus finesse of the used FPI is important and has to be high enough, in order to geometrically isolate the Cabannes spectrum from the one of the overlapped particle signal. Using high finesse FPIs, however, necessitates precise adjustment of the irradiation geometry and beam divergence. In [42], for comparable intensities of the Cabannes and the particle signal, an FPI finesse of 19 was used. The use of an FPI with a finesse of 300 is planned. Such an FPI, however, would have a total transmission of the incident radiation of only about 0.35 % in the best case. Apart from FPIs, other interferometer types as Michelson [43], Mach-Zehnder [44] or Fizeau interferometers [45] have only been proposed for use for measurements of temperature as well as of other air data as wind speed.

An alternative to interference filters proposed by Shimizu in 1983 [46] are atomic or molecular vapor filters (*filtered Rayleigh scattering*). These filters circumvent the disadvantage of interferometers of high mechanical sensitivity and high angular dependency of the passing radiation. The spectral filtering properties of vapor filters are attributed to the specific absorption lines or bands of the filtering gas. These properties can be modified by exactly controlling the vapor temperature and pressure and the length of the enclosing glass cell. Molecular iodine filters at 532 nm [47, 48] and Barium filters at 554 nm [49, 50] were already employed for atmospheric measurements of various air parameters. Other gases as lead vapor at 283 nm [51], mercury vapor at 254 nm [52, 53], potassium vapor at 770 nm [54], iron vapor at 248 nm [55], rubidium vapor at 780 nm [46] and caesium vapor at 389 nm [46] were suggested and also partially used for other applications, e.g. for gas diagnostics in high-speed gas flows. The development of an air data system for aircraft based on mercury filters is also pursued for commercial reasons [56].

To obtain thermodynamic data from the gas to be analyzed, one possibility consists in sweeping the laser wavelength across the filter absorption line. From the transmitted signals and the known spectral absorption line shape of the filter vapor, the Cabannes line can be reconstructed. Another possibility is to use two vapor filters of different spectral width and centered close to the peak of the Cabannes spectrum. Then two different signals can be extracted, the ratio of which is a function of temperature. The former approach was described in [57, 58] for temperature and pressure measurements in unseeded gas flows using iodine filters at the second harmonic Nd:YAG wavelength at 532 nm. The latter approach was demonstrated in [49, 50] for tropospheric temperature

measurements using barium filters at 554 nm together with a dye laser. The barium gas had to be heated to a temperature of 520 °C. For the implementation in aircrafts, the establishment and control of such high temperatures is unrealistic due to safety as well as power supply and consumption reasons. Apart from that fact, the temperature measurement errors reported in [50] coming from the temperature variations of the ovens harboring the two barium cells and from the drift of the non-stabilized dye laser were on the order of 10 K. This is by far too large to be acceptable for the application described herein. A gas temperature of 560 °C and higher was reported to be optimum in terms of filter stability for experiments with lead vapor filters [51]. This vapor temperature, in turn, was not ideal in terms of out-of-band peak optical density, which is needed for the suppression of elastic particle backscatter. Iodine gas is one of the rare spectral vapor filters, which can be used at room temperatures. For this gas, the demands on peak optical density for the suppression of backscatter from dense clouds with a backscatter ratio of up to 10000 were calculated in [59]. However, using the vapor filter design from [59], up to 70 % of the molecular backscatter signal is filtered as well.

Apart from the need for the establishment of high vapor temperatures, a further issue of this filter type is the special demand on the lasers. For the employment of the very most filtering gases, impracticable dye oscillators and dye amplifiers have to be used in order to reach the wavelength of interest. Another general problem of the airborne application of HSRL techniques for the purpose described herein are the Doppler frequency shifts of the backscattered radiation caused by the bulk motion of the air molecules. Indeed, if the air data are measured perpendicular to the flight direction, the Doppler shift of the backscattered radiation due to the aircraft velocity relative to the air mass is avoided, however turbulences in the measurement direction or cross winds during landing can still influence the measurements. E.g., gust wind speeds of 30 m/s in the measurement direction can lead to frequency shifts on the order of 0.1 GHz or 4.3 % with regard to the spectral with of the Cabannes spectrum when using 532 nm laser light (eq. (7.2.2)). This will not only lead to systematic errors sourcing in the shift of the Cabannes spectrum alone, but also sourcing in the shift of the elastic particle backscatter, which is superimposed over the Cabannes spectrum. Here, a shift of 0.1 GHz leads to a large mismatch of the elastic particle backscatter center frequency and the absorption peak of the used filter. The employment of e.g. vapor filters necessitates thus a good stabilization and a tunability of the used laser over a certain spectral range. In [60] the mastering of the spectral stabilization challenge of all optical components is said to be the key to successful data acquisition when using vapor filters.

A general problem of all HSRL diagnostic techniques is the inaccurateness of the current models describing the complex Cabannes spectral profile. However, accurate knowledge about its line shape is needed for the determination of correct atmospheric air data. In recent experiments [61] it was demonstrated that even at low atmospheric pressures of 300 hPa (corresponding to a flight altitude of about 9000 m), the assumption of a Gaussian shaped line profile is inadequate for the description of the Cabannes spectral intensity distribution and shows discrepancies of up to 9 % with regard to the Cabannes peak intensity. The mentioned kinetic model of Tenti [35, 36], although being developed for single-species diatomic gases and neglecting the contribution of the rotational Raman scattering, is seen as the most accurate model [62]. However, using it for the description of the Cabannes spectral intensity distribution still results in errors up to 2 % [61] with regard to the true Cabannes intensity distribution. Thus, in order to obtain temperature and pressure from the analysis of the Cabannes line,

the spectral models still have to be further improved. Moreover, whereas the assumption of a Gaussian line profile considers only atmospheric temperature as being the only parameter influencing its Doppler broadened width, the Tenti model requires at least atmospheric pressure as a further input parameter. A determination of either temperature or pressure with very high accuracy by using HSRL techniques based on only two spectrally fixed filters is thus even not feasible in principle.

Raman scattering is the inelastic molecular complement of the elastic Cabannes scattering process giving also the possibility for air temperature and density measurements. Since the Raman backscattering cross sections are at least three orders of magnitude lower, solar background light potentially affects daytime measurements more than in the case of HSRL techniques. Among the Raman backscattering spectra, the pure rotational Raman (RR) one is of most interest for the application described herein, since having among all Raman spectra by at least two orders of magnitude higher backscatter cross sections. Using sensing techniques based on Raman radiation avoids the issues linked with high-spectral-resolution filtering because, here, the analyzed spectra and thus the spectral bandwidths of the used optical filters are up to five orders of magnitude broader than in the Cabannes case.

In the early 1970s an air data measurement technique using RR backscatter was suggested for lidar by Cooney [9]. The physical basis of this technique is that the population density distribution of the molecular rotational states is temperature dependent and thus underlies the Boltzmann distribution law giving rise to the characteristic spectral distribution of the RR backscatter (see sect. 4.1). The idea of Cooney was to use two measurement channels in order to extract temperature dependent signals from this spectrum. The ratio of these signals is then a function of the air temperature only. In contrast to the measurement methodologies mentioned above, the use of the RR technique gives sufficiently accurate results for the purpose described herein without any external input and knowledge about the atmospheric state. This is demonstrated in the sections 7 and 8.

Being a tool for atmospheric temperature profiling, ground based RR lidar measurements in 1976 ranged up to an altitude of 1 to 2 km [63]. Two narrowband interference filters were used for separation of the different parts of the backscattered RR spectrum. A problem of the interference filters at that time was the deficient capability in spectroscopically separating the intense elastic backscatter from the at least three orders of magnitude weaker RR signals. In 1983 Arshinov et al. [64] performed experiments with a RR lidar system based on a double grating monochromator as the spectrally resolving element. The group showed that a blocking of the elastic backscatter of 8 orders of magnitude was feasible with such equipment. However, the optical transmission of the used monochromator and thus of the whole receiver of 1 % was poor. With improved optical equipment, nighttime RR temperature measurements could be made with interference filters ranging up even into the stratosphere [65, 66]. Measurements at daytime using a combination of a grating spectrometer and a thallium atomic vapor filter for the suppression of elastic backscatter were performed in 1996 by Zeyn et al. [67]. Here, a laser wavelength at around 277 nm, i.e. in the solar-blind spectral region, was used to enable daytime operation. An interesting approach was proposed by Arshinov et al. [68] to master the issue of suppression of elastic backscatter and daylight at visible laser wavelengths. It was suggested to use an additional FPI as a frequency comb to cut the RR nitrogen spectral lines from the solar background located within the spectral gaps between the RR nitrogen lines. Due to the character of the FPI transmission function, simultaneously, the elastic backscatter would be also attenuated. With improved interference filter technology, also daytime temperature profiling was reported by

Behrendt [10, 69-71], Radlach [11, 72] and Di Girolamo et al. [73] using narrow-band interference filters. With rising out-of-band suppression of the interference filters, measurements in optically thin clouds have turned possible as well [10].

The analysis of Raman radiation gives also access to air density measurements: Whereas the intensity distribution within the pure RR spectrum as well as within the rotational-vibrational spectrum of air depends on the air temperature, the integral over the whole respective branch does not. The integrated branch intensities are then proportional to the molecular number density of the air molecules. For meteorological interest, the extracted Q-branch of the rotational-vibrational Raman backscatter had been used as a reference signal at relative humidity retrievals [74-76]. In [69] Behrendt proposed to use a linear combination of the two RR signals needed for the temperature retrievals as a molecular reference signal. This is advantageous due to their higher backscatter intensities by around one order of magnitude. It was also proposed in [77] but not further pursued to measure atmospheric pressure directly by analyzing the magnitude of the collision broadening of the single RR lines. That however would make the use of high-resolution narrow-linewidth filters necessary.

Although there are no scattering components of air which overlap directly with its pure rotational Raman spectrum, there can be non-negligible leakage of elastically backscattered Cabannes and particle radiation through the optical filters applied within this spectrum. Thus, for the extraction of the signals, a strong blocking of the elastic backscatter contribution is crucial, like in the case of HSRL. However, with regard to the latter, the sensitivity to spectral shifts is by far smaller due to the ratio of the widths of the spectra and the ratio of the widths of the used optical filters. For example, the sensitivity of the RR techniques to frequency Doppler-shifts generated by wind is negligible as pointed out in sect. 7.2. This gives rise to much weaker requirements concerning system stability for the achievement of similar accuracies compared to HSRL techniques.

The sufficient independence of the RR measurement technique on assumptions about the atmospheric state together with the demonstrated potential of interference filter based systems for measurements during daytime and in clouds, mechanical ruggedness, relatively simple setup, compactness and the ongoing improvement in interference filter technology, have been the reasons to focus on the RR technique and the interference filter technology within the framework of this thesis project. In the further sections, the mentioned concerns about weak RR scattering intensities, solar background, sufficient blocking of elastic radiation and system stability are analyzed in detail and the suitability of the RR interference filter technique for airborne, short-range measurements of local air data based on a 532 nm laser is demonstrated in simulation and experiment.

4 Relevant atmospheric light scattering processes

In the following the physical scattering effects are outlined which are important for the understanding of the measurement methodology (chapter 5) and the optimization and performance calculations (chapter 7) of the laboratory apparatus described herein (chapter 6). First an overview is given, then the specific atmospheric scattering particularities, estimations and mathematical models used for the atmospheric simulations are described in detail.

4.1 Overview of laser light scattering processes in the atmosphere

Light photons propagating through the atmosphere partially will be scattered by air molecules, which are much smaller than the wavelength of the used laser light. In the relevant part of the atmosphere (troposphere and the lower stratosphere) these are mostly nitrogen and oxygen, the fractions of which stick together in a fixed relation. Different types of molecular scattering are distinguished, characterized by the amount of energy transfer from the incident photon on the scattering molecule. The nomenclature clarified in [78, 79] is used in this work. An overview is given in Figure 4.1-1 for an excitation laser wavelength of 532.07 nm, which is also used here.

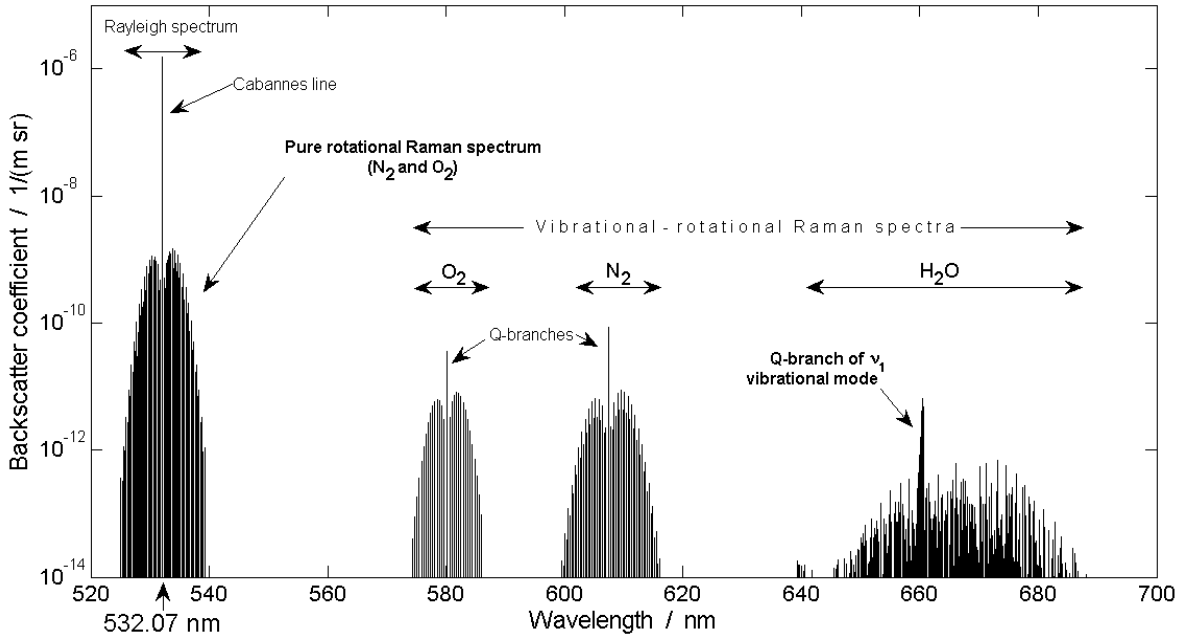

Figure 4.1-1. Backscatter coefficients for 532.07 nm laser light scattered from atmospheric air molecules at a temperature of 295 K and molecular number densities ($2.55 \cdot 10^{25}$ m^{-3}) present at sea level. The Cabannes, the pure rotational Raman and the water vapor spectrum were calculated with data from sections 4.2 to 4.5. The water vapor molecular number density is 4 % of the total air number density. The rotational-vibrational spectra of O_2 and N_2 were calculated with formulas and constants obtained from [80].

Scattered light is classified in rotational-vibrational Raman scattering, featuring the largest energy shifts, and Rayleigh-scattering. The rotational-vibrational scattering is generated by transitions from or to specific molecular vibrational and rotational states. It is composed of the spectrally narrow Q-branch, which is the result of the sole change of the vibrational quantum state, and surrounding rotational-vibrational lines, which are generated by an additional change of the rotational quantum state.

Rayleigh scattering comprises Cabannes scattering and pure rotational Raman scattering, the latter being located on both sides of the Cabannes line within a wavelength interval of around ±5 nm (for a laser wavelength of 532.07 nm), depending on the air temperature. The spectral widths of the Cabannes lines is much smaller and is at 300 K about 2.6 GHz (FWHM) or 2.5 pm, equivalently [62]. The integral over all pure rotational Raman line intensities is about 2.5 % of the Cabannes line intensity [60]. The Cabannes line is mathematically shortly treated in sect. 4.4. Rotational Raman scattering is a consequence of an energetically comparably small change of only the rotational quantum state of a molecule. The mathematical model for the calculation of the light energy shifts and scattering cross sections is found in sect. 4.3. Due to the smaller energy differences between the ground state and the different rotational energy states, thermally induced excitations of higher rotational states are probable in the atmosphere. This leads to the formation of rotational Raman bands on both spectral sides of the Cabannes line and of the vibrational Q-branches. The pure rotational band located at higher wavelengths is termed the Stokes band, the one located at lower wavelengths the anti-Stokes band. At atmospheric temperature conditions the air molecules are virtually all in the vibrational ground state. This allows mainly light induced transitions from the ground state to the first excited vibrational state causing thus the formation of relatively intense Stokes rotational-vibrational bands, whereas the anti-Stokes rotational-vibrational counterparts are 3 to 6 orders of magnitude weaker [80] and do not play a role for the optical determination of atmospheric properties.

Depending on the temperature and pressure range as well as the initial laser wavelength and the scattering angle, the Cabannes line can assume different spectral shapes. At low pressures, high temperatures and small light wavelengths (e.g. in the UV), the Cabannes line of backscattered light is Gaussian in good approximation (Knudsen limit) [62]. In the other case, side knobs, termed the Brillouin doublet, appear in the Cabannes spectrum, which are located to both sides of the unshifted central Gross or Landau-Placzek line (hydrodynamic limit). The Brillouin lines arise due to enhanced scattering from density fluctuations causing a change of the kinetic state of correlatively moving air molecules. The density fluctuations are generated by acoustic waves propagating through the atmosphere with the speed of sound. Tenti was one of the first having accurately described the spectral shape of the Cabannes spectrum with a kinetic theory (S6 model), which is still often applied today [35, 36].

Besides the abundant and well mixed tropospheric air constituents notably nitrogen (78.08 %), oxygen (20.95 %) and the inert gas argon (0.93 %), water vapor is the only one appearing in considerable but variable concentrations. Whereas nitrogen and oxygen are generating Raman spectra, argon does not, since it exists atomically and has no anisotropic part in the polarizability. The Raman spectra of water vapor by reason of its molecular structure are more complicated than the ones of nitrogen and oxygen. The water vapor spectra are calculated in sect. 4.5.

Apart from scattering by air molecules, light can be scattered by larger particles as well, e.g. being of the order or bigger than the used light wavelength. These particles can be water droplets e.g. in clouds or haze, ice crystals, dust, fumes, anthropogenic pollution and other aerosol. Particles scatter

the largest part of the light elastically, so that the elastic backscatter spectra of particles and molecules are overlapping. Due to the much higher backscatter cross sections of particles, the total elastic backscatter, e.g. in clouds, can be intensified by several orders of magnitude. The first quantitative explanation of scattering by spherical particles, as for example liquid droplets, was found by Mie [81]. An estimation of the relative elastic backscattering power of particles and molecules is made in sect. 4.6.

4.2 Energetic description of Raman scattering

In a scattering process between a light photon and a molecule, an amount of energy ΔE, corresponding to the energy difference of the two molecular states involved, can be exchanged. This leads to a change of the wavenumber $\tilde{\nu} = 1 / \lambda$ of the photon with the wavelength λ by the amount

$$\Delta\tilde{\nu} = \tilde{\nu}_S - \tilde{\nu}_L = \frac{\Delta E}{hc} \ . \tag{4.2.1}$$

$\tilde{\nu}_L$ is the wavenumber of the incident laser light photon and $\tilde{\nu}_S$ is that of the scattered one. c is the speed of light and h is Planck's constant. For Cabannes scattering, the molecular quantum state is not changed. In the general case of Raman scattering, the interaction between photon and molecule can evoke a change of either the rotational quantum state or the vibrational quantum state or both. The energy levels of homo-nuclear diatomic molecules like nitrogen or oxygen are yield by the quantum mechanical model of the freely rotating harmonic oscillator [82]:

$$E_{vib,\nu} = hc\tilde{\nu}_{vib}\left(\nu + 1/2\right) , \tag{4.2.2}$$

for the vibrational states with the specific molecular vibrational wavenumber $\tilde{\nu}_{vib}$ and the vibrational quantum number $\nu = 0,1,2,\ldots$ The rotational energy levels are

$$E_{rot,J,\nu} = hc\left[B_\nu J\left(J+1\right) - D_\nu J^2\left(J+1\right)^2\right] \ , \tag{4.2.3}$$

with the rotational wavenumber $J = 0,1,2,\ldots$ B_ν is the specific rotational constant and D_ν the centrifugal distortion, which both depend on the actual vibrational state ν of the molecule. The centrifugal distortion is negligible for small rotational quantum numbers [83] leading to an energetically equidistant separation of the rotational levels. Finally, rotational-vibrational energy states are well characterized by the sum of the individual energies

$$E_{rot-vib,J,\nu} = E_{rot,J,\nu} + E_{vib,\nu} \ . \tag{4.2.4}$$

In the thermodynamic equilibrium, the probability of occupancy of the rotational and vibrational states complies with the Boltzmann statistics. But within tropospheric temperature ranges nearly all

molecules are in their vibrational ground state $v = 0$. Thus, for the pure rotational spectrum only B_0 and D_0 are relevant. For the rotational-vibrational states, the light induced excitation of the first vibrational state $v = 1$ necessitates the consideration of B_1 and D_1. For oxygen and nitrogen, the molecular constants are listed in Table 4.2-1.

Not all transitions between different states are allowed, but are governed by selection rules, which can be for example inferred from molecular symmetry group theory [84, 85]. The selection rules for an optical change of the rotational quantum number and the vibrational quantum number for homonuclear diatomic molecules are

$$\Delta J = J_2 - J_1 = 0, \ \pm 2 \tag{4.2.5}$$

and

$$\Delta v = v_2 - v_1 = 0, \ \pm 1 \ . \tag{4.2.6}$$

J_1 and v_1 are the initial rotational and vibrational energy levels and J_2 and v_2 the final ones. $\Delta J = 0$ and $\Delta v = 0$ generate Cabannes scattering. A sole change of the rotational state by $\Delta J = +2$ or $\Delta J = -2$ gives rise to the Stokes or anti-Stokes pure rotational Raman spectrum, respectively. A sole change of the vibrational states by $\Delta v = +1$ or $\Delta v = -1$ gives rise to the Stokes and anti-Stokes vibrational Q-branches, respectively.

Table 4.2-1: Molecular constants for the calculation of the Raman spectra of oxygen and nitrogen. The references the constants are taken from are added below the values.

Gas	$\tilde{\nu}_{vib}$	B_0 (cm^{-1})	B_1 (cm^{-1})	D_0 (cm^{-1})	γ^2 (cm^6)	g_J		I
						J even	J odd	
N_2	2330.7 [82]	1.98957 [86]	1.97219 [86]	$5.76 \cdot 10^{-6}$ [86]	$0.51 \cdot 10^{-48}$ [87]	6	3	1
O_2	1556.4 [82]	1.43768 [88]	1.42188 [89]	$4.85 \cdot 10^{-6}$ [88]	$1.27 \cdot 10^{-48}$ [87]	0	1	0

4.3 RR backscattering cross sections and spectral shifts

A detailed theoretical description of pure rotational Raman scattering can be found in [82, 90-92]. Here, the most important equations for the understanding of the rotational Raman scattering process of oxygen and nitrogen are given.

The differential backscattering cross section $(d\sigma / d\Omega)^{\pi}_{rot,J}$ generating the pure rotational Raman line correspondent to the initial state J (index π denotes light scattered at 180°) is [93]

$$\left(\frac{d\sigma}{d\Omega}\right)^{\pi}_{rot,J} = \frac{7}{4}\frac{64}{45}\pi^4 b_J \left(\tilde{\nu}_L + \Delta\tilde{\nu}_{rot,J}\right)^4 \gamma^2 F_{rot,J} \ . \qquad (4.3.1)$$

γ is the anisotropy of the molecular polarizability tensor and the molecular specific indicator for the strength of the rotational Raman scattering intensity. The constants for the relevant molecules oxygen and nitrogen are listed in Table 4.2-1. In consideration of eq. (4.2.1) and (4.2.3) the selection rules from eq. (4.2.5) and (4.2.6) for pure rotational Raman transitions, the wavenumber changes in the Stokes case (ΔJ = + 2) are

$$\Delta\tilde{\nu}_{rot,J,St} = \tilde{\nu}_{rot,J} - \tilde{\nu}_{rot,J+2} = -B_0\,2(2J+3) + D_0\left[3(2J+3) + (2J+3)^3\right] \qquad (4.3.2)$$

$$\text{with} \quad J = 0,1,2... \ ,$$

where J is the quantum number of the initial rotational state, and in the anti-Stokes case (ΔJ = - 2)

$$\Delta\tilde{\nu}_{rot,J,aSt} = \tilde{\nu}_{rot,J} - \tilde{\nu}_{rot,J-2} = B_0\,2(2J-1) - D_0\left[3(2J-1) + (2J-1)^3\right] \qquad (4.3.3)$$

$$\text{with} \quad J = 2,3,4... \ .$$

b_J is the Placzek-Teller coefficient, a factor describing the dependence of the scattering intensity on the initial rotational state. For the stokes and Anti-Stokes case it is [94]:

$$b_{St,J} = \frac{3(J+1)(J+2)}{2(2J+1)(2J+3)} \qquad (4.3.4)$$

and

$$b_{ASt,J} = \frac{3J(J-1)}{2(2J+1)(2J-1)} \ . \qquad (4.3.5)$$

Since the occupation of the rotational states of a gas in thermal equilibrium at a temperature T follows a Boltzmann distribution, the rotational Raman spectrum is temperature dependent. A normalized factor $F_{rot,J}$ weights the strength of every line according to the temperature dependent relative population $N_{rot,J} / N$ of the correspondent initial quantum state J:

$$F_{rot,J} = \frac{N_{rot,J}}{N} = \frac{g_J(2J+1)\ \exp\left[-E_{rot,J}/k_B T\right]}{\Phi} \ . \qquad (4.3.6)$$

g_J is the specific statistical w λ eight factor dependent on the nuclear spin I and rotational quantum number J. Φ denotes the normalization factor, the state sum, and is for homo-nuclear molecules in the angular-momentum ground state [95]:

$$\Phi = (2I+1)^2 k_B T / (2hcB_0) \ . \qquad (4.3.7)$$

The summarized differential backscattering cross section of homo-nuclear diatomic molecules generating the pure rotational Raman line correspondent to the initial quantum state J is

$$\left(\frac{d\sigma}{d\Omega}\right)^{\pi}_{rot,J} = \frac{112}{15}\frac{\pi^4 g_J hcB_0}{(2I+1)^2 k_B T}\left(\tilde{\nu}_L + \Delta\tilde{\nu}_{rot,J}\right)^4 \gamma^2 \exp\left[-E_{rot,J}/k_B T\right]\cdot X_{rot,J} \qquad (4.3.8)$$

with

$$X_{rot,J} = X_{rot,J,St} = \frac{(J+1)(J+2)}{2J+3}\,, \quad \Delta\tilde{\nu}_{rot,J} = \Delta\tilde{\nu}_{rot,J,St}$$
$$\text{and} \quad J = 0,1,2\ldots \qquad (4.3.9)$$

for the Stokes case and

$$X_{rot,J} = X_{rot,J,aSt} = \frac{J(J-1)}{2J-1}\,, \quad \Delta\tilde{\nu}_{rot,J} = \Delta\tilde{\nu}_{rot,J,aSt}$$
$$\text{and} \quad J = 2,3,4\ldots \qquad (4.3.10)$$

for the anti-Stokes case. At an air temperature of 295 K and for an excitation laser wavelength of 532.07 nm, the differential backscattering cross sections $(d\sigma / d\Omega)^{\pi}_{rot}$ generating the strongest anti-Stokes RR lines are on the order of $4\cdot10^{-35}$ m^2 / sr and thus around 3 orders of magnitude lower than the backscattering cross section generating the Cabannes or total Rayleigh spectrum (sect. 4.4). The pure rotational Raman spectra of oxygen and nitrogen for the used laser wavelength of 532.07 nm were calculated using *Matlab* and are shown in Figure 4.3-1.

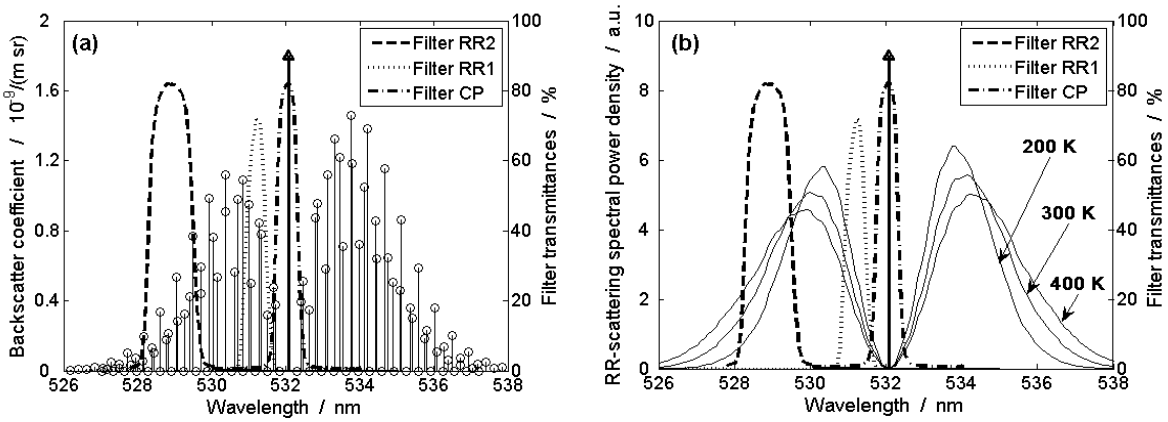

Figure 4.3-1. (a): Backscatter coefficients of the pure rotational Raman spectrum of air consisting of nitrogen and oxygen spectral lines plotted for an air temperature of 295 K and densities present at sea level, and spectral transmission curves of the filters RR1, RR2 and CP (see sect. 6.4). The filter central wavelengths (CWLs) are 531.2 nm, 528.9 nm and 532.07 nm, respectively. (b): Envelopes of the RR

spectrum at different temperatures. The simulation program generating the plots was written in *Matlab*.

4.4 Rayleigh and Cabannes scattering

The Cabannes or Rayleigh scattering cross sections are needed for estimations of the backscatter ratios, where being of relevant magnitude, e.g. in optically dense clouds (sect. 4.6). The Rayleigh cross sections are thus essential for the calculation of the measurement errors made in such clouds (sect. 7.7). With the nomenclature used in [78, 79], Rayleigh scattering is defined as the sum of Cabannes scattering and pure rotational Raman scattering. Formulas for calculating the total Rayleigh scattering cross section σ_{Ray} and the (differential) backscattering cross section $(d\sigma / d\Omega)^{\pi}_{Ray}$ in the case of linearly polarized incident laser light and knowing the molecular properties of the scattering gas are [62]

$$\sigma_{Ray} = \frac{8\pi^3}{3\varepsilon_0^2} \tilde{\nu}_L^{\,4} \left(\frac{45\alpha^2 + 10\gamma^2}{45} \right) \tag{4.4.1}$$

and

$$\left(\frac{d\sigma}{d\Omega} \right)_{Ray}^{\pi} = \frac{\pi^2}{\varepsilon_0^2} \tilde{\nu}_L^{\,4} \left(\frac{45\alpha^2 + 7\gamma^2}{45} \right), \tag{4.4.2}$$

where ε_0 is the vacuum permittivity and α the mean of the isotropic part of the molecular polarizability tensor. For air, which is approximated as a single species, α is often expressed by the refractive index of air n and its number density N with the Lorentz-Lorenz equation [96]:

$$\alpha = \frac{3\varepsilon_0}{N} \frac{n^2 - 1}{n^2 + 2} \,. \tag{4.4.3}$$

n and N are macrophysical properties which can be measured easier. The deviation of the cross sections due to the anisotropy γ is taken account of by the so called King correction factor [97]

$$F_k = \left(\frac{6 + 3\rho_0}{6 - 7\rho_0} \right), \tag{4.4.4}$$

where ρ_0 is the depolarization ratio defined as the horizontally to vertically polarized light scattered at 90° for unpolarized incident light, and also being easy measurable. Inserting eq. (4.4.3) and (4.4.4) into eq. (4.4.1) yields

$$\sigma_{Ray} = \frac{24\pi^3}{N^2} \frac{\left(n^2 - 1\right)^2}{\left(n^2 + 2\right)^2} \tilde{\nu}_L^{\,4} \left(\frac{6 + 3\rho_0}{6 - 7\rho_0} \right). \tag{4.4.5}$$

For backscattering $(d\sigma / d\Omega)^{\pi}_{Ray}$ is then yield by [62]

$$\left(\frac{d\sigma}{d\Omega}\right)^{\pi}_{Ray} = \frac{3\sigma_{Ray}}{8\pi}\frac{2}{2\rho_0} \ . \qquad (4.4.6)$$

Input data for the formulas for σ_{Ray} and $(d\sigma / d\Omega)^{\pi}_{Ray}$ of atmospheric air can be found in [98]. With the data from [98] $(d\sigma / d\Omega)^{\pi}_{Ray} = 6.08 \cdot 10^{-32}$ m^2 / sr for an incident laser wavelength of 532.07 nm. 2.5 % of $(d\sigma / d\Omega)^{\pi}_{Ray}$ are allotted to pure rotational Raman backscatter and 97.5 % to Cabannes backscatter [60]. Thus for the Cabannes backscatter cross section: $(d\sigma / d\Omega)^{\pi}_{Cab} = 0.975 \cdot (d\sigma / d\Omega)^{\pi}_{Ray}$. Because the cross sections of Rayleigh and rotational Raman scattering are both proportional to $\tilde{\nu}_L^4$, this percentage does not change with light wavelength. Thus, in low resolution spectroscopic measurements of the Cabannes line, the contribution rotational Raman scattering can be easily accounted for. The total Rayleigh cross section σ_{Ray} is also calculated with the data obtained from [98] and is $\sigma_{Ray} = 5.16 \cdot 10^{-31}$ m^2 for an incident laser wavelength of 532.07 nm. The product of σ_{Ray} and the molecular number density of air N yields the molecular extinction coefficient (extinction due to scattering) α_{mol}. At sea level $N \approx 2.55 \cdot 10^{25}$ m^{-3} according to the ISA [13] and thus $\alpha_{mol} \approx 1.32 \cdot 10^{-5}$ m^{-1}.

With the formulas from above, a comparison of the intensities of the backscattered Rayleigh or Cabannes spectrum and the ones of the rotational Raman lines can be done: The ratio of the intensities of the total backscattered Rayleigh spectrum and the strongest pure rotational Raman anti-Stokes line for air at a temperature of 295 K is around 1300. The Rayleigh backscatter coefficient β_{Ray} is defined as $\beta_{Ray} = (d\sigma / d\Omega)^{\pi}_{Ray} \cdot N$.

4.5 Raman spectra of water vapor

The water vapor Raman spectra discussed in this section are used in sect. 7.8 for the calculation of all measurement errors linked with the presence of atmospheric water vapor. Besides dry air, water vapor is the only gas in the atmosphere appearing in variable and non-negligible densities, so that the total molecular number density of air is obtained by the adding of the molecular number densities of the two gases. The maximum volume mixing ratio M_{H2O} of water molecules in air is basically determined by the saturation vapor pressure E_{H2O} which is a function of the absolute air temperature T. E_{H2O} can be estimated by the Arden Buck equation [99] (also known as the Magnus equation)

$$E_{H2O}(T) = 611.21 \ Pa \cdot \exp\left(\frac{17.502 \cdot (T - 273.15 \ K)}{T - 32.18 \ K}\right) . \qquad (4.5.1)$$

Assuming the worst case of the air being saturated with water vapor, an altitude profile of the maximally possible value for M_{H2O} is calculated based on the ISA [13] and is shown in Figure 4.5-1. The saturation value for M_{H2O} is yield by

$$M_{H2O} = \frac{N_{H2O}}{N_{moist}} \approx \frac{N_{H2O}}{N_{dry}} = \frac{E_{H2O}(T)}{p} \ , \qquad (4.5.2)$$

with $N_{moist} = N_{dry} + N_{H2O}$ being the molecular number density of moist air and thus the sum of the densities of dry air and water vapor. T is the atmospheric temperature and p the pressure, both obtained from the ISA model.

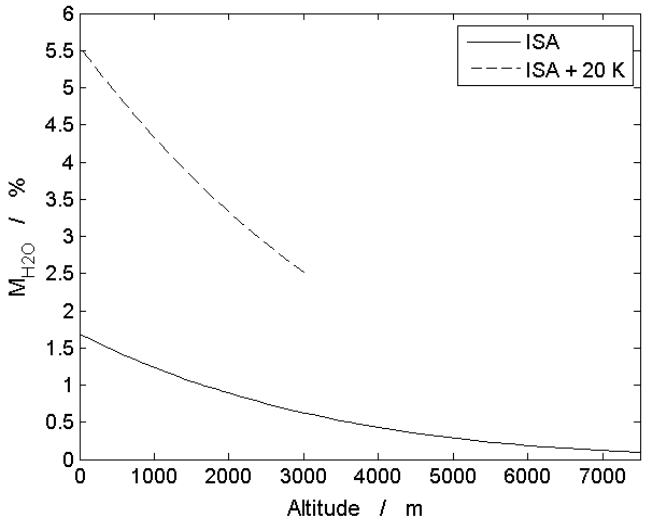

Figure 4.5-1. Saturation values of the water vapor volume mixing ratio M_{H2O} in air as a function of altitude. The atmospheric input data are taken from the *International Standard Atmosphere* (ISA, [13]). The dotted line shows the results of an additionally elevated model temperature by 20 K up to 3000 m.

According to the ISA model, the ground temperature is around 15 °C (≈ 288 K) leading to a saturation value of $M_{H2O} \approx 1.7$ % (solid line in Figure 4.5-1). At an altitude of 7500 m at an ISA model temperature of -34 °C (≈ 239 K) this value falls below 0.1 %. Due to possible higher heat and humidity transfer from the surface into the air at low altitudes, M_{H2O} was exemplarily calculated for temperatures exceeding the ISA model by 20 K as well (dotted line). At sea level temperatures of 35 °C (≈ 308 K) M_{H2O} is maximally ≈ 5.5 %.

4.5.1 Pure RR spectrum

Being a nonlinear asymmetric top molecule, the rotational Raman spectrum of water vapor is much more complex than the spectra of N_2 and O_2. A model of the Stokes side was set up and validated by Avila et al. [100]. For any anti-Stokes line (J --> J+2) and its Stokes counterpart (J+2 --> J), the ratio of the intensities is that of the population of the upper (J + 2) to the lower level (J). Based on this rule, here, the needed data for the anti-Stokes side were calculated from the data of the Stokes side given in [100]. The pure rotational spectrum is plotted in Figure 4.5-2.

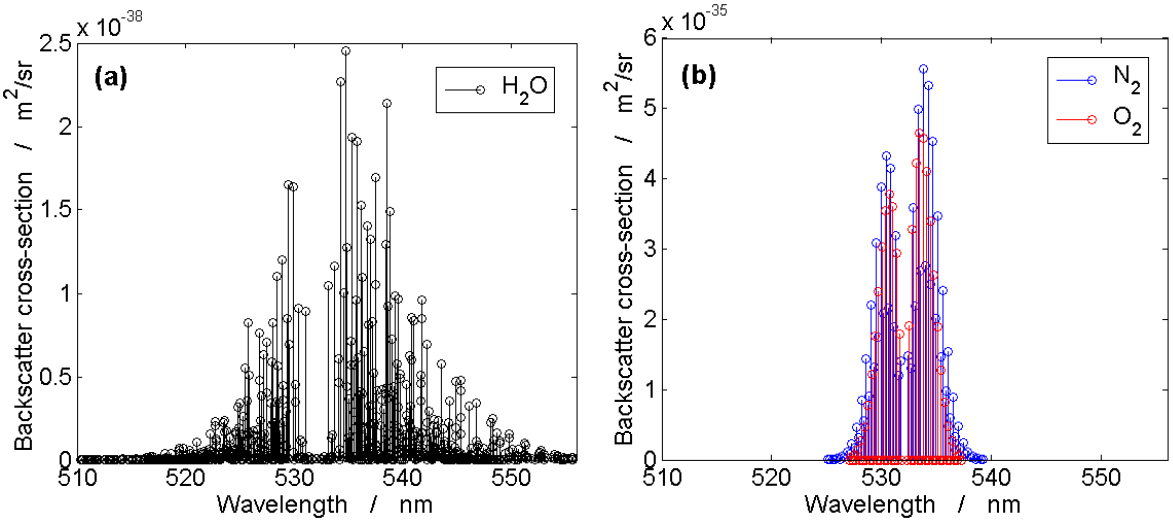

Figure 4.5-2. (a) Pure rotational Raman spectrum of water vapor at 310 K. The water vapor number density amounts 4 % of the air number density at sea level. (b) Pure rotational Raman spectrum of oxygen and nitrogen at sea level for comparison. Note that the water vapor spectral lines are about 2000-fold weaker (y-axis).

As pointed out in [100], the weakness of the rotational Raman lines of water vapor in tropospheric air is attributed to three reasons. First, the water vapor particle density in comparison with that of oxygen or nitrogen is at least one order of magnitude smaller. Second, in tropospheric temperature ranges, the scattered energy within the water vapor spectrum is distributed among the tenfold number of rotational lines than in oxygen or nitrogen and within a larger spectral interval. Third, the summed-up energy of the whole rotational spectrum is about two orders of magnitude weaker due to the small anisotropy of the water vapor molecular polarizability γ (cf. eq. (4.3.1)). All these facts result in line intensities, which are by 4 to 5 orders of magnitude weaker than those of the oxygen and nitrogen. However, the spectra of dry air and water vapor are overlapping and cannot be separated. This was taken into account in sect. 7.8.1 with regard to temperature and density measurement errors.

4.5.2 Rotational-vibrational Raman spectrum

The spectral region of the Q-branch of the water vapor OH stretching band ν_1 at a spectral shift of 3654 cm^{-1} is plotted in Figure 4.5-3. In Figure 4.1-1 it can be also found as a semi-logarithmic plot. The formulas and the necessary data to calculate this spectrum were obtained from Avila et al. [101]. The line intensities of the rotational-vibrational Raman spectrum of water vapor are much stronger than in the case of its pure rotational Raman spectrum. The differential cross section of the summed Q-branch lines amounts to about 10^{-34} m^2 / sr and is thus on the order of those of the strongest pure rotational lines of dry air, i.e. of N_2 and O_2.

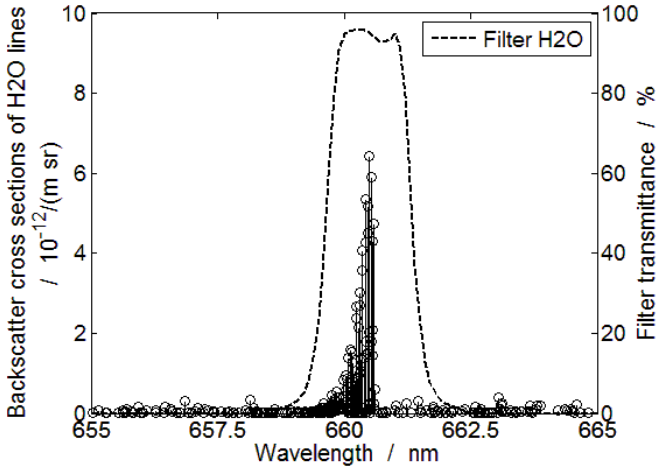

Figure 4.5-3. Q-branch of the ν_1 vibrational mode of water vapor at 310 K and spectral transmission curve of the water vapor filter H_2O. The water vapor molecular density is assumed to be 4 % of the ground molecular air density. The backscattered water vapor spectrum is red-shifted by around 3654 cm^{-1} or around 128 nm with regard to the used laser wavelength at 532.07 nm. The used spectral water vapor data are taken from [101].

4.6 Elastic particle scattering - extinction coefficient and backscatter ratio

Although the number density of atmospheric particles is negligible in comparison to the number density of atmospheric air molecules, the power of elastically scattered radiation by particles can be several orders of magnitude higher than the one of molecules. This leads, first, to relatively high extinction of propagating light and, second, to relatively intense elastic backscatter. The elastic scattering by spherical particles with diameter on the order of the light wavelength was firstly quantitatively described by Mie in 1908 [81]. Further information about the Mie theory can be found in [102-104]. Although this theory considers only spherical particles, in practice, scattering by atmospheric aerosols, dust particles, cloud droplets, ice crystals, etc. is often incorrectly grouped together under the umbrella term Mie scattering. Descriptions of scattering characteristics of particle shapes other than spherical were made e.g. for thin discs and oblate spheroids [105], cylindrical rods [106], for sharp-edged particles with monoclinic, orthorhombic or hexagonal crystal structures [107], and others [108, 109]. In reality, an exact quantitative formulation of the scattering characteristics and scattering intensities with one theoretical model is, however, hardly possible, since they are dependent on particle shape, geometric size, refractive index, composition, number density, incident laser wavelength, scattering geometry, and others. Moreover, the properties of atmospheric particle accumulations are not uniform, but are subject to fluctuations and distributions which are rarely known. The intention of this section is thus not to give formulas to calculate the elastic backscattering intensities for particle layers of different types and concentrations but rather to give an estimation of the highest values for the backscatter ratio R and the atmospheric extinction coefficient α. High values

of R and α give rise to two measurement errors: The leakage error and the atmospheric extinction error. The magnitude of these errors and methods for their reduction are discussed in sect. 7.7.

R is defined as the ratio of the total elastic to total molecular backscatter:

$$R = \frac{\beta_{par} + \beta_{Ray}}{\beta_{Ray}} \quad , \tag{4.6.1}$$

with the elastic backscatter coefficient for molecules β_{Ray} and for particles β_{par}. Each backscatter coefficient is the product of the backscatter cross section and the density of the scattering air molecules or particles, respectively. For air molecules this is

$$\beta_{Ray} = N \cdot \left(\frac{d\sigma}{d\Omega} \right)^{\pi}_{Ray} \quad , \tag{4.6.2}$$

with N being the molecular number density of air and $(d\sigma / d\Omega)^{\pi}_{Ray}$ the Rayleigh backscattering cross section (sect. 4.4). For β_{Ray} it is of minor importance if the total Rayleigh cross section is taken or only the Cabannes cross section, since, as mentioned in sect. 4.4, they differ only by 2.5 %. Inserting $(d\sigma / d\Omega)^{\pi}_{Ray} = 6.08 \cdot 10^{-32}$ m^2 / sr for an incident laser wavelength of 532.07 nm and the air molecular number density at 6000 m (for a cloud assumed at 6000 m) $N_{6000m} = 1.37 \cdot 10^{25}$ m^{-3} according to the ISA yields $\beta_{Ray} = 8.3 \cdot 10^{-7}$ sr^{-1}m^{-1}.

In the troposphere optically dense clouds are the cause for the most intense elastic backscatter. An estimation of the order of magnitude of β_{par} appearing in these clouds can be made assuming a certain visibility range r_s and a certain cloud lidar ratio L_{par}. r_s is defined as the light path after which the contrast K drops to 2 %. K is defined by

$$K = K_0 \cdot \exp\left(-\alpha_{par} r_s\right) . \tag{4.6.3}$$

α_{par} is the mean extinction on the light path and K_0 is the initial contrast at the beginning of the light path and therefore $K_0 = 1$. α_{par} can then be calculated for a given r_s by

$$\alpha_{par} = \frac{-\ln(0.02)}{r_s} \quad . \tag{4.6.4}$$

For example, for a visibility range of $r_s = 100$ m, $\alpha_{par} \approx 0.04$ m^{-1}. This extinction coefficient surpasses the molecular one which is $\alpha_{mol} \approx 1.32 \cdot 10^{-5}$ m^{-1} at sea level (sect. 4.4) by 3 orders of magnitude.

The lidar ratio L_{par} denotes the ratio of the extinction coefficient α_{par} and the backscatter coefficient β_{par}:

$$L_{par} = \frac{\alpha_{par}}{\beta_{par}} \ . \qquad (4.6.5)$$

The lidar-ratio of strongly scattering water clouds (for 532 nm light) is around L_{par} = 20 sr, leading to a backscatter coefficient of β_{par} = 0.002 $sr^{-1}m^{-1}$ for r_s = 100 m. With these values, the backscatter ratio is $R \approx 2400$. For smaller visibility ranges, R can be higher, e.g. for r_s = 20 m, $R \approx 11800$. These scenarios are only special cases, but it is sufficient to estimate the possible order of magnitude for R to show the dominance of the elastic particle backscatter and to show later on (sect. 7.7) the influences on the optical measurement errors. If the lidar ratio L_{par} was higher than 20 sr, the backscatter ratio R would decrease. R would decrease as well if an identical cloud was located at altitudes lower than the assumed 6000 m, since then the molecular backscatter would increase. For this reason, a backscatter ratio R on the order of 10^4 is assumed to be the worst case influencing maximally the optical measurements.

The backscattered rotational Raman and Rayleigh power is strongly rising with decreasing laser wavelengths due to the proportionality to $\tilde{\nu}_L^4$ (see eq. (4.3.8) and eq. (4.4.2), respectively). The elastic backscatter of the most clouds, in contrast, has at best a linear dependency on the laser wavelength due to the larger size of their particles [110]. Thus, the backscatter ratios at different laser wavelengths are not equal, but generally get significantly smaller at shorter wavelengths. For example, if assuming the modeled cloud having backscattering characteristics being independent on the incident light wavelength, the estimated backscatter ratios are decreased by a factor of around 5 when comparing the values for 532 nm and 355 nm: At 355 nm and the visibility ranges r_s = 100 m or 20 m, R = 480 or 2400, respectively.

4.7 Solar spectral radiance

Air data systems on aircrafts operate during nighttime and daytime. For the assessment of the parasitic background light detected by the optical measurement system during daytime, the solar radiance has to be known. The solar spectral radiance Ψ describes the radiant flux ξ at the wavelength λ that falls within a given solid angle Ω from a specified direction on a particular area A. It is defined as

$$\Psi = \frac{d^3\xi}{dA' d\Omega' d\lambda'} \ . \qquad (4.7.1)$$

The program *LibRadTran* [111, 112] is a recognized tool to calculate solar radiances for different modeled atmospheric scenarios (see publication list in [113]). Figure 4.7-1 shows exemplarily the spectral distribution of daytime solar radiances at earth ground calculated with that program for upward looking measurement systems. In clear sky the values are highest for blue or UV wavelengths, what can be explained with the Rayleigh scattering cross section being proportional to $\tilde{\nu}_L^4$ (sect. 4.4) and thus enhancing the scattering of short-wave light. In overcast sky the radiance peak values are shifted towards visible wavelengths due to enhanced particle scattering, which has cross sections of weaker wavelength dependence [110].

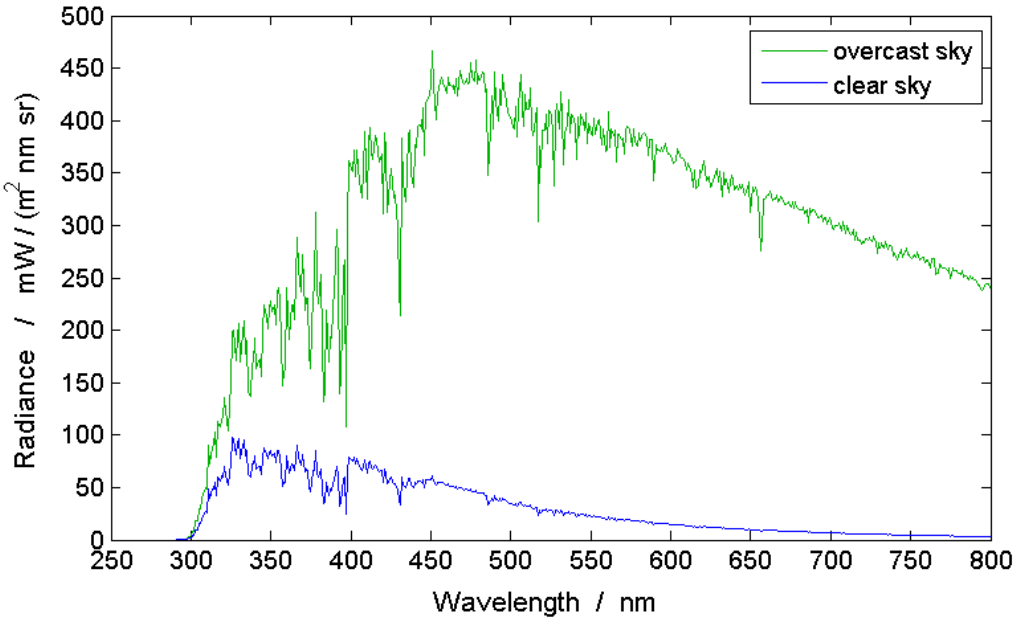

Figure 4.7-1. Solar radiation spectrum calculated with *LibRadTran* [111, 112].

Radiance values for different flight scenarios and viewing directions from aircraft were simulated as well. For the simulations, the following input parameters were used (Figure 4.7-2): on the one hand the solar position, described by the solar zenith angle θ' and the solar azimuth angle φ', and on the other hand the receiver viewing direction, defined by the viewing zenith angle θ and the viewing azimuth angle φ.

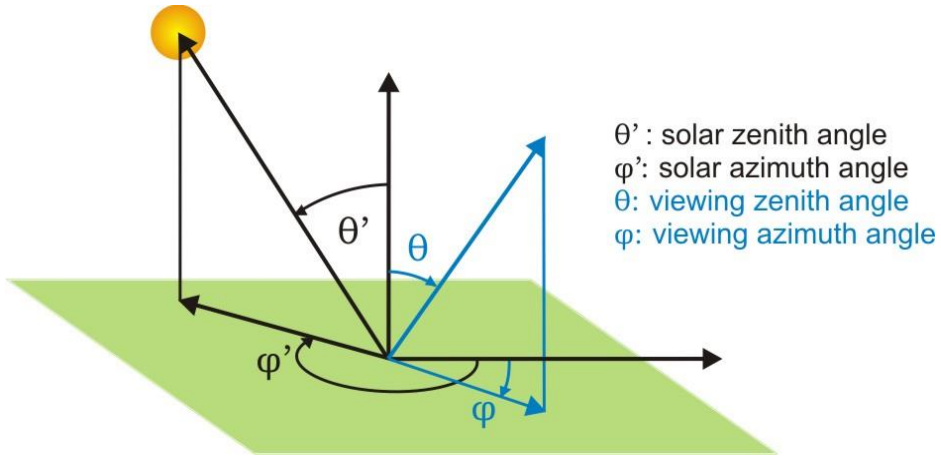

Figure 4.7-2. Definition of the solar position by the angles θ' and φ' and the viewing direction by the angles θ and φ.

Figure 4.7-3 and Figure 4.7-4 give radiance values at a wavelength of 532 nm for four representative flight situations: Figure 4.7-3 shows the simulation results for radiances expected at an altitude of

13000 m in a cloudless and aerosol-free atmosphere during daytime. For different φ values, the results of an angular scan of θ are shown. In all plots the solar position and thus the irradiation direction is always kept fix at $\theta' = 45°$ and $\varphi' = 0°$. Lowest radiance values are appearing for $\theta = 0°$, that means for upward looking systems. For $\theta = 90°$, i.e. sideward looking systems, horizon brightening occurs, which is also described in [114]. This brightening effect dominates in cases of low surface albedo (Figure 4.7-3 (a)). In cases with high surface albedo (Figure 4.7-3 (b)), e.g. over snow covered surfaces, a downward looking system poses the worst solution. For altitudes other than 13000 m these radiance characteristics do not change much qualitatively and quantitatively and are not plotted here.

In Figure 4.7-4 an opaque water cloud is additionally introduced into the atmosphere located at an altitude from 6 to 8 km and the radiances expected above and under the cloud are shown. Above the cloud (Figure 4.7-4 (a)) the radiances are quite similar to those present above a high albedo surface. However, the values are maximized when the viewing direction is pointing downwards onto the cloud ($\theta > 90°$) and is additionally turned towards the sun (φ is approaching 0°). This behavior is due to the straying properties of the model cloud, which enhances the scattered intensity for the cases where the light scattering angle is approaching the reflection angle at the cloud top. Figure 4.7-4 (b) pictures the worst case where the aircraft is located between a high albedo surface and the cloud. Here, no advantageous viewing direction can be fixed in general, but rather all viewing directions show strongly elevated radiance values, e.g. by reason of multiple reflections between cloud and surface. The radiance for the worst case is chosen to be 500 mW / (m^2 sr nm) at 532 nm. This value is taken for the calculations of the additionally introduced errors by the detection of solar radiation at measurements during daytime (sect. 7.6). It should be noted, however, that most surfaces represent no ideal lambertian scatterers but show glancing angles or directional components as it is the case in Figure 4.7-4 (a) by which the strayed background can increase by many orders of magnitude. The dynamic range of the detected background signal can thus be very large.

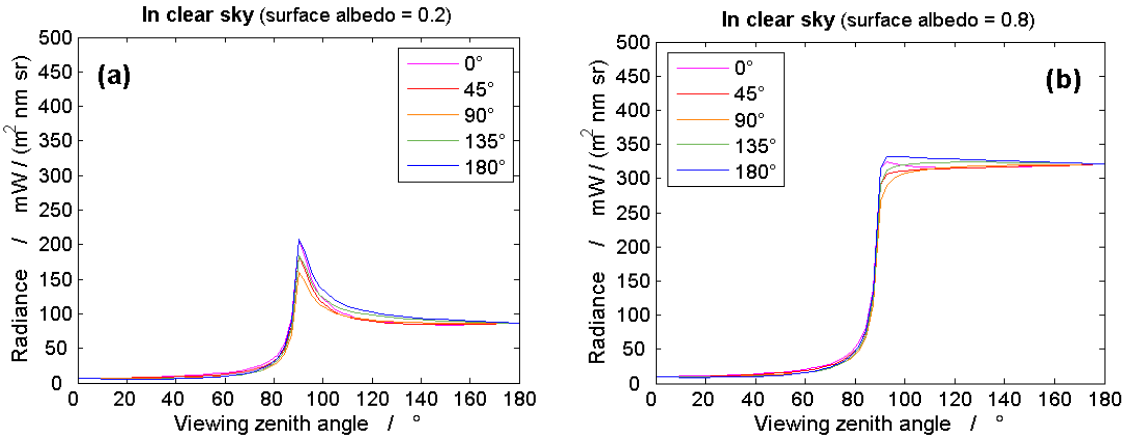

Figure 4.7-3. Expected solar radiances in a clear sky in dependence on different viewing directions for surface albedos of 0.2 (a) and 0.8 (b).

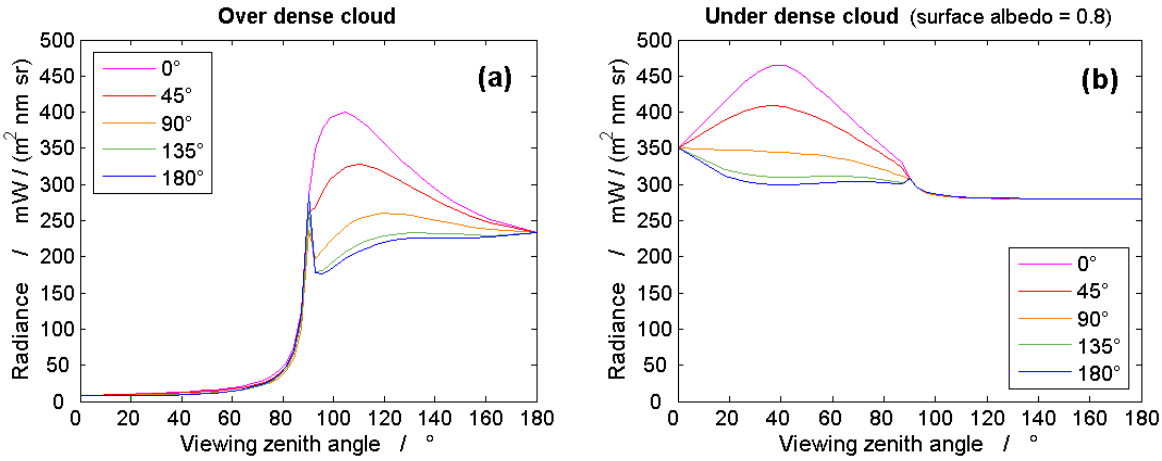

Figure 4.7-4. Expected solar radiances in an overcast sky in dependence on different viewing directions above the cloud layer (a) and between the cloud layer and a surface with an albedo of 0.8 (b).

A further point to consider is that the short range light detection system presented in this work has a relatively big field of view of about 83 mrad (sect. 6.1) in order to collect efficiently the backscattered laser light. The probability of being exposed to direct solar irradiance is thus higher as for most ground based lidar systems using comparably large receiving telescopes with small field of views usually on the order of only a few mrad. Exposure to direct solar irradiation during operation has to be avoided, e.g. by mechanical shutters, since it will lead to saturation or even damage of the detectors and make measurements impossible. In the general case, the lowest risk of being exposed to high radiance is found for the vertically upward looking direction. With regard to the installation point of the air data system, the top of the aircraft fuselage would thus be favorable.

5 Measurement methodology

5.1 Air temperature and molecular number density measurement

For a future aircraft-carried measurement system, the backscattered laser light will be measured in a fixed volume centered at a fixed distance of the order of 1 m. This is close to the aircraft skin but outside the disturbed area of the fuselage flows. The installation location of the window for the measurement system which is inside the aircraft has to satisfy three conditions: First, it has to guarantee the accessibility to the unperturbed air mass, second, it has to minimize the detection of solar background and reflected direct solar radiation (e.g. by the Earth surface), and third it should minimize the susceptibility to mechanical damage, dirt deposits or optical property change of the window. Such an installation point could be the upper front part of the aircraft fuselage, leading to a vertically upward pointing direction, as it is proposed in sect. 4.7 and also applied in airborne lidar systems [115]. The atmospheric air present in a certain thermodynamic state and assumed to be in thermal equilibrium generates a molecular backscatter spectrum as shown in Figure 4.1-1. The relevant spectral components are discussed is sect. 4.

The principle of temperature measurement exploits the fact that the occupation probabilities of the rotational states of the air molecules follow a temperature dependent Boltzmann distribution. This gives rise to the characteristic intensity distribution of the lines within the RR spectrum (Figure 4.3-1). Two interference filters are located within the anti-Stokes side of the RR spectrum of air. One is placed on the lower and one on the higher wavelength edge of the spectrum to extract signals with intensities of opposite temperature dependence. In the following, the RR filter or the channel with the RR filter located spectrally closer to the elastic scattering line is named RR1 and the filter or channel with filter located farer away is named RR2. The transmitted signal energies by RR1 and RR2 as a function of temperature for the designed system using the real data of the used interference filters are exemplarily shown in Figure 5.1-1. Although the Stokes part of the RR spectrum is stronger, the anti-Stokes side is used, in order to avoid interference with fluorescence of glass of the optical receiver components or with fluorescence of aerosols [116, 117].

For temperature measurements, a parameter Q to be calibrated is defined [118]:

$$Q(T) = \frac{U_{RR2}(T,N)}{U_{RR1}(T,N)} \ . \qquad (5.1.1)$$

T is the air temperature and N the molecular number density. U_{RR1} and U_{RR2} are the detected signals in the channels RR1 and RR2 (see also Appendix B). In this ratio, all light intensity related parameters, which vary for both channels by the same amount, like e.g. the air density N, cancel, letting Q be an unambiguous function of temperature (Figure 5.1-2 (a)). By measuring Q, the air temperature can thus be directly derived. The calibration function setting the air temperature into relation with Q is presented in sect. 5.2.

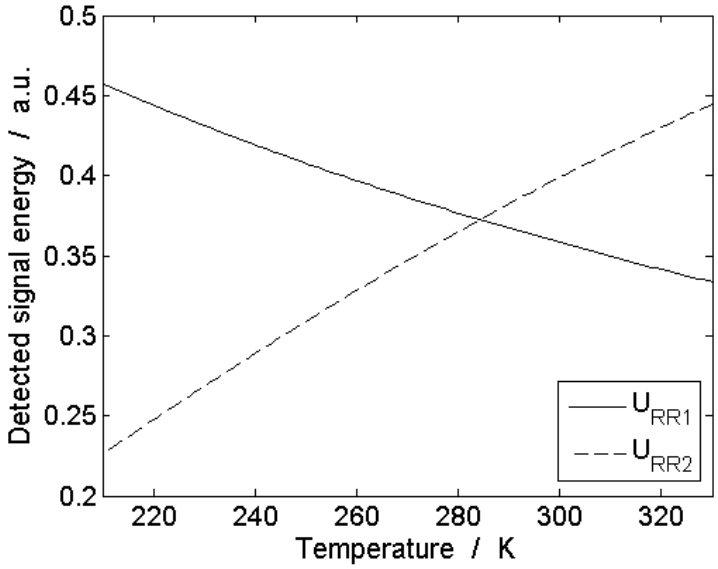

Figure 5.1-1. Temperature dependence of the filtered RR signals. The filter CWLs are 531.2 nm for filter RR1 and 528.9 nm for filter RR2.

In the case of molecular number density measurements a parameter *S* is defined:

$$S(N) = \left(U_{RR1}(T,N) + c_1 U_{RR2}(T,N)\right) \cdot \left(1 + c_2 Q(T) + c_3 Q^2(T)\right) . \quad (5.1.2)$$

If the detector response is linear, U_{RR1} and U_{RR2} will be directly proportional to the molecular number density of air *N*, and thus *S* will be as well. The coefficients c_1, c_2 and c_3 are calculated by a least squares fit over temperature in such a way that *S* varies negligibly with temperature. A simple linear combination of U_{RR1} and U_{RR2} (left factor of eq. (5.1.2)) can vary by more than 0.5 % with temperature over the whole temperature span (Figure 5.1-2 (b)). The multiplication of a further temperature term (right factor of eq. (5.1.2)) reduces this residual variation by around one order of magnitude to < 0.03 % and can be further reduced by adding more temperature coefficients of higher order to the temperature term. Since the RR spectrum is mainly made up of oxygen and nitrogen lines and contributions from other molecular gases including water vapor are negligibly small (see sect. 7.8.1), *S* is proportional to the density of dry air. The usage of the RR spectrum for the density measurement instead of e.g. the nitrogen vibrational Raman signal is advantageous because of higher RR backscatter coefficients by around one order of magnitude.

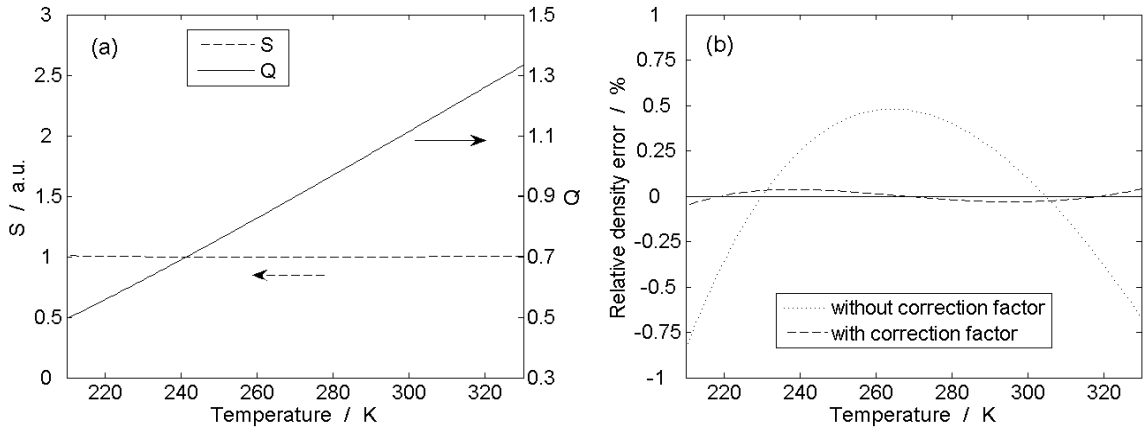

Figure 5.1-2. (a): The two defined parameters Q for temperature measurement and S for density measurement. Q is independent on density, S is negligibly dependent on temperature. (b): Residual relative density error due to the temperature variation of S with and without the temperature correction factor (right factor of eq. (5.1.2)). With correction factor the error is reduced to < 0.03 %.

5.2 Calibration of temperature and density measurement

For the temperature measurement, different calibration functions were already discussed exhaustively in [10]. The exponential calibration function recommended therein and also in [71] for the use over a broad temperature range is

$$Q(T) = \exp\left[\frac{c_1'}{T_{calib}^2} + \frac{c_2'}{T_{calib}} + c_3'\right] . \qquad (5.2.1)$$

Rearrangement yields

$$T_{calib} = \frac{-2c_1'}{c_2' + \sqrt{c_2'^2 - 4c_1'\left(c_3' - \ln(Q)\right)}} , \qquad (5.2.2)$$

with c'_1, c'_2 and c'_3 being the three temperature calibration coefficients. T_{calib} is the calibrated temperature. The calibration error ΔT_C is defined as

$$\Delta T_C = T_{calib} - T . \qquad (5.2.3)$$

The simulated calibration error for the measurement apparatus described herein (see sect. 6) including the real data of the used interference filters, leads to a theoretical systematic calibration error smaller than 0.02 K made for the whole temperature range from 210 K to 330 K (Figure 5.2-1). This error is small compared to the expected statistical measurement uncertainties discussed later. This accounts for

all central wavelengths (CWLs) of the interference filters RR1 and RR2, which can be adjusted in terms of performance optimization (see sect. 7.5).

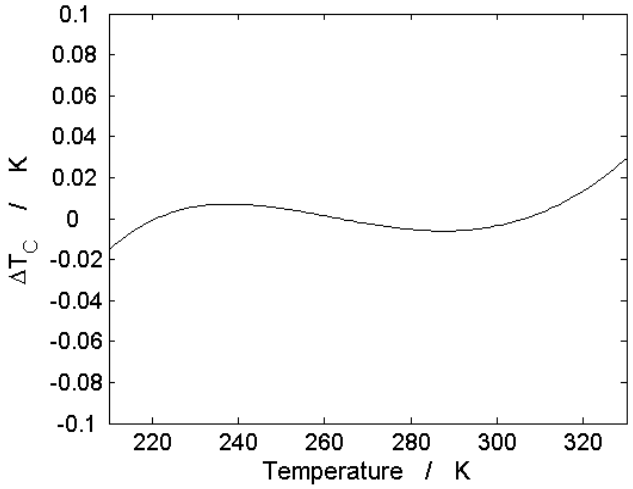

Figure 5.2-1. Systematic error of the temperature calibration due to the used calibration function (eq. (5.2.2)). The CWLs are chosen to be 531.2 nm for filter RR1 and 528.9 nm for filter RR2.

The molecular number density measurement is calibrated with the function S (eq. (5.1.2)) multiplied with a further proportionality factor a. The multiplication with a single factor a is sufficient in this idealized model, where the two RR signals U_{RR1} and U_{RR2} are assumed to be directly proportional to the molecular number density (linear detector response). In practice this is not always the case (see sect. 8.2.2). The calibrated molecular air density N_{calib} is then

$$N_{calib} = a \cdot S \quad . \tag{5.2.4}$$

a comprises all apparatus and atmospheric parameters that affect both RR channels similarly. a accounts also for the contribution of other gases, which make up a constant fraction of the atmospheric gas composition. In the troposphere this is mainly argon with a fraction of 0.93 %. Gases making up a variable fraction of the gas composition are not considered in the calibration and have to be measured separately if their relative amount is not negligible. That is the case for atmospheric water vapor (see sect. 4.5 and 7.8.2). For that reason this density calibration is only valid for dry air. The other calibration coefficients c_1, c_2 and c_3 account for optical properties differing in channels RR1 and RR2. In particular, all coefficients are a function of the interference filter properties including peak transmission, central wavelength (CWL) and transmission bandwidth. Thus, with regard to optimization and performance calculations in sect. 7.5, a set of 4 calibration constants has to be determined independently for each CWL pair of RR1 and RR2 to be examined.

The calibration error ΔN_C is defined as

$$\Delta N_C = \frac{N_{calib} - N}{N} \ , \tag{5.2.5}$$

were N is the true air molecular number density. ΔN_C is equal to the error shown in Figure 5.1-2 (b) thus < 0.03 % for the whole temperature span from 210 K to 330 K. This is negligibly small with respect to the simulated statistical uncertainties described in sect. 7.

5.3 Measurement of moist air density, atmospheric pressure, backscatter ratio, particle backscatter coefficient, and volcanic ash

In addition to the pure rotational Raman channels RR1 and RR2 two further interference-filter-based channels are applied to correct for potential systematic measurement errors. The third channel, named channel H_2O, is implemented for detecting the water vapor vibrational-rotational Raman backscatter (Figure 4.5-2), hence providing moisture information. Air moisture can make up a few percent of total air density in the hotter lower troposphere (see sect. 4.5). Thus, to provide the total density of moist air with sufficient accuracy, the water vapor molecular number density has to be measured as well. Water vapor cannot be measured with the RR channels, since its contribution to the pure rotational Raman spectrum of atmospheric air (see sect. 4.5.1 and 7.8.1) is negligibly weak. Because the water vapor density and the temperature are measured, the relative air humidity can also be derived with the three channels.

By treating the atmospheric air as a mixture of two ideal gases, notably dry air and water vapor, the molecular number density of moist air N_{moist} can be written as the sum of the molecular number densities of dry air $N_{dry} = N_{calib}$ (eq. (5.2.4)) and the one of water vapor N_{H2O}:

$$N_{moist} = N_{dry} + N_{H2O} \ . \tag{5.3.1}$$

N_{H2O} is directly proportional to the output signal U_{H2O} from channel H_2O:

$$N_{H2O} = b \cdot U_{H2O} \ , \tag{5.3.2}$$

with the proportionality constant b. Instead of measuring the water vapor density, often the water vapor volume mixing ratio is measured. This is done by comparing the detected measured water vapor backscatter to a molecular reference signal, which is the nitrogen vibrational Raman signal in most cases [69, 74-76]. In the approach presented herein, the measured dry air density $N_{dry} = N_{calib}$ or rather S, which is measured with the RR channels, is used as reference signal as proposed in [69] due to the around one order of magnitude larger detected signal intensities. It has to be remarked here, that the

water vapor RR spectrum does not offer a possibility for water vapor concentration measurements. This is because any of the weak H_2O RR lines cannot be isolated from the N_2 or O_2 RR lines with sufficient signal-to-noise ratio (cf. sect. 4.5.1). With the water vapor volume mixing ratio, the signal N_{moist} is calculated by

$$N_{moist} = N_{dry}\left(1 + M_{H2O}\right) , \tag{5.3.3}$$

where M_{H2O} denotes the water vapor volume mixing ratio relative to dry air. M_{H2O} is measured by:

$$M_{H2O} = b' \frac{U_{H2O}}{S} , \tag{5.3.4}$$

with b' being the calibration constant. Relative humidity Φ is then obtained by

$$\Phi = \frac{k_B T}{E_{H2O}} M_{H2O} N_{dry} . \tag{5.3.5}$$

k_B is the Boltzmann constant and E_{H2O} is the saturation water vapor pressure to be directly derived from the measured temperature T.

Finally, with the parameters measured on the basis of the described measurement principles, the atmospheric pressure p_{total} can be calculated using the ideal gas equation

$$p_{total} = N_{moist} k_B T_{calib} . \tag{5.3.6}$$

Alternatively, instead of the ideal gas equation, the van-der-Waals equation for real gases can be used. However, this does not lead to significant benefit in accuracy.

The fourth channel, named channel *CP* (Figure 4.3-1), extracts elastically scattered radiation (Cabannes and particle scattering). The backscatter ratio R and the backscatter coefficient β_{par} can then be derived. R and β_{par} are used to minimize errors due to elastic signal leakage in the Raman channels in optically thick clouds and to correct atmospheric extinction effects. This is further discussed in sect. 7.7.

The backscatter ratio R is defined as the total elastic backscatter to molecular elastic backscatter and measured using the output signal U_{CP} of channel *CP* and the molecular reference S:

$$R = \frac{\beta_{par} + \beta_{Ray}}{\beta_{Ray}} = \frac{U_{CP}}{S} \frac{S_0}{U_{CP,0}} . \tag{5.3.7}$$

β_{Ray} is the Rayleigh backscatter coefficient (sect. 4.4). $U_{CP,0}$ and S_0 are signals used for normalization and recorded in a particle free atmosphere.

The particle backscatter coefficient β_{par} is determined with the measured backscatter ratio R and the measured molecular number density N_{calib}:

$$\beta_{par} = (R-1)\cdot\beta_{Ray} = (R-1)\cdot N_{calib}\cdot\left(\frac{d\sigma}{d\Omega}\right)^{\pi}_{Ray} . \qquad (5.3.8)$$

$(d\sigma / d\Omega)^{\pi}_{Ray}$ is the Rayleigh backscatter cross section obtained from sect. 4.4.

In presence of unusually high particle backscatter, the measurement of relative air humidity Φ and the particle backscatter coefficient R enables additionally to discriminate between scattering from water clouds, where humidity is close to saturation and layers consisting of other particles, as e.g. volcanic ash, where the relative humidity is significantly smaller than 100 % [119]. The implementation of a polarization sensitive detection in channel CP will further increase the capabilities to distinguish the backscatter from spherical water cloud particles and non-spherical and thus strongly depolarizing (volcanic ash) particles. An implementation of a volcanic ash detector on aircraft could be interesting for flight safety as well as for economic reasons, like the extensive air travel disruption after the 2010 eruption of the Eyjafjallajökull volcano in Iceland demonstrated.

With the help of the measured parameters, the atmospheric extinction is accounted for as well. The derivation of the extinction and the extinction corrected air density is described in more extensive context in sect. 7.7.2.

In summary, with the described 4 interference filter-based channels, the following atmospheric parameters can be determined without further knowledge about the atmospheric state:

- Measurement of air temperature independent from air density and pressure
- Measurement of total density of both dry and moist air with negligible dependence on air temperature
- Measurement of absolute and relative humidity
- Measurement of elastic backscatter ratio and particle backscatter coefficient
- Discrimination between scattering from cloud particles and non-cloud particles as e.g. volcanic ash
- Taking into account of atmospheric extinction

6 Instrumental description

The theoretical performance analysis and the optimization calculations discussed in sect. 7 as well as the experiments presented in sect. 8 are based on the system parameters of the laboratory measurement system. The whole laboratory measurement system (Figure 6-1) consists of the laboratory prototype measurement apparatus and an atmospheric-simulation chamber system (denoted in the following as the atmospheric simulator) for the generation of typical atmospheric states encountered by aircrafts with regard to air temperature, pressure and humidity. The prototype measurement apparatus is composed of a frequency-doubled Nd:YAG laser source and a receiver for the collection of the light scattered inside the atmospheric simulator. An oscilloscope and a PC are connected to the receiver to record and analyze the data. The properties and the setup of all these parts are described in the following. A focus is put on the used interference filters being the important core part of the receiver.

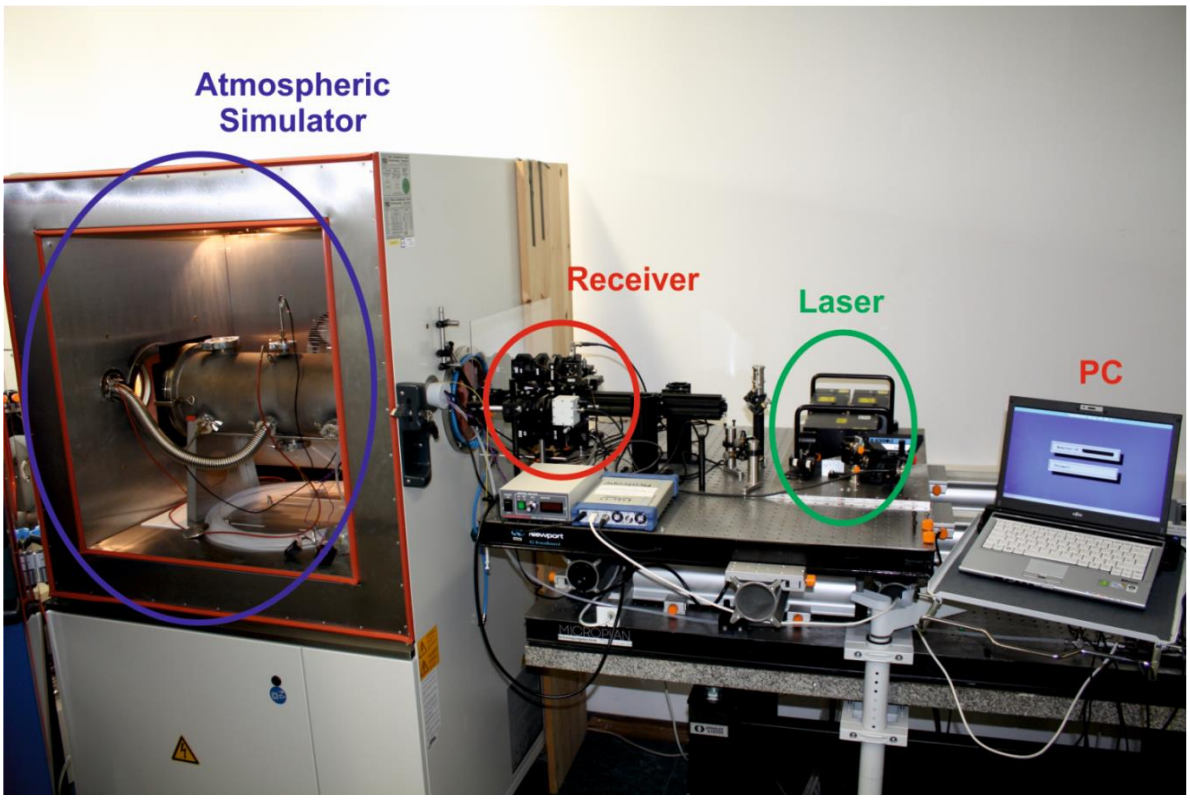

Figure 6-1. Whole laboratory measurement setup including atmospheric-simulation chamber system (atmospheric simulator), receiver, laser and PC.

6.1 Laser and receiver system

A frequency doubled, pulsed Nd:YAG laser operating at 532.07 nm from *BigSky* (now *Quantel*) is used as light source (Figure 6.1-1). The laser data are summarized in Table 6.1-1.

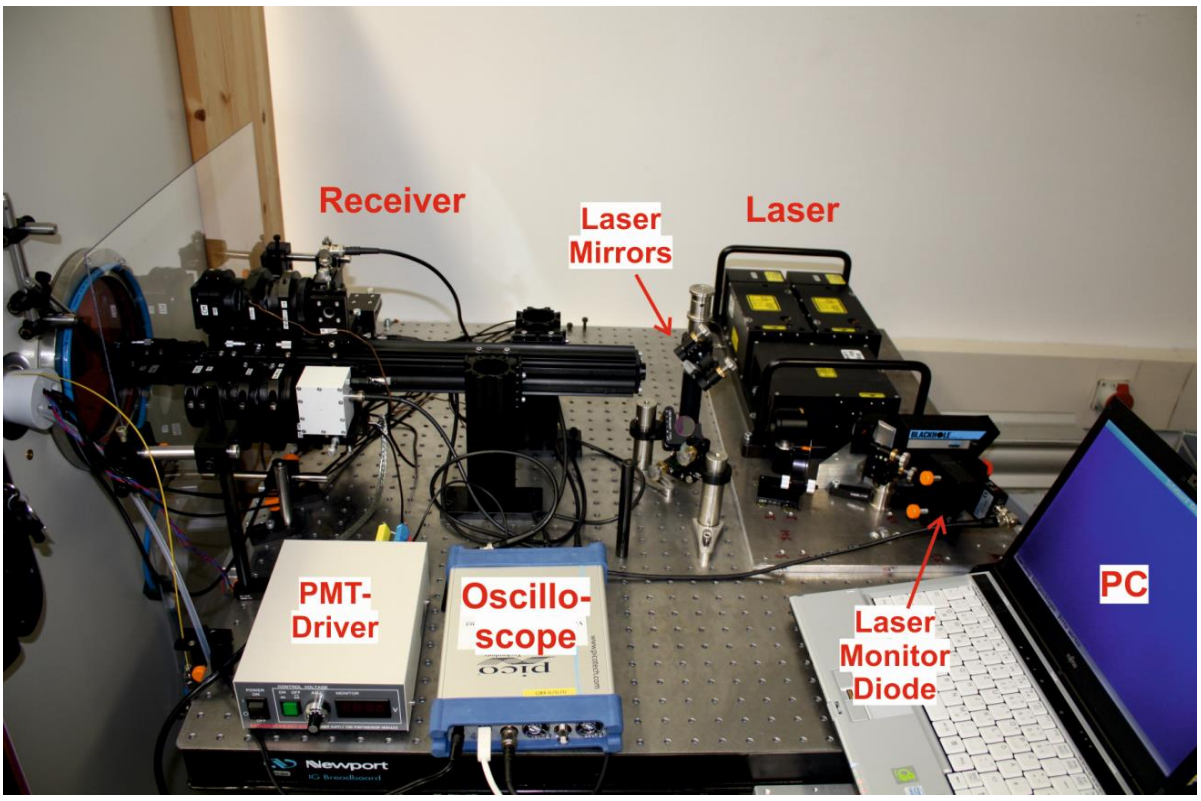

Figure 6.1-1. Layout of the optical breadboard including laser, receiver and peripheral electronics and mechanics. The board is located in front of the atmospheric simulator.

Table 6.1-1. Specifications of the used laser source taken from the manufacturer data sheet. The values of the pulse energy and the mean power out into parenthesis were additionally measured behind the atmospheric-simulation chamber, i.e. behind the measurement volume.

Laser model	*BigSky* CFR-S 200, frequency doubled Nd:YAG, flash lamp pumped, pulsed, multimode, unseeded, water cooled
Wavelength	532.07 nm
Pulse energy	200 mJ (118 mJ)
Pulse energy stability (peak to peak)	± 6 %
Pulse duration	≈ 10 ns
Repetition rate	10 Hz
Mean power	2 W (1.18 W)
Linewidth	< 2 cm^{-1} (equals < 0.057 nm at 532 nm)
Frequency jitter	unknown
Temperature drift	unknown

Although the performance calculations and the experiments are focused on the used laser wavelength at 532.07 nm, the results can be adapted for other laser wavelengths. The laser average

power and pulse energy is intentionally very large, because for first laboratory experiments this is advantageous for optimization. However, in the future airborne application, a laser with other wavelength and lower pulse power and higher repetition rate may be employed. See sect. 7.9 and 7.10 for the theoretical analysis and sect. 8.4.3 and 8.4.4 for the experimental results concerning the demands on and the choice of other laser sources.

Since the receiver layout (Figure 6.1-2 and Figure 6.1-3) is multi-static, i.e. the laser output beam and the received input beam of each channel are passing different lens systems, the measurement volume is geometrically defined and fixed. Thus, gated detection is dispensable and pulsed laser operation not required by principle. However, using a pulsed laser source raises significantly the signal-to-noise ratio (SNR) and thus the measurement precision, especially in presence of solar background light. The nominal laser spectral width is < 2 cm^{-1} and is of minor importance for the measurements as long as it remains constant. The resulting broadening of the RR spectral lines is taken into account by the calibration as well as the effect of the laser beam diameter and divergence on the detected signal power.

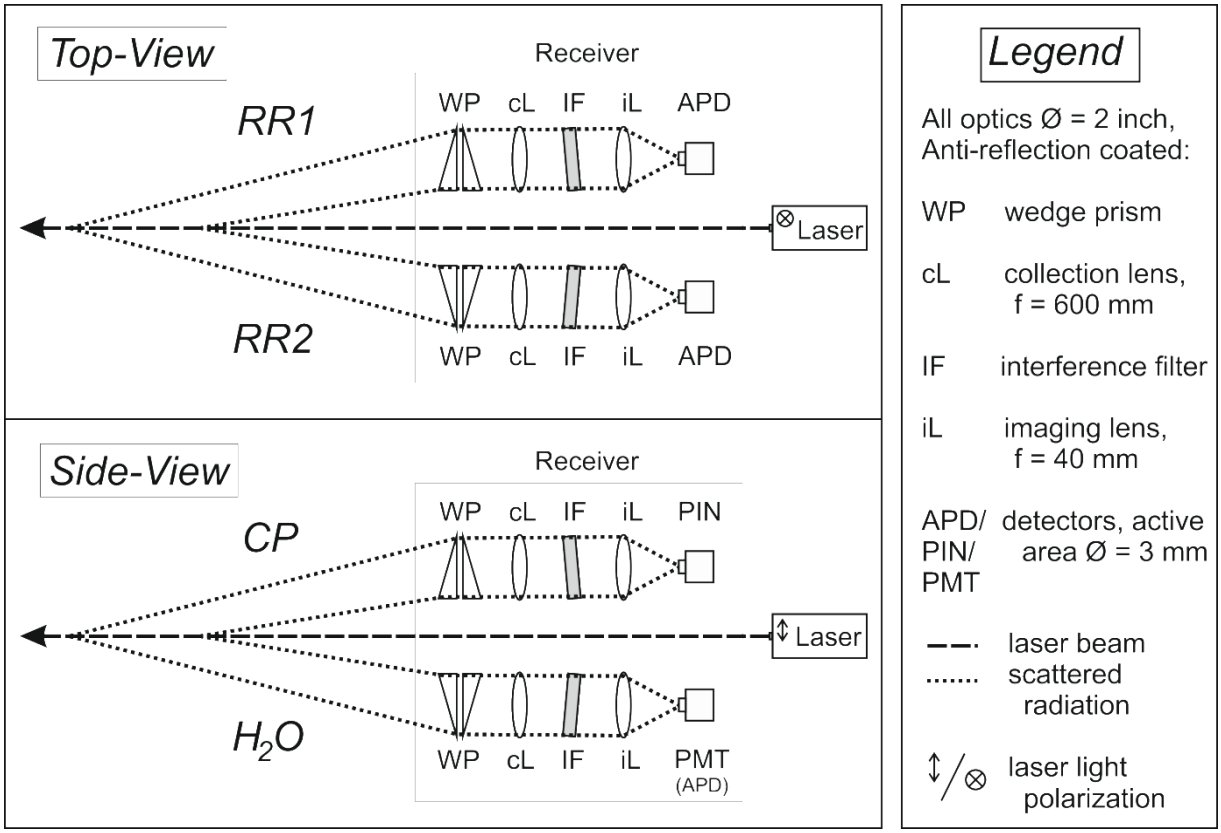

Figure 6.1-2. Concept of the laboratory emitter and receiver system. A pulsed laser emits light into the atmosphere. Four channels detect and spectrally filter the light backscattered from the measurement volume at distances around 0.4 m < l_{scatt} < 0.83 m (compare to Figure 6.2-2).

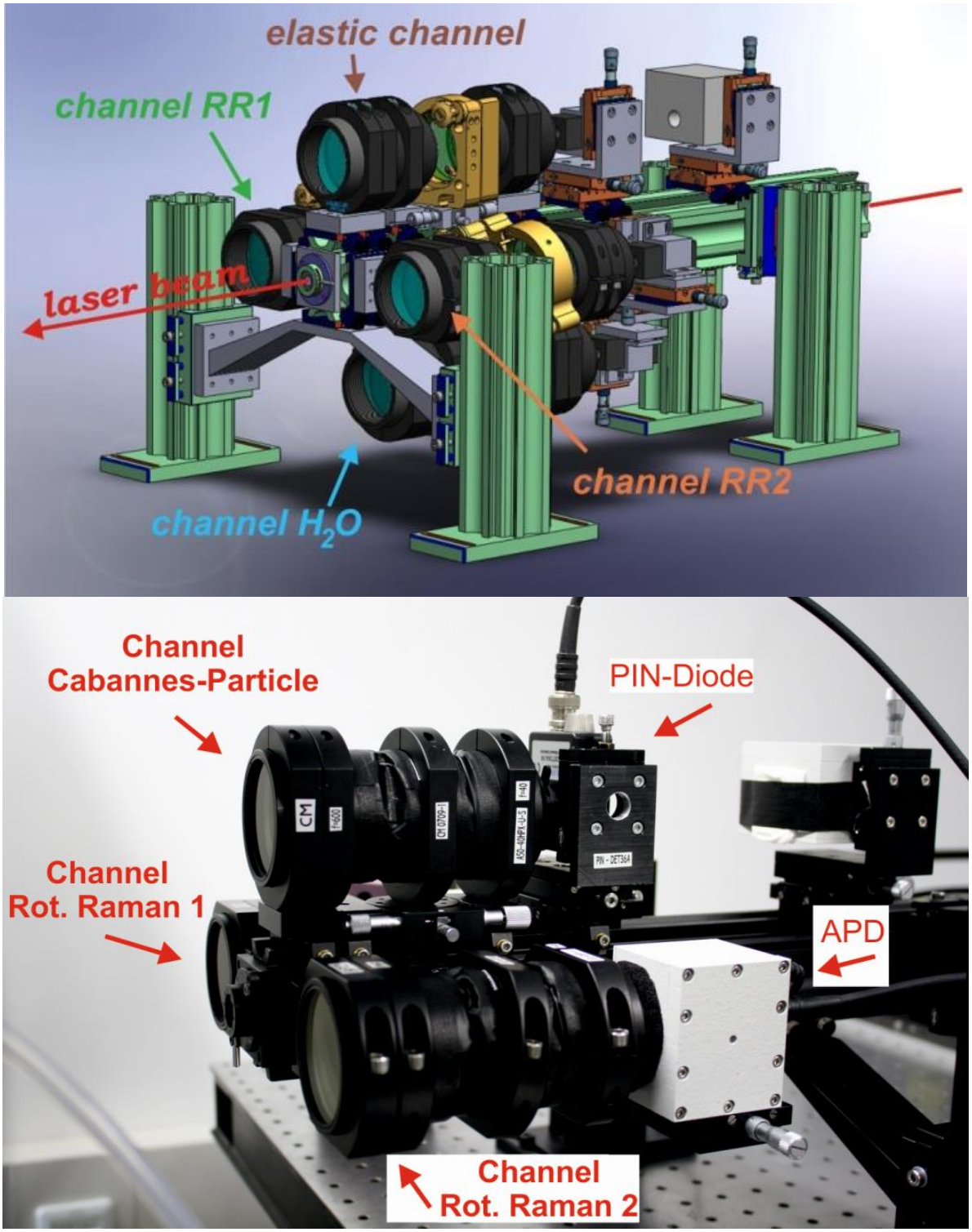

Figure 6.1-3. CAD drawing of the whole receiver made with the program *SolidWorks* (top), and photo of the receiver laboratory setup (bottom) with the channels *RR1*, *RR2* and *CP*. Channel H_2O was not set up at the time of photo acquisition.

The receiver is set up of the four described measurement channels *RR1*, *RR2*, *CP* and *H_2O* to be seen in Figure 6.1-2. The optical components listed in this figure are identical in each channel except for the interference filters used for extracting the different backscattered signals and an additional long-pass interference filter (*Chroma:* HQ600lp) in channel *H_2O* used to augment the rejection of elastically backscattered light. Figure 6.1-3 shows additionally a CAD drawing (top) and a photo (bottom) of the receiver. Channel H_2O was missing at the time of photo acquisition. Each interference filter is mounted on a rotation stage to allow the adjustment of the angel of incident radiation. All channels are built symmetrically around a hollow construction rail encircling the emitted laser beam. The optical components are mounted on custom-built adaptor plates, which in turn are mounted on slides, which are compatible with the construction rail. To maximize the detected optical backscatter, the receiver channels are built as close as possible around the construction rail, i.e. the construction height for each channel, or in other words the distance of the channel axes to the axis of the emitted laser beam, is minimized. This is achieved by clamping the rotation stages from the side using further adaptor plates instead of mounting them on top of the latter. Thus, the construction height of each channel is reduced by approx. 30 mm to 81 mm resulting in a calculated signal gain of about 20 % due to a larger beam overlap of the transmitted and received light beam. The rotational Raman channels are arranged in the plane perpendicular to the polarization of the laser light to further increase the collected RR backscatter, whereas the elastic channel and the water vapor channel are arranged in the plane parallel to the laser polarization.

All optics are appropriately anti-reflection (AR) coated and have a diameter of 2 inch. For channel RR1 and RR2, respectively, a custom-made temperature stabilized avalanche photo diode (APD) detector (*Laser Components:* SAR3000) with a transimpedance amplification electronics (*Menlo Systems*) is used. The upper frequency limits of the detection bandwidths of the APDs are 350 MHz. The active-areas of the APDs have a diameter of 3 mm. In the case of channel CP, a simple PIN photodiode detector (*Thorlabs:* DET36A) with a 3 mm diameter pinhole is employed due to at least 500 times higher scattering intensities. The choice of these detector types is a result of the optimization calculations in sect. 7.4. For channel H_2O, a photomultiplier (PMT; *Hamamatsu*: H6780) with an external driver is employed instead of an APD detector, although the latter is recommended by the optimization calculations in terms of maximization of the signal-to-noise ratio (SNR). This decision was made, because the output voltages of the APD detector, which was employed beforehand were too low to be monitored with the oscilloscope (*PicoTechnology*: PicoScope 6000 series). The four channel oscilloscope has a frequency bandwidth of 350 MHz and a real time sampling rate of 5 giga-samples / s (≙ 1.25 giga-samples / s per channel), and a resolution of 8 bits. In order to monitor the change of the laser pulse energy from shot to shot, a further PIN photodiode detector (*Thorlabs:* DET10A) is employed. The receiver arrangement for all channels together is about 200 mm long and has a diameter of 230 mm. It can be integrated behind a flush aircraft window of maximally 200 mm diameter.

6.2 Measurement volume

The pulse energy of the detected light signals in the receiver channels and thus the statistical measurement uncertainties of the derived atmospheric parameters are largely influenced by the length and the distance of the measurement volume, i.e. the section of the laser light path in front of the receiver, where light is scattered and detected by the channels. The measurement volume is set by the overlap of the central laser beam with the receiving volume of each channel, defined by the optical properties of the components in each channel and by their alignment with respect to each other. The optical components are two wedge prisms, a collection (or collimation) lens of 600 mm focal length, an imaging lens of 40 mm focal length and the respective detector area. The wedges are used to refract the collected light by 8.1° in the direction of the channel axis. The scattering geometry and the arrangement of the receiver and the vacuum tube, which encloses the measurement volume, are shown in Figure 6.2-1. The field of view of each channel amounts FOV = 83 mrad and allows for efficient collection of radiation, resulting in a measurement volume of around 430 mm length centered at a distance of about 550 mm in front of the receiver. This distance can be increased by using a collection lens of higher focal length and adapting the refraction angel of the wedges. Calculations show, that the detected signal pulse energies in each channel will remain virtually unchanged, since the resulting signal loss due to a larger measurement distance will be compensated by the signal gain due to the increase of the length of the measurement volume.

With the imaging equations for the lenses, the ray propagation geometry and the optical properties of the used components in each channel, the amount of light energy received from different locations within the measurement volume is calculated and expressed by the function $\Omega_{scatt}(l_{scatt})$ (Figure 6.2-2). Ω_{scatt} in the physical sense is the solid angle of that part of backscattered radiation, which passes the receiver and hits the detector as function of the scattering distance from the receiver l_{scatt}. The integral of Ω_{scatt} over l_{scatt} is directly proportional to the detected optical pulse energy. This relation is used in the lidar equation in sect. 7.3.

Because the knowledge about the measurement volume is crucial for the correct calculation of the detected signal energies and their measurement uncertainties, the results of the computations shown in Figure 6.2-2 were additionally cross-checked with the help of a ray tracing program (*Optalix*). This is presented in Figure 6.2-37.3, which illustrates the length and the position of the measurement volume from the point of view of the scattering geometry.

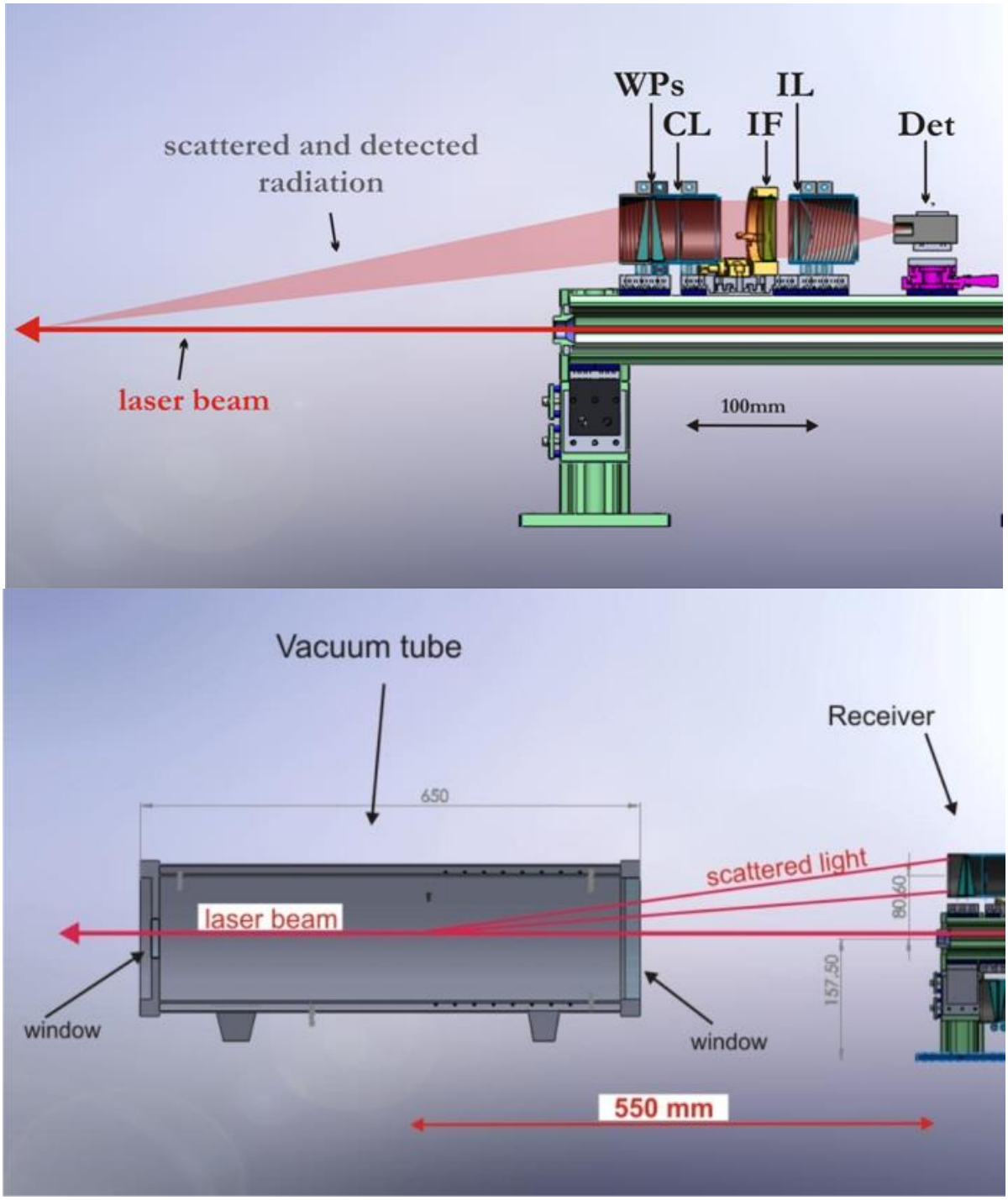

Figure 6.2-1. Ray propagation geometry shown in a cross-sectional drawing exemplarily for only one channel (top) and arrangement of the receiver and the vacuum tube (bottom), which is described below. The images were made with the program *SolidWorks*. The legend for the top image can be found in Figure 6.1-2.

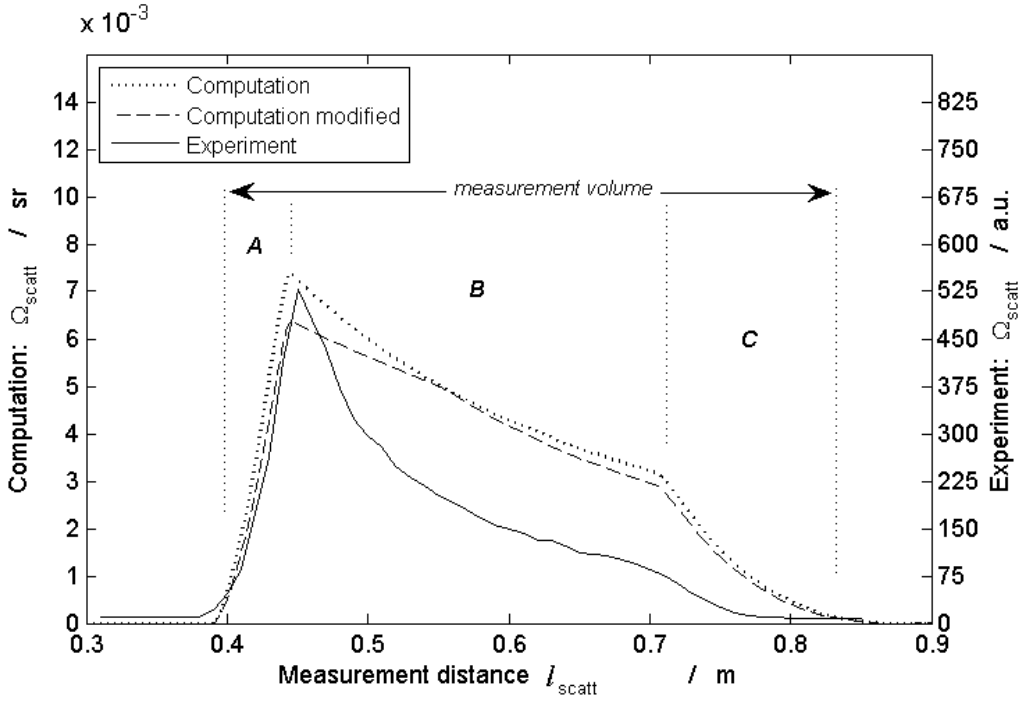

Figure 6.2-2. Solid angle $\Omega_{scatt}(l_{scatt})$ of that part of backscattered radiation, which is detected in each receiver channel, as function of the scattering distance from the receiver l_{scatt}. The amount of light energy detected from different distances l_{scatt} in front of the receiver is proportional to $\Omega_{scatt}(l_{scatt})$. The function Ω_{scatt} for the current laboratory setup sets the measurement volume limits to distances from $l_{scatt} \approx 0.4$ m to $l_{scatt} \approx 0.83$ m. Two versions of computed Ω_{scatt} are shown. Dotted curve: The typical quadratic decrease of Ω_{scatt} (region *B*) is limited by intensity drops, where the collected light does not fully hit the detector (region *A* and *C*). Dashed curve: This curve accounts also for shadowing effects caused by the divergent light inside the receiver. At a scattering distance of about 550 mm (equal to the focal point of the collection lens in front of the receiver) no shadowing occurs, since the light beam inside the receiver is fully collimated and collinear to the channel axis. Solid curve: The experimentally measured devolution of Ω_{scatt}.

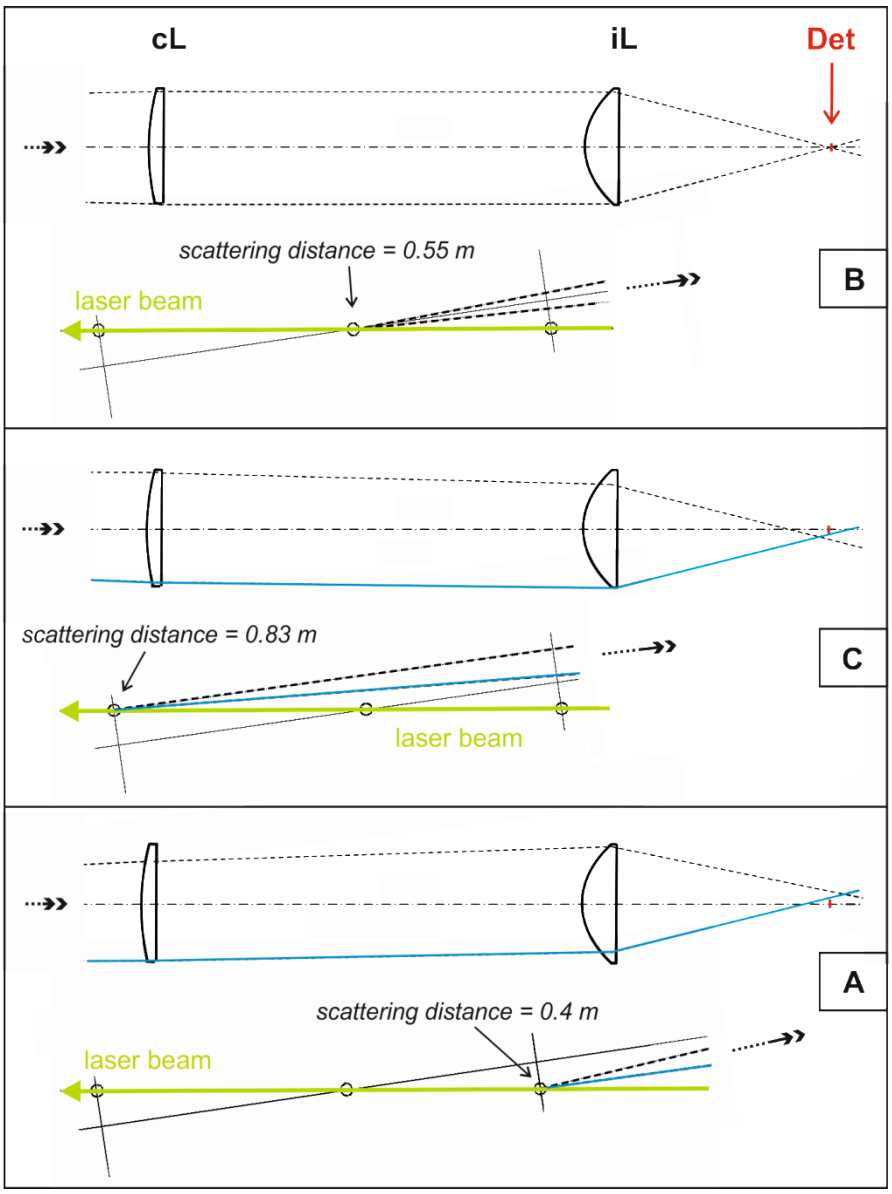

Figure 6.2-3. Illustration of the length and the position of measurement volume in front of the receiver on the basis of the ray propagation geometry of one measurement channel. The plot was made with the help of a ray tracing program (*Optalix*). cL: collection lens; iL: imaging lens; Det: detector. Top part: Radiation scattered and collected from around the focal point of the collection lens in front of the receiver (550 mm) and fully falling onto the detector. This corresponds to region B in Figure 6.2-2. Center part: Radiation scattered and collected from the farer edge of the measurement volume. Only the outer rays (blue) of the collected light beam fall onto the detector (region C in Figure 6.2-2). Bottom part: Radiation scattered and collected from the nearer edge of the measurement volume. Here, again, only the outer rays (from the same channel side) of the light beam fall onto the detector (region A in Figure 6.2-2).

6.3 Atmospheric simulator

An atmospheric-simulation chamber system (denoted as atmospheric simulator) consisting of two chambers had been set up to simulate the atmospheric states encountered at a typical flight envelope from sea level to an altitude of around 13000 m (Figure 6-1 and Figure 6.3-1). A large temperature test chamber is capable of generating temperatures from around 230 K to 330 K. Smaller temperatures are possible but are accompanied by icing of the chamber interior. Two anti-reflection (AR) coated windows (ion-assisted deposition process) on both chamber sides are installed to transmit the laser radiation. Inside the chamber, a windowed vacuum tube is connected to a rotary vane pump. A control valve is used for the adjustment of air pressures ranging from 100 hPa to 1000 hPa, thus covering the pressure altitudes from sea level to more than 13000 m according to the *International Standard Atmosphere* (sect. 2).

The temperature distribution inside the vacuum tube is monitored with four PT100 Class 1/10 DIN B probes (*Omega*), together with a data acquisition module (*Omega*: PT-104A). The pressure is monitored with a temperature-stabilized capacitance diaphragm vacuum gauge (*Oerlikon Leybold Vacuum:* Ceravac CTR 101) located outside the temperature test chamber and connected to the vacuum tube (Figure 6.3-2). The pressure sensor is connected to a control and data display unit (*Vacom*: MVC-3 C). The precisions of the chamber temperature and pressure measurement electronics (sensor plus data acquisition) under the laboratory experimental conditions according to the data sheet are better than 0.01 K for the whole measurement range of interest and better than 0.01 % (1000 hPa) to 0.05 % (200 hPa), respectively, and thus better than the precisions expected of the optical temperature, density and pressure measurements. The accuracy of the chamber temperature measurement electronics is of minor importance, since the generated systematic measurement deviations stay the same and can be considered in the calibration. The absolute accuracy of the chamber pressure measurement electronics (gauge plus control unit) is better than 0.25 % (at 1000 hPa) to 0.65 % (at 200 hPa) of the measured pressure value when used at common laboratory temperatures. The absolute accuracy of the chamber pressure measurement system is essential for the assessment of the linearity of the RR detectors (sect. 8.2.2). Apart from the proportionality factor a (eq. (5.2.4)), the errors of the temperature and density calibration coefficients should thus be negligible. The temperature measured inside the vacuum tube is integrated into the temperature control loop of the temperature test chamber.

10 m of rolled-up tubing for the injection of pressurized dry air are located inside the temperature test chamber and connected to the vacuum tube, in order to allow pre-heating or pre-cooling of the inflowing air. A preceding metering valve allows an exact dosage of the latter. A capillary pipe is connected to the vacuum tube through which distilled water can be injected for experiments in a moist atmosphere. The generated water vapor is monitored with a capacitive humidity probe (*Sensirion:* SHT75 Chip). Two fans can be connected to the tube flanges in order to circulate the injected air inside the vacuum tube.

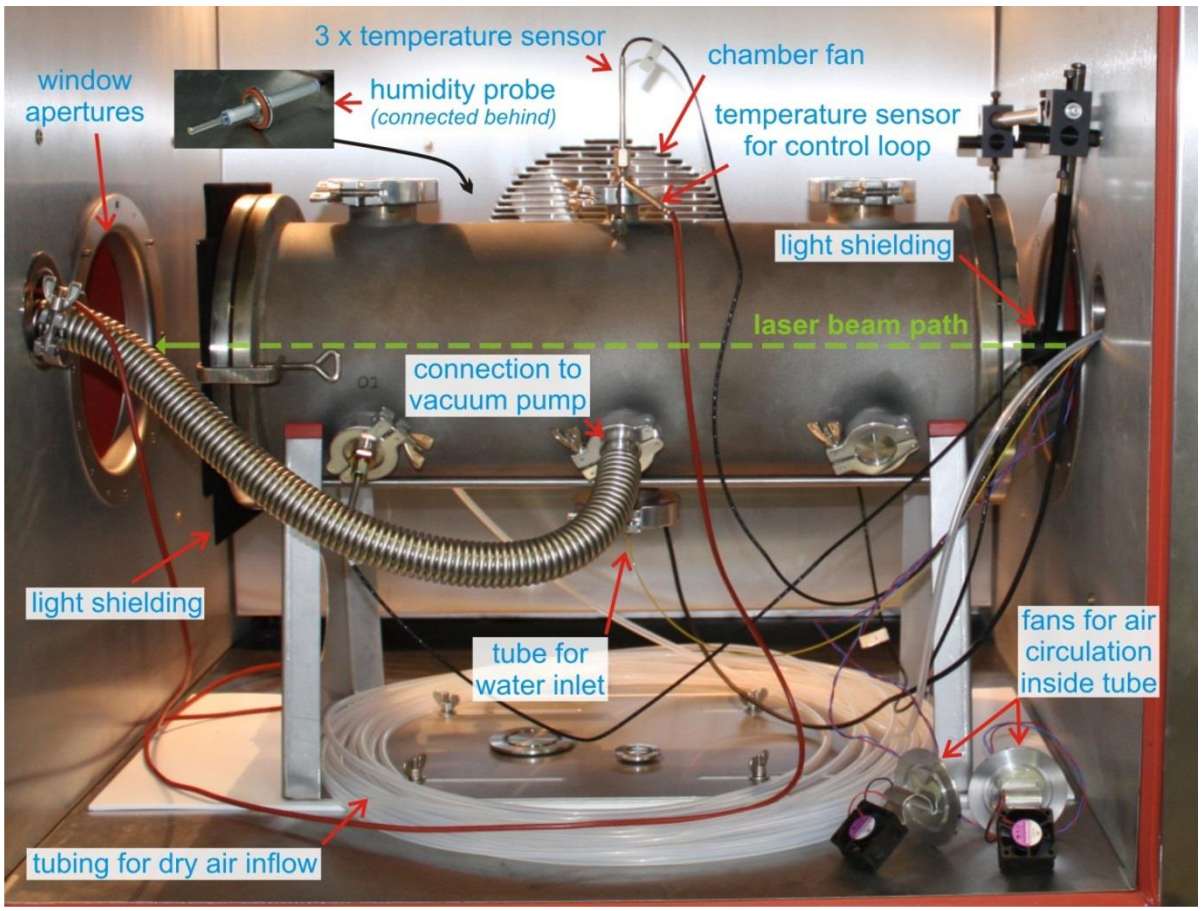

Figure 6.3-1. Vacuum tube located inside the temperature test chamber.

The 650 mm long vacuum tube is large enough to enclose the whole measurement volume of the receiver and to guarantee a free light path between the scattering volume and the receiver collection optics. Since stray light from the windows still remains important, especially for the elastic channel CP, further light shielding elements are placed where necessary. The leak tightness of the vacuum tube is around 0.1 hPa / min at a pressure of 200 hPa inside the tube what is not ideal but sufficient for the experiments. In order to prevent condensation and icing of water vapor on the windows inside the temperature test chamber, the chamber is continuously purged with dry air (nominal dew point of -60 °C). The resulting small overpressure in the interior additionally prevents the outer air from intrusion. Outside the chamber two ring pipes blow dry air onto the chamber windows prohibiting fogging and icing from outside. A big fan integrated into the back wall of the temperature test chamber circulates the air to guarantee air temperature homogeneity inside the temperature test chamber but outside the vacuum tube. Figure 6.3-2 shows the view on the back-end of the atmospheric simulator.

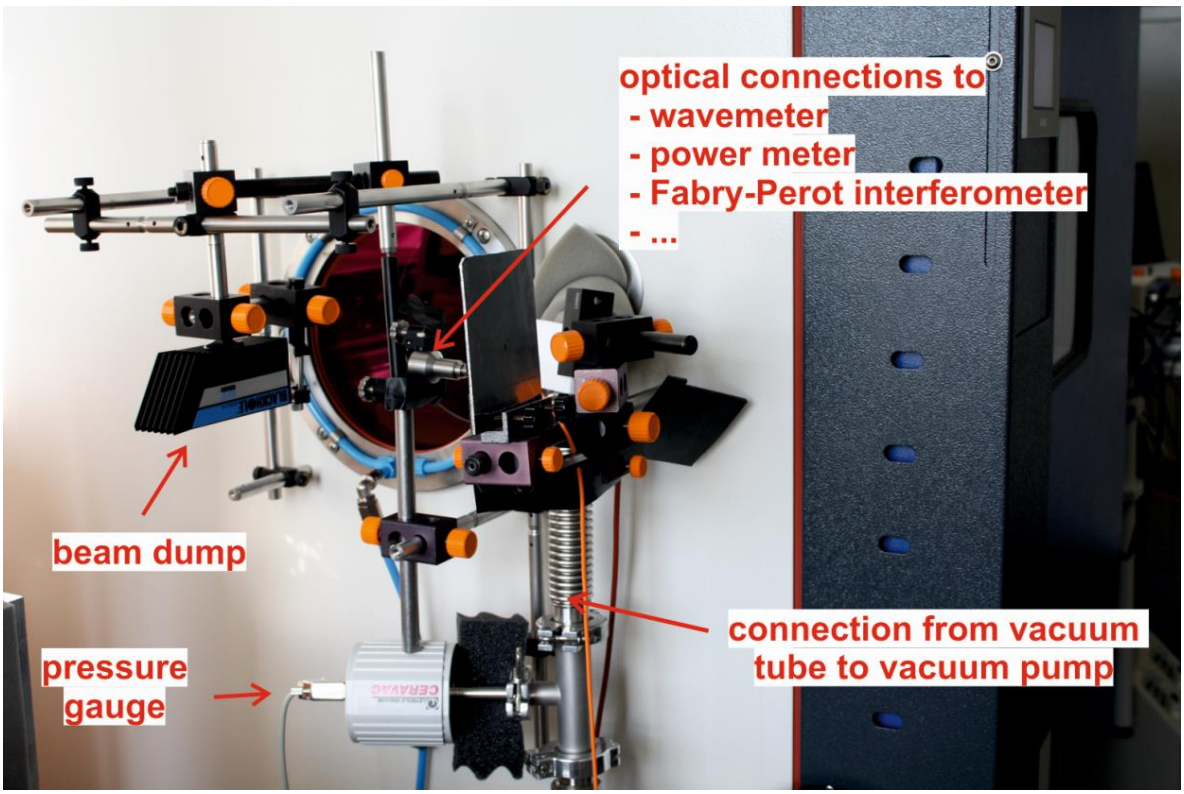

Figure 6.3-2. Back-end view on the atmospheric simulator. The beam dump is for the absorption of the main laser beam after traveling through the vacuum tube and the temperature test chamber. A beam splitter in front of the beam dump separates a partial beam for different analysis purposes.

6.4 Interference filters

6.4.1 Modeled spectral transmission functions

Table 6.4-1 lists the functions and the optical properties of the specified and custom-made interference filters used for the four measurement channels *RR1*, *RR2*, *CP* and H_2O. Figure 4.3-1 and Figure 4.5-2 illustrate their spectral transmission bands. The transmission bands can be wavelength-tuned by changing the angle of the incident radiation onto the filters. This permits an optimization of the filtering properties, in particular with regard to the central transmission wavelengths (CWLs) of the RR filters [71]. The dependency of the CWL on the angle of incidence φ_{RR} (= tilting angle with respect to receiver axis, to be adjusted with the rotation stage) with *RR* = *RR1* or *RR2* is [120]:

$$CWL_{RR}(\varphi_{RR}) = CWL_{RR,0}\sqrt{1-\left(\sin(\varphi_{RR})/n_{RR}\right)^2}\ , \qquad (6.4.1)$$

where $CWL_{RR,0}$ is the CWL of the respective RR filter at φ_{RR} = 0°, hence perpendicular incidence, and n_{RR} is its effective index of refraction.

Table 6.4-1: Functions and optical properties of interference filters. The values put into brackets are the correspondent angles of incidence φ.

	RR1	RR2	CP	H_2O
Spectral position	Higher wavelength edge of RR spectrum	Lower wavelength edge of RR spectrum	Laser wavelength	v_1 vibrational mode of water vapor
Function	Temperature and density measurement	Temperature and density measurement	Elastic backscatter detection, leakage and extinction correction	Moist air density correction, water cloud - particle layer (e.g. volcanic ash) discrimination
CWL tuning range	530.2 nm (7°) - 531.2 nm (0°)	527.7 nm (9°) - 529.3 nm (0°)	532.07 nm (4°)	660.5 nm (3°)
FWHM bandwidth $\Delta\lambda$	0.54 nm (0°)	1.20 nm (0°)	0.56 nm (4°)	1.70 nm (3°)
Peak transmission τ	73 % (0°)	85 % (0°)	82 % (4°)	96 % (3°)
Temperature drift	all filters 2 pm / K			

The filter manufacturer delivered transmission tables for a couple of integer values of φ_{RR} for each RR filter, which characterized the spectral pass-band shape. The delivered transmission band shapes for these φ_{RR} are shown in Figure 6.4-1 (a). However, in order to perform optimization calculations and to find out the optimum CWLs for RR1 and RR2, a function for each filter respectively is needed describing for each desired φ_{RR} (and thus CWL) its transmission at each desired wavelength. The setting up of this filter function denoted as F_{RR} was done in three steps.

First, the function CWL_{RR} (eq. (6.4.1)) was fitted to the CWLs of the datasheet transmission bands shown in Figure 6.4-1 (b). In this way intermediate CWLs could be calculated for φ_{RR} values other than those listed in the manufacturer data sheet. By the way, the effective indices of refraction were yield for RR1 and RR2, which are $n_{RR1} = 1.96$ and $n_{RR2} = 2.02$.

Second, for each φ_{RR} from the datasheet, the measured transmission data were fitted with a cubic spline curve. Thus, filter transmission values as a function of each possible wavelength within the spectral transmission band were obtained.

Third, the transmission band shapes as a function of the CWLs were derived: A linear morphing algorithm was implemented to approximate the spectral transmission band shapes also for other possible CWLs than those delivered by the manufacturer. This was necessary, since the measured transmission bands, especially for filter RR2, changed significantly in shape and peak value within the spectral tuning range of the filters, e.g. the peak transmission for filter RR2 changed by nearly 10 % between $\varphi_{RR2} = 0°$ to $\varphi_{RR2} = 8°$. With the results of the three steps, a spectral transmission function $F_{RR}(\lambda,\varphi_{RR})$ for filter $RR = RR1$ or $RR2$ was generated accepting floating-point values of the

wavelength λ within the transmission band and floating-point values of the angle of incidence φ_{RR}. With $F_{RR1}(\lambda,\varphi_{RR1})$ and $F_{RR2}(\lambda,\varphi_{RR2})$ the computational optimizations were done.

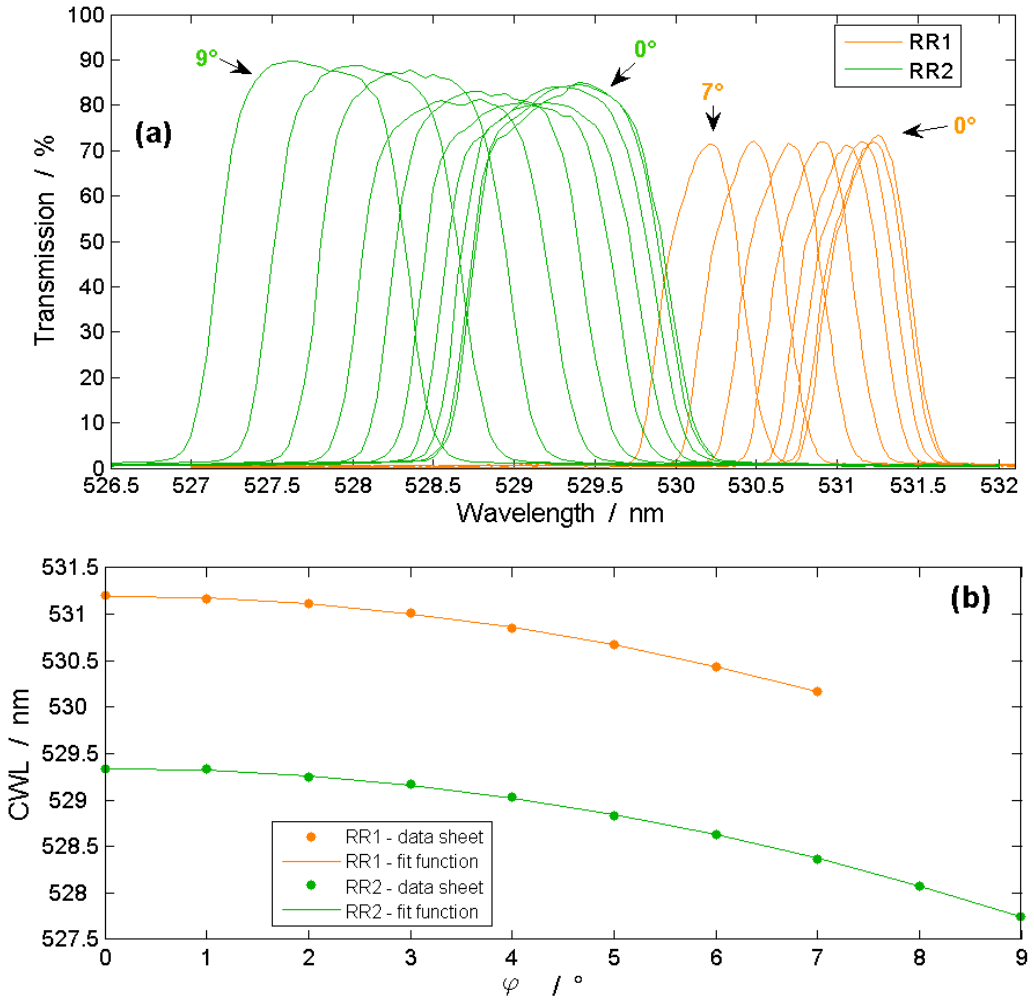

Figure 6.4-1. (a) Datasheet transmission bands of the two used filters RR1 and RR2 for different angles of incidence φ_{RR}. (b) Datasheet CWLs of the RR filters as function of φ_{RR}. Additionally the function CWL_{RR} is computationally fitted to the filter data sets, respectively.

6.4.2 Effect of beam divergence inside the receiver channels

Due to the intentionally large field of view of FOV = 83 mrad and the compactness of the multi-static receiver layout, the measurement volume is very large and the scattered and collected light from the edges of this volume, i.e. from $l_{scatt} \approx 0.4$ m and $l_{scatt} \approx 0.8$ m (cf. Figure 6.2-2), is divergent in fact when passing the RR interference filters, which are each located between a collection and an imaging lens. For example, light beams scattered at 0.45 m and 0.8 m have calculated divergence full cone angles up to about 1.2°. In addition, the angles of the center rays of these light beams differ by 4.3°. Since the interference filter transmission band shapes were measured with collimated light beams by

the manufacturer, the different angles of transmitted radiation might lead to significant changes of the transmission band shape. In order to calculate the resulting effective spectral transmission function $F_{RR,eff}$ for an adjusted φ_{RR}, the transmission functions F_{RR} were integrated over the real angles of incidence of all light rays appearing inside the receiver and passing the RR filter and weighted with their normalized frequency of occurrence. The calculation is explained in Appendix A. Figure 6.4-2 shows $F_{RR,eff}$ and F_{RR} for both RR filters for different angles of incidence φ_{RR}. The CWLs obtained using $F_{RR,eff}$ instead of F_{RR} for a given φ_{RR} are shifted only by less than 0.05 nm towards lower wavelengths and the drop of the filter peak transmission is less than 2 %.

This low sensitivity of the RR filters to non-parallel light, on the one hand, can be partially attributed to the relatively high effective indices of refraction n_{RR1} = 1.96 and n_{RR2} = 2.02 of the RR filters (see sect. 6.4.1), which lead to a strong parallelizing effect of the passing light beams. On the other hand, the highest light beam divergence angels appearing between the collection and the imaging lens are perpendicular to the tilting angles of the interference filters and are thus added quadratically. Therefore, for big filter tilting angles, the angles of the light rays between the lenses have lower impact on the total incident angle on a filter. For small tilting angles, the interference filter function does not change much anyway due to the $\sin^2$-dependency in eq. (6.4.1). Since the consideration of the divergences of the light beams passing the RR filters leads to small differences between F_{RR} and $F_{RR,eff}$, these differences were not accounted for and as mentioned in sect. 6.4.1 F_{RR} was used for further calculations.

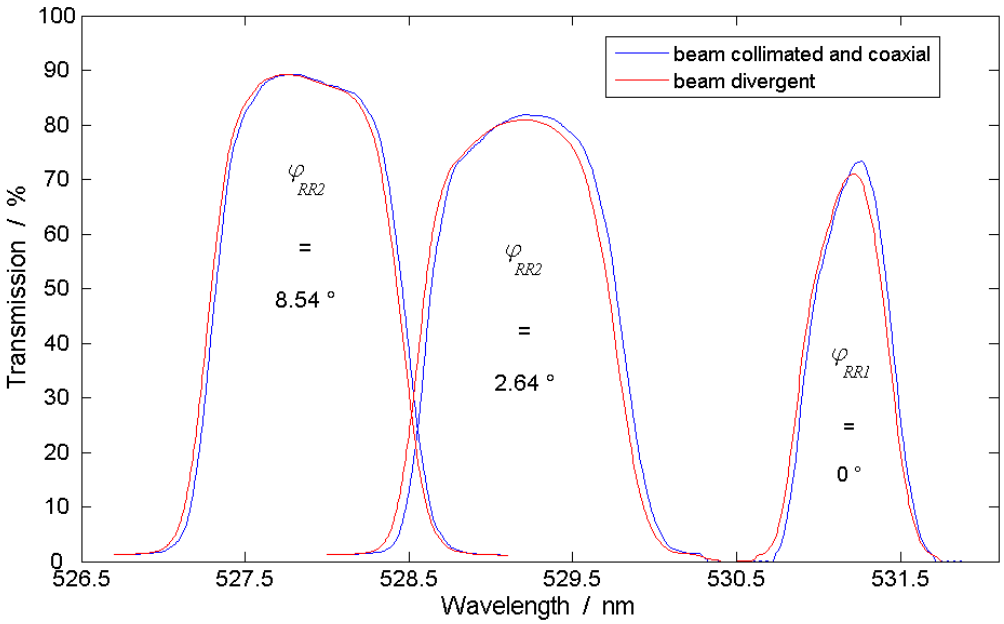

Figure 6.4-2. Transmission band shapes (blue) for both RR filters described by the function F_{RR} in the case of ideally collimated light beams within the receiver channels compared to the transmission band shapes (red) described by the function $F_{RR,eff}$ for divergent and thus realistic light beams. For filter *RR1* the band shapes correspondent to φ_{RR1} = 0° (≙ 531.2 nm) are exemplarily shown, for filter *RR2* the band shapes for φ_{RR2} = 2.64° (≙ 529.2 nm) and 8.54° (≙ 527.9 nm) are shown.

6.4.3 Modeled and real RR filter transmission functions

Figure 6.4-3 shows the experimentally transmitted signal power through the filter in channel RR1 obtained from a spectral sweep over the RR spectrum at 296 K. The result is compared to the result obtained from a calculated spectral sweep, which is a convolution of the function F_{RR1} and the modeled RR spectrum. The distinct RR lines are clearly pronounced and prove the very good accordance of the computational model and the experimental result. The very good accordance between model and experiment illustrates the predicting potential of the modeled filter functions F_{RR} and the RR spectral model on the one hand and the good experimental alignment of the optical receiver components on the other hand.

The smoothing of the RR peaks found in the experiment for wavelength smaller than about 530.1 nm is attributed to the increasing bandwidth of the RR filter due to relatively large angles of incidence of > 7°. Since the manufacturer did not deliver data for such high angles, the compliance between the theoretical and experimental curves is deteriorating below 530.1 nm. It should be noted, that for the results illustrated in Figure 6.4-3, another filter was used in channel RR1 having a bandwidth of only 0.49 nm (instead of normally 0.54 nm) at an angle of incidence of 0°. This was done, since the single RR lines can be resolved much better with this filter than with the one usually used in channel RR1, thus allowing for better comparison between computational model and experiment. For all other measurements presented in this thesis the RR1 filter from Table 6.4-1 is used.

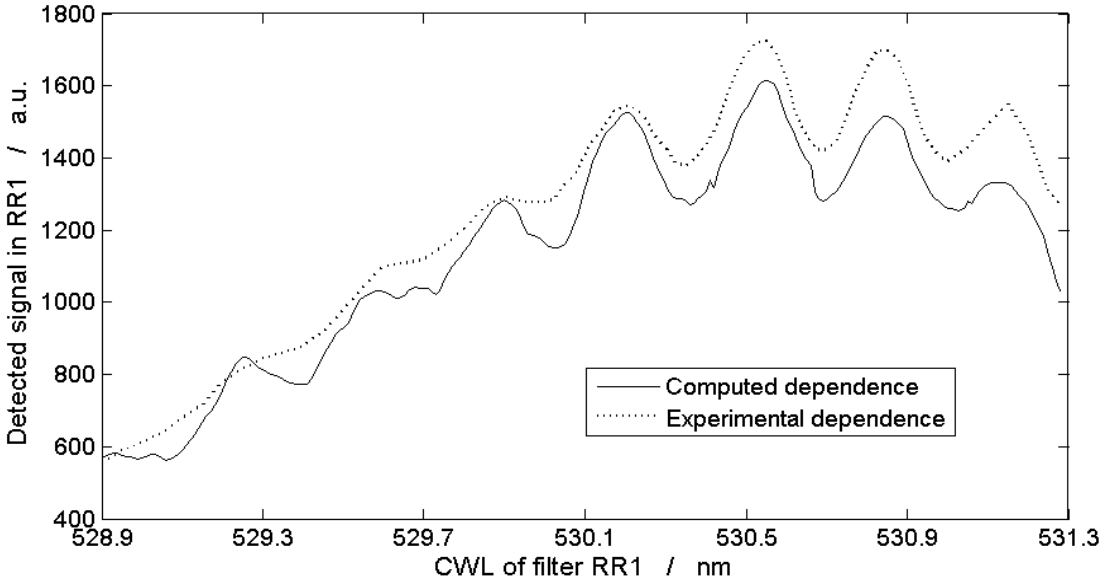

Figure 6.4-3. Transmitted power through the filter located in channel RR1 obtained from experiment and computational model. Note: For this measurement only, the filter in channel RR1 was replaced by another filter having a bandwidth of only 0.49 nm at an angle of incidence of 0°. The better spectral resolution of that filter due to the low bandwidth made an observation of the distinct pure rotational Raman lines possible, which can be seen in this figure. Here, the computer model was adapted to this filter.

7 Computational performance, error and optimization calculations for an aircraft-integrated sensor

In this chapter the magnitudes of potential systematic errors and statistical measurement uncertainties for an aircraft-integrated sensor are computed using the atmospheric scattering model and the programed model of the used measurement apparatus. Where practical feasibility is given, methods are presented for the reduction of the systematic errors. The stability of the calibration functions for the primarily measured parameters temperature and density is assessed in case of fluctuation of the operating parameters of the measurement apparatus (sect. 7.1). In this context, the impact of the headwind on the measurement accuracies is referred to as well (sect. 7.2). The optimum positioning of the manufactured interference filters RR1 and RR2 (sect. 6.4) within the RR spectrum leading to a minimization of the statistical measurement uncertainties is discussed for temperature, density and pressure measurements, independently (sect. 7.5). The magnitudes of the statistical uncertainties, having their inevitable physical basis in the shot noise of the backscattered and detected RR photons, are calculated for the optimized system settings. The increase of the measurement uncertainties coming from additional noise of the detector electronics (sect. 7.4) and noise from the elimination of the detected solar background at daytime measurements (sect. 7.6) are considered as well as the uncertainty increase introduced by the correction of the elastic backscatter leakage in the RR channels (sect. 7.7). Additional errors caused by the measurement of air moisture by channel H_2O are analyzed as well (sect. 7.8). All computational simulations presented in the following were written using *Matlab*. These calculations were also the basis for the iterative design optimization and the construction of the measurement apparatus described in sect. 6. The height dependent input parameters of the model simulations are based on the ISA [13]. According to the ISA, T = 288.15 K, $N = 2.547 \cdot 10^{25}$ 1/m^3 and p = 1013.25 hPa at an altitude of 0 m, and T = 216.65 K, $N = 5.543 \cdot 10^{24}$ 1/m^3 and p =165.8 hPa at 13000 m. All uncertainty values, unless otherwise stated, were calculated for temperatures, densities and pressures acquired by the detection of the backscatter of one single laser pulse. The uncertainties denote the 1-σ standard deviations of the measured values of the air parameters. A part of these results can also be found in [121].

7.1 Stability of calibration

Fluctuations of the measurement conditions, especially in an aircraft, can be mechanically, electrically and thermally induced. These fluctuations can lead to decalibration of the temperature and density measurement and thus to systematic measurement errors. In this section, the ruggedness of the used calibration functions T_{calib} (eq. (5.2.2)) for temperature and N_{calib} (eq. (5.2.4)) density measurements is examined with regard to two important experimental instabilities:

(1) A drift of the laser wavelength or, equivalently, an unidirectional spectral drift of the two RR filter CWLs. This scenario leads to anticorrelated changes of the detected RR signal intensities.

(2) An opposed spectral drift of the two filter CWLs leading to correlated changes of the detected RR signal intensities.

Because mechanically and electrically induced instabilities are aircraft specific and thus difficult to quantify, the emphasis in this analysis is put on the thermally induced instabilities affecting the surroundings of the measurement apparatus.

The systematic measurement errors ΔT_{drift} for temperature and ΔN_{drift} for density measurements in case of spectral drifts are defined as

$$\Delta T_{drift} = T_{calib}\left(U_{RR1}, U_{RR2}\right) - T_{calib}\left(U_{RR1,drift}, U_{RR2,drift}\right) \tag{7.1.1}$$

and

$$\Delta N_{drift} = \frac{N_{calib}\left(U_{RR1}, U_{RR2}\right) - N_{calib}\left(U_{RR1,drift}, U_{RR2,drift}\right)}{N_{calib}\left(U_{RR1}, U_{RR2}\right)}\,, \tag{7.1.2}$$

with U_{RR1} and U_{RR2} being the detected RR signals when no drift occurs and $U_{RR1,drift}$ and $U_{RR2,drift}$ the ones in the case of a drift. ΔT_{drift} denotes an absolute error value, whereas ΔN_{drift} denotes a relative one.

Figure 7.1-1 (a) and (b) shows ΔT_{drift} and ΔN_{drift} for case (1) for a spectral shift up to $\Delta\lambda_{drift,x}$ = ± 5 pm, with $x = L$ denoting the laser, $x = RR$ denoting both RR filters, and $x = RR1$ or $RR2$ denoting only one of the two RR filters. Figure 7.1-1 (c) and (d) illustrates case (2). $\Delta\lambda_x$ is positive for a red shift and contrariwise for a blue shift. The density measurement is more robust against spectral filter drifts in the same spectral direction than the temperature measurement, since it is based on a linear combination of the two RR signals. Thus, the loss of signal intensity in the one channel is partially compensated by the signal gain in the other. In contrast to that, due to the principle of setting up a ratio, the temperature measurement is more robust against filter drifts in opposite directions, since the correlated signal gain or loss in both channels partially cancels.

The manufacturer specified the spectral filter drift rate of all filters with +2 pm / K (Table 6.4-1) for a positive temperature change and vice versa for a negative temperature change. This value is indicated to be independent of the angle of incident radiation onto the filters. With this drift rate, a temperature stabilization of all filters within ± 0.5 K (which leads to filter drift of ±1 pm) will lead to systematic measurement errors of < 0.4 K and < 0.06 % for temperature and density measurements, if always the worst case among unidirectional and opposed filter drifts is assumed, respectively. In case (2), for a laser wavelength drift of ±1 pm, the errors are < 0.4 K and < 0.03 %, respectively. Because already such relatively small drifts of a couple of picometers can lead to important measurement errors, the thermal stability of the filters as well as the stability of the laser wavelength are of major concern. The pressure error due to such wavelength drifts of the laser or of the RR filters is the result of the single errors for temperature and density linked via the ideal gas equation. Thermal stabilization to better than ± 0.5 K, e.g. by means of a thermally controlled housing, has to be guaranteed in order to avoid risk of surpassing the maximum error limit for pressure Δp_{max} = 0.1 % specified in sect. 2.

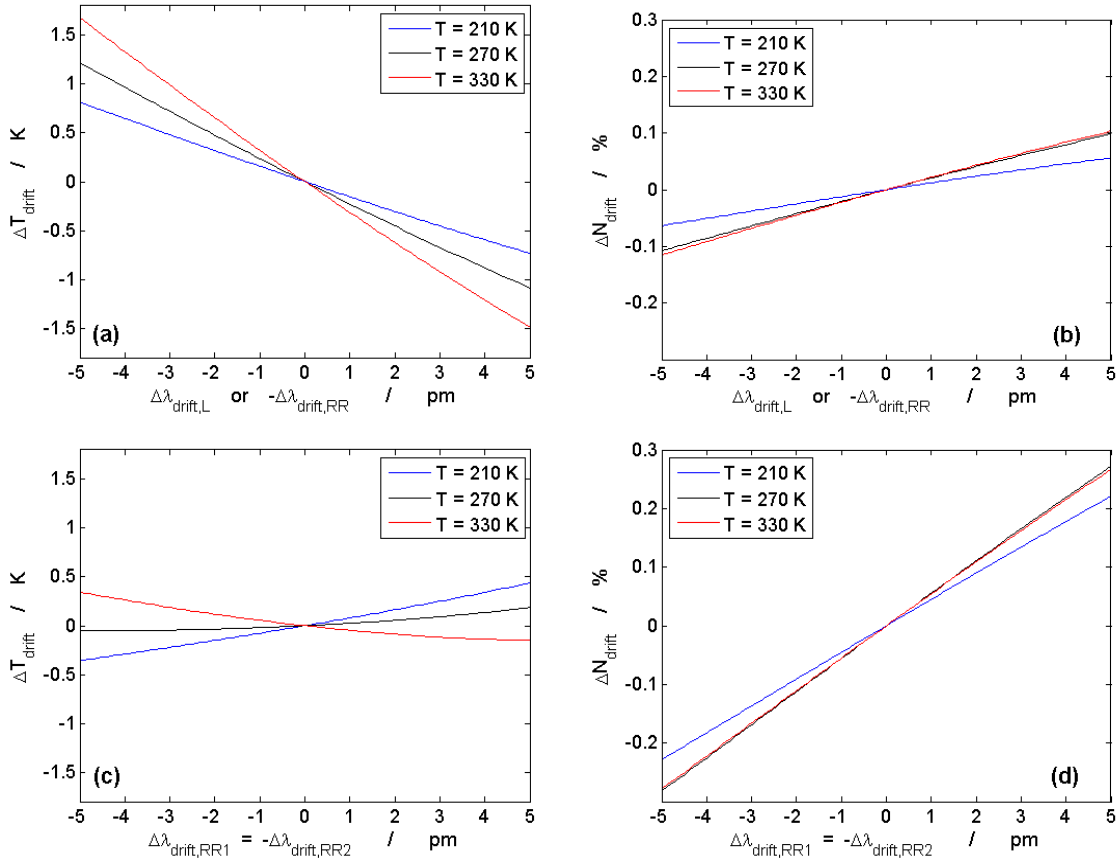

Figure 7.1-1. Systematic temperature (a) and density measurement error (b) made when either both RR filter CWLs are drifting in the same spectral direction, or equivalently, the laser wavelength is drifting in the opposite (indicated by "-" in the x-axis label) spectral direction. Systematic temperature (c) and density measurement error (d) when the RR filter CWLs are drifting in opposite directions.

7.2 Doppler-shift of backscattered radiation

If the air parameters are measured in front of the aircraft, i.e. in the flight direction of the aircraft, the collective motion of air particles relative to the aircraft due to headwind will lead to a Doppler shift $\Delta\lambda_D$ of the backscattered radiation wavelength. The Doppler frequency shift $\Delta\nu_D$ is calculated by [62]

$$\Delta\nu_D = \frac{2\upsilon_a}{\lambda_L} \,, \tag{7.2.1}$$

where λ_L is the laser wavelength and υ_a is the relative velocity between air molecules and aircraft. Inserting eq. (7.2.1) into the relation $\Delta\lambda = \lambda^2 / c \cdot \Delta\nu$, yields the Doppler wavelength shift

$$\Delta\lambda_D = \frac{\lambda_L 2\upsilon_a}{c} \ . \qquad (7.2.2)$$

For 532 nm and an assumed flight speed of 950 km / h, this shift is $\Delta\lambda_D$ = 0.9 pm and leads thus to similar errors as in the case of an equal unidirectional spectral drift of the filter CWLs or the laser wavelength, i.e. < 0.4 K and < 0.06 % (cf. sect. 7.1). Optical measurements in the forward looking direction should thus be avoided. Measurements perpendicular to the flight direction are not critical. This demand is consistent to the conclusion of sect. 4.7, in which a vertically upward measuring direction was recommended.

7.3 Lidar equation for short-range detection and power of detected signal pulses

The optimization and uncertainty calculations were made in three steps described in this section and the subsequent sect. 7.4 and 7.5. First, on the basis of the atmospheric and the laser data, the scattering geometry, and the optical properties of the designed receiver, generalized functions P_X with X = *RR1*, *RR2*, *CP* and H_2O were set up describing the optical peak power per detected signal pulse in each of the receiver channels:

$$P_X = 0.94 \cdot \frac{E_L}{fwhm_L} \cdot K \cdot \beta_X \cdot \int \Omega_{scatt}(l_{scatt}) \cdot dl_{scatt} \ . \qquad (7.3.1)$$

T is the atmospheric temperature and N the molecular number density. The temporal laser pulse shape is approximated by a Gaussian. Thus, the factor 0.94 = $(4 \ln(2) / \pi)^{1/2}$ accounts for the Gaussian shape of the emitted and the received light pulse. E_L = 200 mJ (sect. 6.1) is the nominal laser pulse energy. $fwhm_L$ = 10 ns are the durations of each emitted laser pulse and each received pulse. Their durations are considered as equal. K = 0.9 is a factor accounting for general optical transmission of a channel (without interference filter). $\Omega_{scatt}(l_{scatt})$, which was discussed in sect. 6.2, specifies the amount of detected light energy as a function of scattering distance in front of the receiver. β_X is the convolution of the backscatter coefficient of the radiation of interest with the spectral transmission function of the filter in channel X. For P_{RR1} and P_{RR2} in channel RR1 and RR2, three signal components are distinguished: The respectively detected optical rotational Raman signal $P_{rot,RR}$ (*RR* = *RR1* or *RR2*), the unwanted solar background $P_{B,RR}$ and the elastic signal leakage $P_{leak,RR}$. The latter two will be described in sect. 7.6 and 7.7, respectively. The optical peak power $P_{rot,RR}$ of the detected rotational Raman radiation is yield by inserting

$$\beta_{rot,RR} = \sum_{i,J} N_i F_{RR,i,J}(\varphi_{RR}) \cdot \left(\frac{d\sigma(T)}{d\Omega} \right)^{\pi}_{rot,i,J} \qquad (7.3.2)$$

for β_X in eq. (7.3.1). $F_{RR,i,J}(\varphi_{RR})$ is the spectral filter transmission function (sect. 6.4) at the spectral location of the rotational Raman anti-Stokes line corresponding to the initial energy state J of the molecule type $i = O_2, N_2$. $(d\sigma(T) / d\Omega)^{\pi}_{rot,i,J}$ is the rotational Raman backscatter cross section (sect. 4.3) of the molecule of type i in the initial energy state J. N_i is the molecular number density of molecule type i.

Per each emitted 200 mJ laser pulse, the peak pulse power $P_{rot,RR}$ is around $4 \cdot 10^{-6}$ W to $4 \cdot 10^{-5}$ W ($\approx 4 \cdot 10^{-11}$ mJ to $4 \cdot 10^{-10}$ mJ or $\approx 10^5$ to 10^6 photons), depending on the atmospheric temperature, density and the interference filter settings. The detected optical pulse power P_{CP} in channel CP is calculated by inserting $\beta_{CP} = \beta_{Cab} \cdot \tau_{CP} \cdot R$ for β_X in eq. (7.3.1). β_{Cab} is the Cabannes backscatter coefficient (sect. 4.4), $\tau_{CP} = 0.82$ is the filter CP peak transmission and R the backscatter ratio. For a backscatter ratio $R = 1$, i.e. in clear sky, $P_{CP} \approx 500 \cdot P_{rot,RR}$. Finally, the detected optical power P_{H2O} in channel H_2O is yield analogously using the H_2O filter transmission function and the vibrational-rotational Raman spectrum of water vapor (sect. 4.5.2). At sea level and a water vapor volume mixing ratio of 4 %, $P_{H2O} \approx 0.05 \cdot P_{rot,RR}$.

7.4 Choice of optimum detectors for the receiver channels

After having calculated the expected peak power of the detected optical pulses in channels RR1, RR2, CP and H_2O in sect. 7.3, the optimum detector types giving rise to the highest signal-to-noise ratios (SNRs) for the detection of these signals were determined. A noise analysis of three differently sensitive detector-amplifier systems was carried out: a photomultiplier tube (PMT) with an RF-amplifier, an avalanche photo diode (APD) with a transimpedance amplifier (TIA) and a PIN (*positive-intrinsic-negative*) diode with a 50 Ω load resistor. Technical data of possible state-of-the-art components were taken as a basis for these calculations. The used formulas and parameter values can be found in Appendix B. The dependencies of the SNRs on different incident optical signal powers and on adjustable parameters as detection bandwidth, PMT-gain, APD-gain, and TIA-gain were investigated. The model laser pulse is assumed to have a Gaussian time shape, so that the detection bandwidth for the scattered 10 ns long (FWHM) laser pulse is chosen to be the width of the 3-sigma Fourier transform, thus approximately 100 MHz. For that bandwidth and the expected optical pulse powers $P_{rot,RR}$ in each RR channel and P_{H2O} in channel H_2O, the model calculations suggest that the best detector is the APD together with the TIA. For P_{CP} in channel CP, the PIN diode with a 50 Ω resistor is best.

For the APD detector systems, the calculated optimum gain of the APD leading to the highest SNR was determined as well. With the optimum APD gain, the SNR in each RR channel is about 58 % of the value for the ideal case. In the ideal case, only the shot noise of the incident photons according to Poisson statistics is determining the SNR. Conversely, around 3 times higher laser pulse energy or pulse integration is necessary to achieve the same SNR per pulse as for this ideal case. The optimized detector output functions for the four channels defining their output voltages U_{RR1}, U_{RR2}, U_{CP} and U_{H2O} and their output noise voltages ΔU_{RR1}, ΔU_{RR2}, ΔU_{CP} and ΔU_{H2O} were used in the further calculations.

7.5 Optimum spectral RR filter positioning and statistical measurement uncertainties

After having set up the detector output functions of the receiver channels (see sect. 7.3 and 7.4), the optimum spectral positions (CWLs) of the band shapes $F_{RR}(\lambda,\varphi_{RR})$ (see sect. 6.4) of the manufactured filters RR1 and RR2 could be calculated corresponding to the minimum achievable statistical measurement uncertainties ΔT, $\Delta N / N$ and $\Delta p / p$ for temperature, density and pressure, respectively. The statistical measurement uncertainties originate in the various noise sources at the detector outputs. These calculations were done with U_{RR1}, U_{RR2}, ΔU_{RR1} and ΔU_{RR2} defined in Appendix B and using the formulas from Appendix C (with $P_{B,RR} = P_{leak,RR} = 0$, i.e. background light and signal leakage is not existent). Since the intensity distribution within the RR spectrum, and thus the amplitudes of the filtered signals, change with air temperature, all optimum CWL values depend on air temperature and thus on the measurement altitude. Figure 7.5-1 shows false color plots for different combinations of spectral filter positions and the associated measurement uncertainties for one pulse detection (E_L = 200 mJ) for the lowest and highest flight altitudes of around 0 m and 13000 m. Here, background light was not considered (nighttime measurements). These calculations thus consider only the shot-noise contributions of the signals themselves and the noise of the detectors discussed earlier. For each altitude, the optimum CWLs for temperature determination are located further to the edges of the anti-Stokes RR band, where the amplitudes of the filtered signals are more sensitive to temperature variations. For density determination, the optimum CWLs shift towards the peak of the anti-Stokes RR band in order to raise the transmitted signal amplitudes. Whereas the optimum CWLs of filter RR1 for temperature and density measurements, respectively, nearly do not change with altitude, those for filter RR2 strongly do, due to generally higher temperature dependent variations of the spectral power density at the lower wavelength edge of the anti-Stokes RR band.

The optimum filter CWLs for measurement altitudes of 0 m and 13000 m obtained with the data shown in Figure 7.5-1 are listed with the associated measurement uncertainties (one pulse measurements) in Table 7.5-1. The optimum CWLs for the density measurements could not be reached with the available filter RR2. Thus, the density measurement uncertainties achievable with the wavelength boundary value of 529.3 nm for RR2 were also calculated and put into brackets. The measurement uncertainties for temperature and density using the respective optimum CWLs are plotted in Figure 7.5-2 as a function of measurement altitude. In sect. 8.3.1, these CWLs obtained from the simulations are compared to those found in experiments. Because for one pulse measurements, the measurement uncertainties are too large in some flight scenarios with regard to the error requirements in aviation (sect. 2), either some signal pulses must be integrated or the laser properties have to be changed. This is discussed in sect. 7.9 and 7.10.

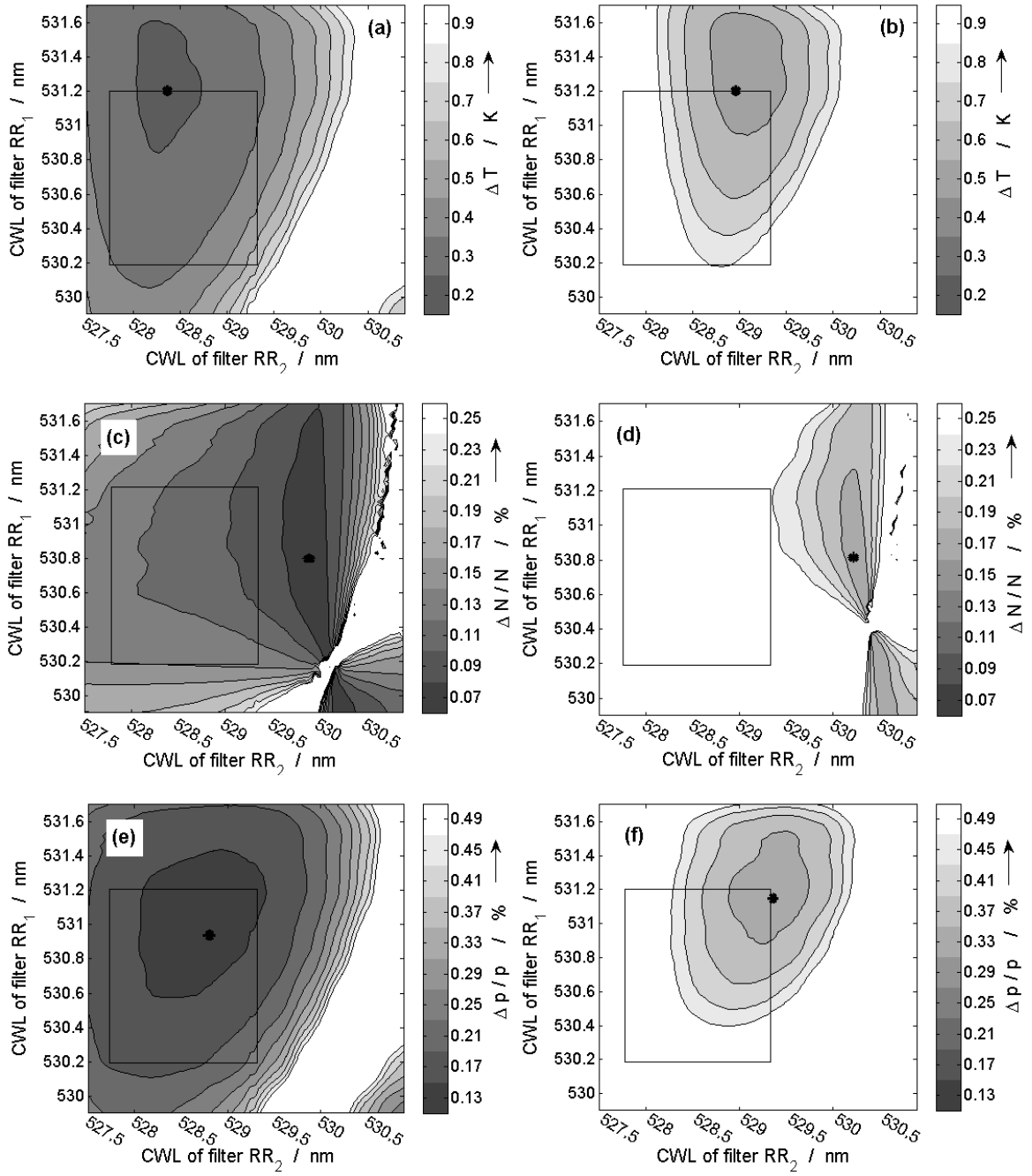

Figure 7.5-1. Calculated statistical measurement uncertainties for nighttime temperature (a), (b), density (c), (d) and pressure (e), (f) measurements at flight altitudes of 0 m (a), (c), (e) and 13000 m (b), (d), (f) when a single laser shot (E_L = 200 mJ) is used. Areas with minimum error correspond to the optimum spectral filter positions for the CWLs of RR1 and RR2. Dots mark the optimum values. Rectangles indicate the tuning ranges of the filters (from Table 6.4-1). For filters with same bandwidths and transmission curves, the uncertainties would be symmetrical to the line connecting equal CWLs. For approximately equal CWLs the highest uncertainties are found. Here, the numerical fit solutions are not stable and lead to singularities (fringes in (c) and (d)).

Table 7.5-1. Optimum CWLs for RR1 and RR2 and achievable statistical measurement uncertainties ΔT, ΔN / N and Δp / p for air temperature T, density N and pressure p in different flight situations (OD_{RR2} = OD_{RR2} = OD_{RR}) when analyzing one single signal pulse. The simulation input parameters were those of the designed measurement system (E_L = 200 mJ). The approximate relative increases of the uncertainties with regard to the respectively lowest ones (nighttime) are put into italicized brackets.

Measurement altitude	0 m	13000 m
T, optimum CWL for …		
RR1	531.2 nm	531.2 nm
RR2	528.3 nm	528.9 nm
ΔT at …		
nighttime in clear sky	0.27 K	0.46 K
daytime in clear sky	0.29 K *(x 1.1)*	0.57 K *(x 1.2)*
daytime in dense clouds (R = 10000, OD_{RR} = 6)	0.92 K *(x 3.4)*	1.38 K *(x 3)*
N, optimum CWL for …		
RR1	530.8 nm	530.8 nm
RR2	529.85 nm (529.3 nm)	530.25 nm (529.3 nm)
ΔN / N at …		
nighttime in clear sky	0.08 % (0.10 %)	0.17 % (0.24 %)
daytime in clear sky	0.09 % (0.11 %) *(x 1.1)*	0.19 % (0.27 %) *(x 1.2)*
daytime in dense clouds (R = 10000, OD_{RR} = 6)	0.19 % *(x 2.4)*	0.36 % *(x 2.1)*
daytime in moist air (M_{H2O} = 4%)	0.10 % (0.12 %) *(x 1.25)*	
p, optimum CWL for …		
RR1	531.0 nm	531.0 nm
RR2	528.8 nm	529.3 nm
Δp / p at …		
nighttime in clear sky	0.16 %	0.34 %
daytime in clear sky	0.17 % *(x 1.1)*	0.38 % *(x 1.2)*
daytime in dense clouds (R = 10000, OD_{RR} = 6)	0.44 % *(x 2.8)*	0.86 % *(x 2.5)*
daytime in moist air (M_{H2O} = 4%)	0.18 % *(x 1.15)*	

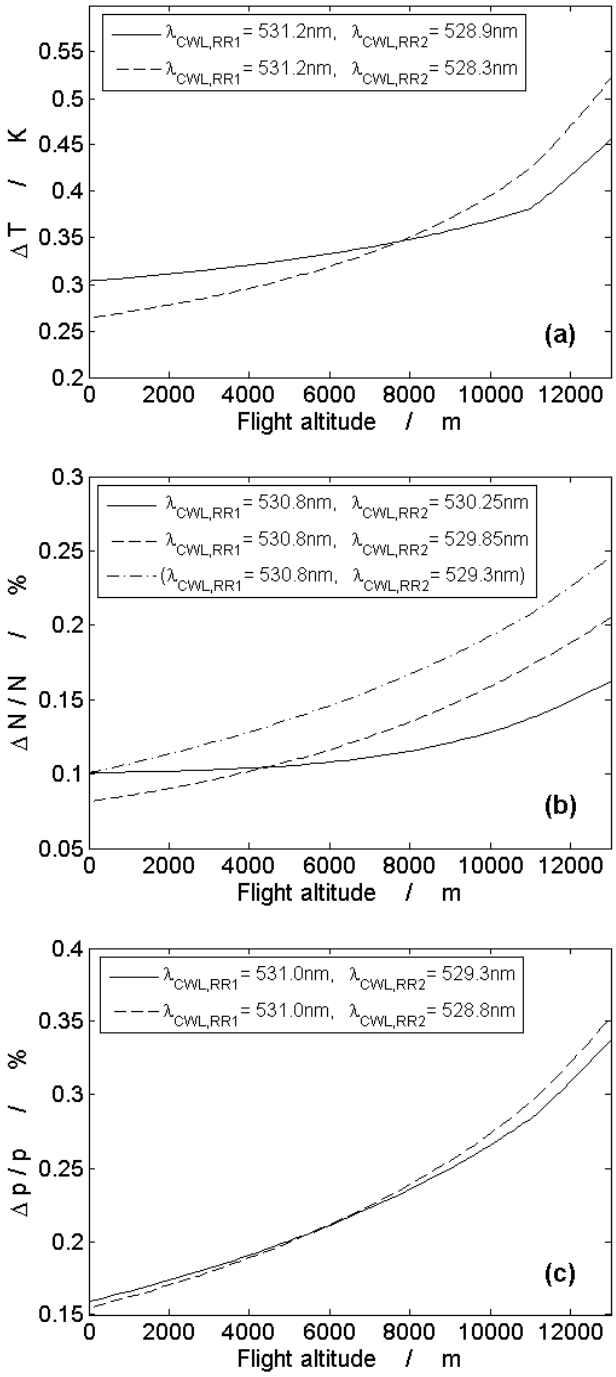

Figure 7.5-2. Statistical temperature (a), density (b) and pressure (c) measurement uncertainties ΔT, $\Delta N / N$ and $\Delta p / p$ using the respectively optimum CWLs of filters RR1 and RR2 for measurements at sea level (dashed lines) and altitudes of 13000 m (solid lines) and for analyzing the backscatter signal of a single laser shot. The temperature plots have a kink at 11000 m due to the characteristics of the ISA (see Figure 2-2) used as input. For density measurements the maximally adjustable CWL of filter RR2 (= 529.3 nm) is additionally plotted.

The relative measurement uncertainties for pressure, which are calculated from temperature and density according to the ideal gas equation, are equal to the quadratic sum of the relative temperature and density measurement uncertainties (see Appendix C). The optimum pressure CWLs are analogously shown in Figure 7.5-1 for measurements at 0 m and 13000 m and listed with the correspondent uncertainties in Table 7.5-1. As expected, the spectral positions of the optimum CWLs for the pressure measurement are a trade-off between the ones for temperature and density measurements and thus located intermediately. Deviations of a couple of tenth of nanometers from these optimum pressure CWLs cause either an improvement of the temperature measurement uncertainty component on the expense of the density measurement uncertainty component or vice versa. Thus, the pressure measurement uncertainty is not that sensitive to maladjustment of the CWLs as the temperature and density measurement alone. This relatively weak dependency on the CWLs can also be recognized in Figure 7.5-2, which comprises the expected pressure measurement uncertainties as function of altitudes for the two possible optimum pressure CWLs.

7.6 Measurements during daytime

At daytime, the solar background radiation is superposed on the RR backscatter and leads to an increase of the detected signal amplitudes in the RR channels. Therefore, the background signals are suppressed by AC high-pass filters inside the detectors. However, the noise generated by the background remains and gives rise to higher output noise voltages of the detectors. This further increases the statistical temperature and density measurement uncertainties. The formulas for calculation of the error at daytime measurements are found in Appendix C (with $P_{B,RR} \neq 0$, $P_{leak,RR} = 0$). To determine the magnitude of the uncertainty increase during daytime operation, the worst case solar spectral radiance of $\Psi = 500$ mW / (m² sr nm) at 532 nm calculated in sect. 4.7 was taken as a basis.

The detected optical background power $P_{B,RR}$ in channel *RR* = *RR1* or *RR2* is calculated by

$$P_{B,RR} = K_{RR} \cdot \Psi \cdot A'_{\mathrm{det}} \cdot \omega_{rec} \cdot \Delta\lambda_{RR} \ , \qquad (7.6.1)$$

where $K_{RR} = K \cdot \tau_{RR}$ is the product of the general optical transmission of each channel $K = 0.9$ and the respective peak filter transmission τ_{RR} (see Table 6.4-1). A'_{det} is the image of the detector active area in front of the receiver and $\omega_{rec} = \pi/4 \cdot FOV^2$ the solid angle seen by the receiver. $FOV = 83$ mrad is the field of view of each receiver channel (sect. 6.1). $\Delta\lambda_{RR}$ is the spectral bandwidth of the respective interference filter. With $\Psi = 500$ mW / (m² sr nm), the signal contribution $U_{RR}(P_{B,RR})$ of the solar background in each of the RR channels is calculated to be 1 to 2 orders of magnitude lower than the rotational Raman signal $U_{RR}(P_{rot,RR})$, depending on the air density and thus flight altitude. The noise increase in the output of each RR channel after background subtraction (described by $\Delta U_{RR}(P_{B,RR})$ in eq. (C.2)) is thus relatively low in comparison with other noise sources and has virtually no influence on the spectral positions of the optimum CWLs and only a weak influence on ΔT, $\Delta N / N$ and $\Delta p / p$ (increased by about 10 - 20 %). These slightly increased measurement uncertainties, called the uncertainties for daytime operation, are included in Table 7.5-1. For the calculations, the same

optimum CWLs as for nighttime operation were used. The maximally detected solar background power in channel CP was calculated analogously. However, because the detected elastic backscatter in channel CP is relatively large, here, solar background plays even a less important role.

7.7 Measurements in optically very dense clouds

7.7.1 Elastic-signal leakage

7.7.1.1 Leakage error magnitude

Aerosol particles and especially cloud droplets intensify the elastic backscatter. Strong particle scattering can make a significant amount of elastically scattered photons pass the RR filters, since the optical densities at the elastic wavelength OD_{RR1} and OD_{RR2} of the real RR filters have finite values. This gives rise to systematic temperature and density measurement errors (leakage errors), which are a function of OD_{RR1} and OD_{RR2} and the atmospheric backscatter ratio R. In clear sky R equals 1; values in optically dense clouds are estimated in sect. 4.6. The measurement of R with the apparatus described herein is explained in sect. 5.3. Calculations of necessary OD_{RR} values leading to a negligible leakage error for R = 50 had already been performed for temperature measurements [10, 71]. Here, these calculations were adapted to the present system and also made for density measurements and for R up to 10000 appearing in optically very dense clouds. The signal leakage in the channel $RR = RR1$ or $RR2$ is modeled as an additionally detected optical signal $P_{leak,RR}$ obtained by inserting $\beta_{leak,RR}$ for β_X in eq. (7.3.1). $\beta_{leak,RR}$ characterizes the leaking elastic backscatter:

$$\beta_{leak,RR} = \left(\beta_{par} + \beta_{Cab}\right)\cdot 10^{-OD_{RR}} = R\beta_{Cab}\cdot 10^{-OD_{RR}} \quad . \tag{7.7.1}$$

β_{par} is the particle backscatter coefficient, β_{Cab} is the Cabannes backscatter coefficient (sect. 4.4). The output voltages in the RR channels are raised and yield by $U_{RR}(P_{rot,RR} + P_{leak,RR})$. Insertion into the calibration functions for temperature T_{calib} (eq. (5.2.2)) and density N_{calib} (eq. (5.2.4)) leads to false temperature values $T_{leak,calib}$ and density values $N_{leak,calib}$. The resulting systematic leakage errors ΔT_{leak} and ΔN_{leak} are defined by

$$\Delta T_{leak}\left(R, OD_{RR1}, OD_{RR2}\right) = T_{calib} - T_{leak,calib} \tag{7.7.2}$$

and

$$\Delta N_{leak}\left(R, OD_{RR1,} OD_{RR2}\right) = \frac{N_{calib} - N_{leak,calib}}{N_{calib}} \quad . \tag{7.7.3}$$

Figure 7.7-1 (a) and (b) show the magnitudes of ΔT_{leak} and ΔN_{leak} related to various values of OD_{RR} and R. $OD_{RR} > 9$ is required for both RR1 and RR2 in very dense clouds with $R \geq 10000$ to obtain leakage errors < 0.5 K for temperature measurements and < 0.4 % for density measurements and $OD_{RR} > 10$ to

make the error negligible. It is remarkable that the temperature measurement is not as sensitive as the density measurement to elastic signal leakage, since the effect of a correlated signal increase in both RR channels partially cancels. This is due to the fact that the temperature measurement is based on setting up a ratio Q (eq. (5.1.1)). For signal leaks in the RR channels which do not lead to a change of Q, the leakage does not lead to an error at all. Thus, since the signals in both RR channels have approximately the same magnitude, OD_{RR1} and OD_{RR2} ideally should be about the same as well. With regard to density measurements, since they are based on a linear combination of the RR signals, elastic signal leakage will lead to an addition of measurement errors in any case. Here, an advantageous combination of OD values does not exist, which would lead to error minimization.

7.7.1.2 Leakage error correction

Although the real RR filters were both designed to have $OD_{RR} > 10$, they may not show such performance in reality. Since the measured elastic signal $U_{CP}(P_{CP})$ in dense clouds is proportional to the leaking signal $P_{leak,RR}$ in each RR channel, it can be used to deduct this signal increase: $U_{RR}(P_{rot,RR} + P_{leak,RR}) - \kappa_{RR} \cdot U_{CP}(P_{CP})$. κ_{RR} is the leakage correction factor and a function of OD_{RR}. κ_{RR1} and κ_{RR2} can be determined via calibration by inserting $U_{RR}(P_{rot,RR} + P_{leak,RR}) - \kappa_{RR} \cdot U_{CP}(P_{CP})$ with $RR = RR1$ and $RR2$ into T_{calib} and N_{calib} and choosing κ_{RR1} and κ_{RR2} in such a way that $\Delta T_{leak} = 0$ and $\Delta N_{leak} = 0$.

However, applying this leakage correction, the systematic leakage error can only be reduced to a statistical residuum. For the calculation of this statistical residuum, the formulas from Appendix C (with $P_{leak,RR} \neq 0$) were used. Since the subtracted signals are noisy, additional noise is generated (described by $\kappa_{RR} \cdot \Delta U_{CP}(P_{CP})$ in eq. (C.2)) and thus the measurement uncertainties ΔT, $\Delta N / N$ and $\Delta p / p$ are raised as well. The magnitude of the additional uncertainty component generated by the leakage correction only is shown in Figure 7.7-1 (c) and (d) for temperature and density measurements. With the leakage correction, equal errors as without leakage correction are already reached at much lower OD_{RR} values. For example, to obtain at a flight altitude of 13000 m in dense clouds ($R = 10000$) a 1-σ measurement uncertainty increase of < 0.5 K or < 0.4 % after leakage correction, values of $OD_{RR} = 7$ or 6 for temperature or density measurements, respectively, are sufficient instead of 9. Even lower OD_{RR} values are sufficient at lower measurement altitudes due to stronger and thus less noisy signals. However, the results from Figure 7.7-1 show the importance of a sufficient blocking of elastic light, since errors due to unblocked light can easily rise up to a couple of Kelvins or percent for temperature and density, respectively, even after correction if the filter blocking is too low. The total measurement uncertainties including the uncertainty increase after solar background and leakage correction for measurement altitudes of 0 m and 13000 m, $R = 10000$ and $OD_{RR1} = OD_{RR2} = 6$ (a value that can be measured and guaranteed by the manufacturer) are also listed in Table 7.5-1 for temperature, density and pressure measurements.

In case the OD_{RR} values proof to be even too low or leakage too large for the application of this correction, the CWLs of the RR filters can be shifted towards lower wavelengths, away from their optimum positions, in order to increase OD_{RR}. Alternatively, a pair of similar RR filters can be cascaded in each channel and thus doubling OD_{RR}. This will reduce the systematic signal

leakage to a negligible value, however, on the expense of RR signal intensities, which in turn increases the measurement uncertainty. In the filter cascading case, the measurement uncertainty increases by 50 - 70 % for air temperature and density due to lower total signal transmission. In the CWL shifting case, if the CWLs of RR1 and RR2 are downshifted by 0.5 nm, the measurement uncertainty increases by the same percentage for temperature measurements. The density measurement is not as sensitive to the wavelength shifting and shows only half of this uncertainty increase.

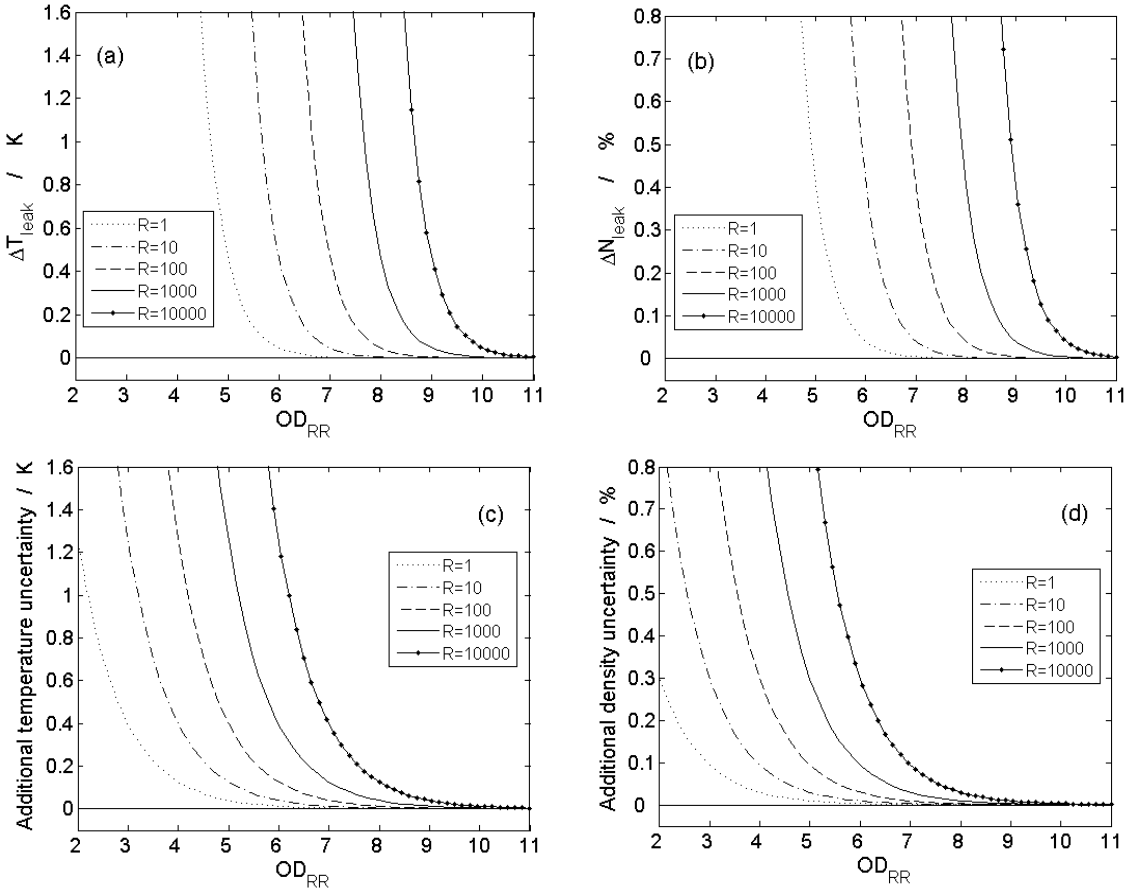

Figure 7.7-1. Systematic leakage error for temperature (a) and density (b) due to leakage of elastically backscattered radiation through the RR filters as function of $OD_{RR1} = OD_{RR2} = OD_{RR}$ and additional statistical measurement uncertainty generated by the leakage correction for temperature (c) and density (d). The calculations for (c) and (d) refer to a flight altitude of 13000 m (worst case). The errors are calculated for different backscatter ratios *R*.

7.7.2 Atmospheric extinction

7.7.2.1 Extinction error magnitude

In dense clouds, apart from the leakage of the elastic backscattered light through the RR filters, atmospheric signal extinction for the double path to the measurement volume and back has to be

considered. This affects the density and pressure measurements, which are based on the detection of absolute signal intensities. Extinction causes these parameters to be systematically underestimated. The measurement error made then is equal to the extinction value. Temperature measurements are not affected, since signal extinction related dependencies cancel when setting up the ratio Q of the two RR signals. Extinction can be caused by, first, optical components of the measurement system, second, atmospheric molecules or, third, atmospheric particles. The contribution of optical components can be accounted for in the calibration since it is supposed not to change during flight. Only the transmission characteristics of the aircraft window - although such a window will be flush-mounted and dirt and water repellent - probably will have to be separately monitored during the whole flight, in order to check for icing, pollution, opacity, scratching etc. This can be done optically as well.

The atmospheric extinction is characterized by the extinction coefficient α. For the calculations, α is assumed to be spatially homogeneous. $\alpha = \alpha_{mol} + \alpha_{par}$ is the sum of the molecular and particle extinction coefficients. Furthermore, the extinction of molecules and particles can be further categorized into extinction due to scattering and extinction due to absorption. In the case of molecules, only molecular extinction by scattering is considered. Molecular absorption is neglected, since in the atmosphere at common flight altitudes at visible laser wavelengths no molecules are present with a significantly high absorption coefficient. α_{mol} is then set by the product of the total Rayleigh scattering cross section of air for 532 nm σ_{Ray} (sect. 4.4) and the molecular number density of air N. The general systematic extinction error e_α is defined as

$$e_\alpha = 1 - \frac{\int_r \Omega_{scatt}(r) \cdot \exp[-2\alpha r]dr}{\int_r \Omega_{scatt}(r)dr} \quad . \tag{7.7.4}$$

Ω_{scatt} is the function describing the measurement volume for the designed measurement apparatus (sect. 6.2). The molecular extinction error $e_{\alpha,mol}$ (due to scattering) is yield by inserting $\alpha = \alpha_{mol}$ into eq. (7.7.4). $e_{\alpha,mol}$ is largest close to sea level where the air density is highest and $\alpha_{mol} = 1.32 \cdot 10^{-5}$ m^{-1} (see sect. 4.4). Insertion yields $e_{\alpha,mol} \approx 10^{-3}$ %. This signal attenuation and even those for UV laser wavelengths and for other measurement distances on the same order of magnitude are negligible. The situation changes when extinction by particles (aerosols, cloud droplets, rain etc.) is considered. According to sect. 4.6, $\alpha_{par} = 0.04$ m^{-1} for a visual range of 100 m in a cloud. Measurements in such a scenario lead to a particle extinction error - and thus to a density and pressure measurement error - of $e_{\alpha,par} = 4.9$ %.

Since the extinction coefficient α generally is wavelength dependent, the extinction for the water vapor channel H_2O has to be evaluated separately. The strong ν_1 vibrational mode of water vapor is located at 660 nm, i.e. by a spectral distance of about 128 nm away from the RR spectrum (sect. 4.5.2). Due to this wavelength shift of the backwards propagating light, differential extinction takes place on the way back from the scattering volume. The differential extinction error e_{diff} made for

the H_2O-signal when taking into account the extinction at the laser wavelength but disregarding the wavelength dependency of the extinction is defined by

$$e_{diff} = \frac{\int_r \Omega_{scatt}(r) \cdot \exp\left[-2\alpha(\lambda_1)r\right]dr - \int_r \Omega_{scatt}(r) \cdot \exp\left[-\left(\alpha(\lambda_1)+\alpha(\lambda_2)\right)r\right]dr}{\int_r \Omega_{scatt}(r)dr}, \quad (7.7.5)$$

with the laser emission wavelength λ_1 and the wavelength λ_2 of the backscatter. Taking the wavelength dependency of σ_{Ray} and thus of α_{mol} defined in sect. 4.4 and calculating with the wavelengths λ_1 = 532 nm and λ_2 = 660 nm, leads to the molecular differential extinction error $e_{diff,mol} \approx 10^{-4}$ %. This is a negligible value. This is also true when using shorter initial UV laser wavelengths or larger measurement distances on the same order of magnitude. In the case of the RR spectrum, which is located near 532 nm within less than 10 nm, the influence of differential extinction effects can be neglected as well for the purpose described herein.

Particle differential extinction depends on the particle size [110]. In general it can be stated that the bigger the particles are, the lower the wavelength dependency is. Droplets found in dense water clouds are relatively large and thus show small wavelength dependence. A measuring scale for that variation is provided by the Ångström exponent δ_{par}, defined for two wavelengths λ_1 and λ_2 as

$$\delta_{par} = \frac{\ln\left(\alpha_{par}(\lambda_1)/\alpha_{par}(\lambda_2)\right)}{\ln\left(\lambda_2/\lambda_1\right)}. \quad (7.7.6)$$

For clouds $-1 < \delta_{par} < 1$ [122]. Assuming $\delta = 1$, that means a linear growth of the extinction coefficient with wavelength, and α_{par} = 0.04 m^{-1} for 532 nm, the systematic error $e_{diff,mol}$ due to neglecting the wavelength dependency of the particle extinction coefficient is $e_{diff,mol}$ = 0.5 %. This is a negligible difference as well, since the statistical measurement uncertainties of the water vapor carry much more weight as it will be described in sect. 7.8.

In summary, for temperature measurements using the presented short-range measurement apparatus, extinction is irrelevant. Nevertheless, atmospheric extinction has to be accounted for, in order to correct the measured density and pressure values. Molecular extinction is weak and fully negligible, whereas particle extinction generally is not, especially in presence of dense clouds. There, the extinction of radiation backscattered and detected from the measurement volume can be as high as a couple of percent. Further errors introduced by differential molecular and cloud-particle extinction are small and negligible. The weak cloud-particle differential extinction originates in a relatively weak wavelength dependence of its extinction coefficient. In particular, this is true for measurements of water vapor at a spectral shift of 128 nm for a laser wavelength of 532 nm: Here, the statistical measurement uncertainty of water vapor (sect. 7.8) is larger than the error due to differential extinction. Thus, an equal extinction can be assumed for all measured signals in all 4 measurement channels and it is sufficient to derive only the extinction value at the laser wavelength, in order to use it for the extinction correction.

In thick water clouds also multiple scattering takes place. The detection of multiple-scattered photons depends mainly on the field of view of the receiver, the scattering angle, the scattering distance, the penetration depth and on the scattering particle density and size [123]. As multiple scattering becomes stronger in optical dense scattering mediums, it correlates with atmospheric extinction. Thus, the detection of multiple-scattered photons results in an apparent reduction of the measured extinction coefficient. As this effective reduction is the same in first order approximation for all four channels, multiple scattering per se is not critical for the measured parameters.

7.7.2.2 Approach for extinction error reduction

The systematic density and pressure measurement errors caused by cloud-particle extinction can be reduced. The highest extinction values appear in dense fog and clouds. There, the reduced transmission can be accounted for using the measured backscatter ratio R (sect. 5.3) and using an assumed value $L_{par,ass}$ of the lidar ratio, i.e. the extinction-to-backscatter coefficient (sect. 4.6). This assumed lidar ratio $L_{par,ass}$ has to match the real lidar ratio L_{par} with sufficient accuracy, in order to successfully reduce the extinction error to a certain level. With the current setup, the real lidar ratio L_{par} cannot be measured. The iterative procedure for this extinction correction of air density with $L_{par,ass}$ is described in Appendix D. Figure 7.7-2 shows the systematic density errors, first, when extinction is existent but neglected and, second, when extinction is derived and used for error reduction. The measurements are assumed to be made at sea level (worst case). The extinction error can be totally eliminated, if the assumed lidar ratio is equal to the real one, i.e. $L_{par,ass} = L_{par}$. For the case of R = 100 and $L_{par,ass}$ = 30 sr, which is shown in the figure, the relative density error can be reduced by 70 % to 0.2 %, if the real lidar ratio is L_{par} = 20 sr and by 80 % to also 0.2 %, if L_{par} = 40 sr. In the case of R = 1000, the density error can be reduced by 50 % to 2.3 %, if L_{par} = 20 sr and by 70 % to also 2.3 %, if L_{par} = 40 sr.

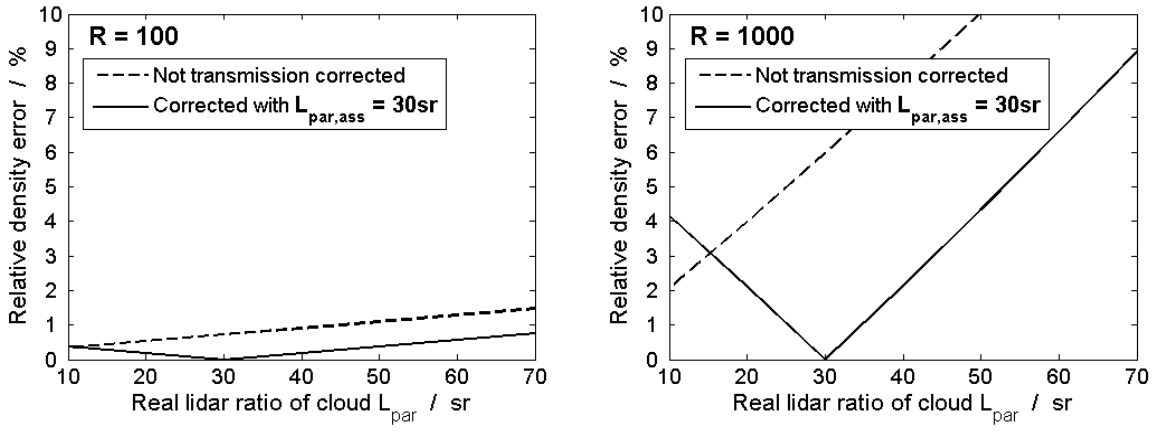

Figure 7.7-2. Systematic measurement errors for density and pressure made by neglecting an existent atmospheric extinction at sea level (dashed lines) and residual systematic errors made after extinction correction based on the assumption of a lidar ratio $L_{par,ass}$ = 30 sr (solid lines). The plots are made for R = 100 (left) and R = 1000 (right).

In an atmosphere with R = 100, this correction thus promises to reduce the extinction error below the required 0.1 % at sea level (sect. 2), if the absolute difference of the assumed and the real lidar ratio is ≤ 5. However, it has to be considered that the lidar ratios of fog, clouds and other particles can vary by 10 sr and even more [124-126]. This makes the correction procedure only applicable with the restriction of fog or clouds with a comparably low R. For much higher measured values of R, the density measurement gets too uncertain and the density values either cannot be used or, alternatively, an air transmission measurement has to be performed to reach the accuracy goal of 0.1 %. Such a measurement can be made, e.g. by implementing a far-range RR measurement channel with an interference filter located at the peak of the RR spectrum. The therewith detected backscatter from a farer measurement distance then has to be compared to the RR backscatter from the near range to derive the atmospheric transmission or extinction.

7.8 Influences of water vapor on measurement error

7.8.1 Influence of the pure rotational Raman spectrum of water vapor

Laser light scattering from atmospheric water vapor generates a specific pure rotational Raman spectrum (sect. 4.5.1). This spectrum overlaps with the one of dry air giving rise to additional light energy passing the RR filters. Neither the intensity distributions of the two spectra nor their temperature dependencies are identical. Since the atmospheric water vapor volume mixing ratio is variable, the relative energies of the two spectra are as well. All these points give rise to systematic temperature, density and pressure measurement errors, which were assessed as well.

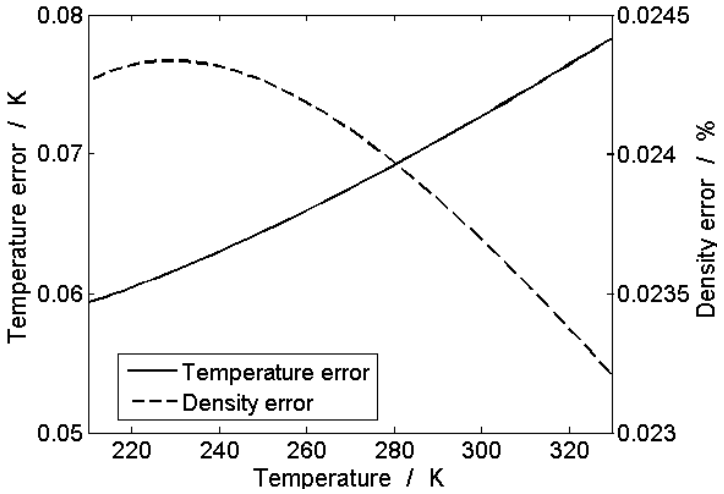

Figure 7.8-1. Systematic air temperature and density measurement errors made at sea level in the presence of atmospheric water vapor as function of air temperatures. The error is caused by the additional detection of spectral power coming from the water vapor RR spectrum. The water vapor volume mixing ratio is assumed to be constantly 4%.

The magnitudes of these errors were calculated as a function of air temperature. For the calculations, the spectral model presented in sect. 4 and the lidar equation given in sect. 7.3 were used. The errors are defined as the difference of the measured temperature and density values, respectively, when using the RR signals generated by a dry atmosphere and when using the RR signals generated by a moist atmosphere. Figure 7.8-1 shows the computed errors of the primary measurement parameters temperature and density for the relevant temperature range from 210 K to 330 K. For the plot, a large and (non-realistically) constant water vapor volume mixing ratio of 4 % at sea level was assumed. Although the mixing ratio is very large, the errors are maximally 0.08 K and 0.025 % for temperature and density measurements, respectively. These errors are so small that they can be ignored. This accounts also for the resulting pressure measurement error, which can be obtained from the errors for temperature and density.

7.8.2 Influence of the vibrational-rotational Raman spectrum of water vapor

For air density and pressure measurements in moist air, the water vapor molecular number density N_{H2O} has to be measured (sect. 5.3). The density of water vapor is measured by filtering the rotational-vibrational spectral region beneath the Q-branch of the water vapor OH stretching band ν_1. The optimum CWL for the used filter H_2O leading to the highest water vapor signals is calculated to be 660.5 nm (Table 6.4-1). This is done by forming a convolution of the spectral filter transmission function and this water vapor spectrum. The water vapor density measurement uncertainty ΔN_{H2O} / N_{H2O} is calculated using the optimized detector output functions of channel H_2O defined in Appendix B including photon noise, solar background noise and noise induced by the specifically optimized APD detectors in channel H_2O. The formulas for the calculation of ΔN_{H2O} / N_{H2O} are found in Appendix C. For daytime measurements, the maximum solar background light power detected in channel H_2O is assumed to be on the same order as in channel RR2. Indeed, filter H_2O is spectrally broader, but the maximum radiance values are decreased at 660 nm by a factor of ≈ 0.8 to 400 mW / (m² sr nm) as estimated with *LibRadTran* (cf. Figure 4.7-1).

Figure 7.8-2 shows the relative measurement uncertainty ΔN_{H2O} / N_{H2O} for the water vapor density N_{H2O} in dependence on the water vapor volume mixing ratio at sea level both for nighttime and daytime measurements. Even at relatively high water vapor volume mixing ratios, the optical water vapor signal P_{H2O} is much weaker than the optical RR signals $P_{rot,RR}$ (see sect. 7.3). The measurement of P_{H2O} is thus more affected by solar background noise. Whereas, solar background is almost negligible at the detection of the RR signals, here, it determines significantly the measurement uncertainty; e.g. for a volume mixing ratio of 4 %, the measurement uncertainty ΔN_{H2O} / N_{H2O} is 1.7 % and thus approximately double as large for daytime measurements than for nighttime measurements, which is 0.9 %.

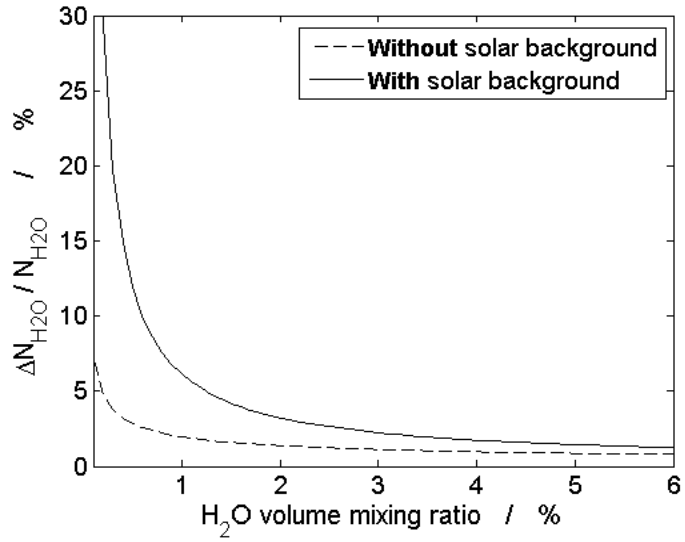

Figure 7.8-2. Calculated water vapor statistical measurement uncertainty $\Delta N_{H2O} / N_{H2O}$ at earth ground made with the measurement apparatus per each single laser pulse (200 mJ) and an APD detector optimized for the detected water vapor light signals (Appendix B). The weakness of the detected water vapor signal leads to a higher sensitivity of the measurement uncertainty to solar background. Here, a spectral radiance of 400 mW / (m² sr nm) is assumed.

If water vapor is present in the atmosphere but not measured and not taken account of in the density determination, the systematic relative air density error made is equal to the water vapor volume mixing ratio (dotted line in Figure 7.8-3). I.e. it can amount several percent. In the other case, if water vapor is measured, this systematic error is eliminated, however, the measurement uncertainty $\Delta N_{H2O} / N_{H2O}$ contributes to $\Delta N_{moist} / N_{moist}$ (and to $\Delta p / p$), which is expressed by the right summand in eq. (C.5). This contribution is also plotted in Figure 7.8-3 for daytime and nighttime measurements. For all ground water vapor mixing ratios up to even 6 % and also above, this uncertainty contribution stays below 0.07 % for daytime (solid line) and below 0.05 % (dashed line) for nighttime measurements. Since the contribution enters into eq. (C.5) quadratically and the dry air density measurement uncertainty $\Delta N_{dry} / N_{dry}$ (left summand in eq. (C.5)) is only a little larger at sea level (see $\Delta N / N = \Delta N_{dry} / N_{dry}$ in sect. 7.5), the magnitude of the total density measurement uncertainty can be maximally raised by around 25 % for moist air at sea level compared to the one for dry air of equal density. For pressure measurements the resulting increase is even less and amounts maximally 15 %.

With rising altitude, the temperature falls and thus the maximum water vapor mixing ratio decreases. Although the water vapor measurement uncertainty $\Delta N_{H2O} / N_{H2O}$ is larger for small mixing ratios (Figure 7.8-2), its contribution to the total density (and pressure) measurement uncertainty is smaller. Because in hot regions close to earth surface, the water vapor mixing ratios can reach the largest values, the contribution of the water vapor measurement to the total density measurement uncertainty can be largest as well. Thus, the measurement scenario close to sea level, and not at high altitudes, poses the worst case for water vapor measurements. For reason of completeness, the uncertainties for daytime measurements at sea level in clear but very moist air with a very high mixing ratio of 4 % were added to Table 7.5-1.

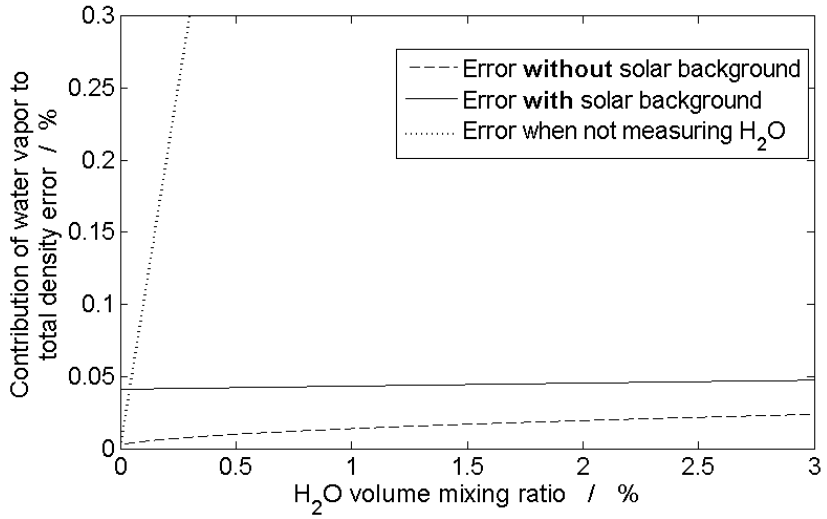

Figure 7.8-3. Systematic air density and pressure error made when water vapor is not measured compared to the impact of the water vapor measurement on the statistical measurement uncertainty of moist air density and pressure (measurement at sea level) when water vapor is measured. Note: For low water vapor volume mixing ratios < 0.04 %, the statistical uncertainty can be higher than the systematic error. This is due to the intrinsic noise of the detector and the noise introduced by solar background.

The spectral intensity distribution within the Q-branch of the water vapor spectrum varies with air temperature [101]. Because of this fact, the H_2O signals are air temperature dependent. The sensitivity of the measured signals to temperature variations depends on the spectral width of the band pass of the interference filter used [127, 128]. With the 1.8 nm broad water vapor Raman filter used here, the air temperature induced systematic error of the detected water vapor signal is calculated to decrease with temperature (and thus to rise with flight altitude) to maximally 2.2 % throughout the relevant part of the atmosphere. However, since for all temperatures this error stays always far below the statistical measurement uncertainty of water vapor (Figure 7.8-2), it carries no weight.

7.9 Laser power requirements obtained from simulations

Onboard measurements of temperature and pressure used for aircraft control have to meet accuracy requirements listed in the aviation standard AS8002 (sect. 2). In general, the maximum allowable measurement errors for temperature are 1.5 K for all measurement altitudes. Those for pressure are close to 0.1 % for 0 m and close to 0.5 % for 13000 m. The magnitude of the statistical temperature and pressure uncertainties for the optical measurements and the magnitude of the increase of these uncertainties after correction of the systematic errors caused by solar background and the signal leakage, are a function of the optical signal energies detected in the channels RR1, RR2, CP and H_2O and thus a function of the laser pulse energy E_L. Figure 7.9-1 (solid lines) shows the necessary values for E_L needed to obtain smaller 1-σ temperature and pressure measurement uncertainties ΔT and Δp / p

than the maximally allowable errors for aviation. The values are calculated for daytime measurements in clear sky with the formulas from Appendix C. The uncertainties are those obtained for a 10-pulse-averaged measurement. In these calculations, the systematic errors consisting of the daylight error and the leakage error are assumed to have been present, but corrected using the described methods. The raised measurement uncertainties due to these corrections are comprised in the results. The noise of the detection electronics is comprised as well. The extinction error is expected to be fully corrected without any influence on ΔT and Δp / p. The measurements are assumed to be performed in dry air.

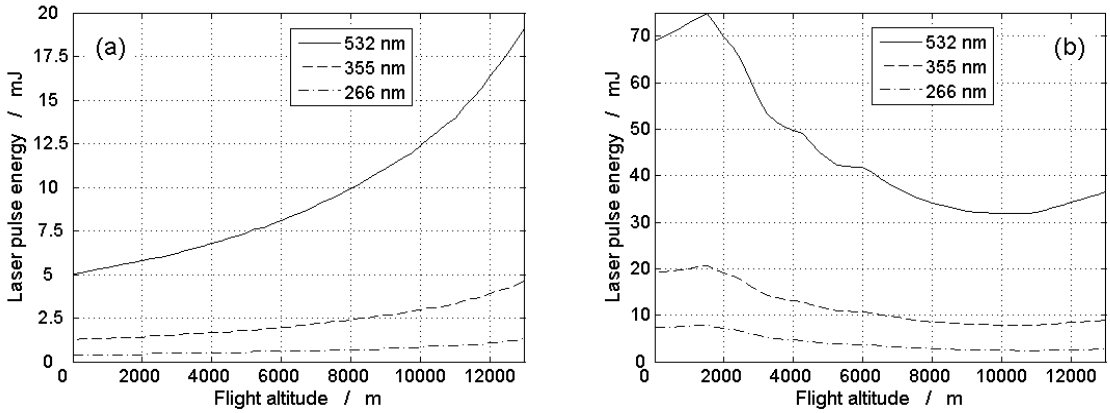

Figure 7.9-1. Laser pulse energies necessary for temperature (a) and pressure measurements (b) at daytime and in clear sky, in order to meet the measurement accuracies defined in sect. 2. 10 pulses are integrated for each measurement. Values for different laser wavelengths are plotted as well.

In an operational airborne measurement system, the optimum CWLs cannot be adjusted in-flight for each flight altitude, but one CWL pair has to be chosen for the measurements at all altitudes. For calculating the data shown in Figure 7.9-1 (a) and (b), the filter CWLs were chosen to be optimum for pressure measurements at sea level, i.e. 531.0 nm for RR1 and 528.8 nm for RR2 at the laser wavelength of 532.07 nm, since there the demands of the aviation standards are highest. The latter is also confirmed in Figure 7.9-1, which illustrates, that the highest laser pulse energies are needed for pressure measurements at low flight altitudes. At sea level and at daytime and in clear sky, a laser pulse energy of > 75 mJ (532 nm) is needed to meet the aviation pressure requirements, whereas half the pulse energy is needed at 13000 m. For measurements in dense clouds with R = 10000 and assuming $OD_{RR1} = OD_{RR2} = 6$, the necessary pulse energy climbs up to the 6-fold value (not shown). The maximum allowable measurement errors for temperature are already undershot at all altitudes with > 18 mJ laser pulses. In dense clouds, the energy has to be increased by a factor of only 1.6.

7.10 UV versus VIS laser wavelengths - theoretical considerations

The described measurement apparatus is based on visible (VIS) laser light at 532 nm. However, ultraviolet (UV) wavelengths would be beneficial for four reasons: First, all molecular backscatter intensities are higher, due to their proportionality to λ_L^{-4} (λ_L = laser emission wavelength), giving rise to

an increase of the detected pulse power $P_{rot,RR}$ by a factor of ~5 for 355 nm versus 532 nm alone. The thereby resulting possibility of employment of weaker lasers is attended by weight and cost reduction. Second, with regard to the mentioned proportionality, the backscatter ratios R are decreased (sect. 4.6), since elastic scattering from cloud droplets has mostly a linear wavelength dependency [110]. This lowers the demands on the necessary suppression of elastic backscatter for the RR filters. Third, eye safety is strongly enhanced. Using a 355 nm laser, the maximally allowable laser power the eye may be exposed to, is approximately 4 orders of magnitude higher than for a 532 nm laser with similar properties [129]. Fourth, dependent on measurement direction from aircraft, the position of the sun and atmospheric conditions, the collected solar background light intensities decrease, especially in clouds (sect. 4.7). For example, simulations with *LibRadTran* [113] for upward looking, cloud facing measurement systems and radiance measurement experiments [114] show, that with increasing degree of cloudiness, the sky radiances increase for all wavelengths but their spectral maximum shifts from UV towards VIS wavelengths. Below around 300 nm even virtually no solar background is present (solar blind region). The decrease of solar background is advantageous with regard to SNR and allows for usage of more compact high repetition laser sources at equal average laser power.

The mentioned aspects lead to a reduction of the required laser pulse energies for the obtainment of equal measurement uncertainties using systems based on UV lasers compared to systems based on 532 nm lasers. This is illustrated in Figure 7.9-1 for 10-pulse-averaged temperature and pressure measurements at 532 nm (solid line), 355 nm (dashed line) and 266 nm (dotted line). In the calculations for the plots, the relationship of the responsivities was assumed to be $\rho_{APD,355nm}$ = 355 nm / 532 nm · $\rho_{APD,532nm}$ and $\rho_{APD,266nm}$ = 266 nm / 532 nm · $\rho_{APD,532nm}$ (in Appendix B: $\rho_{APD} = \rho_{APD,532nm}$), i.e. equal detector quantum efficiencies, and of the solar background radiances $\Psi_{355nm} = 0.5 \cdot \Psi_{532nm}$ and $\Psi_{266nm} = 0 \cdot \Psi_{532nm}$ (in sect. 4.7: $\Psi = \Psi_{532nm}$). The backscatter cross sections were adapted to the laser wavelengths according to the formulas in sect. 4.3. For pressure and temperature measurements the use of 355 nm laser sources leads to a reduction of the necessary laser pulse energies by more than a factor of 3. For 266 nm laser sources, a reduction of even more than a factor of 10 is obtained. However, at that wavelength, high ozone absorption coefficients at high altitudes [130, 131] can lead to signal absorption of a couple of tenth of a percent and could thus pose problems for density and pressure measurements. A further issue at 266 nm is the availability of optics. Interfering fluorescence of the optics, however, is not an issue, since the measurements are done at the anti-Stokes side, i.e. the shorter wavelength side of the RR spectrum, whereas fluorescence takes place at wavelengths being equal or larger than the excitation wavelength.

Although in the practical airborne implementation the use of UV laser wavelengths is generally advantageous due to the mentioned reasons, there is one major disadvantage: The demands on the manufacturing of the important interference filters are higher in the UV and the achieved filter performances are lower nowadays. This was demonstrated with working RR temperature measurement systems [11, 73]. In particular, it was this reason why it was decided to concentrate on a VIS system in a first feasibility study. Furthermore, if using Nd:YAG lasers, loss of about half of the laser pulse energy due to conversion from the fundamental wavelength of 1064 nm to 355 nm instead of 532 nm has to be kept in mind as well [132]. However, because smaller laser pulse energies are required at 355 nm by a factor of more than 3, the general laser power consumption or signal yield at 355 nm would be larger than the loss.

8 Experimental results in flight altitude atmospheric conditions

In this section the laboratory experimental results using the designed measurement apparatus and the atmospheric simulator are described. First preliminary experimental results were published in [133]. Since then, the experimental performance could be improved, especially with regard to the systematic errors, which are described in this chapter prior to the statistical ones. In experiment, other systematic errors sources may be experienced than in the theoretical case treated in the computational simulations in chapter 7. This is clear, since in the simulation, hardware is assumed to behave ideally. Moreover, different errors can be assessed in theory which are difficult to be checked in the laboratory, like errors appearing during measurements in dense clouds or with daytime background radiance. Other errors may dominate in the experiment, which are negligible in the simulations, as e.g. the calibration error. Therefore, chapter 7 is to a great extend complimentary to this one. Nevertheless, where possible, the experimental results are compared to those of the computational simulations. Here, the computational model parameters are always adapted to the experimental ones to make both results comparable. The computational model is finally refined in such a way, that model and experimental results are matching each other. The experimental measurement examples presented in this chapter are typical for the performance of the measurement system. The results were also presented in [134].

In sect. 8.1, as the basis, the detected optical signals are described and the way they are processed to extract the necessary information. In order to better understand and identify the different hardware influences on the systematic errors, the firstly discussed measurements consist in measuring the RR backscatter of air at constant pressure and varying temperature or vice versa. The important dependencies of the RR signals on the temperature of the probed air as being the key property of the working principle of the measurement method are presented. The air inside the measurement volume is manipulated with the atmospheric simulator (sect. 6.3). This is followed in sect. 8.2 by a description and a discussion of the resulting systematic temperature, density and pressure errors including the applied methods for error minimization. These errors are mainly the calibration errors and the non-linearity of the photo detectors, the latter being a technical issue, not a physical one. In sect. 8.3 a discussion follows on the statistical measurement uncertainties. These uncertainties do not originate in the physically inherent statistical nature of the detected optical RR backscatter only, but also in used hardware of the measurement equipment. The specific hardware uncertainty sources are discussed in detail. Additionally, the results of water vapor measurements are presented together with their impact on the total air density and pressure measurement uncertainties for measurements performed in moist air. In sect. 8.4 the measurement uncertainties yield with the apparatus are shown for measurements in air present at different flight altitudes. Based on these uncertainties, general formulas are set up describing analytically and physically correct the expected measurement uncertainties specific for the used measurement apparatus. With the formulas, the measurement uncertainties at 532 nm expected for laser pulse energies other than the experimentally reached 118 mJ as well as for laser wavelengths other than 532 nm are determined. Subsequently, the laser pulse energies required for meeting the aviation error requirements with the used apparatus are identified.

8.1 Optical measurements

8.1.1 Signal analysis and processing

As the very first step, the signals optically detected with the laboratory apparatus using the atmospheric simulator are fundamentally analyzed. All detector output signals are recorded with the oscilloscope described in section 6.1. The four oscilloscope input channels record the signals from channel *RR1* and *RR2*, from a reference PIN-diode monitoring directly the laser pulse energy and either channel *CP* or channel H_2O. Figure 8.1-1 (left) shows typical output signals of the custom-made APDs in the channels *RR1* and *RR2*. These signals are generated by detecting radiation which is scattered inside the atmospheric simulator (sect. 6.3). The electrical pulses are sampled with a frequency of 1.25 Gs/s, so that around 25 non-negative and non-zero samples are taken inside each single of the ≈10 ns long electrical pulses. Each sample is quantized with the oscilloscope's resolution of 8 bits. The APD detectors in the channels *RR1* and *RR2* generate output signals with undershoots. This is attributed to the spectral response of the detectors, which is strongly influenced by the high cut-off frequency of the built-in AC high-pass filters of 10 MHz. Two further modified APD detectors for the RR channels were developed, making also the recording of DC signals possible and thus avoiding the generation of undershoots. However, unfortunately, the technical features of the new APDs made a utilization in the current experimental setup without further change of data acquisition equipment impossible.

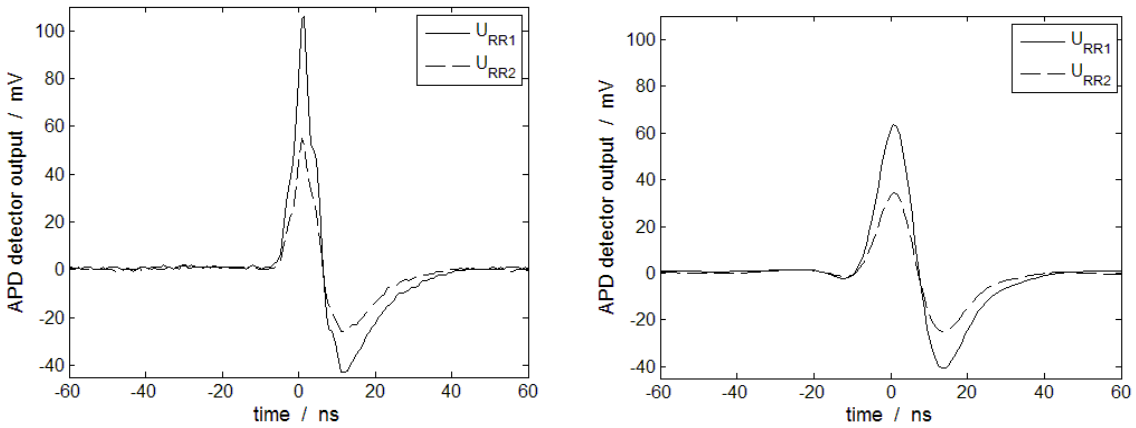

Figure 8.1-1. Examples of typical output signals recorded with the APD detectors in channel RR1 or RR2 not filtered (left) and digitally filtered with a 50 MHz low pass filter (right). The pulses were recorded at a vacuum tube temperature of $T_{chamber}$ = 238 K (-35 °C) and a pressure of $p_{chamber}$ = 951 hPa.

Figure 8.1-2 illustrates other typical temporal pulse shapes observed within a time interval of a couple of seconds. The change of the pulse shapes is generated by the laser. During the regular operation of the laser (a few hours) and especially during the heating-up process (ca. 45 min), the settled emission pulse shape tended to change as well. I.e., the predominating substructure exhibited a

variation not only from shot to shot, but also on a longer time scale of a couple of 10th of minutes. This indicates that these variations could be also induced by temperature changes of the laser. Moreover, the laser output pulse energy was not very stable, but exhibited fluctuations as high as ±6 % from shot to shot, what is probably an effect of the varying flash-lamp-pulse-energy pumping the laser. This variation was accounted for using the reference diode. The changing temporal pulse shape could not be accounted for in the signal processing and could be a source of the observed systematic measurement errors (sect. 8.2.3) as well as of the statistical measurement uncertainties (sect. 8.3.3).

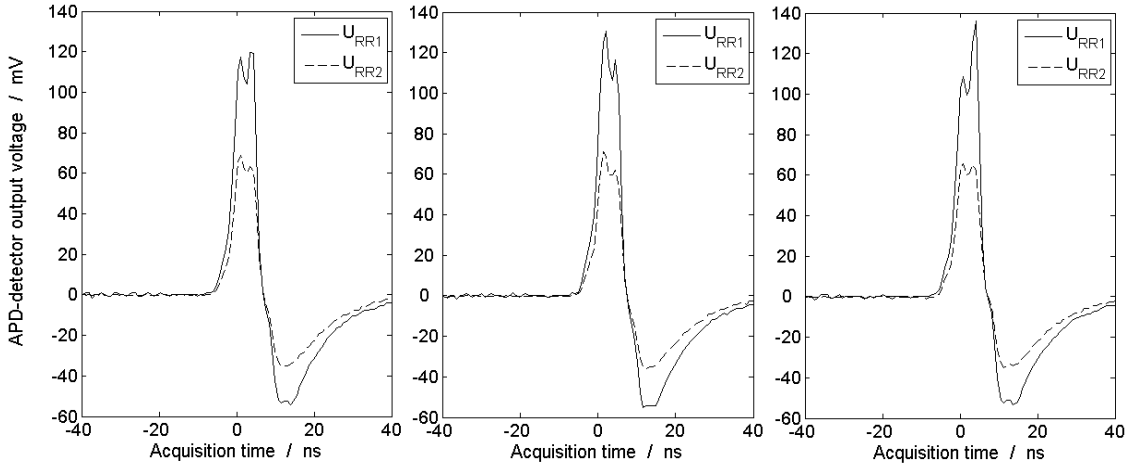

Figure 8.1-2. Other examples of pulse shapes of the unfiltered output signals of the APD detectors in channel RR1 or RR2. The three pulses were recorded within a time interval of a couple of seconds proofing, that the time shape of the emitted laser pulse may even vary from shot to shot (cf. Figure 8.1-1).

To precisely extract the scattered and detected light pulse power from each recorded electrical pulse, different computational post-processing methods using *Matlab* were tried. To check the effectiveness of the different methods, the standard deviations of the determined peak power of 1000 light pulses were set up and compared:

1) Since the power of detected optical pulse is proportional to the time integral of the recorded electrical pulse, the samples of the time signal recorded with the oscilloscope can be summed. Since the number of samples inside each signal pulse is too low (≈25), this method leads to relatively large standard deviations. A reconstruction of the signal by inserting additional virtual samples by applying the Whittaker–Shannon interpolation [135] proved to insignificantly improve the extracted data.

2) The second possibility is based on the assumption that the temporal pulse shape does not change from pulse to pulse, so that the power of detected optical pulse can be assumed to be proportional to the peak of the electrical signal pulse. However, due to interference with noise and the changing substructure (Figure 8.1-2) of the flash lamp pumped laser pulse, this peak cannot be estimated with high accuracy without further computational processing methods. One option, here, is to determine the peak by fitting a function describing the key properties of the temporal pulse shape in a mathematically correct way. Such a function can be a Gaussian bell curve. The peak is then obtained by the fit parameter describing the amplitude. Another option which leads to equal accuracies (but

needs lower calculation time) is to apply a digital low-pass-filter to the electrical signal pulse and then to determine directly the peak sample of the filtered signal. The low-pass filtering smoothes the temporal signal pulse and eliminates its substructure. (Figure 8.1-1; right). A major noise source is the low resolution of the oscilloscope of only 8 bit. This alone can lead to errors of a couple of percent in the determination of the accurate signal pulse peak at lower air densities where small electrical signals are recorded. Due to the low-pass filtering, this noise is reduced as well. Different digital low-pass filters were tested. A low-pass filter with a cut-off frequency of 50 MHz proved to be best (3rd order Butterworth low-pass filter). The exploitation of the oversampling principle in order to obtain a virtually higher sampling rate by inserting virtual zero samples between the real samples and then applying an accurate low pass filter was implemented as well. However, this method did not lead to further accuracy improvements in the signal peak determination.

The laser output pulse energy is permanently monitored in parallel with the laser reference PIN diode and used for normalization of the photo detector signals in all channels. This reference signal is also post-processed by the same digital low-pass filter as the RR signals. Figure 8.1-3 shows exemplarily the normalized RR signal peaks U_{RR1} of channel RR1 for 1000 signal pulses recorded in 100 seconds with the 10 Hz laser. U_{RR1} is defined as $U_{RR1} = \tilde{U}_{RR1} / U_L$, with $\tilde{U}_{RR1}$ being the determined peak voltage of the electrical signal in RR1 and U_L the one of the laser reference signal. The low pass filtering reduces the standard deviation of the time series by a factor ranging from 3 to 10, dependent on the signal amplitude and consequently the relative magnitude of the oscilloscope's quantization noise. The averaging of 10 pulses further reduces the standard deviation by a factor of around 3.

By installing light shielding elements in- and outside the atmospheric simulator and employing highly AR-coated windows and adjusting the measurement volume, no directly reflected light from the windows is collected by the receiver channels. Due to this fact and due to the high optical density of the filters RR1, RR2 and H_2O, virtually no laser stray light coming from the atmospheric simulator is detected in these channels (cf. also Figure 8.1-7). However, in the elastic channel CP, the detected laser stray light intensity is still exceeding the one of the recorded molecular signal. It was realized that microscopic bubbles and inclusions inside the glass of the vacuum tube windows are a major stray light source. Since the stray light output signal is about two orders of magnitude higher than the molecular and particle elastic signal, channel CP is not used for its origin purpose. Instead, the edge of the spectral transmission curve of filter CP is shifted onto the laser emission wavelength. This filter slope is very steep with a change of total transmission of 264 % per nm. In this way, channel CP is used to monitor small wavelength drifts of the laser and of the interference filters (sect. 8.2.3).

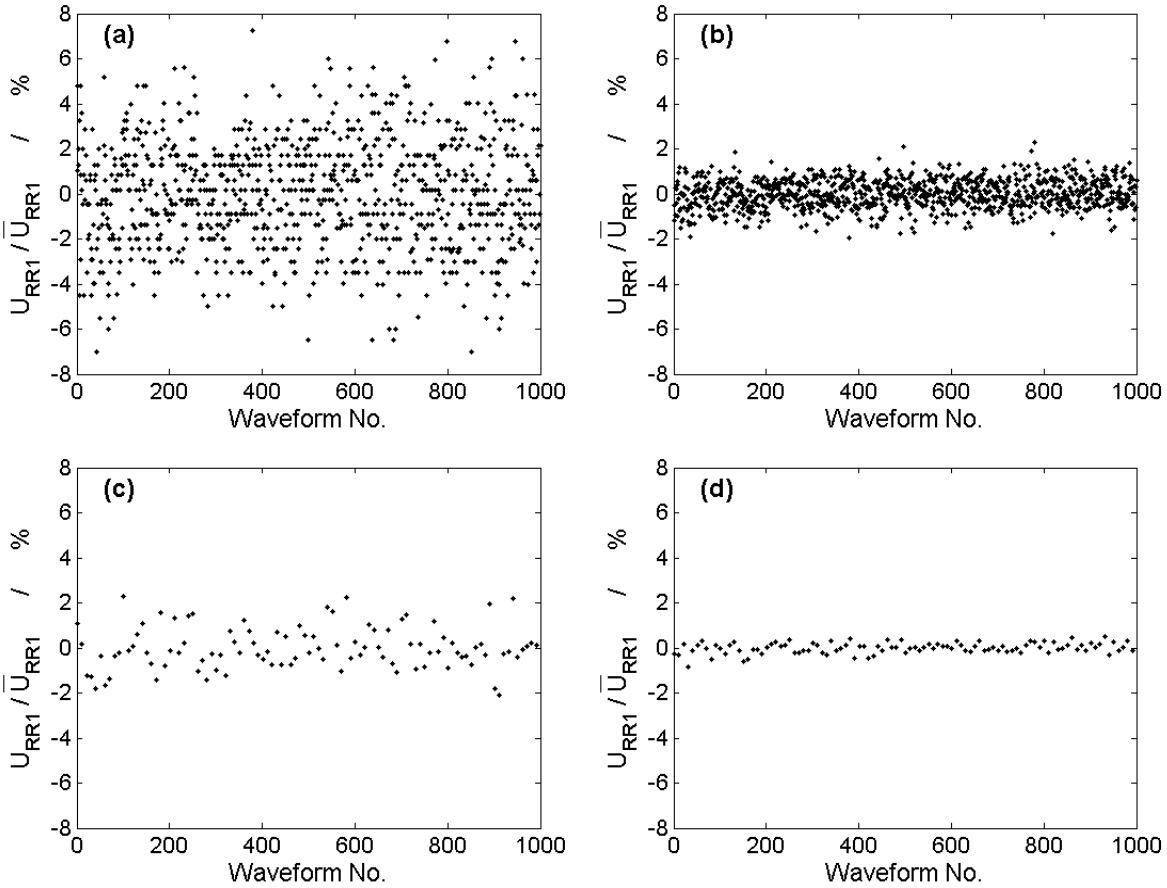

Figure 8.1-3. Deviations of 1000 determined signal peaks U_{RR1} recorded at approximate sea level atmospheric conditions ($T_{chamber}$ = 295 K and $p_{chamber}$ = 950 mbar). The RR1 signal pulses are already normalized to the laser output pulse power. (a): Obtained with unfiltered RR1 signal pulses. The pattern created by the discrete values of U_{RR1} can be seen. The discrete values are generated by the signal quantization of the oscilloscope; (b): Obtained by signal pulse filtering with the digital 50 MHz low-pass filter. (c) and (d): Same as (a) and (b), respectively, but for an average of 10 recorded signal pulses.

8.1.2 RR signal recordings as function of air temperature

For the basic characterization of the measurement system, the temperature dependency of the RR signals on the probed air was analyzed. The existence of a strong temperature dependency of the RR signals is important, because it is the fundamental property the measurement principles are based on. For the analysis, only the air temperature to be optically probed inside the atmospheric simulator was varied. The air pressure, however, was kept constant, in order to minimize its influences onto the measurement results. Constant air pressure inside the atmospheric simulator was established by leaving the vacuum tube opened. The interior pressure was thus equal to the laboratory air pressure. It turned out to be advantageous to keep the measurement time for the temperature series as short as

possible. Therefore, instead of adjusting the tube temperatures sequentially and waiting for equilibration of the temperature distribution, the temperature was raised continuously at a fixed rate of 0.55 K / min from $T_{chamber}$ = 238 K (-35 °C) to 308 K (+35 °C) and the optical measurements were taken in between. Thus, the exterior experimental conditions in the laboratory were kept as constant as possible. This avoided an increase of systematic measurement errors, since possible frequency drifts of the laser, drifts of the RR interference filters or variations of the APD responses e.g. due to variations of the room temperature, were minimized.

The temperature run inside the chamber and the recording time intervals are shown in Figure 8.1-4. The temperature offsets between the curves of the different tube temperature probes are attributed to the calibration errors of the temperature probes themselves and slightly different response times of the probes but not to inhomogeneity of the temperature field inside the vacuum tube. The homogeneity of the temperature field was established by the big fan of the temperature test chamber. Since the temperature increase rate inside the vacuum tube was constant, the systematic temperature measurement errors from the tube sensors were constant as well and thus irrelevant.

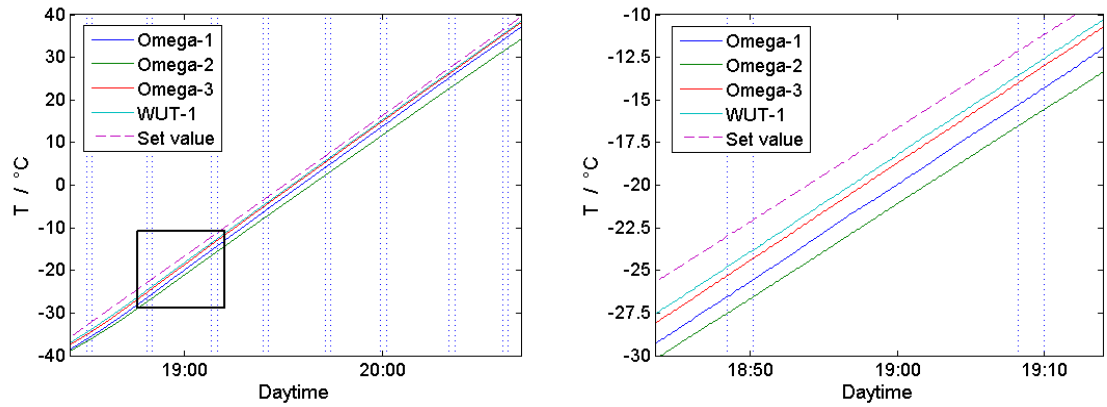

Figure 8.1-4. Temperature progression inside the vacuum tube of the atmospheric simulator measured with the tube-integrated PT100 sensor named *WUT-1* and the three additional PT100 temperature sensors *Omega-1*, *-2*, and *-3*. *WUT-1* indicates the actual value for the temperature control loop for the vacuum tube. The set value of the control loop is shown as well. WUT-1 is also used as the temperature reference sensor for the experiments. Each time interval, in which 1000 signal peaks are optically recorded at a specific temperature, is indicated by vertical dashed lines. The right graph is a magnification of a section of the left graph enclosed by the rectangular box.

Figure 8.1-5 shows U_{RR1} and U_{RR2} as a function of temperatures ranging from around $T_{chamber}$ = 238 K (-35 °C) to 308 K (+35 °C) recorded in steps of around 10 K. $T_{chamber}$ is the temperature of the air inside the measurement volume, which is located inside the atmospheric simulator. U_{RR1} and U_{RR2} were processed as described in sect. 8.1.1. For each temperature, 1000 signal peaks U_{RR1} and U_{RR2} were averaged. The used CWLs of the filters were 531.1 nm for *RR1* and 528.6 nm for *RR2*. The air pressure inside the atmospheric simulator was nearly constantly $p_{chamber}$ = 946 hPa. Possible variations of the recorded values of U_{RR1} and U_{RR2} caused by minor fluctuations of the exterior pressure (and thus

air density inside the simulator) were accounted for by scaling U_{RR1} and U_{RR2} to the mean pressure of 946 hPa.

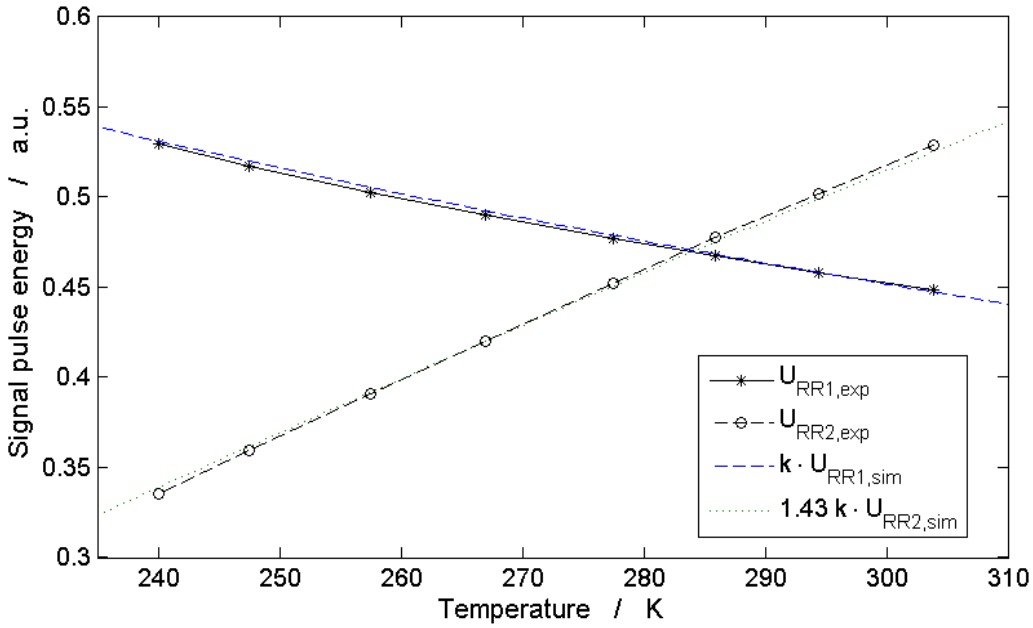

Figure 8.1-5. Average values over 1000 pulses of the two rotational Raman signal peaks U_{RR1} and U_{RR2}. The experimental values differ only by a proportionality factor k from the ones predicted by the computational model (chapter 7). The experimental value $U_{RR2,exp}$, however, is increased by a factor of 1.43. This is due to an adjusted larger APD gain in the experiment than in the simulation. The data were measured and simulated using filter central wavelengths (CWLs) of 531.1 nm for *RR1* and 528.6 nm for *RR2*. Simulation and experiment are in very good agreement: The respective values differ by < 1 %.

In Figure 8.1-5 additionally the experimental temperature dependencies of U_{RR1} and U_{RR2} are compared with their simulated ones yield from the computational model of chapter 7. Here, these simulations were remade taking into account the exact experimental measurement configuration and experimental measurement conditions. The experimental air temperature dependence of both RR signals validates the predictions from simulation. The experimental values differ from the theoretical ones by only < 1 % for both signals RR1 and RR2. This confirms, on the one hand, that the used interference filters match the specifications, that they are tuned to the desired wavelengths, and that the other optics in the RR channels are well aligned. On the other hand, it proves that the computational simulations are well elaborated and highly accurate. Figure 8.1-6 shows the ratios Q_{exp} and Q_{sim} (eq. (5.1.1)) set up with the experimental and computational values for U_{RR1} and U_{RR2}, respectively. Here, Q_{exp} and Q_{sim} are even in better agreement and differ by only < 0.5 %.

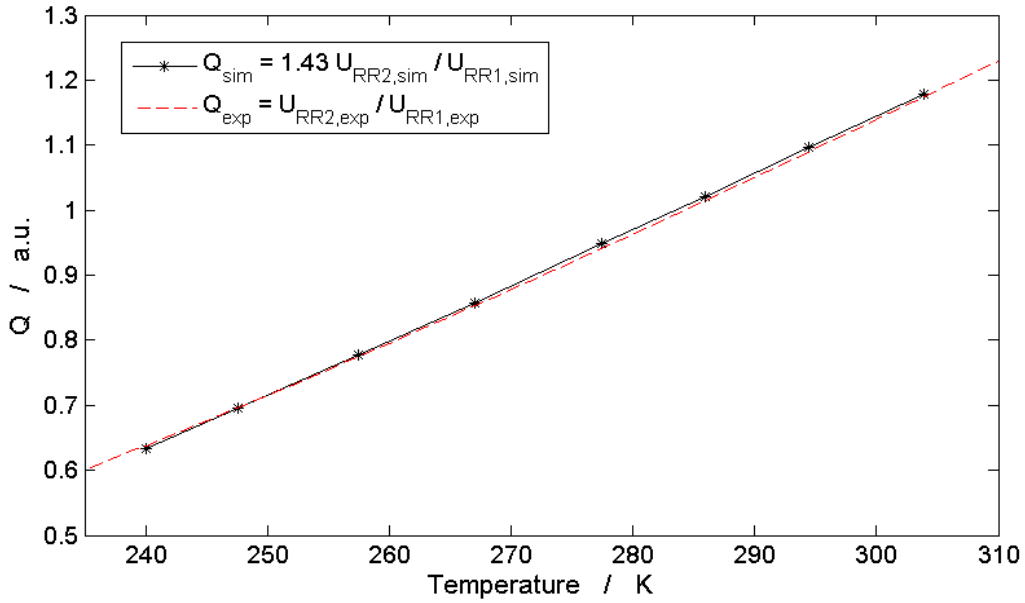

Figure 8.1-6. Ratio $Q(T) = U_{RR2} / U_{RR1}$ of the recorded optical signals shown in Figure 8.1-5. Experimental and simulation values are compared and are in very good agreement to each other. They differ by only < 0.5 %.

8.1.3 RR signal recordings as function of air pressure

In a further step, the RR signals as a function of the pressure of the probed air were investigated. These dependencies were basically needed for characterizing the linearity and the stability of the APD detector response in each RR channel. Linearity and stability of the detector response is essential to maintain the temperature and density calibration for different energies of the backscattered light pulses generated by scattering in different air densities. Linear detector response implies that the detected signals have to be proportional to the air molecular number density. Linearity is a property, which is thus crucial to avoid further systematic measurement errors, others than those evoked by measurements in varying air temperature. Thus, for the analysis of the linearity of the APD responses in both RR channels, the detected optical pulse power in these channels was examined as a function of changing air pressure (at constant air temperature) inside the vacuum tube and thus as a function of the number of scattering molecules. Figure 8.1-7 shows the average values of 1000 recorded signal pulse peaks U_{RR1} and U_{RR2} for vacuum tube pressures ranging from around $p_{chamber}$ = 0 hPa to 950 hPa. Although according to the ISA (sect. 2) the air pressure does not fall below about 150 hPa even at very high flight altitudes, it was interesting to check the amplitude of the RR signals even in a totally evacuated tube at nearly 0 hPa. In this way it could be verified, whether leaking laser stray light was detected or not. The absence of a signal at 0 hPa in Figure 8.1-7 illustrates that this was not the case, proofing that the measurement volume is fully located within the vacuum tube, and that the blocking of elastically scattered stray light by the RR interference filters is sufficiently high.

Since the temperature test chamber was turned off, the temperature of the air inside the vacuum tube $T_{chamber}$ = 298.95 K (25.8 °C) was virtually equal to the laboratory room temperature. A small monotonous temperature drift inside the test chamber, however, occurred during the whole experiment, which was < 0.1 K. The molecular number density variation caused by these minor temperature drifts was accounted for by correcting the measured signal peaks to the temperature reference value of 298.95 K. From Figure 8.1-7 it can be already stated, that the optically detected RR signals in both channels are not exactly proportional to the pressure and - because the air temperature is constant - to the air density. This indicates that the required response linearity is not existent for neither of the RR APD detectors. The exact quantification of these nonlinearities including the thereby generated measurement errors as well as a method to correct these nonlinearities are discussed in detail in sect. 8.2.2 and 8.2.3.

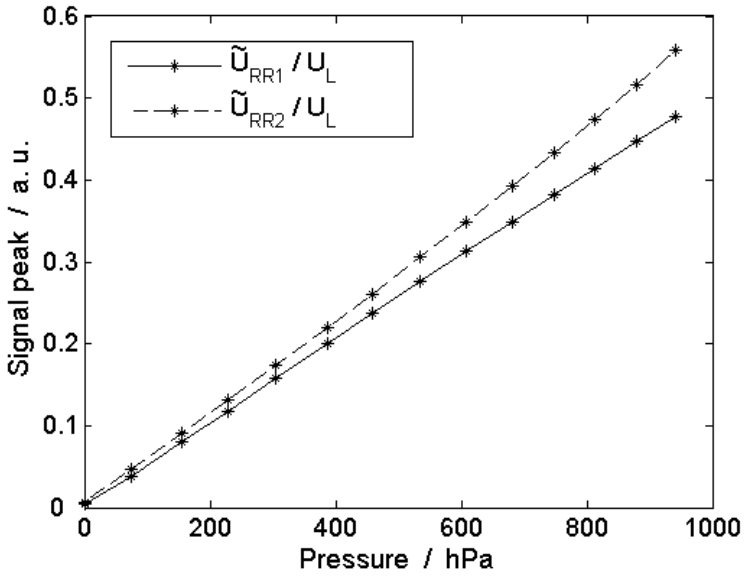

Figure 8.1-7. Normalized signal peaks $U_{RR1} = \tilde{U}_{RR1} / U_L$ and $U_{RR2} = \tilde{U}_{RR2} / U_L$ (cf. sect. 8.1.1) of channels *RR1* and channels *RR2*. For each air pressure value, 1000 normalized peaks were averaged. The air temperature is kept fixed at 298.95 K (25.8 °C).

8.2 Analysis of systematic measurement errors

8.2.1 Calibration and error at different air temperatures

For the calibration of the air temperature and molecular number density measurement, the same data set as in sect. 8.1.2 is taken as basis. The temperature measurement is calibrated as follows: First, the average values of the ratio $Q = U_{RR2} / U_{RR1}$ are set up for each temperature and are inserted into the general temperature calibration function T_{calib} (eq. (5.2.2)). Second, T_{calib} is unambiguously determined by fitting to the reference temperatures $T_{chamber}$. $T_{chamber}$ is measured with the PT100 temperature probe

WUT-1 inside the vacuum tube of the atmospheric simulator (see Figure 8.1-4). In Figure 8.2-1 (left) these optical temperatures T_{calib} (T_{calib} is used simultaneously for the calibration function and for the optically measured temperatures) are compared to the "true" reference temperatures $T_{chamber}$ of the vacuum chamber. Figure 8.2-1 (right) shows the magnitude of the difference of these temperatures $[\Delta T_{syst}]_p = T_{chamber} - T_{calib}$, which is only maximally 0.05 K (solid curve). $[\Delta T_{syst}]_p$ is defined as the systematic temperature measurement error made at constant air pressure. The error of the calibration function obtained from the simulations for exactly this measurement scenario is plotted in Figure 8.2-1 (right) as well (dashed line) and is smaller than 0.02 K (cf. sect. 5.2). Thus, the obtained experimental error is close to this simulated limit.

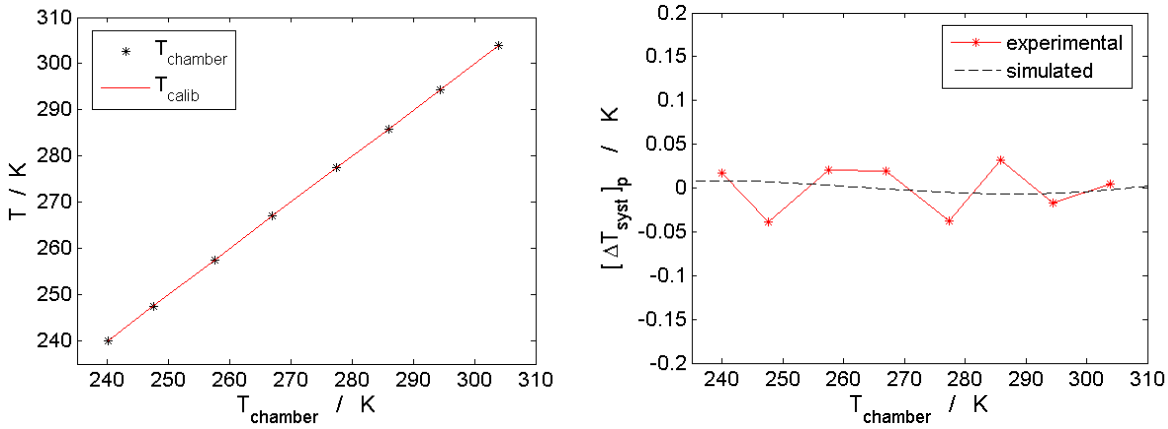

Figure 8.2-1. Left: The optically measured mean temperature T_{calib} compared to the temperature of the vacuum chamber $T_{chamber}$. Right: Systematic measurement errors $[\Delta T_{syst}]_p$ defined as experimental deviations of the measured temperatures T_{calib} from the chamber temperatures $T_{chamber}$ at constant pressure compared to computationally simulated deviations. The latter are only assigned to the calibration function, the former are the sum of this error and the dominating systematic fluctuations during the experiment. The chamber pressure is constantly $p_{chamber}$ = 946 hPa.

An analogous evaluation is made for molecular number density measurements using the respective calibration function N_{calib} (eq. (5.2.4)). Figure 8.2-2 (left) shows the measured density at this experiment relative to N_0. $N_0 = 2.547 \cdot 10^{25}$ 1/m^3 is the molecular number density at sea level according to the ISA (sect. 2). Since the vacuum tube is open, the interior air pressure is equal to the exterior one and constantly $p_{chamber}$ = 946 hPa. Thus, the density changes only with temperature. Figure 8.2-2 (right; solid line) shows the error $[\Delta N_{syst}]_p = (N_{chamber} - N_{calib}) / N_{chamber}$ which is defined as the systematic density measurement error made at constant air pressure. $[\Delta N_{syst}]_p$ is < 0.07 %. Figure 8.2-2 (right; dashed line) shows the simulated error of the density calibration function only (cf. sect. 5.2), which is < 0.03 %. Here, simulated and experimental errors are close together as well.

Figure 8.2-3 illustrates the obtained errors for pressure measurements. The pressure is obtained with the ideal gas equation: $p_{calib} = N_{calib} \cdot k_B T_{calib}$ (sect. 5.3). The systematic pressure error is yield by $[\Delta p_{syst}]_p = (p_{chamber} - p_{calib}) / p_{chamber} = [\Delta N_{syst}]_p + [\Delta T_{syst}]_p / T_{chamber}$. The error values $[\Delta p_{syst}]_p$ stay < 0.06 %, which is the maximum error made at 285 K. Although both the density and the temperature error contribute to the pressure error, it can be seen that for all temperatures $[\Delta p_{syst}]_p$ <

$[\Delta N_{syst}]_p$. This is due to the high anti-correlation of the errors $[\Delta N_{syst}]_p$ and $[\Delta T_{syst}]_p$ in the measurements, which leads to a partial error compensation.

Summing up, all errors are in very good agreement to those obtained in the model calculations and only slightly larger. However, with regard to the strict error requirements in aviation (sect. 2), even usually small error sources have to be eliminated. The potential systematic error sources are discussed in detail in sect. 8.2.3.

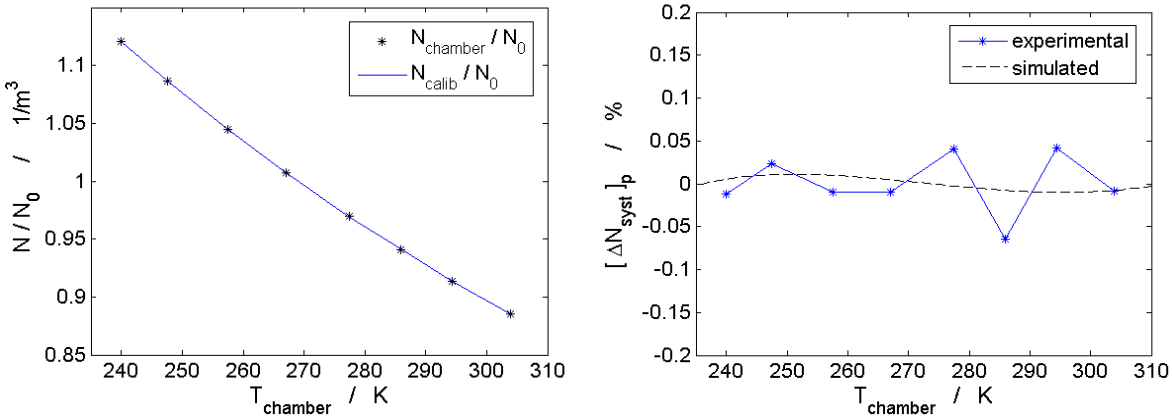

Figure 8.2-2. Same as Figure 8.2-1 but for density measurements.

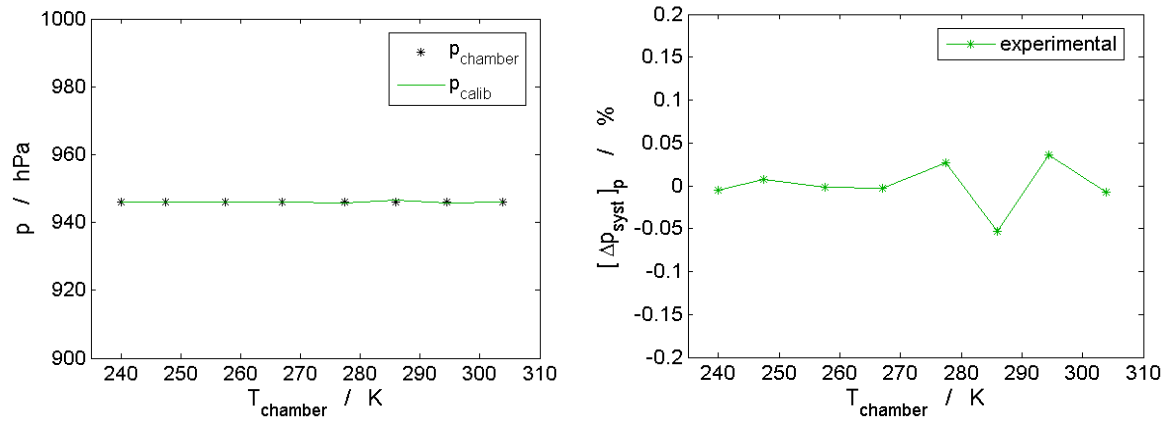

Figure 8.2-3. Same as Figure 8.2-1 but for pressure measurements.

8.2.2 Linearity of detector response and error at different air pressures

In sect. 8.1.3 first investigations were made concerning the dependence of the RR signals on the probed air pressure. The high importance of the linearity of the APD detector response in both RR channels was stressed. In case of the required perfect detector linearity (emphasized by index: *lin*), the functional dependence of the detector output signals U_{RR} with *RR* = *RR1* or *RR2* on the optical input

pulse power P_{RR} and thus from the air pressure $p_{chamber}$ inside the atmospheric simulator is described mathematically by a straight line:

$$U_{RR,lin}(p) = a_{1,RR} \cdot p_{chamber} + a_{2,RR} \quad . \tag{8.2.1}$$

Evidently, P_{RR} is proportional to $p_{chamber}$. $a_{1,RR}$ and $a_{2,RR}$ are the two fit coefficients for each of the RR signals. $a_{1,RR}$ describes the necessary proportionality and $a_{2,RR}$ a possible offset to be subtracted. Although this linear behavior is desired in terms of calibration stability, it is not perfectly featured by the detectors. This is illustrated in Figure 8.2-4 (dashed line), which quantifies the relative deviation (U_{RR} - $U_{RR,lin}$) / U_{RR}. For the figure plots, the data from sect. 8.1.3 were used.

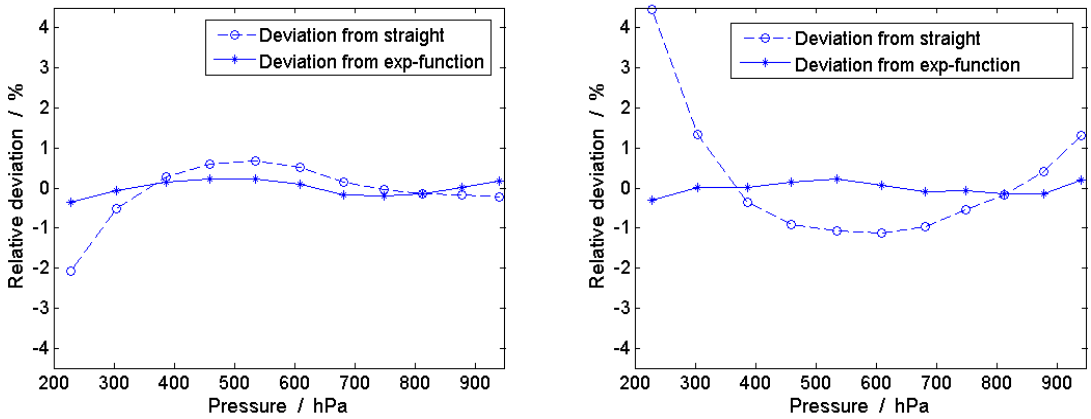

Figure 8.2-4. Relative deviation of the APD detector output shown in Figure 8.1-7 from linearity (dashed line) and from an exponential function fitted to the data (solid line). The left plot refers to channel RR1, the right to channel RR2.

A generally better representation of each of the detector outputs is yield with the exponential function

$$U_{RR,\exp}(p) = b_{1,RR} \cdot \exp\left(b_{2,RR} \cdot p_{chamber}\right) + b_{3,RR} \quad , \tag{8.2.2}$$

where $b_{1,RR}$, $b_{2,RR}$ and $b_{3,RR}$ are the three fit coefficients. The exponential description of the detector outputs (Figure 8.2-4; solid line) deviates systematically less than the linear one by as much as one order of magnitude. The maximum residual deviations from the exponential function amount only around 0.3 % for both RR channels. It is remarkable, that the residual error of channel RR1 is strongly correlated with the one of channel RR2 throughout the whole pressure range. The strong correlation suggests a common error source, which could be the reference pressure sensor of the atmospheric simulator. This sensor has an accuracy ranging from < 0.25 % to < 0.65 %, depending on the pressure to be measured (sect. 6.3), which matches well the observed errors of up to 0.3 %. This assumption is further affirmed by the results of the error discussion in sect. 8.2.3.

In order to minimize the non-linearities of the detector responses down to maximally 0.3 %, a function was set up for each RR channel by inserting the inverse of $U_{RR,exp}$ (eq. (8.2.2)) into $U_{RR,lin}$ (eq. (8.2.1)). This function is denoted in the following as the linearity correction function. It is used in the signal processing of all measurements further presented in the next sections. The function transforms the actually weakly exponential dependence of U_{RR} on the optical input pulse power into the necessary linearized dependence, yielding $U_{RR,corr}$:

$$U_{RR,corr}(U_{RR}) = a_{1,RR} \cdot \frac{\ln\left(\dfrac{U_{RR} - b_{3,RR}}{b_{1,RR}}\right)}{b_{2,RR}} \quad . \tag{8.2.3}$$

Since $a_{2,RR}$ is already subtracted in $U_{RR,corr}$, any signal offsets introduced by elastic stray light inside the atmospheric-simulation chamber and insufficient blocking thereof inside the RR channels as well as offsets introduced by the data acquisition electronics are removed. However, as shown in Figure 8.1-7, these offsets measured in a totally evacuated vacuum tube ($p_{chamber}$ = 0 mbar) are marginally small.

The temperature calibration requires insensitivity of the ratio Q to air density variations and thus also to air pressure variations. Since the temperature of the vacuum tube is constant for the used data set (see sect. 8.1.3), Q has to be constant as well. Figure 8.2-5 (left) shows the relative deviation of the ratios $Q = U_{RR2} / U_{RR1}$ and $Q_{corr} = U_{RR2,corr} / U_{RR1,corr}$ as a function of pressure. It is evident, that the ratio Q_{corr} for the corrected RR signals systematically deviates less as function of pressure and thus density than the uncorrected ratio Q. The maximum variation of Q_{corr} is now even < 0.16 %.

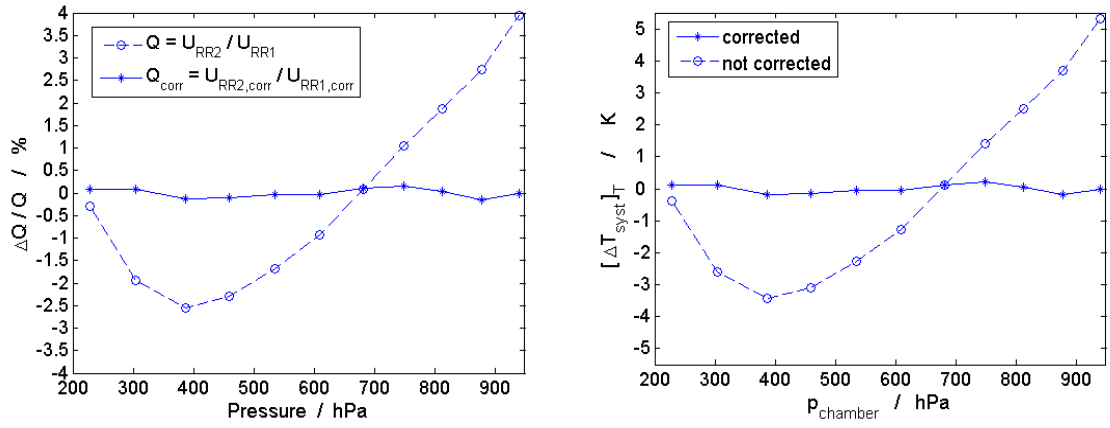

Figure 8.2-5. Left: Relative deviation $\Delta Q / Q$ for Q and Q_{corr} when either using the original RR signals U_{RR1} and U_{RR2} or the corrected ones $U_{RR1,corr}$ and $U_{RR2,corr}$. With the linearity correction: Q_{corr} < 0.16 %. Right: Q inserted into the temperature calibration function T_{calib} and thus transferring the deviations ΔQ into deviations of temperature $[\Delta T_{syst}]_T$. With the linearity correction function: $[\Delta T_{syst}]_T$ < 0.22 K.

The temperature measurement error $[\Delta T_{syst}]_T$ as a function of the air pressure $p_{chamber}$ for a constant air temperature $T_{chamber}$ (indicated by index T) is defined using the temperature calibration function by

$$\left[\Delta T_{syst}\right]_T = T_{calib} - \overline{T}_{calib} \quad , \tag{8.2.4}$$

where $\overline{T}_{calib}$ is the mean measured temperature. $[\Delta T_{syst}]_T$ is shown in Figure 8.2-5 (right). Applying the linearity correction function, the deviation of the measured temperature can be reduced from $[\Delta T_{syst}]_T$ < 5.5 K to < 0.22 K.

In an analogous way as for temperature measurements, Figure 8.2-6 shows how much the density measurements deviate due to non-linearity of the detector response. The density measurement error $[\Delta N_{syst}]_T$ due to systematic nonlinearities of detector response is defined by

$$\left[\Delta N_{syst}\right]_T = \frac{N_{calib} - d \cdot p_{chamber}}{d \cdot p_{chamber}} \quad . \tag{8.2.5}$$

d is a fit constant and is chosen in such a way that the straight $d \cdot p_{chamber}$ deviates least form N_{calib}. No deviation from this straight would denote a perfectly linear response. With the applied linearity correction, the deviations due to nonlinear detector response is reduced from $[\Delta N_{syst}]_T$ < 0.9 % to < 0.36 %. As explained, this residual error could have its source in the accuracy limit of the pressure probe of the atmospheric simulator. Moreover, the mentioned correlation of the RR signals affects the density measurement more than the temperature measurement.

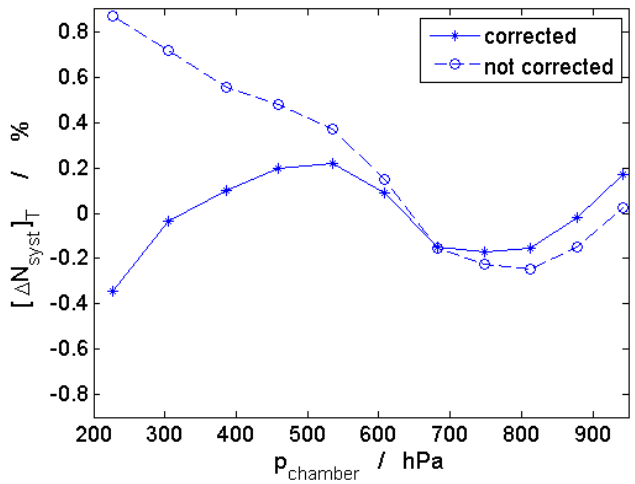

Figure 8.2-6. Same as Figure 8.2-5 (right) but for air density measurements. With the linearity correction: $[\Delta N_{syst}]_T$ < 0.36 %.

Figure 8.2-7 illustrates the same for pressure measurements in an analogous way. The systematic pressure fluctuations $[\Delta p_{syst}]_T$ are calculated by substituting N_{calib} by p_{calib} in eq. (8.2.5).

With the linearity correction, the pressure measurement deviations can be reduced from < 1.25 % to < 0.31 %. It has to be noted that the measurement deviations generated by the detector nonlinearities are pure technical errors. They are neither errors which are inherent to the measurement principle nor errors which are the result of inexact calibration functions.

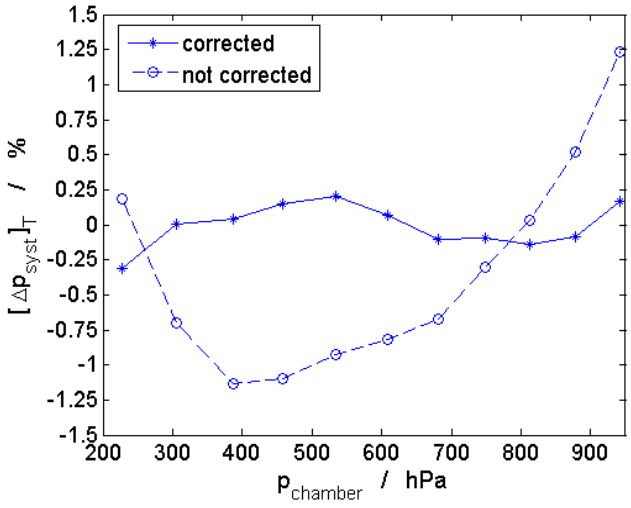

Figure 8.2-7. Same as Figure 8.2-5 (right) but for air pressure measurements. With the linearity correction: $[\Delta p_{syst}]_T < 0.31$ %.

8.2.3 Discussion on systematic errors

In sect. 8.2.1 the systematic errors $[\Delta T_{syst}]_p$, $[\Delta N_{syst}]_p$ and $[\Delta p_{syst}]_p$ were determined as a function of air temperature $T_{chamber}$. The air pressure $p_{chamber}$ was constant, since the vacuum tube was left opened. This has two advantages. First, the big chamber fan is circulating the air mass also inside the vacuum tube, to obtain a maximally constant and homogeneous temperature field inside the measurement volume. Second, errors coming from tube pressure variations and its measurement are avoided. Such errors can be e.g. leakage of external air into the tube, nonlinearities of the photo detectors of the RR channels, and measurement errors of the reference vacuum gauge. The issues linked with the pressure measurement were discussed in sect. 8.2.2. There, the sources of the residual errors could be spotted and are, in the first instance, the non-linear response of the used APD detectors in both RR channels. For those APDs, the applied correction principle, notably represented by the respective linearity correction functions, was described. The residual errors after the linearity correction were attributed to the reference pressure measurement system, which has an accuracy matching these residual errors. In the following, those systematic errors are discussed which cannot be precisely attributed to one error source only. These systematic errors primarily are dominant for measurements done in air of different temperature like those described in sect. 8.2.1.

Figure 8.2-1, Figure 8.2-2 and Figure 8.2-3 in sect. 8.2.1 show $[\Delta T_{syst}]_p$, $[\Delta N_{syst}]_p$ and $[\Delta p_{syst}]_p$ for one data-set. Other data-sets confirm these results with regard to the obtained maximum errors. However, in other data sets, the maximum error peaks appear at various temperatures (not always at 285 K). It can thus be concluded that $[\Delta T_{syst}]_p$, $[\Delta N_{syst}]_p$ and $[\Delta p_{syst}]_p$ are determined by random systematic effects coming e.g. from the experimental setup or instabilities of the experimental conditions and not by systematic deviations of the calibration function itself. Since 1000 signal pulses recorded at each temperature value are averaged, fluctuations of experimental parameters on the timescale of seconds are averaged and do not play a role. The measurement errors shown in Figure 8.2-1 (right) are assigned to fluctuations on the timescale of minutes taking place between two measurements during the heating process of the vacuum tube from one temperature value to the subsequent. The duration of such a whole calibration run shown in Figure 8.2-1 is around 120 min.

According to the calculations from sect. 7.1, temperature drifts of the RR filters or drifts of the laser wavelength could be the cause for systematic measurement errors of the magnitude found for $[\Delta T_{syst}]_p$, $[\Delta N_{syst}]_p$ and $[\Delta p_{syst}]_p$. E.g. drifts of the RR interference filter CWLs by only about 0.2 pm due to varying filter temperature by 0.1 K during the experiment, or laser wavelength drifts of the same magnitude, are calculated to lead to temperature measurement errors of around 0.05 K. It should be remarked, that during the experiments, the laboratory air temperature varied even by about 0.5 K - 2 K, due to waste heat of the atmospheric simulator. Thus, temperature variations of the interference filters of 0.1 K could realistically be generated. In terms of signal intensities, wavelength drifts of 0.2 pm correspond to a change of the RR signal amplitudes of up to 0.03 %.

Another potential systematic error source could be the highly temperature sensitive gain of the RR APD detectors. Although the APDs are actively temperature stabilized, temperature fluctuation cannot be fully excluded. The used APDs (*Laser Components:* SAR3000) have a relatively large indicated temperature drift coefficient of 2 V / K for very high gains near the breakdown voltage. Assuming a temperature fluctuation inside the APDs of 0.1 K would then even lead to a signal amplitude variation on the order of 0.3 %, and thus to ten-fold larger errors than for in the case of temperature drifts of the interference filters or the laser. This entails that the APDs have to be temperature stabilized to better than 0.01 K. Since such high temperature stability is difficult to guarantee, this issue indeed could be a major systematic error source.

A further potential error source is the changing temporal shape and thus the changing frequency spectrum of the emitted laser pulses (see Figure 8.1-2). The electrical RR pulse peaks are extracted after filtering with the 10 MHz AC high-pass filter integrated into the APDs and after digital low-pass filtering with 50 MHz. Generally, frequency filtering always leads to different signal peak values for pulses with equal energy but different pulse shapes. This is because a different fraction of the varying pulse spectra and thus different energy amounts are filtered out. Generally, a laser monitoring PIN detector is used to account for changes in the detected signal pulse energy coming from the laser. However, since the DC PIN detector has a totally different frequency response than the APDs, it can be only used for cancellation of variations of the emitted laser pulse energy but not for the cancelation of variations in the emitted laser pulse shape. The instable laser emission concerning the temporal laser pulse shape leads thus to further systematic errors.

An inhomogeneous temperature field inside the temperature chamber can be rather excluded as a possible error source. The fan of the temperature test chamber generates a continuous circulation of the chamber air, so that small temperature fluctuations average out during the measurements. Errors

coming from the reference temperature measurement equipment can be excluded as well. Their temperature measurement repeatability is much better than the obtained optical systematic errors.

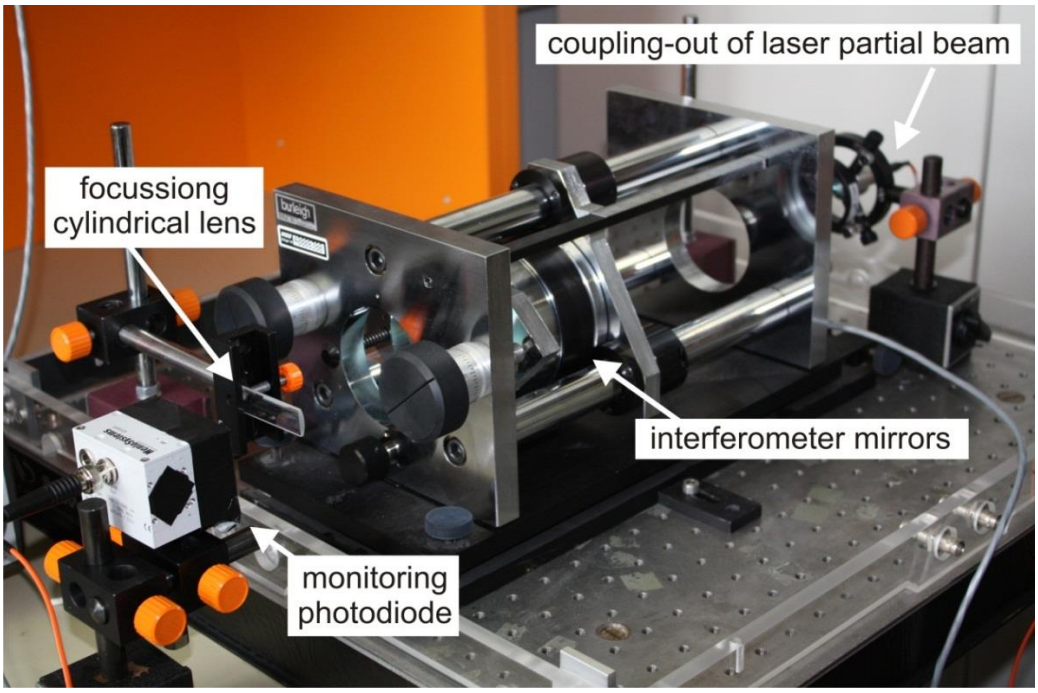

Figure 8.2-8. Fabry-Perot interferometer used to quantify the drift of the laser emission wavelength.

In order to find out whether a laser wavelength drift could be the source of the RR signal fluctuations, the emission wavelength of the laser was monitored over a period of 100 minutes by two different means: First, with an actively controlled Fabry-Perot interferometer (FPI; *Burleigh*: RC-170 with RC-690 mirrors; Figure 8.2-8), second, by measuring the change of the detected signal amplitude in the elastic channel CP. The filter in that channel was adjusted in such a way, that the laser emission spectrum was located on the spectral filter slope (see sect. 8.1.1). A drift measurement with a wavelength meter (*Coherent*: WaveMaster), which had the necessary precision, was not possible. Here, the broad laser resonator mode spectrum being further modified by the frequency doubling process of the laser fundamental wavelength could not be handled by the wave meter. During the measurements with the FPI, the air temperature and the pressure inside the vacuum tube were constantly those of the laboratory, so that the detected signal changes could have their only origins either in an evoked change inside the hardware components of the measurement apparatus or in a change of the analyzing equipment, i.e. the FPI or the channel CP.

The Fabry-Perot interferometer had a finesse of 70 and a free spectral range set to 88 pm. Before the emission wavelength measurement, the laser heated up for one hour to ensure maximum thermal stability. The monitoring was done by separating a partial beam from the laser output and guiding it through the FPI (see Figure 6.3-2). First, the geometric shift of the generated fringe pattern was measured with the help of a photodiode. Then, the change of the laser wavelength was quantified using the free spectral range and the general FPI transmission function. The change of the fringe

pattern was finally compared to the output signals of the RR channels and the elastic channel CP to find correlations. For the laser drift measurements with the elastic filter CP, the edge of its spectral transmission curve was collocated with the laser emission spectrum. Thus, relative drifts of the filter transmission curve and the laser spectrum resulted in a change of the detected signal amplitude. The laser drift was then calculated knowing the steepness of the edge of the filter transmission curve. The absolute transmission on that edge was measured to change by 264 % per nanometer.

The results of the wavelength drift measurements using both methods are shown Figure 8.2-9. The absolute drift values are largely differing. With the elastic channel a wavelength change of maximally 1.1 pm was measured whereas for the FPI the maximum value was 2.6 pm. However, it should be kept in mind, that these measurements are associated with a relative high degree of uncertainty, because the measured drift values are very small. Due to this smallness, minor changes of the experimental conditions could already generate relatively large measurement errors. For example, the measured change of the laboratory room temperature of 0.2 K during this experiment could lead to a spectral drift of the elastic filter by as much as 0.4 pm (temperature drift coefficient is 2 pm / K; see Table 6.4-1). The wavelength measurements with the FPI represent no absolute reference as well, but are also prone to the laboratory temperature variation. Additionally, the FPI measurements had to be done at a low free-spectral-range of the FPI of 88 pm, generating a fringe pattern with relatively moderate resolution. This turned an accurate determination of the laser wavelength drift difficult and led to errors of the same magnitude as the determined laser wavelength drift. In spite of these difficulties in quantitatively measuring the right laser wavelength drift, a correlation between the laser wavelength change measured with the two different means can be seen. This is seen as evidence of a real wavelength drift.

Simultaneously to this analysis, the signals in the channels RR1, RR2 and CP were checked for correlations and anti-correlations between each other. However, here, in the very most cases no correlations were found. Especially an anti-correlation of the signals in RR1 and RR2, which is necessarily generated by a laser wavelength drift, could not be found. The signals in the RR channels rather seemed to fluctuate randomly and independent from each other. For these observations, gain fluctuations of the APDs caused by thermal instability could give an explanation as well. Finally, the lack of correlation could be an indicator for a multicausal or a combination of error sources leading to the resulting systematic measurement errors.

Although the magnitudes of the systematic errors $[\Delta T_{syst}]_p$, $[\Delta N_{syst}]_p$ and $[\Delta p_{syst}]_p$ are astonishingly small for the measurements with the designed measurement apparatus, further effort must be made to eliminate residual errors sources, in order to fulfill the very demanding measurement accuracy requirements (see sect. 2). This is even more important for operation in the harsh environment of an aircraft. While the stability of the apparatus is sufficient for the calibration of the temperature, density and pressure measurement, a further improvement of the long term stability will be advantageous for preservation of the calibration. The unambiguous identification of the origins of the RR signal amplitude fluctuations was very difficult with the disposable equipment regarding the smallness of the systematic changes. Nevertheless, recommendations for improving the measurement stability can be given, based on the results of this section: First, an active stabilization of the laser system or at least injection seeding or a master-oscillator-power-amplifier laser configuration will be beneficial. If sect. 7.1 is taken as calculation basis, the laser wavelength stability has to better than 1 pm. Second, temperature insensitivity of the whole apparatus has to be increased. This particularly necessitates a temperature stabilization of the interference filters by better than 0.5 K, e.g. by means of

a thermal housing. Since the APD detectors in the RR channels are highly temperature dependent as well, here, a thermal stabilization is also of fundamental importance. Assuming a temperature coefficient of 0.4 V / K, stabilization within as low as 0.05 K will be necessary.

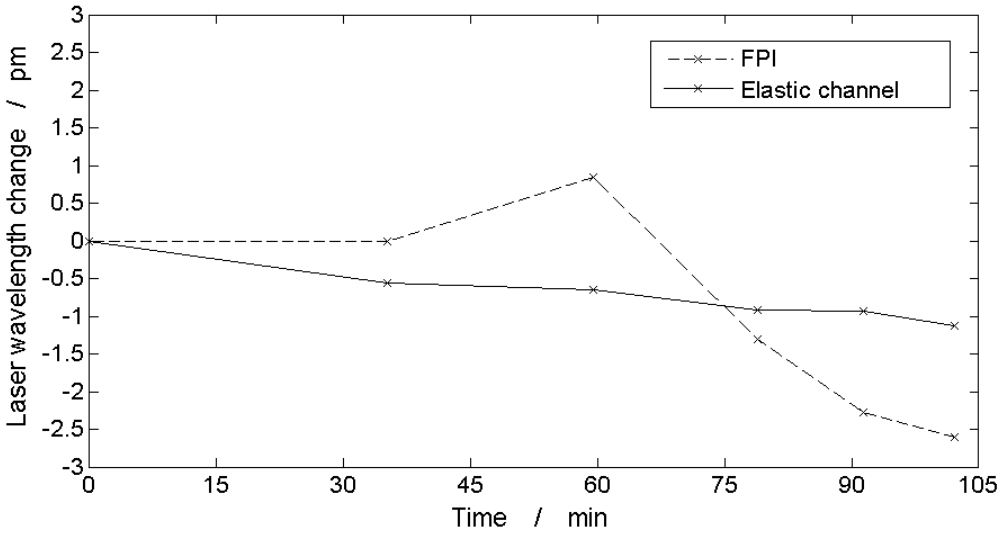

Figure 8.2-9. Measured wavelength change of the laser emission wavelength using the high performance FPI (Figure 8.2-8) and using filter CP with the filter edge tuned to the laser emission wavelength.

8.3 Analysis of statistical measurement uncertainties

The statistical measurement uncertainties for temperature ΔT, for density $\Delta N / N$ and for pressure $\Delta p / p$ are obtained experimentally by determining the standard deviation of the distribution of a series of measured signal pulses. The measurement uncertainties are regarded as a measure for the repetitiveness of a parameter value (temperature, density or pressure) in subsequent measurements in the sense of a measurement precision. The parameter values are yield by inserting the recorded, low pass-filtered, normalized to the laser pulse energy, and linearity-corrected (see sect. 8.1.1 and 8.2.2) signal peaks U_{RR1} and U_{RR2} into the respective calibration function T_{calib}, N_{calib} or p_{calib} (see sect. 8.2.1). Residual systematic errors obtained after these correction procedures and other systematic errors are not comprised in the measurement uncertainties.

8.3.1 Optimum spectral RR-filter positions and detector gains

In order to reach the smallest statistical measurement uncertainties, the theoretically optimum CWLs of the RR interference filters for the measurement setup used herein were calculated in sect. 7.5. Now, in this section, the experimental results are described obtained from the analysis of 1000 signal pulse peaks U_{RR1} and U_{RR2} detected for each CWL pair. In general, the respective optimum CWLs for air

temperature, density and pressure measurements are a function of the air temperature, since the RR spectrum has different widths at different temperatures. The uncertainties at four air temperatures ranging from 238 K to 308 K were examined. The vacuum tube was left opened, so that the pressure $p_{chamber}$ = 963 hPa inside the tube was equal to the air pressure of the laboratory. A pulse energy of the laser beam inside the vacuum tube of 118 mJ could only be reached, instead of the nominal value of 200 mJ (cf. sect. 6.1). Figure 8.3-1 illustrates the 1-σ standard deviations of the measurement uncertainties ΔT, ΔN / N and Δp / p obtained when determining T, N and p from one single signal pulse. The uncertainties are plotted as a function of the CWL of filter RR2, which was varied from 527.8 nm to 529.0 nm in steps of 0.2 nm. The CWL of filter RR1 was kept fixed at 531.1 nm, since, first, the optimum CWLs of RR1 are much less temperature sensitive than the ones of RR2 (see Figure 7.5-1) giving little margin for uncertainty improvement. Second, the very important blocking of elastically scattered radiation of filter RR1 is very susceptible to wavelength changes due to the proximity of this filter to the elastic wavelength and does not permit a presumably advantageous CWL red-shift without increasing the amount of leaked elastic radiation.

In Table 8.3-1 the experimentally found optimum CWLs are compared to the theoretical ones, which are in good agreement to each other. It has to be repeated, that the existence of optimum CWLs for the measurement of temperature, density and pressure sources in a trade-off between those spectral positions, where the filtered signals are strongly temperature dependent and those positions, where the filtered signals are very intense. Therefore, the optimum CWLs for temperature measurements are located at the more temperature sensitive positions, which are further to the edges of the RR spectrum. Those for density measurements are located closer to the intensity peak of the RR spectrum. Differences between the experimental and theoretical optimum CWL values can be due to uncertainty sources not taken into account in the simulations like e.g. the oscilloscope quantization noise and differing noise characteristics of the APD detectors in the RR channels. For the experiments presented in the next sections, the CWLs were chosen to be 531.1 nm for filter RR1 and 528.6 nm for RR2. These CWLs are simultaneously optimum for measurements of temperature and pressure - the two parameters being important for aviation - within the temperature range of interest.

Table 8.3-1. Experimental vs. simulated optimum CWLs of filter RR2 (in nm).

Measured parameter	Experiment	Simulation
T	528.4 – 529.0	528.3 – 528.9
N	528.8 – >529.0	529.8 – 530.2
p	528.6 – >529.0	528.8 – 529.3

The APD gains of the detectors in channels RR1 and RR2 could not be optimized as described in theory, since a reading-off of the current gain values was not possible. Due to technical restraints, the range of possible APD gain values was limited by the following: Firstly, the gain had to be adjusted in such a way that the output signal voltages were matching the oscilloscope's input voltage range which was 1 mV to 5 V. That was already the case for relatively low APD gains. Secondly, the

lower gain bounds were set by values, which still permitted to use the full vertical scale and thus full resolving power of the oscilloscope, necessary to minimize the quantization noise. Thus, the output signal voltages ideally could not be smaller than ≈ 80 mV. Thirdly, the upper gain bounds were set by

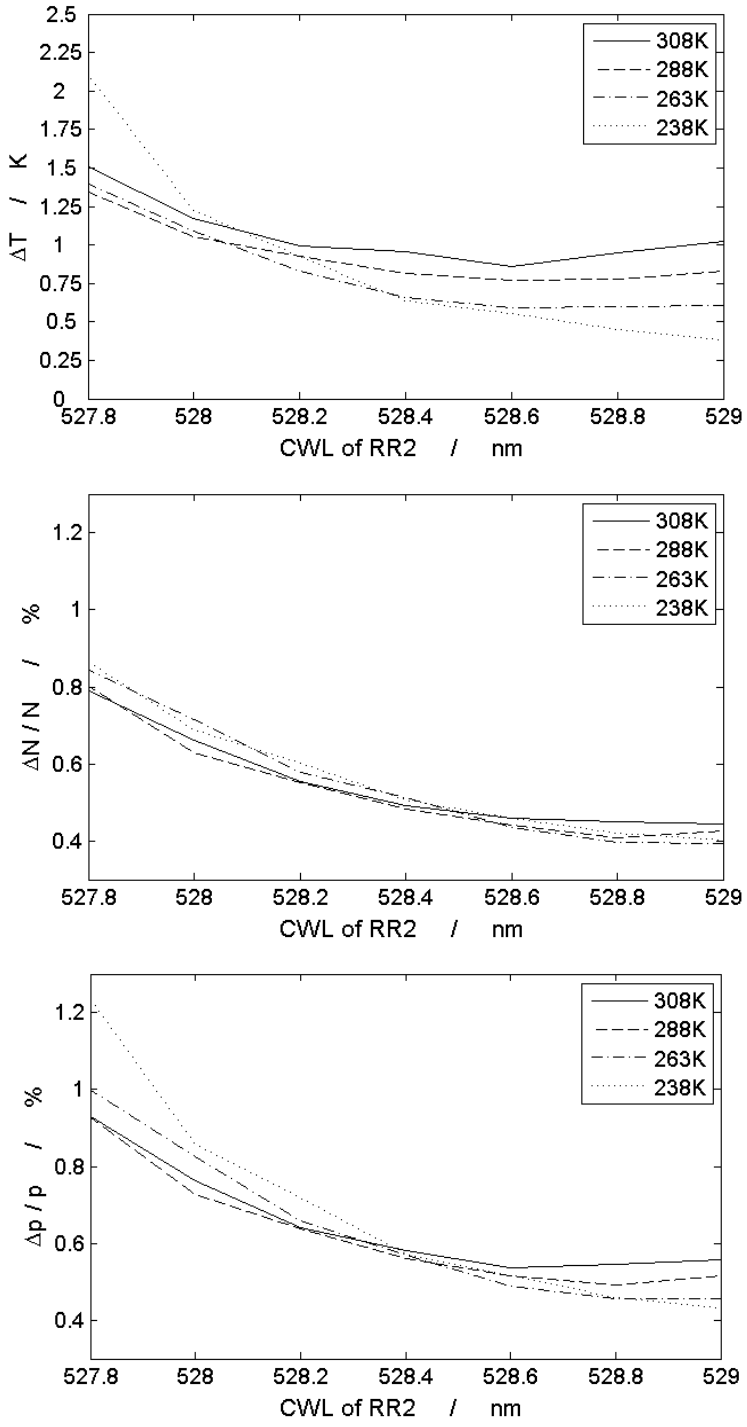

Figure 8.3-1. Statistical measurement uncertainties for temperature ΔT (top), density $\Delta N / N$ (center) and pressure $\Delta p / p$ (bottom). The lowest uncertainties are obtained at the optimum CWLs. For the key parameters temperature and pressure these are 531.1 nm for filter RR1 and 528.6 nm for filter RR2.

the maximally possible output voltage of the detector, which was ≈ 200 mV. Taking into account these facts and in consideration of the dynamic range of the signal pulse power caused by measurements in varying air densities (factor of 0.2 – 1 for RR1 and RR2) and air temperatures (factor of 1 – 1.2 for RR1 and of 1 – 1.7 for RR2) led to a sharp localization of the possible APD gains, which were adjusted and used for further measurement.

8.3.2 Comparison of uncertainties from computational model and experiment

In order to determine the measurement uncertainties ΔT, $\Delta N / N$ and $\Delta p / p$ also at lower molecular number densities present at higher atmospheric altitudes, measurements were done varying the pressure $p_{chamber}$ inside the vacuum tube. In contrast to the temperature altitude profile in the real atmosphere, the chamber temperature $T_{chamber}$ was kept constant for all pressures. This allowed good experimental reproduction and made repeated experiments comparable among each other. Because the statistical measurement uncertainty is clearly dominated by air pressure compared to air temperature, a disregard of the temperature influence does not lead to significantly different results. The experimentally obtained uncertainties were compared with the theoretical values from the simulations (sect. 7.5). The simulations were remade for this purpose taking into account the present experimental conditions and using the adjusted apparatus parameters, including the filter CWLs (531.1 nm for filter *RR1* and 528.6 nm for *RR2*) and the pulse energy of the laser beam (118 mJ). In these comparative computer simulations, solar background and effects appearing in dense clouds, like atmospheric extinction and elastic signal leakage, were disregarded as well.

Figure 8.3-2 illustrates the 1-σ values for ΔT for the detection of the backscatter of one single laser pulse. In order to be consistent, the data used for the plot are the same as those used for the plots in sect. 8.1.3 and for the analysis of the linearity of the detector responses (sect. 8.2.2): In total, 1000 signal pulses U_{RR1} and U_{RR2} are analyzed at each air pressure value $p_{chamber}$. $p_{chamber}$ is varied between 155 hPa and 940 hPa. The air temperature $T_{chamber}$ inside the atmospheric simulator is equal to the laboratory room temperature and constantly 298.95 K (25.8 °C). The actual air densities are proportional to $p_{chamber}$ and obtained via the ideal gas equation.

The measurement uncertainty of ΔT is defined as the 1-σ with of the distribution of ΔT_{calib}, which is obtained by inserting the measured signal pulses U_{RR1} and U_{RR2} into the temperature calibration function T_{calib} determined in sect. 8.2.1. For the determination of the optical temperature per each emitted laser pulse, ΔT is between 2.63 K at a pressure of $p_{chamber}$ = 155 hPa (present at an altitude of 13400 m [13]) and 0.75 K at a pressure of $p_{chamber}$ = 940 hPa (present at sea level). Comparing the computational simulations with these experimental results, the qualitative pressure (and thus density) dependence of the experimental values of ΔT is well described by the simulations. The magnitudes of the uncertainties exceed the simulated ones by a factor of only about 1.5.

Figure 8.3-3 shows the relative density measurement uncertainty $\Delta N / N = \Delta N_{calib} / N_{calib}$. With the current setup and the optimized filter settings, the 1-σ width of $\Delta N / N$ for one pulse detection is between 1.21 % at a pressure of 155 hPa (13400 m) and 0.43 % for 940 hPa (sea level). Here, the

statistical measurement uncertainties found in the experiment exceed the simulated ones by a factor of about 2.5.

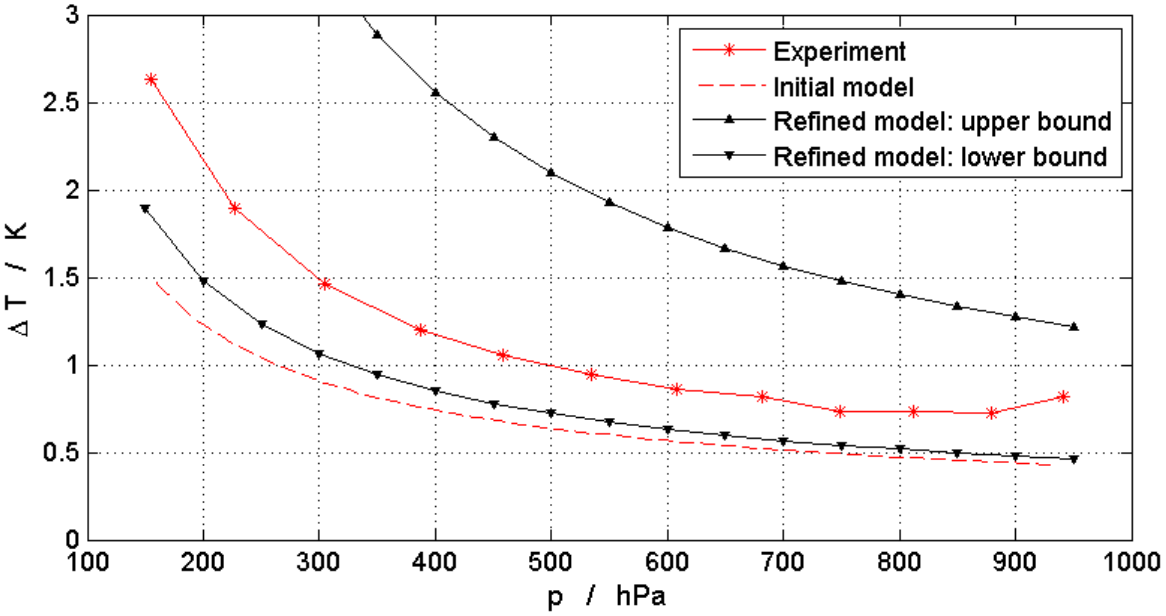

Figure 8.3-2. Experimental 1-σ temperature measurement uncertainties ΔT as function of air pressure when analyzing one single shot. Since the temperature is kept constant at 298.95 K (25.8 °C), the pressure variation is proportional to the air density. The slight uncertainty increase at the highest pressure value of 940 hPa is due to saturation effects inside the APD detector of channel RR2. Additionally, the uncertainties are shown calculated with the initial computational model as well as the refined model further discussed in sect. 8.3.3. Both models were adapted for the present experimental conditions to make all results comparable.

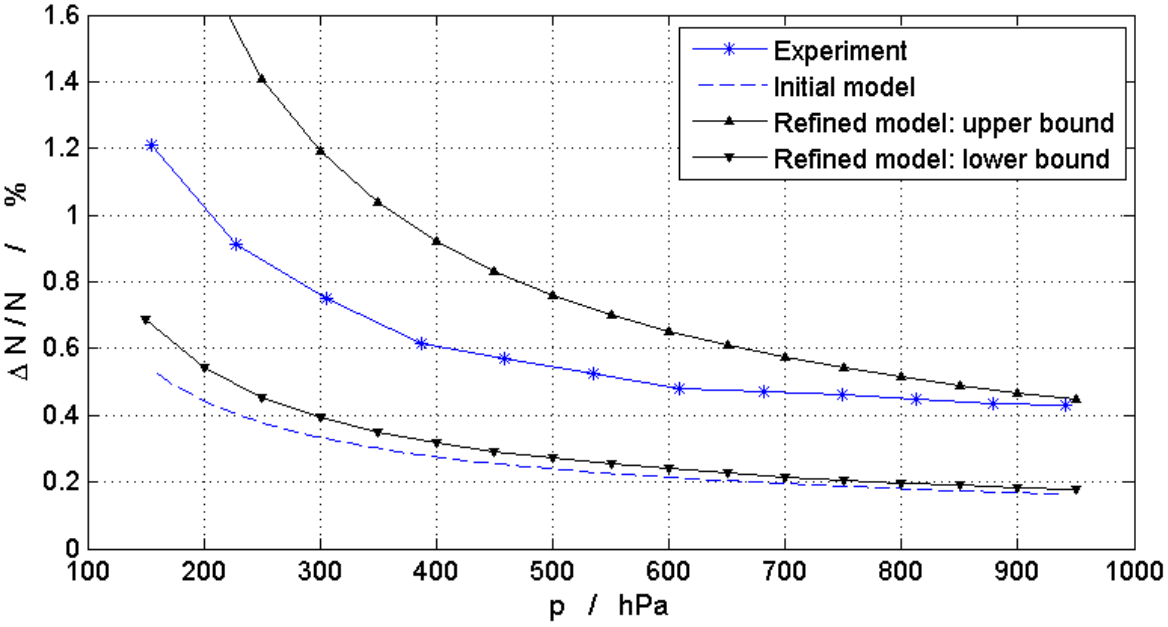

Figure 8.3-3. Same as Figure 8.3-2 but for density measurements.

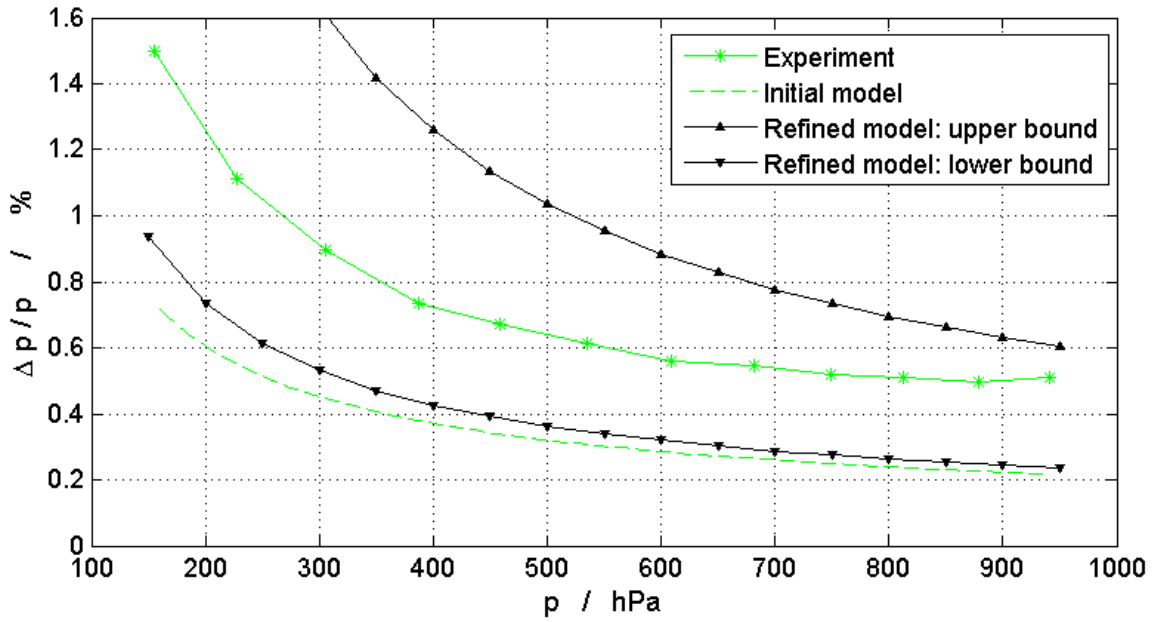

Figure 8.3-4. Same as Figure 8.3-2 but for pressure measurements.

The analogue consideration of the relative pressure measurement uncertainty $\Delta p / p$ is illustrated in Figure 8.3-4. The 1-σ width of $\Delta p / p$ for one pulse detection is between 1.50 % at a pressure of 155 hPa (13400 m) and 0.51 % for 940 hPa (sea level). Here, the statistical measurement uncertainties found in the experiment exceed the simulated ones by a factor of about 2.2.

8.3.3 Discussion on statistical uncertainties and refined computational model

Although the theoretical simulations describe the qualitative density and pressure devolution of the experimental measurement uncertainties ΔT, $\Delta N / N$ and $\Delta p / p$ well, the experimental uncertainties are larger by a factor of 1.5 to 2.5 than the simulated ones (sect. 8.3.2). This is an effect of the difference between the behavior of the idealized computer model including the assumptions made therein and the factual experimental conditions and parameters. The most important reasons leading to these discrepancies can be given:

The statistical uncertainties are directly linked with the pulse power detected in each RR channel. It was thus checked, whether these discrepancies could source in a difference between the simulated and experimentally detected optical pulse powers. The simulated optical peak pulse power P_{RR1} in channel RR1 for the laser pulse energy E_L = 118 mJ, the pulse length *fwhm* = 10 ns, a RR1 filter CWL of 531.0 nm, a vacuum tube pressure of 950 hPa and temperature of 295 K is found using eq. (7.3.1) and is $P_{RR1} \approx 35 \cdot 10^{-6}$ W. The experimental value for P_{RR1} for equal conditions in the atmospheric-simulator was measured in two different ways. First, by replacing the APD detector in

channel RR1 with a highly sensitive power meter (*Newport*: 835 Optical Power Meter). The thereby measured mean power was divided by the laser repetition rate of 10 Hz and the pulse length *fwhm* of 10 ns (taking also into account the Gaussian nature of the pulse by the factor 0.94; see eq. (7.3.1)) resulting in a peak pulse power of $P_{RR1} \approx 30 \cdot 10^{-6}$ W. Since the RR optical power falling onto the power meter is very small, the measured values fluctuated strongly. Additionally, the background had to be subtracted. The power of the background was on the same order of magnitude as the averaged signal itself, even in the almost dark laboratory.

The second way for measuring P_{RR1} consisted in directly using the APD detector in channel RR1. The APD was calibrated beforehand by generating an output voltage for a known optical input power. For this purpose, the pulse energy of a partial beam of the leaser was measured with an energy meter (*Coherent*: LabMax with sensor PM10), attenuated with 3 neutral density filters (*Schott*: NG-9 glass) by more than 10 orders of magnitude and then focused with a lens onto the APD. The exact transmission value for the neutral density filters needed for this calibration was also determined by two different means. First, by calculating their transmission from the datasheet and the thickness of the filter glass plates, second, by measuring the transmission value of each neutral density filter individually with another laser with equal emission wavelength. With the calibrated APD, the pulse power was determined to be $P_{RR1} \approx 20 \cdot 10^{-6}$ W and $\approx 25 \cdot 10^{-6}$ W, respectively. The simulated value $P_{RR1} \approx 35 \cdot 10^{-6}$ W is larger by about a factor of about 1.4 than the mean of the three experimental values which is $P_{RR1} \approx 25 \cdot 10^{-6}$ W. Thus, a difference of a factor of only $\sqrt{1.4} \approx 1.2$ between the simulated and experimental statistical uncertainties found in sect. 8.3.2 could be explained. However, it has to be noted here as well, that the measurement of very weak signals generally is very uncertain due to the individual uncertainties of the power / energy meters as well as the uncertainties of the determined optical transmissions of each of the used optical components, background light and environmental influences affecting the measurements. However, these results can be seen as an indication, that the experimentally measured signals in the RR channels are slightly weaker than the simulated ones.

A reason for the weaker experimental RR signals could be the AC high-pass filters inside the APD detectors filtering a significant part of the spectral power density at frequencies up to 10 MHz. Another important reason could be signal loss due to beam divergence or beam obstruction inside the receiver channels and the thereby generated shadowing effects, even though these effects were tried to be taken account of as good as possible in the simulations (cf. Figure 6.2-2). A resulting increase of the experimental uncertainties could also be partially attributed to insufficiently stable laser operation. In sect. 8.2.3, the changing predominant substructure of the temporal laser pulse shape (Figure 8.1-2) on a time scale of 10th of minutes was argued to be a possible cause for the increase of the systematic measurement errors. With the same reasoning, only on a shorter time scale, i.e. from shot to shot, these pulse shape variations could lead to an increase of the experimental statistical measurement uncertainties. Apart from the temporal pulse shape, also the laser pulse energy (i.e. the integral over the temporal pulse shape) is not stable from shot to shot, but may show variations of ±6 % from the mean value. These variations are monitored with the reference diode in order to normalize the recorded RR signal pulses to the laser pulse energy. However, since the monitoring of the laser pulse energy is also afflicted with uncertainty, this correction is not perfect but augments uncertainty as well.

Furthermore, noise components generated by the read-out electronics (as the oscilloscope quantization noise due to the digitizing of the analogue output signals of the photo detectors,

oscilloscope input amplifiers, etc…) have not been taken into account in the computational simulations. Neither are the effects of the further signal processing by the low-pass filtering (sect. 8.1.1). Thus, due to these different assumptions, discrepancies between simulation and experiment are unavoidable. At last, it has to be noted that noise components appearing at frequencies of a couple of tenth MHz and higher, as it is also the case here, are influenced by the exact electronic detector architecture and are difficult to simulate.

It was pointed out, that the exact knowledge of the detected optical pulse energies in the RR channels is crucial for the determination of the statistical uncertainties due to the physically inherent statistical nature of photonic signals. However, the computational modeling of the optical signal energies (see also sect. 6.2) is complex and cannot consider every influence present in practice. On the other hand, the experimental measurement of the optical signal energies for verification reasons is highly uncertain: The three measured optical pulse energies just described are differing by up to 20 % from the mean. In order to consider both circumstances, the model used in the computational simulations has been refined. On the one hand, the ratio between measured and simulated optical pulse energies was included into the computational model, giving a new calculation basis for the expected statistical measurement uncertainties. On the other hand, the uncertainty of 20 % for the measured optical pulse power has been included into the model as well. The simulation results of this refined computational model having now an upper and lower uncertainty bound are included into Figure 8.3-2, Figure 8.3-3 and Figure 8.3-4. With the refined model, the simulated and experimental statistical measurement uncertainties are always consistent within the mentioned borders.

8.3.4 Influence of water vapor measurement on statistical uncertainties

For the optical acquisition of the correct density and pressure of moist air, the water vapor concentration also has to be measured. This necessity had already been demonstrated in sect. 7.8. Thus, the influence of the water vapor measurement on the statistical measurement uncertainty of the total pressure of moist air was investigated experimentally as well.

Water can be injected inside the vacuum tube of the atmospheric simulator via a capillary tube (see sect. 6.3). To generate water vapor, the vacuum tube is totally evacuated so that the boiling point of the injected water is undershot and the water directly starts to evaporate after injection. In order to maximally diminish the laser stray light level for the optical measurements, the vacuum tube walls were manufactured with a rough black-painted surface. Unfortunately, this surface tended to adsorb a significant part of the injected water molecules. This effect was intensified when the tube pressure was raised by adding dry air into the tube. Hence, a multiple of the calculated water vapor saturation amount had to be injected inside the tube to install a high relative humidity. During the equilibration of the air inside the atmospheric simulator, the anti-reflection coatings of the tube windows, although being very dense due to the ion-aided coating deposition process, started to incorporate water vapor as well. During the first water vapor experiments, this led to coating damages caused by the laser beam spot on the window surfaces. Therefore, the water vapor measurements presented below were performed at the pressure generated by the water evaporation only, without addition of dry air. Moreover, it was ensured by tests, that the accuracy of the used humidity probe did not deteriorate at low operating pressures. For the water vapor measurements, a further change had to be made: a PMT

detector at very high gain (≈10^5) and characteristically very low quantum efficiency at 660 nm had to be used inside channel H_2O. This detector choice is not recommend by the performance calculations done in sect. 7.4 in terms of SNR. But the output voltages of the custom-made APD detector, which was designed for that purpose beforehand, turned out to be too small to be monitored with the used data acquisition equipment.

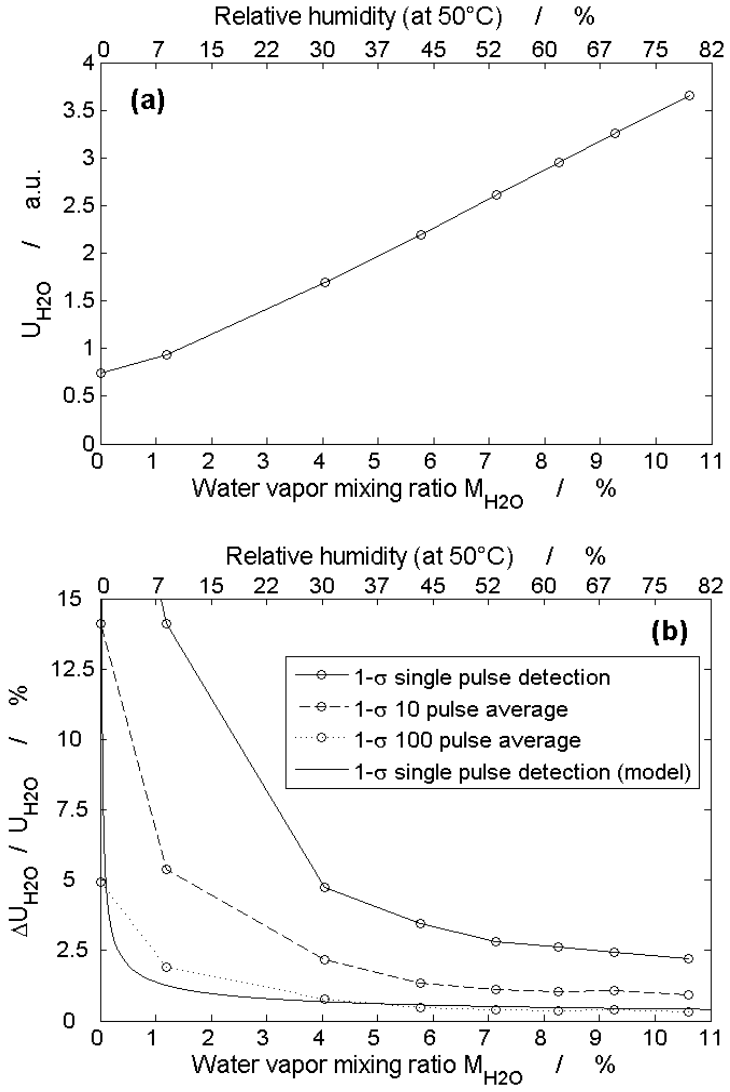

Figure 8.3-5 (a): Optical water vapor signal U_{H2O} in dependence on the water vapor concentration determined with the chamber relative humidity sensor at 50 °C for a dry air partial pressure of 1000 hPa. (b): Relative uncertainty $\Delta U_{H2O} / U_{H2O} = \Delta N_{H2O} / N_{H2O}$ in dependence of the measured water vapor mixing ratio M_{H2O}.

Figure 8.3-5 (a) shows the output signals U_{H2O} (which are also processed as described in sect. 8.1.1 and normalized to the laser pulse energy) of that PMT detector in channel H_2O as a function of the water vapor mixing ratio inside the vacuum tube. The amount of water vapor is measured as

relative humidity by the tube probe at a vapor temperature of $T_{chamber}$ = 50 °C. The relative humidity is converted using the Arden Buck equation [99] into the equivalent water vapor volume mixing ratio M_{H2O} taking a partial pressure of dry air of 1000 hPa as a basis. In Figure 8.3-5 (a) the mean of 1000 recorded signal pulses is plotted against different values of M_{H2O}. The detected water vapor signal U_{H2O} should be proportional to M_{H2O} (eq. (5.3.4)). However, it can be seen that the relation between U_{H2O} and M_{H2O} is not exactly linear. This nonlinearity comes from the vacuum tube humidity probe, which is not specified for measurements of relative humidity below 10 %. Additionally, there is an offset in the optical signal. This offset was supposed to come from an insufficient blocking of elastically scattered radiation at 532 nm in the channel H_2O. However, the serial connection of two interference filters in channel H_2O and additional insertion of high optical density long-pass filters proved this assumption to be false. Probably this offset has its origin in a fluorescence activity inside the water vapor interference filter or a leak of elastic light through the optics mounts in the channel.

The 1-σ relative uncertainties $\Delta U_{H2O} / U_{H2O}$ of the optical water vapor signal for single pulse measurements and for a 10- and 100-pulse-averaged measurements can be read off from Figure 8.3-5 (b) and amount 1.9 %, 0.8 % and 0.3 % at M_{H2O} = 10.6 %, respectively. For the calculation, the signal offset had already been removed beforehand. The 3-σ uncertainties are threefold larger. $\Delta U_{H2O} / U_{H2O}$ is equal to the relative measurement uncertainty of water vapor density $\Delta N_{H2O} / N_{H2O}$ itself (eq. (C.6)). The uncertainty of the water vapor measurement $\Delta N_{H2O} / N_{H2O}$ contributes also to the uncertainty of the total air density of moist air $\Delta N_{moist} / N_{moist}$. This additional measurement uncertainty is calculated by the square root of the right summand of eq. (C.5) and is plotted in Figure 8.3-6. The uncertainty contribution rises together with M_{H2O}. The worst case in terms of measurement uncertainty is attained for measurements in hot air at low altitudes, where M_{H2O} can reach the highest values. For the very high water vapor volume mixing ratio of 10.6 %, this uncertainty component is 0.22 % (1-σ) for single pulse detection. For 10- and 100-pulse-averaged measurements, the 1-σ values are 0.09 % and 0.03 %, respectively. Combining this additional uncertainty with the experimental uncertainties $\Delta N / N$ for dry air density measurements at sea level (sect. 8.3.2), will lead to an increase of the total density uncertainty for measurements in moist air with respect to dry air by maximally 20 %: E.g. comparing the additional uncertainty of 0.22 % (1-σ, single pulse detection) to $\Delta N / N = \Delta N_{dry} / N_{dry}$ = 0.43 % (1-σ, single pulse detection) from sect. 8.3.2, leads to $\Delta N_{moist} / N_{moist}$ being elevated by < 20 % with respect to $\Delta N_{dry} / N_{dry}$ only. The increase of pressure measurement uncertainty for measurements in moist air will be even lower and only maximally 13 % when using the mentioned values. This is due to the Gaussian uncertainty propagation.

In Figure 8.3-5 (b) and Figure 8.3-6 the experimental results are compared with values computed in the simulations (see also sect. 7.8.2). Again, the simulations were adapted for the specific measurement scenario present in this experiment. The simulated uncertainty values for $\Delta N_{H2O} / N_{H2O}$ are smaller by a factor of around 5. For the temperature and density and pressure measurements, the difference between theory and experiment was only 1.5 to 2.5 (see sect. 8.3.2). Apart from the arguments listed in sect. 8.3.3, this could be additionally explained by the fact, that a relatively inefficient PMT detector is used in channel H_2O, instead of the detector, which is recommended by the calculations in sect. 7.4. It has thus to be noted, that there is still much potential for improvement for the detection of water vapor by using e.g. a well-designed APD detector.

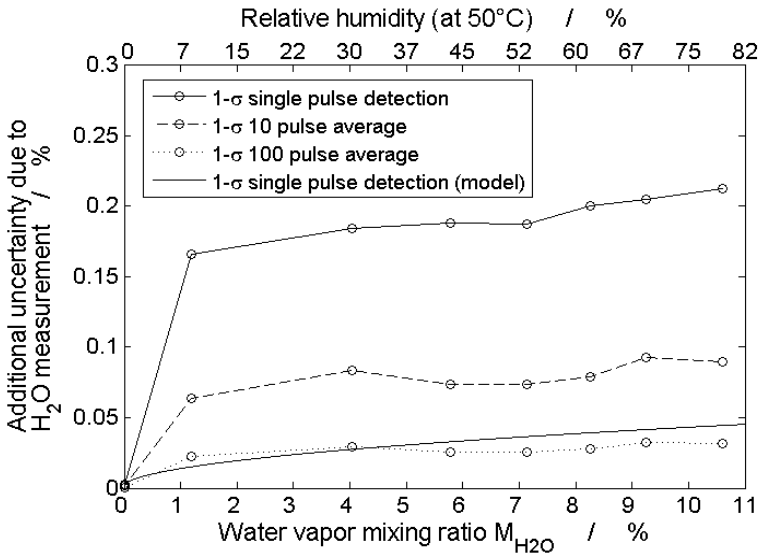

Figure 8.3-6. Additional uncertainty due to the measurement of water vapor to be added quadratically to the density measurement uncertainty of dry air.

8.4 Statistical measurement uncertainties as a function of flight altitude

8.4.1 Measured data

In order to check the performance of the measurement apparatus in more realistic atmospheric conditions, atmospheric scenarios encountered by aircrafts at different flight altitudes were generated with the atmospheric-simulation system. This was done in a similar way as in sect. 8.3.2, but varying both the air temperature and the air pressure. Additionally, the laser pulse energy was varied in order to analyze its influence on the measurement uncertainties. The vacuum tube air temperature $T_{chamber}$ and pressure $p_{chamber}$ was varied corresponding to ISA-altitudes [13] ranging from 500 m to 10300 m. At each virtual flight altitude 1000 values of U_{RR1} and U_{RR2} were recorded for laser pulse energies E_L varying from 12 mJ (10 % of the maximum laser output pulse energy) to 118 mJ (100 %). The different values of E_L were yield via a set of neutral density filters in front of the laser beam. First, the temperature, density and pressure measurements were calibrated with the recorded data. With the calibration and the standard deviations of the recorded pulses, the statistical measurement uncertainties ΔT, ΔN / N and Δp / p were determined both as a function of altitude and as a function of the laser pulse energy. The uncertainties were determined for the analysis of single pulses as well as for the analysis of the averages of blocks of every 10 or 100 consecutive pulses. The 1-σ uncertainties for the 100-pulse-average detection are illustrated in Figure 8.4-1 and the further analysis is concentrated on the 100-pulse-average detection. The uncertainties for single-pulse-detection and for 10-pulse-average detection are not shown. However, because the uncertainties proved to be proportional to 1 / $\sqrt{n}$ with n

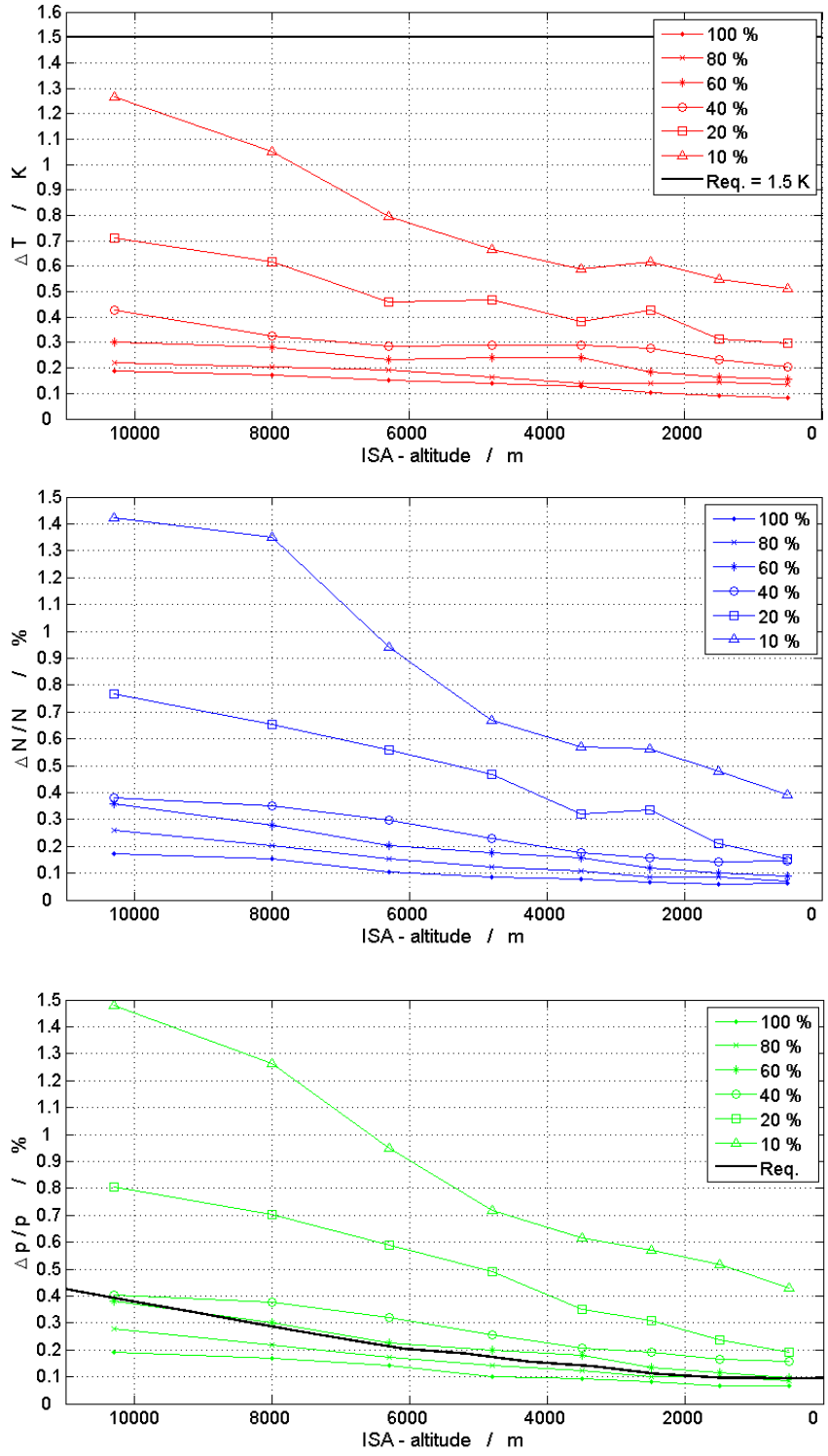

Figure 8.4-1. Results of the measurements performed with the atmospheric-simulation chamber. The plots illustrate the statistical measurement uncertainties ΔT (top), $\Delta N / N$ (center) and $\Delta p / p$ (bottom) as a function of measurement altitude for different laser pulse energies (100 % ≙ 118 mJ). The 1-σ uncertainties for 100-pulse-average detection are shown. For temperature and pressure measurements, the requirements set by the standard AS8002 (sect. 2) are indicated by black lines. For density measurements, no similar requirements are specified in the aviation standards.

being the number of averaged pulses, the uncertainty values for single-pulse-detection and 10-pulse-average detection can easily be calculated.

The altitude devolutions of the uncertainties shown in Figure 8.4-1 are not smooth, since it was difficult to exactly reproduce equal attenuations with the neutral density filter set for each altitude. Moreover, the laser output pulse shape and the measurement conditions, like the laboratory temperature, varied relative strongly, since the duration of the whole experiment was more than 12 hours. Due to the long total data acquisition time for this experiment, also the pressure leakage rate of the vacuum tube (around 0.1 hPa / min at a pressure of 200 hPa), especially at the high altitudes where pressure is low, perturbed the adjustment of equal atmospheric conditions. It has to be remarked, that the APD detector of channel RR1 sustained an electronic defect before this experiment. Although the detector could still be used, the noise was increased in the output. For example, this defect entailed an increase of the 1-σ standard deviation for the determination of the signal pulse power U_{RR1} of up to 40 % for measurements at sea level. Additionally, the experimental uncertainties ΔT, ΔN / N and Δp / p increased by around 20 % at sea level.

In Figure 8.4-1 (top) the accuracy measurement requirements for temperature and pressure for civil aviation (sect. 2) are indicated as well. For temperature measurements, the 1-σ statistical uncertainties for 100-pulse-averaged measurements (Figure 8.4-1 top) undershoot these accuracy requirements even when only using 10 % (≈ 12 mJ) of the pulse energy of the laboratory laser. For pressure, a pulse energy of 60 % (≈ 71 mJ) of the laboratory laser is required for the achievement of the necessary accuracies (1-σ, 100-pulse-average).

8.4.2 General uncertainty functions

With regard to the flight critical air parameters temperature T and pressure p and their experimental measurement uncertainties ΔT and Δp / p, three dependencies were derived:

1) The exact pulse energies needed at each flight altitude in order to diminish the 1-σ measurement uncertainties below the maximum allowable errors set by the aviation requirements (see sect. 8.4.3).
2) Extrapolation of the uncertainties to higher laser pulse energies and thus the calculation of the laser pulse energies necessary to meet the accuracy requirements also with 3-σ measurement uncertainties (see sect. 8.4.3).
3) Calculation of the necessary laser pulse energies also for other laser wavelengths to be used (see sect. 8.4.4).

For this, a general uncertainty function ΔX_{stat} was set up describing ΔT and Δp / p, respectively, in an accurate way. The general uncertainty function ΔX_{stat} of an optical signal X is dependent on the detected optical pulse energy E_{det}:

$$\Delta X_{stat} = \frac{\Delta X}{X} = \frac{\sqrt{(\Delta A)^2 + (\Delta B(E_{\mathrm{det}}))^2}}{X} \quad . \tag{8.4.1}$$

The first summand ΔA describes the contribution of those uncertainty components which are independent on E_{det}. The magnitude of ΔA is set by permanent noise sources, which are even present when the laser is turned off. Examples for such noise sources are the detected background radiation and noise introduced by detector electronics (cf. Appendix B) or by the data acquisition like quantization noise. The second summand ΔB describes the contribution of the uncertainty components, which are only dependent on E_{det} and thus governed by Poisson statistics. Because both uncertainty components are statistically independent from each other they are added quadratically according to the Gaussian uncertainty propagation law. ΔA_0 and ΔB_0 are defined as the values for $E_{det,0}$. The latter is the detected pulse energy when using the maximum laser pulse energy $E_{L,0}$ = 118 mJ (100 %) at the lowest experimental measurement altitude of 500 m (cf. sect. 8.4.1). Then it can be written

$$\Delta X_{stat,0} = \frac{\sqrt{(\Delta A_0)^2 + (\Delta B_0)^2}}{X_0} \quad . \tag{8.4.2}$$

If $E_{det,0}$ changes by a factor n_E, X_0 will do so as well. The uncertainty contribution ΔA does not change, whereas ΔB increases by $\sqrt{n_E}$ according to Poisson statistics yielding

$$\Delta X_{stat} = \frac{\sqrt{(\Delta A_0)^2 + \left(\sqrt{n_E}\,\Delta B_0\right)^2}}{n_E X_0} = \frac{\sqrt{\left(\frac{1}{n_E}\Delta A_0\right)^2 + \left(\frac{1}{\sqrt{n_E}}\Delta B_0\right)^2}}{X_0} \quad . \tag{8.4.3}$$

In the experiment, the detected pulse energy E_{det} can change due to change of the laser pulse energy E_L or due to air density change inside the tube $N_{chamber}$. n_E can be written as $n_E = E_L / E_{L,0} \cdot N_{chamber} / N_{chamber,0}$, with $N_{chamber,0}$ being the density at 500 m. If this functional dependence is inserted into eq. (8.4.3), and if $\Delta A'_0 = \Delta A_0 / X_0$ and $\Delta B'_0 = \Delta B_0 / X_0$ this results in:

$$\Delta X_{stat} = \sqrt{\left(\frac{E_{L,0} \cdot N_{chamber,0}}{E_L \cdot N_{chamber}}\Delta A'_0\right)^2 + \left(\sqrt{\frac{E_{L,0} \cdot N_{chamber,0}}{E_L \cdot N_{chamber}}}\Delta B'_0\right)^2} \quad . \tag{8.4.4}$$

For each measurement altitude, the 1-σ uncertainties ΔT and Δp / p measured in sect. 8.4.1 can be plotted as function of E_L, respectively, and the function ΔX_{stat} can be fitted to the experimental data to obtain the fit constants $\Delta A'_0$ and $\Delta B'_0$. For the fits to the temperature data, ΔX_{stat} has to be multiplied with $T_{chamber}$, since the measured temperature uncertainties ΔT are absolute values, whereas ΔX_{stat} denotes a relative uncertainty. The fits for 100-pulse-averaged measurements are shown in Figure 8.4-2 and the fit constants $\Delta A'_0$ and $\Delta B'_0$ obtained at each altitude for ΔT and Δp / p respectively, are plotted in Figure 8.4-3. Since E_L is known and the change of $N_{chamber}$ with altitude is accounted for, the values for $\Delta A'_0$ and $\Delta B'_0$ for ΔT and Δp / p, respectively, would not change with altitude, if also the temperature dependence of the measured uncertainties would be accounted for by the function ΔX_{stat}. This is not the case, so that theoretically $\Delta A'_0$ and $\Delta B'_0$ - although practically negligibly - vary with the

measurement altitude. Since there are relatively large fluctuations in the determination of the values of $\Delta A'_0$ and $\Delta B'_0$ (see Figure 8.4-3), this weak temperature dependency is masked anyway. Hence, for the setup of ΔX_{stat} for temperature and pressure, the average values of these constants were taken, respectively. By taking these average values, the uncertainty of ΔX_{stat} itself is minimized on the expense of a physically correct account of its (practically negligible) temperature dependency.

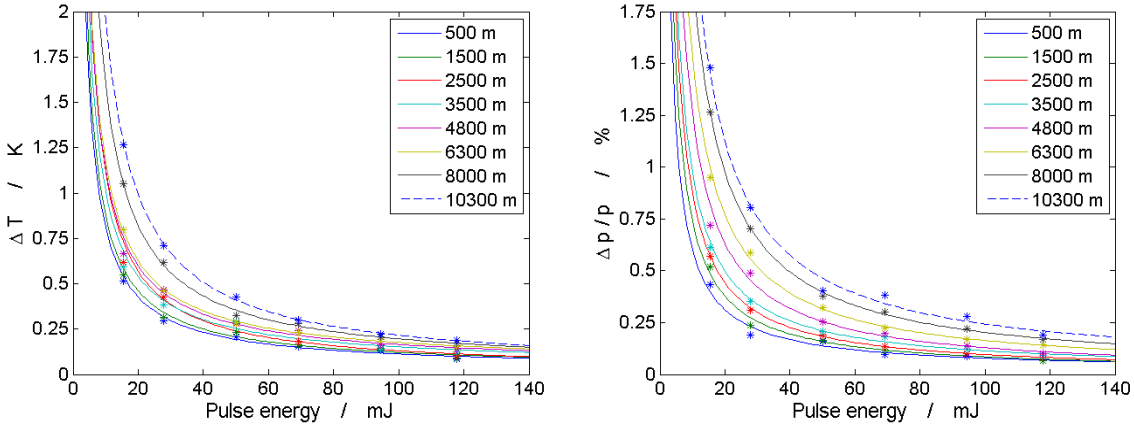

Figure 8.4-2. Dots: Statistical measurement uncertainties ΔT (left) and $\Delta p / p$ (right) as a function of different laser pulse energies E_L and different measurement altitudes. The data used in this figure are the same as those in Figure 8.4-1. Solid lines: Uncertainty functions ΔX_{stat} for temperature and pressure measurements, respectively, obtained via fits to these data.

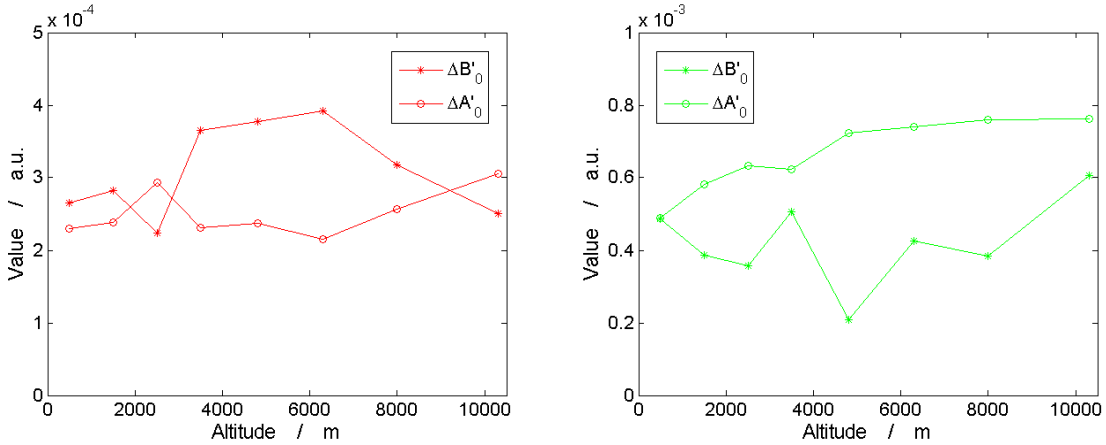

Figure 8.4-3. Fit constants of the fits of ΔX_{stat} shown in Figure 8.4-2 made for the different altitudes for temperature (left) and pressure measurements (right). Their average values over all altitudes, denoted as $\Delta A'_{0,T}$ and $\Delta B'_{0,T}$ for temperature and $\Delta A'_{0,p}$ and $\Delta B'_{0,p}$ for pressure, are used to form the general uncertainty functions $\Delta X_{stat,T}$ and $\Delta X_{stat,p}$.

In the following, these general uncertainty functions are denoted as $\Delta X_{stat,T}$ for temperature measurements with the averaged fit constants $\Delta A'_{0,T}$ and $\Delta B'_{0,T}$ and $\Delta X_{stat,p}$ for pressure measurements with the averaged fit constant $\Delta A'_{0,p}$ and $\Delta B'_{0,p}$. Analogously to the setup of the functions $\Delta X_{stat,T}$ and

$\Delta X_{stat,p}$, which describe the 1-σ uncertainties of 100-pulse-averaged measurements here, the same procedure can be repeated to obtain similar functions, which describe the 1-σ uncertainties of single-pulse and 10-pulse-averaged measurements, respectively. The functions describing 3-σ uncertainties are just the threefold of the ones for 1-σ.

8.4.3 Required laser pulse energies at 532 nm

With the functions $\Delta X_{stat,T}$ and $\Delta X_{stat,p}$, which were set up individually for ΔT and Δp / p in sect. 8.4.2 on the basis of the experimental data, the exact laser pulse energies $E_{L,min}$ can be calculated, which are necessary to reduce the temperature and pressure measurement uncertainties below the maximum allowable errors for aviation ΔT_{max} and Δp_{max} defined in sect. 2. The values for $E_{L,min}$, if regarding 1-σ measurement uncertainties, are yield by solving the inequations $\Delta X_{stat,T}(E_{L,min}) < \Delta T_{max}$ or $\Delta X_{stat,p}(E_{L,min}) < \Delta p_{max}$, respectively. For 3-σ uncertainties, the following inequations have to be solved: $3 \cdot \Delta X_{stat,T}(E_{L,min}) < \Delta T_{max}$ or $3 \cdot \Delta X_{stat,p}(E_{L,min}) < \Delta p_{max}$.

Figure 8.4-4 (top; solid lines) shows the results for $E_{L,min}$ for 100-pulse-averaged temperature measurements. Since ΔT_{max} = 1.5 K is constant for all measurement altitudes, the necessary laser pulse energies $E_{L,min}$ increase with altitude being maximum at the highest altitude of 10300 m (worst case scenario for temperature measurements). This is evident, since the measurement uncertainties increase with altitude as well due to falling molecular air density. The rising uncertainty has to be countered then by an increase of laser pulse energy. In order to stay below ΔT_{max}, $E_{L,min}$ has to be larger than 11 mJ (35 mJ) for 1-σ (3-σ) 100-pulse-averaged measurements.

Figure 8.4-4 (top; dashed lines) also shows the required pulse energies for the case that the noise components, which do not depend on the laser power and are described by $\Delta A'_{0,T}$ (see sect. 8.4.2), can be further decreased: If $\Delta A'_{0,T}$ is reduced to 25 % of the present value, the necessary pulse energies considering 3-σ uncertainties drop by around 65 %. This drop is significant and it shows the importance as well as the remaining potential of the measurement apparatus in reducing the measurement uncertainties by using further improved detection and data acquisition equipment.

Figure 8.4-5 (top; solid lines) illustrates equivalently the necessary values $E_{L,min}$ for pressure measurements as function of measurement altitude. In contrast to the temperature measurements, the highest pulse energies are needed for measurements close to sea level (worst case scenario for pressure measurements), since here, the maximally allowable errors are lowest ($\Delta p_{max} \approx 0.1$ %) and thus most challenging. In order to stay below Δp_{max}, $E_{L,min}$ has to be larger than 95 mJ (355 mJ) for 1-σ (3-σ) 100-pulse-averaged measurements.

Comparing Figure 8.4-5 with Figure 8.4-4 (top; dashed lines) it can be seen as well, that the laser power independent noise components defined by $\Delta A'_{0,p}$ have less influence on the necessary $E_{L,min}$ values in the case of pressure measurements than in the case of temperature measurements: If $\Delta A'_{0,p}$ is reduced to 25 % of the present value, $E_{L,min}$ drops by only around 45 % for 100-pulse-averaged measurements when considering 3-σ uncertainties. This low influence of laser-power-independent noise is clear, since the larger E_L gets (e.g. as also necessary for 10-pulse-averaged measurements), the more the measurement uncertainty $\Delta X_{stat,p}$ is dominated by the right summand of eq. (8.4.4), i.e. noise components which are dependent on the laser power, as the photon shot noise.

The obtained values for $E_{L,min}$ are dependent on the mean values of $\Delta A'_0$ and $\Delta B'_0$ for temperature and density, respectively. These mean values, however, are not determinable from experiment with a negligible error, since their spreading is large (cf. Figure 8.4-3). Besides, although being practically irrelevant, the mean values do not account for the weak temperature dependence of $\Delta A'_0$ and $\Delta B'_0$ (sect. 8.4.2). Thus, upper and lower bounds for $E_{L,min}$ were calculated for temperature and pressure measurements, respectively. This was done by using the respective functions ΔX_{stat} with the average values of $\Delta A'_0$ and $\Delta B'_0$ increased or decreased by the amount of their standard deviations (≈ 20 %). The resulting bounds are shown in Figure 8.4-4 (bottom) and Figure 8.4-5 (bottom).

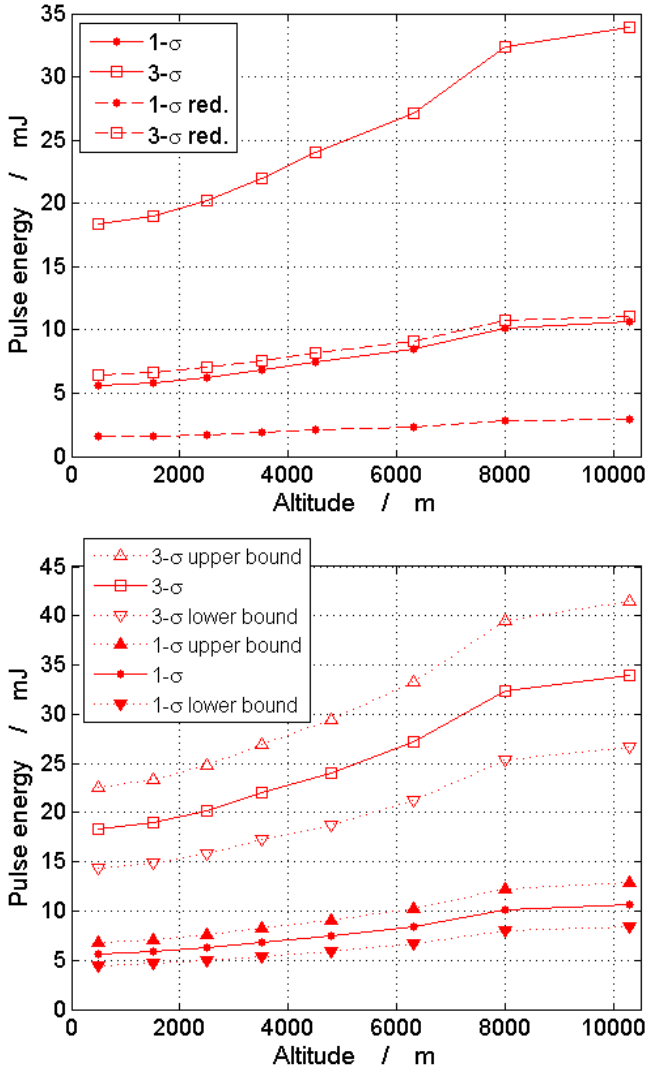

Figure 8.4-4. Top: Laser pulse energies $E_{L,min}$ necessary in order to meet the temperature measurement requirements at different measurement altitudes specified for aviation in sect. 2. The solid lines show the values obtained with the uncertainty functions $\Delta X_{stat,T}$ when analyzing the average of 100 pulses with the measurement apparatus. The dashed lines show the potential of uncertainty reduction when succeeding in lowering the non-laser-pulse-energy dependent noise. Bottom: Upper and lower bounds for $E_{L,min}$ when assuming both $\Delta A'_{0,T}$ and $\Delta B'_{0,T}$ being 20 % higher or lower, respectively.

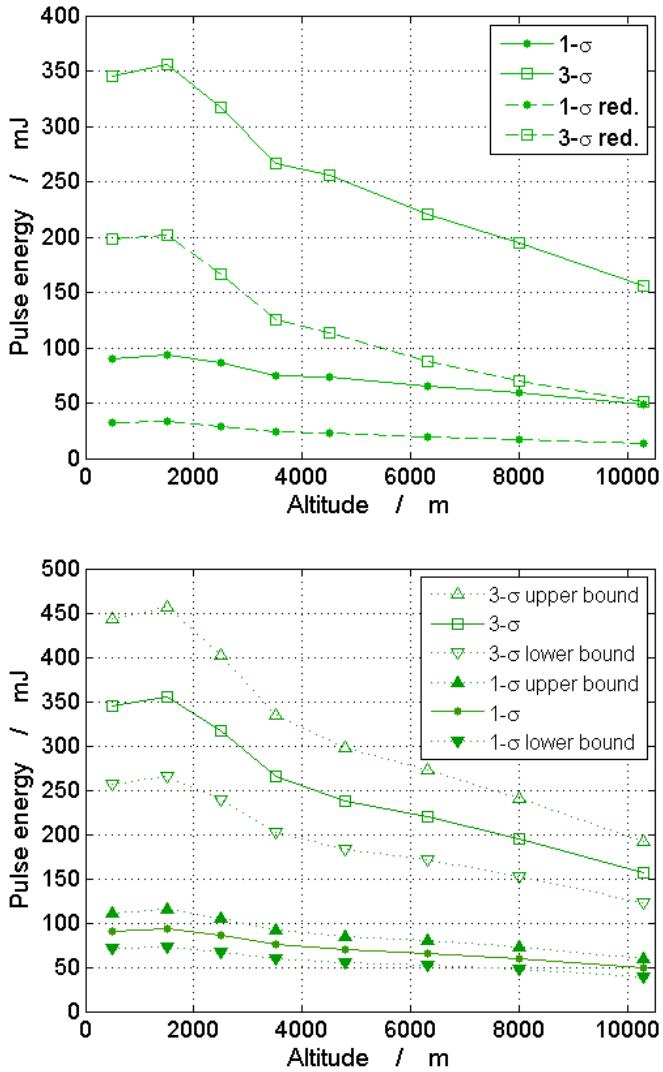

Figure 8.4-5. Same as Figure 8.4-4 but for air pressure measurements.

8.4.4 Required laser pulse energies at UV wavelengths

In sect. 8.4.3, the laser pulse energies $E_{L,min}$, which are necessary for the attainment of experimental statistical measurement uncertainties ΔT and Δp / p being smaller than the maximally allowable measurement errors in aviation (sect. 2) were assessed with the help of the functions $\Delta X_{stat,T}$ and $\Delta X_{stat,p}$. These resulting values for $E_{L,min}$, which refer to the utilization of the laboratory measurement apparatus including the laboratory laser with an emission wavelength of λ_L = 532 nm have been relatively large, especially for pressure measurements. Hence, in this section, the minimum laser pulse energies $E_{L,min}$ were estimated, when using the same measurement apparatus, but a laser with smaller emission wavelength λ_L. In sect. 7.10, the advantages and the issues of the usage of shorter laser wavelengths had already been discussed. For the extrapolation, here, the functions $\Delta X_{stat,T}$ and $\Delta X_{stat,p}$

were used as well. Additionally, the dependency of the detected signal power on λ_L was accounted for in $\Delta X_{stat,T}$ and $\Delta X_{stat,p}$. This was done by substituting n_E in eq. (8.4.3) by $n_E \cdot n_\sigma \cdot n_n$. The factor $n_\sigma = (532\ \text{nm})^4 / \lambda_L^4$ is the ratio of the RR backscattering cross sections (sect. 4.3) at 532 nm with regard to λ_L. $n_n = \lambda_L / 532\ \text{nm}$ is the ratio of the photon numbers at 532 nm with regard to λ_L for equal pulse energies at the two wavelengths. At all regarded laser wavelengths, equal detector quantum efficiencies as at 532 nm, i.e. 70 % (cf. Appendix B), were assumed.

Figure 8.4-6 (top) shows $E_{L,min}$ for 100-pulse-averaged temperature measurements as function of the laser wavelength λ_L. The pulse energies necessary at a measurement altitude of 10300 m, which is the worst case scenario for temperature measurements (see sect. 8.4.3), are taken as a basis for the calculations. Considering 1-σ (3-σ) measurement uncertainties, the required laser pulse energy drops to 3 mJ (10 mJ) for 355 nm laser wavelength and to 1.5 mJ (4 mJ) at 266 nm laser wavelength. The relative drop of $E_{L,min}$, if being capable of reducing the laser power independent noise quantified by $\Delta A'_{0,T}$ and $\Delta A'_{0,p}$ to 25 %, is the same as mentioned in sect. 8.4.3 and also comprised in Figure 8.4-6 (top; dashed lines). Figure 8.4-6 (bottom) shows the upper and lower bounds for $E_{L,min}$ values when assuming both $\Delta A'_{0,T}$ and $\Delta B'_{0,T}$ simultaneously being 20 % higher or lower, respectively (cf. sect. 8.4.3).

Figure 8.4-7 (top) illustrates $E_{L,min}$ for 100-pulse-averaged pressure measurements. Here, as opposed to temperature measurements, pulse energies necessary at a measurement altitude at 1500 m were taken as a basis for the calculations, since for pressure measurements the accuracy demands are highest at this altitude. Regarding 1-σ (3-σ) measurement uncertainties, $E_{L,min}$ decreases to 27 mJ (110 mJ) for 355 nm laser wavelength and to 12 mJ (45 mJ) for 266 nm laser wavelength. As explained for 532 nm in sect. 8.4.3, a reduction of $\Delta A'_{0,T}$ and $\Delta A'_{0,p}$ to 25 % has more positive effect when using generally smaller pulse energies, e.g. like in the case of temperature measurements. Figure 8.4-7 (bottom) shows the upper and lower bounds for $E_{L,min}$ when assuming both $\Delta A'_{0,p}$ and $\Delta B'_{0,p}$ simultaneously being 20 % higher or lower, respectively.

Table 8.4-1 summarizes the minimally required laser pulse energies $E_{L,min}$ obtained in sect. 8.4.3 and 8.4.4 from 100-pulse-average measurements with the current measurement setup. The table lists also the values required for 10-pulse-average measurements, which were obtained by repeating the whole analysis from sect. 8.4.1 to sect. 8.4.4 analogously. The values required for single-pulse measurements using the current measurement setup are too large to be applicable in an aircraft and are not listed. Moreover, Table 8.4-1 gives a rough estimation of the applicability of the potential laser source needed to perform the measurements with an update rate of 1 Hz. Highly precise (3-σ) temperature measurements are well feasible using UV laser sources, e.g. a 100 Hz laser with an average power of about 1 W. Density measurements, in contrast to that, pose an issue. Here, 100 Hz sources at 266 nm with an average power of about 4.5 W would be needed for high-precision measurements. A 450 mW laser and update rates of 0.1 Hz would rather be feasible. However, issues at 266 nm laser wavelengths are the availability of optics, the technical feasibility of the interference filters and ozone absorption (cf. sect. 7.10).

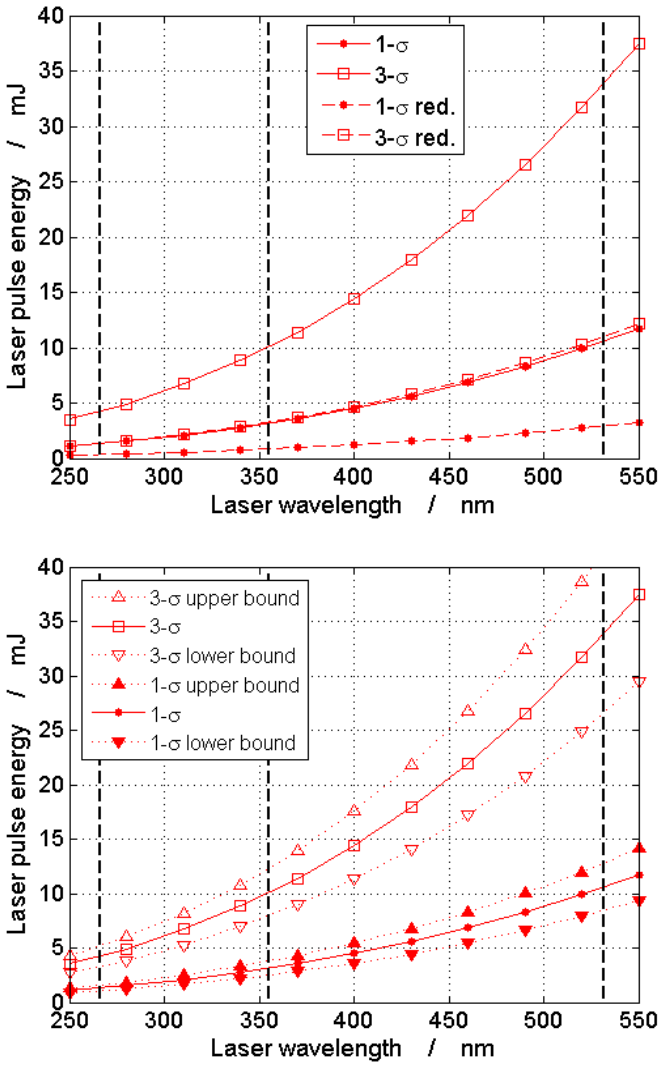

Figure 8.4-6. Top: Minimum laser pulse energies $E_{L,min}$ needed in order to meet the temperature measurement requirements for aviation (sect. 2) at different laser wavelengths λ_L. The values for $E_{L,min}$ are required when analyzing the average of 100 pulses. The measurement altitude is 10300 m, which poses the "worst case" for temperature measurements. The solid lines describe the values expected to be required with the current measurement apparatus, the dashed lines describe those expected to be required when reducing the noise, which is not dependent on the laser pulse energy to 25 %. Bottom: Upper and lower bounds for $E_{L,min}$ when assuming both $\Delta A'_{0,T}$ and $\Delta B'_{0,T}$ being 20 % higher or lower, respectively (cf. sect. 8.4.3).

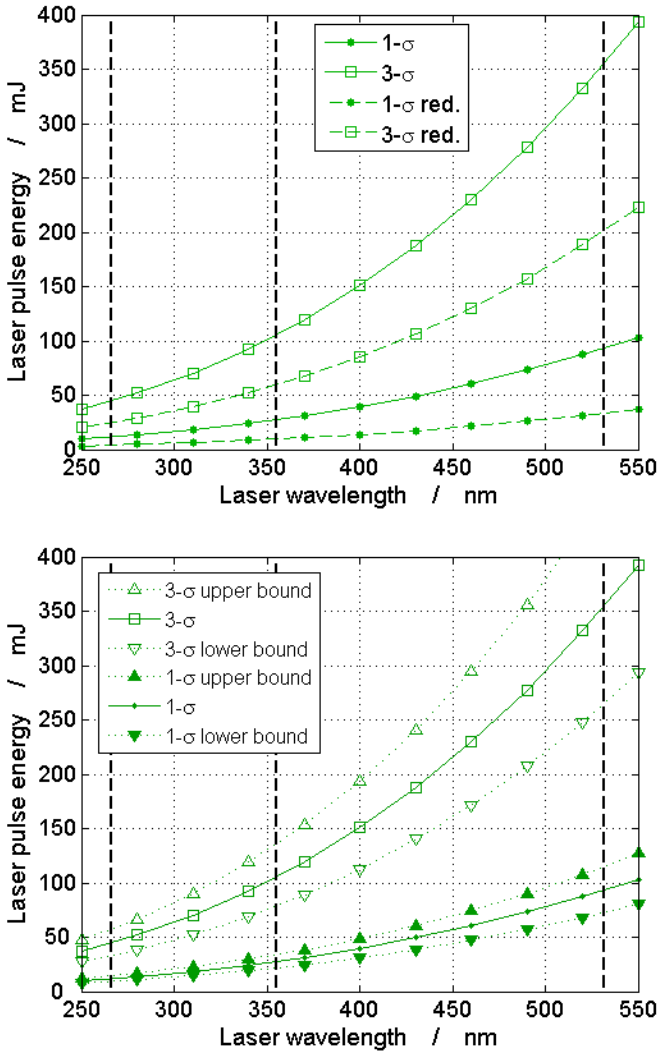

Figure 8.4-7. Same as Figure 8.4-6 but for air pressure measurements. Here, the measurement altitude is 1500 m, which poses the "worst case" for pressure measurements.

Table 8.4-1. Overview of the laser pulse energies necessary to reach the measurement error requirements specified in sect. 2 for 10-pulse-average measurements and 100-pulse-average measurements with the current measurement system. These values were discussed in sect. 8.4.3 and 8.4.4. A subjective assessment of the airborne applicability of a laser source in terms of radiation power making measurements with 1 Hz update rate possible is color coded: Red: rather unrealistic – Yellow: questionable – Green: realistic.

			532 nm	355 nm	266 nm
10 pulses	Temperature	1σ	35 mJ	10 mJ	4 mJ
10 pulses	Temperature	3σ	130 mJ	40 mJ	17 mJ
10 pulses	Pressure	1σ	380 mJ	115 mJ	47 mJ
10 pulses	Pressure	3σ	2100 mJ	650 mJ	270 mJ
100 pulses	Temperature	1σ	11 mJ	3 mJ	1.5 mJ
100 pulses	Temperature	3σ	35 mJ	10 mJ	4 mJ
100 pulses	Pressure	1σ	95 mJ	27 mJ	12 mJ
100 pulses	Pressure	3σ	355 mJ	110 mJ	45 mJ

9 Summary, conclusions and outlook

A novel concept for a short-range optical air data system for aircraft control and safety was developed. The measurement methodology is based on techniques known from lidar. These techniques are developed further exploiting four interference filter based measurement channels to detect elastic and Raman backscatter from air. A wide range of atmospheric parameters, such as temperature, molecular number density, pressure, humidity, and the particle backscatter coefficient can be acquired. With the latter two parameters, the system can distinguish between scattering coming from clouds or from other aerosol layers, e.g. volcanic ash. A computational model was programmed fully describing the optical, mechanical and geometrical setup of the laboratory apparatus prototype and allowing for the calculation of the power and the noise of all detected signals as a function of the fundamental system parameters. This permitted a performance analysis of the system in terms of measurement uncertainties. These uncertainties were modeled as being the result of the physically inherent statistical nature of the detected signal photons and the statistical noise generated by the detector electronics. Detailed design considerations and optimization calculations for the direct measurement parameters, notably air temperature and density, as well as pressure were made. Operation during daytime and in optically very dense clouds was simulated and the impact of the respective worst case scenarios on the systematic measurement errors as well as on the statistical measurement uncertainties was calculated quantitatively. Systematic errors generated by solar background radiation, elastic signal leakage to the RR channels, atmospheric signal extinction, and the presence of atmospheric water vapor, were regarded as well. Methods were proposed to correct these systematic errors, which, however, necessarily led to an increase of the statistical measurement uncertainties. This increase of the statistical measurement uncertainties due to systematic error correction was quantified as well.

Based on the results of the computational simulations, a first measurement system was designed and set up in the laboratory. The measurement system is composed of a 532 nm laser, a four channel receiver including data acquisition electronics and an atmospheric simulator for the generation of atmospheric states in terms of air temperature, pressure and moisture. The specification of the optical, mechanical and electronic core components as interference filters and photo detectors, which were custom-made, were worked out as well.

Laboratory experiments were performed validating the predictions from computational simulations with regard to systematic errors and statistical measurement uncertainties. Appearing differences between experiment and computational model were analyzed in detail. The systematic measurement errors experimentally achieved at air temperatures varying from 238 K to 308 K and constant air pressure are < 0.05 K, < 0.07 % and < 0.06 % for temperature, density and pressure, respectively. These errors are larger than the model calibration errors set by the individual calibration functions by a factor of about two only. The experimental systematic errors for measurements at air pressures varying from 200 hPa to 950 hPa and constant air temperature are < 0.22 K, < 0.36 % and < 0.31 %, respectively. Here, these errors are larger than in the case of measurements in constant air pressure, because the superimposed inaccuracies of the used hardware equipment itself weigh more, notably the nonlinearities of the vacuum gauge and of the used APD detectors. Before these measurements, these nonlinearities of the two RR APD detector responses had been reduced to a minimum by applying a correction function, respectively. Residual systematic error sources were analyzed in detail.

In order to minimize the statistical measurement uncertainties, especially for pressure measurements, the optimum central wavelengths of the RR filters were determined by simulations and verified experimentally. The experimental optimum CWLs for the used apparatus are 531.1 nm for filter RR1 and 528.6 nm for RR2, the theoretical ones are similar and 531.0 nm for RR1 and 528.8 nm. The minor differences are due to slightly differing assumptions made in the idealized model not really present in the experiment. The experimentally achieved 1-σ statistical measurement uncertainties for the analysis of each single detected signal pulse range from 0.75 K to 2.63 K for temperature, from 0.43 % to 1.21 % for density, and from 0.51 % to 1.50 % for pressure, respectively, for measurement altitudes of 0 m to 13400 m. Also here the experimental results were compared to those from the model, which was adapted to the exact measurement scenario present in the laboratory. Discrepancies between experiment and model were analyzed in detail and the model was refined in such a way to accurately describe the experimental uncertainties.

It was not possible in the laboratory to experimentally generate all of the measurement scenarios treated in the model simulations. Such scenarios are measurements while being exposed to strong daylight or measurements in clouds. However, since the simulation and experimental results were in good accordance in those scenarios which were experimentally examined, the theoretical simulations are expected to give a good estimation for the experimental performance also for those measurement scenarios not being generable in the laboratory. Although detected background light is normally eliminated by high-pass filtering, the background noise remains in the signals and the measurement uncertainties deteriorate. However, according to the simulations, this noise is expected to have a relatively small impact on the statistical measurement uncertainties. For operation during daytime being exposed to a solar background radiance of 500 mW / (m² sr nm), a value which was assumed to be the upper radiance limit, the above mentioned experimental temperature, density and pressure measurement uncertainties are expected to rise only maximally by a factor of about 1.1 at sea level and by a factor of 1.2 at altitudes of 13000m.

A significant source of error when using filters with insufficient suppression of the elastic backscatter is the elastic signal cross-talk in the rotational Raman channels in optically dense clouds with very high backscatter ratios. This leakage can be eliminated with the proposed correction technique using the signals detected in the elastic channel. The inherent statistical nature of this correction raises the measurement uncertainties. If the RR filter optical densities at the elastic wavelength are equal to only 6 - the maximum value that can be really guaranteed by the manufacturer - the measurement uncertainties in clouds with backscatter ratios of 10000 are expected to rise in the worst case by a factor of about 3.4 for temperature, 2.4 for density and 2.8 for pressure. For such significant increases, however, the leakage can be strongly reduced by shifting the pass-bands of the RR filters towards lower wavelengths, or can be virtually eliminated by cascading two equal filters in each RR channel. Improvements in interference filter technology will further reduce this error contribution.

Atmospheric particle extinction also present in dense clouds is expected to systematically degrade the density and pressure measurement errors. The temperature measurements are not affected. With the proposed correction technique, the extinction error in clouds with a backscatter ratio of up to about 100 can be reduced from the percentage range down to below 0.1 % for the signals in all four detector channels. For clouds with higher backscatter ratios, an additional extinction measurement might be needed, which can also be performed optically. In clear sky, extinction is fully negligible for the measurement configuration.

The density of atmospheric water vapor has to be measured as well in order to obtain the total density of moist air. Especially close to sea level, water vapor volume mixing ratios can be as high as a couple of percent. The determination of the water vapor density for very high mixing ratios of over 5 % leads to an increase of the total density uncertainty for measurements in moist air with respect to measurements in dry air. Simulation and experiment proved that this uncertainty increases with rising water vapor amount, i.e. it can reach the highest values close to sea level, where air is hottest. Experiments performed in the atmospheric simulator showed, that the maximum increase of the total density measurement uncertainty, which can be attained when water vapor is measured as well, is about 20 % (1-σ) for single pulse detection. Regarding the density measurement uncertainties which are far below 0.5 % at sea level, the absolute increase is very small. This is true even for very high water vapor mixing ratios up to 10 %, what is a value that covers and even exceeds those being common in reality. Measuring water vapor to determine the density of moist air affects also the pressure measurement uncertainty, since pressure is derived from density. However, the pressure measurement is affected less. The increase of the pressure measurement uncertainty in moist air is smaller and maximally 13 %. These values are well confirmed by the computational model calculations.

The qualification of such a measurement apparatus for aircraft control in aviation prerequisites the compliance with certain error margins set in aviation standards. The margin for temperature measurements at all flight altitudes is 1.5 K. Those for pressure measurements at altitudes from 0 m to 13000 m range from 0.1 % to 0.5 %, respectively. Because the measurement uncertainties can be reduced by raising the laser pulse energy, the aviation standards identify minimum laser pulse energy values, which are necessary to meet the error requirements. The necessary laser pulse energies for the used measurement apparatus were determined experimentally. For 100-pulse-averaged temperature measurements, the energy has to be larger than 11 mJ (35 mJ), when regarding 1-σ (3-σ) uncertainties at all measurement altitudes. For 100-pulse-averaged pressure measurements, the laser pulse energy has to be larger than 95 mJ (355 mJ), when regarding 1-σ (3-σ) uncertainties at all measurement altitudes. For single pulse and for 10-pulse-averaged pressure measurements at 532 nm, the required laser pulse energy values are unrealistically large for application in an aircraft.

It was further shown, that especially the temperature measurement uncertainties correspondent to the required minimum laser pulse energies are largely dominated by laser-power-independent noise. If it were possible to reduce this noise to 25 % of the present value, the necessary pulse energies considering 3-σ temperature uncertainties would drop by around 65 % for 100-pulse-averaged measurements. In regard to pressure, this drop is 45 % for 100-pulse-averaged measurements. This uncertainty decrease is significant and shows the importance as well as the remaining potential of the measurement apparatus for reducing the measurement uncertainties by further improved low-noise detection and data acquisition equipment.

It was explained, that the utilization of UV laser wavelengths, e.g. 355 nm instead of 532 nm, will significantly reduce the required laser power, the contribution of solar background radiation and the backscatter ratios. Furthermore, it will drastically increase eye safety tolerance by 4 orders of magnitude. Thus, the experimental results concerning the required minimum laser pulse energies were extrapolated from 532 nm to UV wavelengths: With regard to 1-σ (3-σ) temperature uncertainties for 100-pulse-averaged measurements, the required laser pulse energy drops significantly to 3 mJ (10 mJ) at 355 nm and to 1.5 mJ (4 mJ) at 266 nm. Analogously, with regard to 1-σ (3-σ) pressure

uncertainties, the required laser pulse energy drops to 27 mJ (110 mJ) at 355 nm and to 12 mJ (45 mJ) at 266 nm. However, when decreasing the laser wavelength down to 266nm, ozone absorption has to be considered, which can be too high even at such short measurement distances.

Apart from the errors coming from the calibration functions, no measurement-system-related systematic errors were supposed to be present in the idealized computational model. In the experiments, however, it was proven that and quantified how much instable or inaccurate operation of the used hardware core components give rise to a significant proportion of the experimentally yield systematic measurement errors as well as to the statistical measurement uncertainties. Such components can be the laser source, the interference filters, the photo detectors, and the data acquisition electronics. As mentioned, the generated experimental errors and uncertainties were reduced to a minimum in the framework of this thesis and are very small. Nevertheless, as a conclusion from the error and uncertainty analysis carried out, some hardware modifications can be recommended, which are crucial for the further improvement of the measurement performance as well as the long-term stability of the measurement system: Based on simulation results and experiments, it was calculated, that the laser wavelength should be actively stabilized to better than 1 pm. This is advantageous for the suppression of both long term temperature wavelength drifts and of wavelength jitter from shot-to-shot. A single-mode laser with a more stable temporal pulse shape and more stable output pulse energy would be beneficial for reducing the measurement uncertainties as well. Calculations showed, that the interference filters should be simultaneously stabilized to better than 0.5 K, e.g. by means of a thermal housing, in order to sufficiently reduce wavelength drifts. Furthermore, the thermal drift of the highly temperature sensitive APD detectors in the RR channels should be even lower than 0.05 K. The 10 MHz AC high-pass filters of the current APD detectors should be removed. This will lead to signal gain and reduce thus the measurement uncertainties as well. At last, a reduction of the quantization noise, which is generated by the digitizing of the analogue detector output signals inside the oscilloscope, should be aspired, in order to further reduce the measurement uncertainties. This can be done by using a 12-bit oscilloscope, instead of the 8-bit one. Concerning the atmospheric simulator equipment, a more stable vacuum gauge with better linear response and better measurement repeatability will be advantageous for excluding systematic measurement errors resulting from hardware other than that of the laser and receiver system.

The next steps concerning the further development of the measurement system consist in modifying the apparatus to UV wavelengths and improving the mentioned hardware. The generally better signal-to-noise ratio achievable in the UV makes the use of UV lasers with lower pulse power and higher repetition rate possible. Such lasers are beneficial in terms of weight and cost reduction. The possibility for further size reduction of the receiver, especially concerning the receiver length, will raise its potential for the airborne implementation. Flight tests in different environments will give a final proof of suitability of the optical air data apparatus described in this thesis. Looking ahead, the application of such an apparatus in civil aviation will generate a dense high-update-rate network of a large variety of atmospheric data. This will give the possibility of data commercialization, as well as data assimilation in new highly accurate weather forecasting models.

Appendix A

Taking into account a more exact or more realistic ray propagation geometry inside each receiver channel, the backscattered and collected radiation from the measurement volume has to be considered inside each receiver channel as a divergent beam consisting of rays which pass each RR interference filter at different angles. This necessitates a modification of the transmission function $F_{RR}(\lambda,\varphi_{RR})$ leading to an effective transmission function $F_{RR,eff}(\lambda,\varphi_{RR})$. φ_{RR} is denoted as the angle of incidence, but means more exactly the tilting angel of the respective filter relatively to the channel axis. Regarding a divergent beam inside each receiver channel, φ_{RR} determines the real angles of incidence φ'_{RR} of all light rays of the divergent beam present inside the receiver. Correctly, $F_{RR}(\lambda,\varphi_{RR})$ has thus to be written as $F_{RR}(\lambda,\varphi_{RR},\varphi'_{RR})$. To obtain $F_{RR,eff}(\lambda,\varphi_{RR})$ for a desired *tilting* angle φ_{RR}, the transmission functions $F_{RR}(\lambda,\varphi_{RR},\varphi'_{RR})$ have to be summed over φ'_{RR} and weighted with their normalized frequency of occurrence $W(\varphi'_{RR})$:

$$F_{RR,eff}(\lambda,\varphi_{RR}) = \int_{-\pi/2}^{\pi/2} F_{RR}(\lambda,\varphi_{RR},\varphi'_{RR}) \cdot W(\varphi'_{RR}) d\varphi'_{RR} \quad . \tag{A.1}$$

$W(\varphi'_{RR})$ is calculated with the imaging equations for the lenses, the ray propagation geometry and the optical properties of the used channel components. φ'_{RR} is dependent on the scattering distance l_{scatt} and the point where the scattered light hits the collection lens defined by the polar coordinates of the lens r_{lens} and θ_{lens}. $W(\varphi'_{RR})\ d\varphi'_{RR}$ can be transformed into the product of the normalized lens area increment and the normalized product of the scattering distance increment and the solid angle $\Omega_{scatt}(l_{scatt})$ (see sect. 7.5):

$$W(\varphi'_{RR}) d\varphi'_{RR} = \frac{r_{lens} d\theta_{lens} dr_{lens}}{A_{lens}} \cdot \frac{\Omega_{scatt}(l_{scatt}) dl_{scatt}}{\int_0^{\infty} \Omega_{scatt}(l_{scatt}) dl_{scatt}} \quad . \tag{A.2}$$

A_{lens} is the area of the collection lens. Inserting eq. (A.2) into eq. (A.1) yields

$$F_{RR,eff}(\lambda,\varphi_{RR}) = \frac{\int_0^{\infty}\int_0^{2\pi}\int_0^{R_{lens}} F_{RR}(\lambda,\varphi_{RR},l_{scatt},r_{lens},\theta_{lens}) \cdot r_{lens} \cdot \Omega_{scatt}(l_{scatt}) dr_{lens} d\theta_{lens} dl_{scatt}}{A_{lens} \cdot \int_0^{\infty} \Omega_{scatt}(l_{scatt}) dl_{scatt}} \quad . \tag{A.3}$$

R_{lens} is the radius of the collection lens.

Appendix B

In the following, the formulas used for the noise analysis of the potential detector-amplifier systems are introduced. The formulas for the resulting detector output signal voltages and detector noise voltages in the four measurement channels RR1, RR2, CP and H_2O are given as well. The calculations are based on the electronic properties of the detectors and the optical input pulse powers $P_{rot,RR1}$, $P_{rot,RR2}$ and P_{CP} as well as P_{H2O} (sect. 7.3) expected in the respective channels. The technical data of the detector system components, which all meet the bandwidth requirement of 100 MHz (sect. 7.5), are included as well.

Three differently sensitive types of detection systems were assessed for their suitability to detect $P_{rot,RR1}$, $P_{rot,RR2}$, P_{CP} and P_{H2O}: A biased PIN diode with a 50 Ω load resistor, an avalanche photodiode (APD) followed by a transimpedance amplifier (TIA) and a photomultiplier tube (PMT) followed by a high-speed RF signal amplifier. The noise characteristics of detector components were calculated by the following formulas, which can be found in [136-139].

The output voltages $U_{out,PD}$ of the respective photo detector-amplifier system *PD = PIN*, *APD* or *PMT* are yield by:

$$U_{out,PD}\left(P_{opt}\right) = P_{opt} M_{tot,PD} \rho_{PD} R_{F,PD} \ . \tag{B.1}$$

P_{opt} is the optical pulse power falling onto the detector. $M_{tot,PD}$ is the total gain of the respective detector-amplifier system: For the PIN system $M_{tot,PIN} = M_{PIN} = 1$. For the APD system, the gain is that of the APD $M_{tot,APD} = M_{APD} = 1 – 200$. For the PMT system, the PMT gain $M_{PMT} = 10^3$ - 10^7 is multiplied with the gain of the RF amplifier $M_{RF} = 60$, so that $M_{tot,PMT} = M_{PMT} \cdot M_{RF}$. ρ_{PD} is the responsivity of the photo detectors at $M_{tot,PD} = 1$: $\rho_{PIN} = \rho_{APD} = 0.3$ A / W at 532 nm (quantum efficiency = 70 %) and 0.48 A / W at 660 nm (60 % higher than at 532 nm), $\rho_{PMT} = 0.075$ A / W. $R_{F,PD}$ is the load or feedback resistance turning photocurrent into a voltage. For the PIN system, $R_{F,PIN} = 50$ Ω. $R_{F,APD} = 2.5$ kΩ is the feedback resistance of the TIA. $R_{F,PMT} = 50$ Ω is the input impedance of the RF amplifier.

The noise voltages of the detector systems are assumed to be Gaussian with respect to amplitude distribution and white with respect to spectral distribution. The frequency filters limiting the detection bandwidth to frequencies of $B = 100$ MHz are assumed to have a square frequency response. The noise voltages $\Delta U_{sens,PD}$ of the photo sensors only (without amplifiers) of the detector system *PD = PIN, APD, PMT* are calculated by:

$$\Delta U_{sens,PD}\left(P_{opt}\right) = \sqrt{R_{F,PD}^2 \cdot 2e\left(I_{DS,PD} + M_{PD}^2 F_{PD}\left(I_{DB,PD} + \rho_{PD} P_{opt}\right)\right) \cdot B} \ . \tag{B.2}$$

e is the elementary charge, $I_{DS,PD}$ the surface leakage current (neglected). $I_{DB,PIN} = I_{DB,APD} = 1$ nA and $I_{DB,PMT} = 0.2$ nA are the respective dark currents. F_{PD} is the excess noise factor. PIN diodes have no excess noise: $F_{PIN} = 1$. For an APD:

$$F_{APD} = k_{eff} \cdot M_{APD}\left(1 - k_{eff}\right)\left(2 - 1/M_{APD}\right) , \tag{B.3}$$

with k_{eff} being the effective ratio of the electron to hole ionization coefficients. For VIS-light-sensitive silicon APDs k_{eff} = 0.02. In the case of PMTs [138]:

$$F_{PMT} = \delta/(\delta - 1) \,, \tag{B.4}$$

where δ = 6 is the secondary emission ratio (usually the average value is δ = 3 – 6, depending on the gain of the PMT). For the PMT, noise amplification by a factor of M_{RF} has to be accounted for.

The noise voltage $\Delta U_{amp,PD}$ generated by the amplifier is calculated as follows:

$$\Delta U_{amp,PD} = \sqrt{\left(e_{n,PD}^2 + 4k_B T_{PD} R_{F,PD} + \left(R_{F,PD} i_{n,PD} \right)^2 + \frac{\left(2\pi B C_{PD} e_{n,PD} R_{F,PD} \right)^2}{3} \right) \cdot B} \,. \tag{B.5}$$

T_{PD} = 300 K is the temperature of $R_{F,PD}$. Since the PIN detector system has only a 50 Ω load resistance, the second term describing the Johnson noise is relevant. The other terms are relevant for the TIA with $e_n = 1 \cdot 10^{-9}$ V / √Hz and $i_n = 2.5 \cdot 10^{-12}$ A / √Hz being the input voltage noise density and input current noise density. The last summand describes the generated TIA noise by its total input capacitance C_{TIA} = 10 pF (sum of amplifier input capacitances and photodiode capacitance). The noise generated by the RF amplifier is taken into account by the square root of its typical noise factor NF_{RF} = 1.8.

To obtain the total noise voltage $\Delta U_{out,PD}$ for the PIN and the APD system, the noise components of the photo sensor and the amplifying device are added quadratically according to the Gaussian error propagation law:

$$\Delta U_{out,PD}\left(P_{opt}\right) = \sqrt{\left(\Delta U_{sens,PD}\left(P_{opt}\right)\right)^2 + \left(\Delta U_{amp,PD}\right)^2} \,. \tag{B.6}$$

The total noise generated by the PMT system is calculated with $\Delta U_{out,PMT} = \Delta U_{sens,PMT} \cdot M_{RF} \cdot NF_{RF}$. Noise induced by further post processing electronics, e.g. oscilloscopes, is not considered.

The SNRs for the three detector systems are defined by $SNR_{PD} = U_{out,PD} / \Delta U_{out,PD}$ with *PD* = *PIN*, *APD* or *PMT*. The SNRs and thus the choice of the best detector type are dependent on the optical input pulse power (Figure A-1). The best detector system will yield the highest SNRs. The PIN diode is best for the detection of relatively strong optical pulse energies, where the noise contribution of the signal itself, the shot noise, is dominant ($\Delta U_{sens,PD} > \Delta U_{amp,PD}$). At lower signal amplitudes, the noise components of the electronics (and thus $\Delta U_{amp,PD}$) become dominant, making an amplification of the signal and thus the use of the APD detector system advantageous (in order to obtain $\Delta U_{sens,PD} \approx \Delta U_{amp,PD}$). At very weak optical signals necessitating very high signal amplification, intrinsic noise sources of the photo sensor like dark current and excess noise become dominant and have to be small. Here, although having lower quantum efficiency, the PMT detector system is favorable. In Figure A-1, the expected optical signals $P_{rot,RR1}$, $P_{rot,RR2}$, P_{CP} and P_{H2O} are marked as well, so that the optimum detector systems for the detection of these signals can be chosen. For the detection of $P_{rot,RR}$ as well as P_{H2O} the APD detector system is most suitable, whereas due to higher optical input signals, a PIN diode is best for the detection of P_{CP}.

Since SNR_{APD} is also a function of the APD-gain M_{APD}, the optimum values of M_{APD} maximizing SNR_{APD} were determined for the expected magnitudes of $P_{rot,RR}$ as well (Figure A-2). The optimum values are M_{APD} = 6.5 for RR signals measured at ground and M_{APD} = 12 for RR signals measured at 13000 m. The optimum value for M_{APD} increases with altitude due to weaker backscattered signals at higher altitudes. The best tradeoff for all altitudes is M_{APD} = 10. The SNRs achieved then differ by less than 1 % from the optimum ones. The optimum gain for the APD in channel H_2O is 5 times higher and around M_{APD} = 50 for a water vapor volume mixing ratio of 4 %. In the presented optimization and performance calculations, the output functions of the respectively optimized detectors used for the channels RR1, RR2, CP and H_2O are denoted as follows: U_{RR} = $U_{out,APD}$ with *RR* = *RR1* or *RR2*, U_{CP} = $U_{out,PIN}$ and U_{H2O} = $U_{out,APD}$ for the output signal voltages and $\Delta U_{RR} = \Delta U_{out,APD}$, $\Delta U_{CP} = \Delta U_{out,PIN}$ and $\Delta U_{H2O} = \Delta U_{out,APD}$ for the output noise voltages.

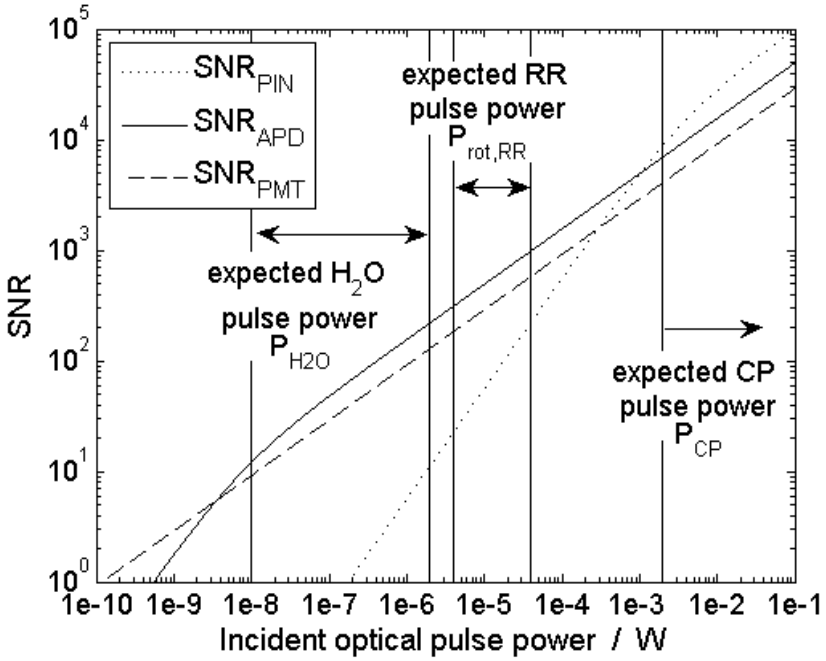

Figure A-1. Calculated SNRs for the four compared detector systems at their maximum gain for a detection bandwidth of 100 MHz. For the pulses detected in the RR channels and the H_2O channel APD systems are best, for the pulses in channel CP, the PIN system is best.

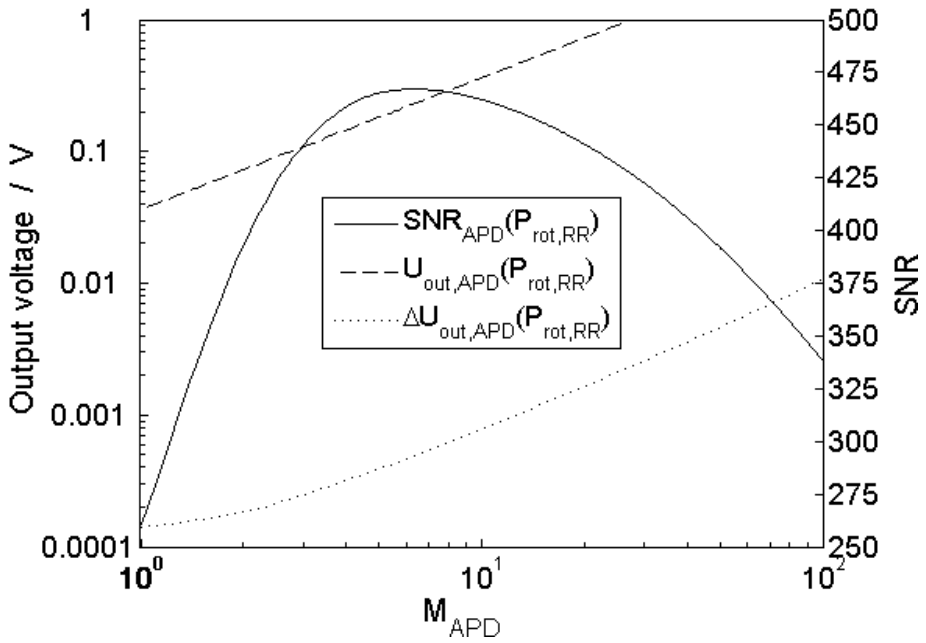

Figure A-2. Different noise components of the APD + TIA detector system and resulting optimum APD gain to be adjusted for the detection of the expected signal amplitudes at ground, shown exemplarily for the RR channels. The TIA-gain is adjusted to the maximum value determined by its gain-bandwidth-product and the 100 MHz detection bandwidth requirement. The optimum APD gain here is $M_{APD} = 6.5$.

Appendix C

In this appendix, the equations are presented which are used for the calculation of the air temperature, density, and pressure measurement uncertainties expected to be made with the laboratory measurement apparatus. They are used to optimize the CWLs of the RR filters (sect. 7.5) and to calculate the measurement uncertainty increase caused by correction of systematic errors, notably the error due to the detection of solar background (sect. 7.6) and the leakage error (sect. 7.7). Dependencies of the measurement uncertainty on the laser pulse energy (sect. 7.9) and the laser wavelength (sect. 7.10) were also examined with these equations. The detector output functions for each channel used in the following formulas are defined in Appendix B.

The detected rotational Raman radiation $P_{rot,RR}$ (sect. 7.5) (*RR* = *RR1* or *RR2*) can be superimposed by a solar background signal $P_{B,RR}$ (sect. 7.6) and a leaking elastic signal $P_{leak,RR}$ (sect. 7.7). The two latter signal contributions - if present, otherwise $P_{B,RR} = P_{leak,RR} = 0$ - are thus measured separately and subtracted from the total output signal in each RR channel to obtain the respective rotational Raman signal alone:

$$U_{RR}\left(P_{rot,RR}\right) = U_{RR}\left(P_{rot,RR} + P_{B,RR} + P_{leak,RR}\right) - U_{RR}\left(P_{B,RR}\right) - \kappa_{RR} U_{CP}\left(P_{CP}\right) . \qquad \text{(C.1)}$$

The signal leakage is measured indirectly with channel CP. κ_{RR} is the leakage correction factor (sect. 7.7). Since all measured signals are noisy, the total noise is increased after subtraction. The resulting total noise voltage $\Delta U_{tot,RR}$ is then according to the Gaussian error propagation:

$$\Delta U^2_{tot,RR}\left(P_{rot,RR}\right) = \Delta U^2_{RR}\left(P_{rot,RR} + P_{B,RR} + P_{leak,RR}\right) + \Delta U^2_{RR}\left(P_{B,RR}\right) + \kappa^2_{RR}\Delta U^2_{CP}\left(P_{CP}\right) . \qquad \text{(C.2)}$$

The first summand describes the noise of the total signal detected in an RR channel, the second one the uncertainty increase due to solar background correction, and the third one the uncertainty increase due to leakage correction. The 1-σ temperature measurement uncertainty $\Delta T = \Delta T_{calib}$ is calculated inserting eq. (C.1) and (C.2) in the formula adapted from [11]:

$$\Delta T = \frac{\partial T}{\partial Q}\Delta Q = \frac{\partial T}{\partial Q} Q \sqrt{\frac{\Delta U^2_{tot,RR1}}{U^2_{RR1}} + \frac{\Delta U^2_{tot,RR2}}{U^2_{RR2}}} \quad , \qquad \text{(C.3)}$$

with $Q = U_{RR2} / U_{RR1}$ defined in eq. (5.1.1).

The 1-σ relative density measurement uncertainty for dry air $\Delta N_{dry} / N_{dry} = \Delta N_{calib} / N_{calib}$ is calculated using the partial derivatives of N_{calib} - defined in eq. (5.2.4) - and eq. (C.1) and (C.2):

$$\frac{\Delta N_{dry}}{N_{dry}} = \sqrt{\left(\frac{\partial N_{calib}}{\partial U_{RR1}}\Delta U_{tot,RR1}\right)^2 + \left(\frac{\partial N_{calib}}{\partial U_{RR2}}\Delta U_{tot,RR2}\right)^2} \Big/ N_{calib}$$

$$\frac{\Delta N_{dry}}{N_{dry}} = a \cdot \left[\left(\left(1 + c_2\frac{U_{RR2}}{U_{RR1}} + c_3\frac{U_{RR2}^2}{U_{RR1}^2}\right) + \left(U_{RR1} + c_1 U_{RR2}\right)\left(-c_2\frac{U_{RR2}}{U_{RR1}^2} - 2c_3\frac{U_{RR2}^2}{U_{RR1}^3}\right)\right)^2 \Delta U_{tot,RR1}^2\right.$$

$$\left. + \left(c_1\left(1 + c_2\frac{U_{RR2}}{U_{RR1}} + c_3\frac{U_{RR2}^2}{U_{RR1}^2}\right) + \left(U_{RR1} + c_1 U_{RR2}\right)\left(c_2\frac{1}{U_{RR1}} + 2c_3\frac{U_{RR2}}{U_{RR1}^2}\right)\right)^2 \Delta U_{tot,RR2}^2\right]^{\frac{1}{2}} \Big/ N_{calib}$$

(C.4)

In presence of moisture, the 1-σ relative density measurement uncertainty for moist air $\Delta N / N = \Delta N_{moist} / N_{moist}$ is given by

$$\frac{\Delta N}{N} = \frac{\Delta N_{moist}}{N_{moist}} = \sqrt{\left(\frac{\Delta N_{dry}}{N_{moist}}\right)^2 + \left(\frac{\Delta N_{H2O}}{N_{moist}}\right)^2} = \sqrt{\left(\frac{1}{1+M_{H2O}}\right)^2\left(\frac{\Delta N_{dry}}{N_{dry}}\right)^2 + \left(\frac{M_{H2O}}{1+M_{H2O}}\right)^2\left(\frac{\Delta N_{H2O}}{N_{H2O}}\right)^2} \quad ,$$

(C.5)

with the relative measurement uncertainty of the water vapor density $\Delta N_{H2O} / N_{H2O}$. The latter is equal to the relative measurement uncertainty of the output voltage U_{H2O} of channel H_2O:

$$\frac{\Delta N_{H2O}}{N_{H2O}} = \frac{\Delta U_{H2O}}{U_{H2O}} \quad , \tag{C.6}$$

with ΔU_{H2O} being the noise voltage of this channel.

The 1-σ relative pressure measurement uncertainty $\Delta p / p = \Delta p_{calib} / p_{calib}$ is the Gaussian sum of the ones for T and N:

$$\frac{\Delta p}{p} = \sqrt{\left(\frac{\Delta T}{T}\right)^2 + \left(\frac{\Delta N}{N}\right)^2} \quad . \tag{C.7}$$

Both rotational Raman signals $P_{rot,RR1}$ and $P_{rot,RR2}$ and thus $\Delta U_{tot,RR1}$, $\Delta U_{tot,RR2}$, and ΔT, $\Delta N / N$, $\Delta p / p$ are functions of the spectral transmission line shape $F_{RR1}(\lambda,\varphi_{RR1})$ and $F_{RR2}(\lambda,\varphi_{RR2})$ (sect. 6.4) and thus of the angles of incidence φ_{RR1} and φ_{RR2} and the CWLs of filter RR1 and RR2. This relation is used to minimize ΔT, $\Delta N / N$, $\Delta p / p$. Furthermore, $P_{rot,RR1}$ and $P_{rot,RR2}$ are functions of the laser pulse energy and the laser wavelength as well.

Appendix D

The extinction corrected density is derived in three steps. In step 1, the backscatter ratio R is measured with the two RR channels and channel CP (sect. 5.3). With R and the assumed lidar ratio $L_{par,ass}$, the extinction coefficient α_{par} is deduced:

$$\alpha_{par} = L_{par,ass} \cdot \beta_{par} = L_{par,ass} \cdot (R-1)\beta_{Cab} \ . \tag{D.1}$$

The molecular backscatter coefficient β_{Cab} is the product of the measured molecular air density $N_{meas} = N_{calib}$ (eq. (5.2.4)) and the Cabannes backscatter cross section $(\partial\sigma/\partial\Omega)^{\pi}_{Cab}$:

$$\beta_{Cab} = N_{meas} \cdot \left(\frac{\partial \sigma}{\partial \Omega} \right)^{\pi}_{Cab} \ . \tag{D.2}$$

The transmission τ_{par} is obtained from a calibration function $\tau_{par} = f(\alpha_{par})$. The calibration of τ_{par} has to be done beforehand with externally measured values of α_{par}.

In step 2, a first transmission corrected density $N_{meas,corr1}$ is calculated by

$$N_{meas,corr1} = \frac{N_{meas}}{\tau_{par}} \ . \tag{D.3}$$

In step 3, the two earlier steps are repeated with N_{meas} substituted by $N_{meas,corr1}$ and a new transmission value $\tau_{par,corr1}$ is obtained, by the help of which $N_{meas,corr2}$ - a more accurate density value - is calculated, and so on. The corrected density value is thus obtained iteratively. With the extinction corrected density value, the extinction corrected pressure value can then be obtained.

References

[1] Moir, I. and A. Seabridge, *Civil Avionics Systems*, 2003, Bury St Edmunds: Professional Engineering Publishing.

[2] Cézard, N., et al., *Performance evaluation of a dual fringe-imaging Michelson interferometer for air parameter measurements with a 355 nm Rayleigh-Mie lidar.* Appl. Opt., 2009. **48**(12): p. 2321-2332.

[3] Jentink, H.W. and R.K. Bogue, *Optical air flow measurements for flight tests and flight testing optical flow meters.* NLR-TP-2005-256, 2005.

[4] Watkins, C.B., et al., *Molecular optical air data system (MOADS) prototype II*. in *Laser Radar Technology and Applications IX, Proceedings of the SPIE*. 2004.

[5] Schmitt, N.P., et al., *A340 flight test results of a direct detection onboard UV lidar in forward-looking turbulence measurement configuration*. in *15th Coherent Laser Radar Conference CLRC*. 2009. Toulouse, France.

[6] Rabadan, G.J., et al., *Airborne lidar for automatic feedforward control of turbulent in-flight phenomena.* J. Aircraft, 2010. **47**(2): p. 392-403.

[7] *Neslie Project*. [Retrieved October 2012]. Available from: http://www.neslie-fp6.org.

[8] *Daniela Project*. [Retrieved October 2012]. Available from: http://www.danielaproject.eu.

[9] Cooney, J.A., *Measurement of Atmospheric Temperature Profiles by Raman Backscatter*. J. Appl. Meteorol., 1972. **11**: p. 108-112.

[10] Behrendt, A., *Fernmessung atmosphärischer Temperaturprofile in Wolken mit Rotations-Raman-Lidar*. PhD Thesis, University of Hamburg, Department of Physics, 2000.

[11] Radlach, M., A. Behrendt, and V. Wulfmeyer, *Scanning rotational Raman lidar at 355 nm for the measurement of tropospheric temperature fields.* Atmos. Chem. Phys., 2008. **8**: p. 159-169.

[12] *Aerospace Standard AS8002: Air data computer - Minimum performance standard*. SAE International - The Engineering Society For Advancing Mobility Land Sea Air and Space. [Retrieved October 2012]. Available from: www.sae.org.

[13] *International Standard Atmosphere*. International Civil Aviation Organization. [Retrieved October 2012]. Available from: http://www.icao.int.

[14] Mason, J.B., *Lidar Measurement of Temperature: a New Approach.* Appl. Opt., 1975. **14**(1): p. 76-78.

[15] Bösenberg, J., *Differential-Absorption Lidar for Water Vapor and Temperature Profiling*, in *Lidar: Range-Resolved Optical Remote Sensing of the Atmosphere*, C. Weitkamp, Editor 2005, Springer Series in Optical Sciences: New York. p. 213-239.

[16] Theopold, F.A. and J. Bösenberg, *Differential absorption lidar measurements of atmospheric temperature profiles: Theory and experiment.* J. Atmos. Ocean. Tech., 1993. **10**: p. 165-179.

[17] Ansmann, A., *Errors in ground-based water-vapor DIAL measurements due to Doppler-broadened Rayleigh backscattering.* Appl. Opt., 1985. **24**(21): p. 3476-3480.

[18] Browell, E.V., S. Ismail, and S.T. Shipley, *Ultraviolet DIAL measurements of O3 profiles in regions of spatially inhomogeneous aerosols.* Appl. Opt., 1985. **24**(17): p. 2827-2836.

[19] Bösenberg, J., *Ground-Based Differential Absorption Lidar for Water-Vapor and Temperature Profiling: Methodology.* Appl. Opt., 1998. **37**(18): p. 3845-3860.

[20] Wulfmeyer, V., *Ground-Based Differential Absorption Lidar for Water-Vapor and Temperature Profiling: Development and Specifications of a High-Performance Laser Transmitter.* Appl. Opt., 1998. **37**(18): p. 3804-3824.

[21] Proffitt, M.H. and A.O. Langford, *Ground-based differential absorption lidar system for day or night measurements of ozone throughout the free troposphere.* Appl. Opt., 1997. **36**(12): p. 2568-2585.

[22] Korb, C.L., et al., *Airborne and ground based lidar measurements of the atmospheric pressure profile.* Appl. Opt., 1989. **28**(15): p. 3015-3020.

[23] Bowman, M.R., A.J. Gibson, and M.C.W. Sandford, *Atmospheric Sodium measured by a Tuned Laser Radar.* Nature, 1969. **221**(5179): p. 456-457.

[24] Beatty, T.J., et al., *CEDAR lidar observations of sporadic Na layers at Urbana, Illinois.* Geophys. Res. Lett., 1988. **15**(10): p. 1137-1140.

[25] Hake, R.D., et al., *Dye-laser observations of the nighttime atomic sodium layer.* J. Geophys. Res., 1972. **77**(34): p. 6839-6848.

[26] Tilgner, C. and U. von Zahn, *Average properties of the sodium density distribution as observed at 69°N latitude in winter.* J. Geophys. Res.-Atmos., 1988. **93**(D7): p. 8439-8454.

[27] Felix, F., et al., *Laser Radar Observations of Atmospheric Potassium.* Nature, 1973. **246**(5432): p. 345-346.

[28] Jegou, J.-P., et al., *Lidar measurements of atmospheric lithium.* Geophys. Res. Lett., 1980. **7**(11): p. 995-998.

[29] Granier, G., J.P. Jégou, and G. Mégie, *Resonant lidar detection of Ca and Ca+ in the upper atmosphere.* Geophys. Res. Lett., 1985. **12**(10): p. 655-658.

[30] Granier, C., J.P. Jegou, and G. Megie, *Iron atoms and metallic species in the Earth's upper atmosphere.* Geophys. Res. Lett., 1989. **16**(3): p. 243-246.

[31] Gibson, A.J., L. Thomas, and S.K. Bhattachacharyya, *Laser observations of the ground-state hyperfine structure of sodium and of temperatures in the upper atmosphere.* Nature, 1979. **281**(5727): p. 131-132.

[32] Gelbwachs, J.A., *Iron Boltzmann factor LIDAR: proposed new remote-sensing technique for mesospheric temperature.* Appl. Opt., 1994. **33**(30): p. 7151-7156.

[33] Cattolica, R., *OH rotational temperature from two-line laser-excited fluorescence.* Appl. Opt., 1981. **20**(7): p. 1156-1166.

[34] Massey, G.A. and C. Lemon, *Feasibility of measuring temperature and density fluctuations in air using laser-induced O2 fluorescence.* IEEE J. Quant. Electron., 1984. **20**(5): p. 454-457.

[35] Tenti, G., C.D. Boley, and R.C. Desai, *Kinetic Models and Brillouin Scattering in a Molecular Gas.* Can. J. Phys., 1972. **50**(2158-2173).

[36] Tenti, G., C.D. Boley, and R.C. Desai, *On the Kinetic Model Description of Rayleigh-Brillouin Scattering from Molecular Gases.* Can. J. Phys., 1974. **52**(4): p. 285-290.

[37] Rye, B.J., *Molecular Backscatter Heterodyne Lidar: A Computational Evaluation.* Appl. Opt., 1998. **37**(27): p. 6321-6328.

[38] Seasholtz, R.G., A.E. Buggele, and M.F. Reeder, *Flow Measurements Based on Rayleigh Scattering and Fabry-Perot Interferometer.* Opt. Laser. Eng. , 1997. **27**: p. 543-570.

[39] Hua, D., M. Uchida, and T. Kobayashi, *Ultraviolet Rayleigh-Mie lidar with Mie-scattering correction by Fabry-Perot etalons for temperature profiling of the troposphere.* Appl. Opt., 2005. **44**(7): p. 1305-1314.

[40] Lock, J.A., R.G. Seasholtz, and W.T. John, *Rayleigh-Brillouin scattering to determine one-dimensional temperature and number density profiles of a gas flow field.* Appl. Opt., 1992. **31**(15): p. 2839-2848.

[41] Mielke, A., et al., *Time-average measurement of velocity, density, temperature, and turbulence velocity fluctuations using Rayleigh and Mie scattering.* Exp. Fluids, 2005. **39**(2): p. 441-454.

[42] Mielke, A.F., K.A. Elam, and C.J. Sung, *Development of a Rayleigh Scattering Diagnostic for Time-Resolved Gas Flow Velocity, Temperature, and Density Measurements in Aerodynamic Test Facilities*. in *Instrumentation in Aerospace Simulation Facilities, 2007. ICIASF 2007. 22nd International Congress on*. 2007.

[43] Schwiesow, R.L. and L. Lading, *Temperature profiling by Rayleigh-scattering lidar.* Appl. Opt., 1981. **20**(11): p. 1972-1979.

[44] Bruneau, D., *Mach-Zehnder Interferometer as a Spectral Analyzer for Molecular Doppler Wind Lidar.* Appl. Opt., 2001. **40**(3): p. 391-399.

[45] Stoffelen, A., et al., *The Atmospheric Dynamics Mission for global wind field measurement.* Bull. Am. Meteorol. Soc., 2005. **83**: p. 73-87.

[46] Shimizu, H., S.A. Lee, and C.Y. She, *High spectral resolution lidar system with atomic blocking filters for measuring atmospheric parameters.* Appl. Opt., 1983. **22**(9): p. 1373-1381.

[47] Hair, J.W., et al., *High-Spectral-Resolution Lidar with Iodine-Vapor Filters: Measurement of Atmospheric-State and Aerosol Profiles.* Appl. Opt., 2001. **40**(30): p. 5280-5294.

[48] Piironen, P. and E.W. Eloranta, *Demonstration of a high-spectral-resolution lidar based on an iodine absorption filter.* Opt. Lett., 1994. **19**(3): p. 234-236.

[49] Alvarez, R.J., et al., *High-Spectral Resolution Lidar Measurement of Tropospheric Backscatter Ratio Using Barium Atomic Blocking Filters.* J. Atmos. Ocean. Tech., 1990. **7**(6): p. 876-881.

[50] She, C.Y., et al., *High-spectral-resolution Rayleigh-Mie lidar measurement of aerosol and atmospheric profiles.* Opt. Lett., 1992. **17**(7): p. 541-543.

[51] Voss, E., C. Weitkamp, and W. Michaelis, *Lead-vapor filters for high-spectral-resolution temperature lidar.* Appl. Opt., 1994. **33**(15): p. 3250-3260.

[52] Yalin, A.P. and R.B. Miles, *Ultraviolet filtered Rayleigh scattering temperature measurements with a mercury filter.* Opt. Lett., 1999. **24**(9): p. 590-592.

[53] Zetterberg, J., et al., *Two-Dimensional Temperature Measurements in Flames Using Filtered Rayleigh Scattering at 254 nm.* Appl. Spectrosc., 2008. **62**(7): p. 778-783.

[54] Bloom, S.H., et al., *Helicopter plume detection by using an ultranarrow-band noncoherentlaser Doppler velocimeter.* Opt. Lett., 1993. **18**(3): p. 244-246.

[55] Gölz, P. and P. Andresen, *Atomic vapor filter for two-dimensional Rayleigh imaging experiments with a narrow-band KrF excimer laser.* Appl. Opt., 1996. **35**(30): p. 6054-6061.

[56] *Ophir Corporation*. [Retrieved October 2012]. Available from: www.ophir.com.

[57] Boguszko, M. and G.S. Elliott, *On the use of filtered Rayleigh scattering for measurements in compressible flows and thermal fields.* Exp. Fluids, 2005. **38**(1): p. 33-49.

[58] Forkey, J.N., et al., *Demonstration and characterization of filtered Rayleigh scattering for planar velocity measurements.* AIAA J., 1996. **34**(3): p. 442-448.

[59] Esselborn, M., *Lidar-Messung der Extinktion des atmosphärischen Aerosols am Beispiel der Feldstudie SAMUM-1*. PhD Thesis, Ludwig-Maximilians-Universität München, Department of Physics, 2008.

[60] She, C.-Y., *Spectral Structure of Laser Light Scattering Revisited: Bandwidths of Nonresonant Scattering Lidars.* Appl. Opt., 2001. **40**(27): p. 4875-4884.

[61] Witschas, B., et al., *Spontaneous Rayleigh-Brillouin scattering of ultraviolet light in nitrogen, dry air, and moist air.* Appl. Opt., 2010. **49**(22): p. 4217-4227.

[62] Miles, R.B., W.R. Lempert, and J.N. Forkey, *Laser Rayleigh scattering.* Meas. Sci. Technol., 2001. **12**(5): p. R33.

[63] Cooney, J. and M. Pina, *Laser radar measurements of atmospheric temperature profiles by use of Raman rotational backscatter.* Appl. Opt., 1976. **15**(3): p. 602-603.

[64] Arshinov, Y.F., et al., *Atmospheric temperature measurements using a pure rotational Raman lidar.* Appl. Opt., 1983. **22**(19): p. 2984-2990.

[65] Vaughan, G., et al., *Atmospheric temperature measurements made by rotational Raman scattering.* Appl. Opt., 1993. **32**(15): p. 2758-2764.

[66] Nedeljkovic, D., A. Hauchecorne, and M.L. Chanin, *Rotational Raman lidar to measure atmospheric temperature from the ground to 30 km.* IEEE T. Geosci. Remote., 1993. **31**: p. 90-101.

[67] Zeyn, J., W. Lahmann, and C. Weitkamp, *Remote daytime measurements of tropospheric temperature profiles with a rotational Raman lidar.* Opt. Lett., 1996. **21**(16): p. 1301-1303.

[68] Arshinov, Y., et al., *Daytime operation of a pure rotational Raman lidar by use of a Fabry-Perot interferometer.* Appl. Opt., 2005. **44**(17): p. 3593-3603.

[69] Behrendt, A., et al., *Combined Raman lidar for the measurement of atmospheric temperature, water vapor, particle extinction coefficient, and particle backscatter coefficient.* Appl. Opt., 2002. **41**(36): p. 7657-7666.

[70] Behrendt, A., T. Nakamura, and T. Tsuda, *Combined temperature lidar for measurements in the troposphere, stratosphere, and mesosphere.* Appl. Opt., 2004. **43**(14): p. 2930-2939.

[71] Behrendt, A. and J. Reichardt, *Atmospheric temperature profiling in the presence of clouds with a pure rotational Raman lidar by use of an interference-filter-based polychromator.* Appl. Opt., 2000. **39**(9): p. 1372-1378.

[72] Radlach, M., *A scanning eye-safe rotational Raman lidar in the ultraviolet for measurements of tropospheric temperature fields*. PhD Thesis, University of Hohenheim, Department of Natural Sciences, 2008.

[73] Girolamo, P., et al., *Rotational Raman lidar measurements of atmospheric temperature in the UV.* Geophys. Res. Lett., 2004. **31**: p. L01106.

[74] Mattis, I., et al., *Relative-Humidity Profiling in the Troposphere with a Raman Lidar.* Appl. Opt., 2002. **41**(30): p. 6451-6462.

[75] Veselovskii, I.A., et al., *Raman lidar for the study of liquid water and water vapor in the troposphere.* Appl. Phys. B-Lasers O., 2000. **71**(1): p. 113-117.

[76] Whiteman, D.N., et al., *Demonstration measurements of water vapor, cirrus clouds, and carbon dioxide using a high-performance Raman lidar.* J. Atmos. Ocean. Tech., 2007. **24**(8): p. 1377-1388.

[77] Ivanova, I.D., L.L. Gurdev, and V.M. Mitev, *Lidar Technique for Simultaneous Temperature and Pressure Measurements Based on Rotational Raman Scattering.* J. Mod. Optic., 1993. **40**: p. 367-371.

[78] Young, A.T., *Rayleigh scattering.* Appl. Opt., 1981. **20**(4): p. 533-535.

[79] Young, A.T. and G.W. Kattawar, *Rayleigh-scattering line-profiles.* Appl. Opt., 1983. **22**(23): p. 3668-3670.

[80] Wandinger, U., *Raman Lidar*, in *Lidar: Range-Resolved Optical Remote Sensing of the Atmosphere*, C. Weitkamp, Editor 2005, Springer Series in Optical Sciences: New York. p. 241-271.

[81] Mie, G., *Beiträge zur Optik trüber Medien, speziell kolloidaler Metallösungen.* Ann. Phys., 1908. **25**: p. 377-445.

[82] Long, D.A., *The Raman Effect*, 2002, New York: John Wiley & Sons.

[83] Weber, A., *High-resolution rotational Raman spectra of gases*, in *Raman spectroscopy of gases and liquids*, A. Weber, Editor 1979, Springer: Berlin.

[84] Bunker, P.R., *Fundamentals of Molecular Symmetry*, P. Jensen, Editor 2005, IOP Publishing Ltd.

[85] Herzberg, G., *Molecular Spectra and Molecular Structure*, 1950, Krieger Publishing Company.

[86] Bendtsen, J., *The rotational and rotation-vibrational Raman spectra of $^{14}N_2$, $^{14}N^{15}N$ and $^{15}N_2$.* J. Raman Spectrosc., 1974. **2**: p. 133.

[87] Buldakov, M.A., I.I. Matrosov, and T.N. Popova, *Determination of the anisotropy of the polarizability tensor of the O_2 and N_2 molecules.* Opt. Spectrosc+, 1979. **46**(5): p. 488-489.

[88] Butcher, R.J., D.V. Willetts, and W.J. Jones, *On the Use of a Fabry-Perot Etalon for the Determination of Rotational Constants of Simple Molecules-The Pure Rotational Raman Spectra of Oxygen and Nitrogen.* Proc. R. Soc. Lond., A, 1971. **324**(1557): p. 231-245.

[89] Loëte, M. and H. Berger, *High resolution Raman spectroscopy of the fundamental vibrational band of $^{16}O_2$.* J. Mol. Spec., 1977. **68**(2): p. 317-325.

[90] Long, D.A., *Raman spectroscopy*, 1977: McGraw-Hill.

[91] Suschtschinskij, M.M., *Ramanspektren von Molekülen und Kristallen*, 1974: Heyden & Son.

[92] Placzek, G., *Rayleigh-Streuung und Raman-Effekt*, in *Handbuch der Radiologie*, G. Marx, Editor 1934, Akademische Verlagsgesellschaft. p. 205.

[93] Penney, C.M., R.L.S. Peters, and M. Lapp, *Absolute rotational Raman cross sections for N2, O2, and CO2.* J. Opt. Soc. Am., 1974. **64**(5): p. 712-716.

[94] Placzek, G. and E. Teller, *Die Rotationsstruktur der Ramanbanden mehratomiger Moleküle.* Zeitschrift für Physik, 1933. **81**(3-4): p. 209-258.

[95] Herzberg, G., *Molecular Spectra and Molecular Structure I. Spectra of Diatomic Molecules*, 1950: Van Nostrand.

[96] Born, M. and E. Wolf, *Principles of Optics*. 6th ed, 1980, Oxford: Pergamon.

[97] Bates, D.R., *Rayleigh scattering by air.* Planet. Space Sci., 1984. **32**: p. 785-790.

[98] Bucholtz, A., *Rayleigh scattering calculations for the terrestial atmosphere.* Appl. Opt., 1995. **34**(15): p. 2765-2773.

[99] Buck, A., *New equations for computing vapor pressure and enhancement factor.* J. Appl. Meteorol., 1981. **20**: p. 1527–1532.

[100] Avila, G., et al., *The rotational Raman spectra and cross sections of H2O, D2O, and HDO.* J. Mol. Spectrosc., 2003. **220**(2): p. 259-275.

[101] Avila, G., et al., *The Raman spectra and cross-sections of H2O, D2O, and HDO in the OH/OD stretching regions.* J. Mol. Spectrosc., 2004. **228**(1): p. 38-65.

[102] van de Hulst, H.C., *Light scattering by small particles*, 1981, Dover: New York.

[103] Bohren, C.F., *Absorption and scattering of light by small particles*, D.R. Huffmann, Editor 1983, Wiley-Interscience: New York.

[104] Mishchenko, M., *Scattering, Absorption, and Emission of Light by Small Particles*, L. Travis, Editor 2002, Cambridge University Press.

[105] Mishchenko, M.I., D.J. Wielaard, and B.E. Carlson, *T-matrix computations of zenith-enhanced lidar backscatter from horizontally oriented ice plates.* Geophys. Res. Lett., 1997. **24**(7): p. 771-774.

[106] Wang, R.T. and H.C. van de Hulst, *Application of the exact solution for scattering by an infinite cylinder to the estimation of scattering by a finite cylinder.* Appl. Opt., 1995. **34**(15): p. 2811-2821.

[107] Muinonen, K., et al., *Light scattering by randomly oriented crystals.* Appl. Opt., 1989. **28**(15): p. 3051-3060.

[108] Barber, P.W. and S.C. Hill, *Light Scattering by Particles: Computational Methods*, 1990, Singapore: World Scientific Publishing. 261.

[109] Mishchenko, M.I., J.W. Hovenier, and L.D. Travis, *Light scattering by nonspherical particles: theory, measurements, and applications*, 2000, San Diego Academic Press. 690.

[110] Measures, R.M., *Laser Remote Sensing*, 1984, New York: John Wiley & Sons.

[111] *libRadtran Program*. [Retrieved October 2012]. Available from: http://www.libradtran.org.

[112] Mayer, B. and A. Kylling, *Technical note: The libRadtran software package for radiative transfer calculations - description and examples of use.* Atmos. Chem. Phys., 2005. **5**(7): p. 1855-1877.

[113] *libRadtran Publication list*. [Retrieved October 2012]. Available from: http://www.libradtran.org/doku.php?id=publications.

[114] Wuttke, S. and G. Seckmeyer, *Spectral radiance and sky luminance in Antarctica: a case study.* Theor. Appl. Climatol., 2006. **85**(3-4): p. 131-148.

[115] Browell, E.V., S. Ismail, and W.B. Grant, *Differential absorption lidar (DIAL) measurements from air and space.* Appl. Phys. B, 1998. **67**: p. 399-410.

[116] Gelbwachs, J. and M. Birnbaum, *Fluorescence of Atmospheric Aerosols and Lidar Implications.* Appl. Opt., 1973. **12**(10): p. 2442-2447.

[117] Kitada, T., et al., *Strange Behaviour of the Measurement of Atmospheric Temperature Profiles of the Rotational Raman Lidar*. in *Proceedings of the 17th International Laser Radar Conference*. 1994. Sendai, Japan.

[118] Behrendt, A., *Temperature measurements with lidar*, in *Lidar: Range-Resolved Optical Remote Sensing of the Atmosphere*, C. Weitkamp, Editor 2005, Springer Series in Optical Sciences: New York. p. 273-305.

[119] Gasteiger, J., et al., *Volcanic ash from Iceland over Munich: mass concentration retrieved from ground-based remote sensing measurements.* Atmos. Chem. Phys., 2011. **11**(5): p. 2209-2223.

[120] Macleod, H.M., *Thin-Film Optical Filters*. 2. ed, 1986, Bristol: Adam Hilger Ldt.

[121] Fraczek, M., A. Behrendt, and N. Schmitt, *Laser-based air data system for aircraft control using Raman and elastic backscatter for the measurement of temperature, density, pressure, moisture, and particle backscatter coefficient.* Appl. Opt., 2012. **51**(2): p. 148-166.

[122] Galvez, M.C.D., M.C. Alarcon, and T. Kobayashi, *Angstrom coefficient of tropospheric cloud and aerosol derived from a three-wavelength Mie lidar system*. in *Lasers and Electro-Optics, 1999. CLEO/Pacific Rim '99. The Pacific Rim Conference on*. 1999.

[123] Bissonnette, L.R., *Lidar and Multiple Scattering*, in *Lidar: Range-Resolved Optical Remote Sensing of the Atmosphere*, C. Weitkamp, Editor 2005, Springer Series in Optical Sciences: New York. p. 43-103.

[124] Mattis, I., et al., *Multiyear aerosol observations with dual-wavelength Raman lidar in the framework of EARLINET*. J. Geophys. Res.-Atmos., 2004. **109**: p. 13203-.

[125] Mueller, D., et al., *Aerosol-type-dependent lidar ratios observed with Raman lidar.* J. Geophys. Res., 2007. **112**: p. D16202.

[126] Seifert, P., et al., *Cirrus optical properties observed with lidar, radiosonde, and satellite over the tropical Indian Ocean during the aerosol-polluted northeast and clean maritime southwest monsoon.* J. Geophys. Res., 2007. **112**: p. D17205.

[127] Whiteman, D.N., *Examination of the Traditional Raman Lidar Technique. I. Evaluating the Temperature-Dependent Lidar Equations.* Appl. Opt., 2003. **42**(15): p. 2571-2592.

[128] Whiteman, D.N., *Examination of the Traditional Raman Lidar Technique. II. Evaluating the Ratios for Water Vapor and Aerosols.* Appl. Opt., 2003. **42**(15): p. 2593-2608.

[129] *BGV B2 - Unfallverhütungsvorschrift Laserstrahlung*, April 1, 1988 as amended on January 1, 1997 with implementation instructions from October 1995 updated edition April 2007: Berufsgenossenschaft Elektro Textil Feinmechanik.

[130] Fortuin, J.P.F. and H. Kelder, *An ozone climatology based on ozonesonde and satellite measurements.* J. Geophys. Res., 1998. **103**: p. 31709-31734.

[131] Malicet, J., et al., *Ozone UV spectroscopy. II. Absorption cross-sections and temperature dependence.* J. Atmos. Chem., 1995. **21**(3): p. 263-273.

[132] Gurzadyan, G.G., V.G. Dmitriev, and D.N. Nikogosyan, *Handbook of nonlinear optical crystals*. 3. ed. Springer series in optical sciences. Vol. 64. 1999, Berlin, New York: Springer-Verlag.

[133] Fraczek, M., A. Behrendt, and N. Schmitt, *Optical air temperature and density measurement system for aircraft using elastic and Raman backscattering of laser light*. in *Electro-Optical Remote Sensing, Photonic Technologies, and Applications IV, Proceedings of the SPIE*. 2010.

[134] Fraczek, M., A. Behrendt, and N. Schmitt, *Short-range optical air data measurements for aircraft control using rotational Raman backscatter.* Opt. Express, 2013. **21**(14): p. 16398-16414.

[135] Shannon, C.E., *Communication in the presence of noise.* Proc. IRE, 1949. **37**(1): p. 10-21.

[136] Kovalev, V.A. and W.E. Eichinger, *Elastic Lidar.Theory, Practice, and Analysis Methods* 2004, Hoboken, N.J.: John Wiley & Sons.

[137] Wilson, J. and J.F.B. Hawkes, *Optoelectronics: An Introduction*, ed. P.J. Dean, 1983, London: Prentice-Hall International.

[138] Davis, C.C., *Lasers and Electro-Optics: Fundamentals and Engineering*, 1996, Cambridge, U.K.: Cambridge Univ. Press.

[139] Graeme, J., *Photodiode Amplifiers: Op Amp Solutions*, 1995, New York: McGraw-Hill.

Acknowledgments

I would like to take the opportunity to express my profound gratitude to Professor Dr. Volker Wulfmeyer, who gave me the possibility and created the basis for the composition of this dissertation at the Institute of Physics and Meteorology of the University of Hohenheim. I am sincerely grateful for his review of this dissertation.

I am especially thankful to Dr. Andreas Behrendt, Institute of Physics and Meteorology, University of Hohenheim, for his invaluable support and his friendly and continuous cooperativeness in all phases of my dissertation. All my appreciation.

I would like to cordially acknowledge Dr. Nikolaus Schmitt, who supervised me in EADS Innovation Works Germany, EADS Deutschland GmbH. He always found time to kindly help me with various scientific and technical problems and gave me much precious advice and motivation also for private life within the last years. Without him, this thesis would not have been possible.

Great thanks go to all my colleagues from the EADS Innovation Works Germany Optronics Team and, in particular, Wolfgang Rehm, Dr. Ulrich Martin, Hermann Diehl and Wolfgang Legner for the support in their domains of expertise and for many constructive discussions.

Thanks to my Ph.D. student colleagues at EADS notably Sebastian Beer, Natsuki Miyakawa, Kevin Müller, and Sumit Paul for having motivating conversations and a great time in the company's everyday life.

Furthermore, in particular, I would like to thank Felix Steinebach, whom I have known since the very first day of my studies and who was a true companion during the last ten years, both in professional as well as in private life. It is an honor for me to be your friend.

I am very grateful to Sarah for the patience, her understanding and her love. You had to miss out on a lot of things in the recent past. We'll catch up on everything.

Finally, many thanks to my family and my friends, who were always behind me. At this point, I would like to express all my gratitude to my grandparents. Their trust and belief in me made me the person I am today. Dziękuję Wam, moim dziadkom, za Waszą miłość, za Wasze zaufanie i Waszą wiarę we mnie.

Thanks to everyone, who contributed to the success of this work and whom I have not mentioned here by name.

Part of this work was carried out in the frame of the NESLIE project under contract AST5-CT-2006-030721 funded by the European Commission under FP6, and the DANIELA project under contract ACP7-GA-2008-212132 funded under FP7.